Computational Optimization of Minimum Ionizing Timing Detector Components
Improving Timing Resolution through Numerical Design Optimization

Reales Gutiérrez, G.

DOI
10.4233/uuid:3e64aa37-f3d5-4779-bb88-156e5e593790

Publication date
2025

Document Version
Final published version

Citation (APA)
Reales Gutiérrez, G. (2025). *Computational Optimization of Minimum Ionizing Timing Detector Components: Improving Timing Resolution through Numerical Design Optimization*. [Dissertation (TU Delft), Delft University of Technology]. https://doi.org/10.4233/uuid:3e64aa37-f3d5-4779-bb88-156e5e593790

Important note
To cite this publication, please use the final published version (if applicable).
Please check the document version above.

Computational Optimization of Minimum Ionizing Timing Detector Components

Improving Timing Resolution through Numerical Design Optimization

Computational Optimization of Minimum Ionizing Timing Detector Components

Improving Timing Resolution through Numerical Design Optimization

Dissertation

for the purpose of obtaining the degree of doctor
at Delft University of Technology
by the authority of the Rector Magnificus, prof. dr. ir. T.H.J.J. van der Hagen,
chair of the Board for Doctorates
to be defended publicly on
Monday 30 June 2025 at 17:30

by

Guillermo REALES GUTIÉRREZ

Master's Degree in Aeronautical Engineering, Higher Technical School of Aeronautical and Space Engineering, Technical University of Madrid, Spain.

This dissertation has been approved by the promotors. Composition of the doctoral committee:

Rector Magnificus,	chairperson
Prof.dr.ir. A. van Keulen,	Delft University of Technology, *promotor*
Dr. A. M. Aragón,	Delft University of Technology, *promotor*
Dr.ir. J. F. L. Goosen	Delft University of Technology, *copromotor*
Independent members:	
Prof.dr.ir. M. Langelaar	Delft University of Technology
Prof.dr. M. Spiropulu	California Institute of Technology
Dr. K. Dreimanis	Riga Technical University
Dr. R.E. Christiansen	Technical University of Denmark
Reserve member:	
Prof.dr.ir. Just Herder	Delft University of Technology
Other member:	
Dr. A. Bornheim	California Institute of Technology

The authors would also like to express appreciation to the MTD collaboration for its invaluable contributions.

Keywords: Numerical Optimization, Topology Optimization, Surface... Optimization, Scintillation, Thermoelectricity, Stress Constraints, Non-Convexity, Electromagnetics, Multi-Physics, Reliability, LYSO, Temperature, Thermoelectric cooler, Particle detector, timing resolution

Printed by: Gildeprint

Cover by: Guillermo Reales Gutiérrez

ISBN 978-94-6384-745-2

An electronic copy of this dissertation is available at
https://repository.tudelft.nl/.

Contents

Summary

The objective of particle detectors in high-energy physics research is to reveal the fundamental laws of nature. The Minimum Ionizing Particle Detector (MTD) has been designed to enhance the timing precision of the CMS (Compact Muon Solenoid) detector at CERN to 50 ps under the increased number of particle impacts after upgrading the Large Hadron Collider (LHC) to the High-Luminosity LHC. The Barrel Timing Layer (BTL) segment of the MTD uses silicon photodetectors (SiPMs), whose timing accuracy depends on their operating temperature and the number of photons they detect. This dissertation presents numerical methods to improve the timing precision of these SiPMs through the design of thermoelectrical coolers and scintillation crystals.

On the one hand, thermoelectrical coolers (TECs) can lower the SiPMs temperature, reducing signal-to-noise ratio and recovering radiation-induced damage through controlled annealing procedures. We provide an analytical model to study the landscape of TEC topology optimization with a lower temperature objective, power constraints and two density design variables. This study leads to the recommendation of penalization coefficients for SIMP (solid isotropic material with penalization) in the form of $k_p = k_\sigma > k_\alpha$ with k_p the thermal conductivity, k_σ the electrical conductivity and k_α the Seebeck's penalization coefficient to reduce the nonconvexity induced by the power constraint. These coefficients reduce nonconvexity from power constraints, allowing FEM topology optimization via SIMP to achieve lower material volumes and temperatures without volume constraints and filtering schemes. FEM optimization examples are provided, which incorporate electrical working points through a voltage gradient design variable and constant material properties. These examples reduce the temperature by up to 10 °C compared to the optimal electrical working point of the original designs. Finally, comparing these results with designs with non-linear, temperature-dependent properties shows that the use of constant material properties can lower computational costs and improve design performance. Although optimized designs achieve lower temperatures, TECs are fragile. The construction of the BTL highlights this fragility, prompting an extension of the design to address operational thermal and mechanical loads. This work introduces a FEM-based topology optimization for the coupled thermoelectromechanical problem using SIMP. This also includes the formulation with nonlinear material properties, and how to deal with the checkerboarding with the extended mechanical degreeCelsiuss of freedom. The optimized designs reduce stress concentrations by half while enhancing cooling capabilities.

On the other hand, we complement the lower signal-to-noise ratio obtained from using TECs, with an increased number of photon impacts enhancing the SiPM signal. The number of photons created or the scintillation light yield depends on the material composition of the scintillators. However, the photon arrival count at SiPMs is influenced by their reflective surfaces and volume. We provide a model of BTL within GEANT4, a ray-

tracing particle-matter interaction software. This model incorporates the effect of the particle impact location and is used in conjunction with NSGAII (non-dominated sorting genetic algorithm) to optimize scintillator shapes to increase the photon detection count. The study uses multiple objective functions based on the stochastic nature of the arrival photons. From these results, the recommended objective function is the mean light collection per energy deposition and the ionizing particle track length, reducing statistical errors and accounting for energy deposition. The results provide relative gains to the original designs in the objective function between 15 and 38%.

To overcome the computational limits of Monte Carlo methods, we follow up by translating the scintillation equations into a transient wave for FEM simulations, matching GEANT4 pulse shapes. Furthermore, we perform a shape optimization using a static frequency domain scintillation model replicating the variable influence within GEANT4. The optimal designs obtained with FEM are validated within GEANT4, obtaining gains of the order of 7.7%. These gains were achieved with less than 1% of the computational resources needed to perform the GEANT4 optimizations.

1

Introduction

One of the main objectives of particle detectors is to detect, trace, and measure the behaviour of subatomic particles originating from a collision or a decay, an event. The beginning of particle detectors can be traced to the discovery of radioactivity by H. Becquerel in 1896 through the blackening of a photographic plate from the radiation emitted by a uranium sample. Since then, methods have been refined to detect and accurately measure their energy and momentum and define the spatial coordinates of their tracks. Today, detection is performed mainly through electronic means with e. g., silicon pixel detectors, with ever-increasing data rates of up to GHz in the form of time (ps), spatial location (µm) and energy resolutions (eV) [1]. These technologies have been transferred to other industries and fields. In the security sector, we can find particle detectors as airport scanners to avoid transporting radioactive substances [2] or detecting explosives using diffraction methods [3]. We can find examples of particle detectors to monitor our health, from simple X-ray scanners to PET (positron emission tomography) and SPECT (magnetic resonance imaging). Advances in particle detectors applied to medicine allow for early detection of possible diseases (such as different cancers and Alzheimer's disease) with lower risk of harm to the patient and a higher likelihood of recovery [4, 5]. Many industries also look at this technology to prospect underground cavities through muography [6] or to verify the structural integrity of inaccessible structures [7]. These detectors are also fundamental for studying material structures at the smallest scales using techniques such as scanning electron microscopy or x-ray diffraction [8]. Finally, these detectors are indispensable for high-energy physics research, enabling scientists to study the fundamental constituents of matter and the forces that govern their interactions with measurements of the particles corresponding to the boson of Higgs in 2012 [9].

The discovery of the Higgs boson happened at CERN, which houses the world's largest and most powerful particle accelerator today, the Large Hadron Collider (LHC). The LHC allows proton collisions at energies up to 7 TeV, meaning that each proton bunch, a tightly packed group of protons, is accelerated to an energy level 7 trillion times greater than an electron at rest, allowing the study of fundamental particles and forces at unprecedented scales. The LHC consists of an accelerator ring with two beams circulating in opposite directions and 4 experiments along its 27 km circumference. The LHC will be upgraded to the High-Luminosity LHC (HL-LHC) [10] in the next maintenance period or

1

long shutdown (LS), namely LS3, starting 2026. The upgrade of LHC has as an objective the increase in its luminosity, defined as the rate at which the particles collide in the accelerator per cross-sectional area, from the nominal luminosity of LHC of 10^{34} s/cm^2 to a $5-7$ times higher value. This increase in luminosity is expected to provide further insights into previously unknown particle physics phenomena and reduce the uncertainty on the current measurements taken by LHC, e. g., the Higgs boson mass. This higher luminosity working regime will be performed continuously under nominal operation with proton-proton collisions of up to 14 TeV.

The Compact Muon Solenoid (CMS, [11]) experiment is a general-purpose particle detector positioned around an interaction point of the LHC designed to measure the mass and momentum of particles produced in proton-proton collisions, allowing a complete reconstruction of the event. This is achieved through multiple detectors working together in a cylindrical shape around the collision point. Figure 1.1 shows a cross section of the barrel part of CMS, highlighting a segment through the $x-y$ plane and example particle tracks, including muons, electrons, photons, and hadrons. The Tracker detector first captures the path of charged particles as they move through a 4 T magnetic field. Beyond the Tracker, the electromagnetic calorimeter (ECAL), made from dense lead tungstate crystals, absorbs photons and electrons, converting their energy into detectable light. Next, the hadronic calorimeter (HCAL) absorbs hadrons, such as protons and neutrons, using alternating layers of dense absorber materials such as brass and scintillating tiles to measure their energy. Surrounding these systems is the superconducting solenoid, which generates the powerful 4 T magnetic field that curves the paths of charged particles, allowing their momentum to be measured. This large solenoid is supported by the Iron Yoke, which also serves a dual purpose: enhancing the magnetic field and housing the Muon Chambers. The muon chambers, made from drift tubes, cathode strip chambers, and resistive plate chambers, detect muons that penetrate the entire detector, as muons are less likely to be absorbed by the calorimeters. To fully enclose the collision point, the cylindrical barrel, whose cross section is shown in Figure 1.1, is enclosed with disk-like structures called endcaps with the same working as the barrel layers for particles emitted at small angles with respect to the beam.

The current configuration of the CMS meets operational requirements, but the upcoming high-luminosity phase will challenge the event reconstruction algorithms. These systems are responsible for identifying and linking each detected particle to its specific collision point (vertex). Currently, in each bunch crossing, approximately 20 events are produced; this number is expected to increase by an order of magnitude to around 200 with HL-LHC [10]. As the luminosity increases, CMS will face difficulties in distinguishing between collisions that occur very close together in space, relying solely on spatial information from the detected particles. To overcome this, a "4D" reconstruction algorithm is proposed. This approach considers not only the spatial trajectory of particles but also their precise flight time, which will help differentiate collisions that occur close to each other in both space and time. Figure 1.2 illustrates the improvement offered by such a timing detector with a resolution of 30 ps. In this figure, the x axis represents the position along the beam line, with zero indicating the designed collision point for both opposing beams, and the y axis represents time, with zero corresponding to the moment when the proton bunches completely overlap. The red dots show collision

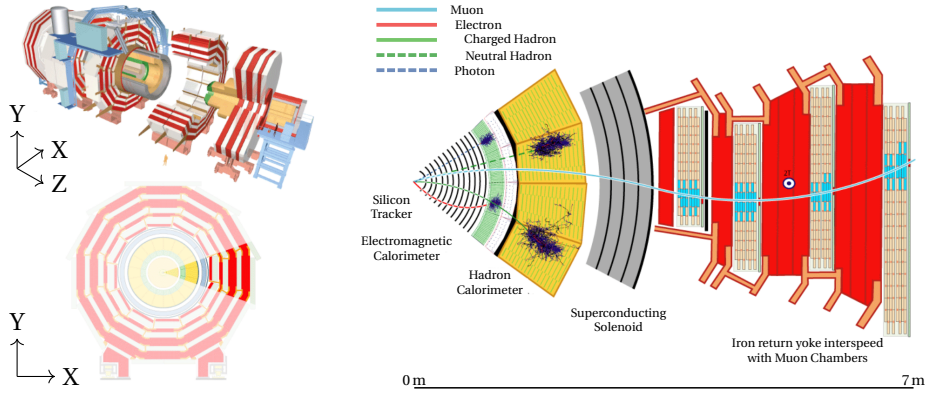

Figure 1.1.: Cross-sectional view of the CMS detector at CERN's LHC, showing its major components: the silicon tracker, electromagnetic and hadron calorimeters, superconducting solenoid, and muon chambers. The detector identifies particles such as muons, electrons, hadrons, and photons based on their interaction with these layers. Particle trajectories are illustrated in different colors: muons (blue), electrons (red), charged hadrons (green), neutral hadrons (green dashed), and photons (blue dashed). This figure has been modified from David Barney [12].

vertices reconstructed without using timing information, where the system struggles to separate collisions that occur close together in the z direction (along the beam). In contrast, the blue circles and black crosses depict the results of the 4D reconstruction using the proposed timing detector. These results show that the algorithm can clearly separate events that would otherwise appear merged, providing a significant improvement in accuracy, reducing the likelihood of merging nearby collisions.

The timing information of the particles will be incorporated into the CMS through a new timing detector, the MTD [14]. This detector is a specialized time-of-flight detector capable to distinguish events happening in quick succession. As this detector is introduced in an upgrade of CMS, this will take the space previously allocated to a heat screen to avoid heat transfer between the Tracker and ECAL detectors with a maximum radial envelope of 40 mm. The modular design of BTL includes 72 trays comprising independent electronics and cooling systems. Each tray has 2 cooling loops that carry biphasic CO2 (in gas and liquid state) for cooling purposes, read-out electronics, and 72 sensing modules. Each module is then comprised of two photodetector and scintillator packages, a copper housing, read-out electronics for each package, and an insulation layer. Finally, each photodetector and scintillator package comprises 16 scintillator bars, 32 SiPMs or silicon photomultipliers, and 4 thermoelectrical coolers within the same electronic board. This package is the smallest sensing unit in the barrel timing layer (BTL). It is in these scintillation crystals that the energy deposited by the ionising particles is converted into light, and the photodetectors transform these photons into an electric signal, which we can postprocess. This entire assembly is exemplified in Figure 1.3 for one tray.

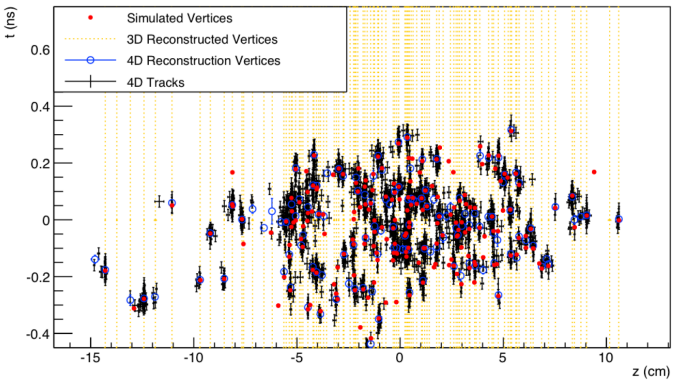

Figure 1.2.: Simulated and reconstructed vertices in a bunch crossing with 200 pileup interactions, assuming a MIP timing detector with 30 ps time resolution covering the barrel and endcaps. The horizontal axis is the z position along the beam line, where the 0 is the centre of the IR. The vertical axis is time, with 0 being the point in time when the beams completely overlap in z. The simulated vertices are the red dots. The vertical yellow lines indicate 3D-reconstructed (i. e., no use of timing information) vertices, with instances of vertex merging visible throughout the display. The black crosses and the blue open circles represent tracks and vertices reconstructed using a method that includes the time information and is therefore referred to as 4D. Many of the vertices that appear to be merged in the spatial dimension are clearly separated when time information is available. This figure and description are taken from CMS [13].

Considering all the BTL detector components, the overall timing precision can be calculated through the quadratic sum of each element's standard deviation from the optical processes to the electrical readout. This can be written as

$$\sigma_t = \sqrt{\left(\sigma^{clock}\right)^2 + \left(\sigma^{digi}\right)^2 + \left(\sigma^{ele}\right)^2 + \left(\sigma^{phot}\right)^2 + \left(\sigma^{DCR}\right)^2}. \tag{1.1}$$

This expression assumes all contributions are statistically uncorrelated, allowing the total variance to be expressed as the sum of individual variances. In the previous equation, the different components that affect total timing resolution σ_t are defined as the clock reference system σ^{clock}, the digitation process σ^{digi}, the electronics σ^{ele}, the photon detection σ^{phot}, and the dark count rate σ^{DCR}. σ^{clock} measures uncertainty from time reference systems. σ^{digi} represents errors in the conversion of analogue to digital signals. Electronics introduce noise and delay that affect the measurement (σ^{ele}). σ^{phot} covers time uncertainty in detecting photons due to their arrival times from their generation location within the scintillator. Finally, σ^{DCR} measures the uncertainty due to the dark count rate (DCR). This DCR is the main source of noise in the SiPMs, resulting from thermally generated electrons that create an avalanche in the photodiode. The overall timing resolution of BTL is estimated to be less than 50 ps at the end of life. These results

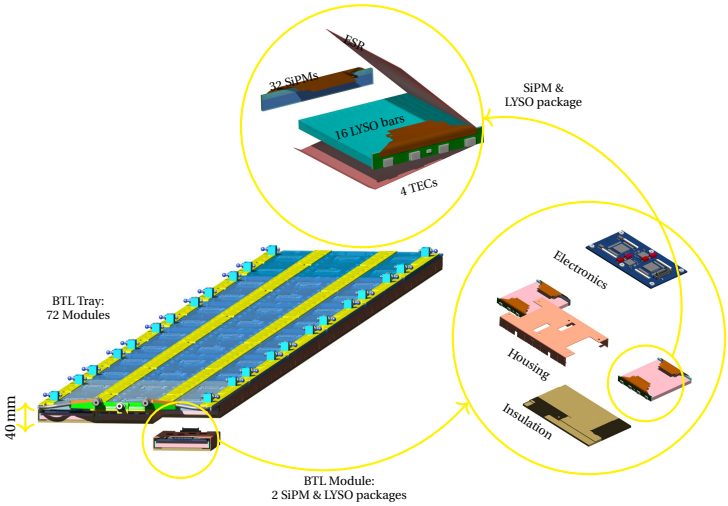

Figure 1.3.: Barrel Timing Layer module composed of 16 LYSO bars and 32 SiPM channels within a copper module for heat transfer and structural stiffness.

recover the current precision of CMS with the increased luminosity of HL-LHC.

The estimated timing performance of BTL is based on experimental measurements of the photodetectors [15, 16], scintillating crystals [17] and the CO2 biphasic cooling system [18]. The most influential elements to BTL's performance are the scintillator and SiPMs due to their large contribution to the total time resolution compared to the rest of components following Equation (1.1) with values of σ^{phot} around 25-30 ps and an end of life σ^{DCR} of 50 ps. The DCR of the SiPMs will start at a near-zero value. However, radiation-induced damage will increase the DCR during the expected life of the detector. The overall performance of BTL can be improved through the design and optimization of its different components to reduce the DCR and photon arrival time uncertainties.

1.1. Scintillation crystals

From the detection process of ionization particles using scintillation crystals, the first component of the time resolution (see Equation (1.1)) that affects our results is σ^{phot}. This σ^{phot} is governed by the statistics of the arrival time of the photons from their origin within the scintillation crystals to the SiPMs. The scintillation process, by which we convert ionizing radiation into visible photons, is tightly tied to the material properties of the scintillation crystals. While there exist organic and inorganic scintillators, for harsh environments with high radiation doses and high-energy physics applicators, only inorganic crystals provide high ratios of photon emissions and stopping power (with the ability to extract energy from ionizing impacting particles) versus radiation hardness (deterioration under radiation).

Scintillation in inorganic crystals occurs when electrons are excited from the valence band to the conduction band, followed by deexcitation at impurity sites, producing

photons. Inefficiencies arise when defects such as substitutional impurities or vacancies trap electrons, return to their ground state without emitting photons (e. g., thermal quenching), or are reabsorbed, reducing photon yield [19]. The schematics of this local process within the scintillator can be visualized in Figure 1.4b. Figure 1.4a further shows a macro schematic of an ionizing particle flying through a scintillator, the photons created in a point energy deposition and their arrival at a glued SiPM. We can improve these properties through material research and adjustment of impurity concentrations [20]. This often involves the use of rare-earth doping agents, which are costly due to geopolitical factors and have expensive manufacturing processes. For the particular case of BTL, the price of scintillating LYSO:Ce crystals can be estimated to be approximately \$4000/kg [21].

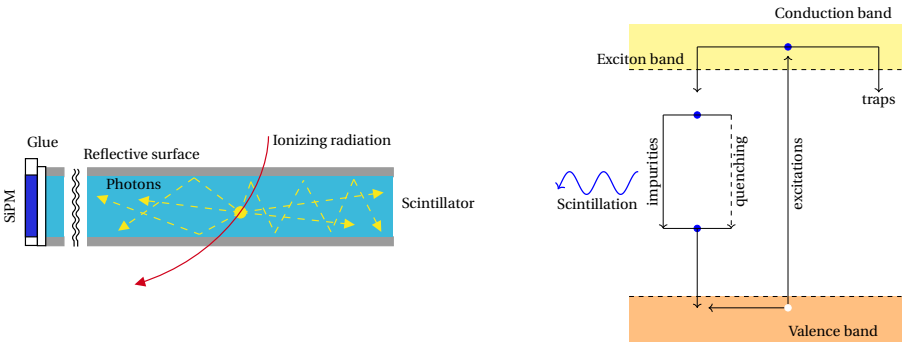

(a) (b)

Figure 1.4.: Schematics of the scintillation process. Figure 1.4a depicts an ionizing particle (in red) hitting a scintillator, causing local energy deposition and photon generation. These photons travel toward an optically glued SiPM. A reflective coating surrounds the scintillator to prevent light loss. Figure 1.4b focuses on the local processes near the energy deposition site. An electron is excited from the valence band to the conduction band, moving until it encounters an impurity. At this point, the electron may either deexcite via scintillation, emitting a photon or undergo quenching without emission.

The default design of the LYSO:Ce scintillators used in BTL can be seen in Figure 1.5 submitted to an exciting wavelength. These 3x3x57mm crystals are packaged in a reflective ESR (enhanced specular reflector) coating glued to localized regions to avoid losing as many photons as possible and attached to SiPM packages at each of their ends according to Figure 1.3 and Figure 1.4. These crystals have been experimentally tested in successive measurement campaigns to improve their light with respect to their Ce doping composition and the capabilities of the manufacturers [17].

The composition of the material is not the only way to improve overall σ^{phot}. Furthermore, the literature shows that the geometrical shape [22], optical surfaces [23], and coatings [24] of scintillating crystals also affect the overall light collection by the photodetector. In this manner, nonconventional shapes can focus the photons onto the photodetectors and change the track length of the ionizing particles across the scintil-

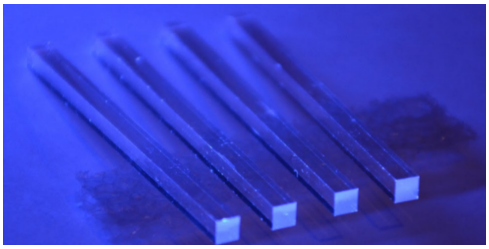

Figure 1.5.: LYSO:Ce bars under an exciting source used within BTL. This figure is taken from CMS [13].

lator. The use of particle-matter interaction software can alleviate time and monetary costs by testing multiple geometries without the need for an experimental setup. Indeed, we find examples in the literature of the characterisation of scintillators' geometries through GEANT4 – a particle-matter interaction software based on ray-tracing [25] – such as Danevich *et al.* [26], which compares 4 different shapes of scintillators in relation to the light extraction characteristics. We can also see some optimizations of the shape of these crystals through parametric analysis of their thickness ratio in Min *et al.* [27].

These particle-matter interaction software packages tend to use ray tracing algorithms and stochastic data to simulate the behaviour of physical particles. In the case of the scintillation and optical processes, these stochastic data include the deviation of the number of photons created in each time step taken from normal distributions, the photon direction after its generation and non-specular reflections, the wavelength of the generated photons, etc. These facts lead to the need for gradient-free optimization algorithms for the optimization of scintillator designs.

1.2. Thermoelectrical cooling technology

Thermoelectricity converts electron flow into heat transfer using electrical conductors with different properties. As shown in Figure 1.6, the Fermi level, which indicates a 50% probability of finding an electron, is near the valence band (the highest energy band filled with electrons) in p-type semiconductor materials and closer to the conduction band (the energy band where electrons are free to move) in n-type materials. Electrons release heat when they move from the n-type to the p-type because of their difference in energy, and absorb it when moving in the opposite direction. This is the Peltier effect, where a current applied through dissimilar conductors creates a heat-pumping effect. A thermoelectric cooler (TEC), composed of multiple semiconductor connections in series to a DC source, can be used to actively cool a surface in contact with it using the Peltier effect, as depicted in Figure 1.6.

Applications of this technology include electronics and medical devices cooling, cryogenics, and heat recovery for more efficient systems [28]. Thermoelectric coolers offer an appealing alternative to conventional compression-based systems due to their miniaturization capabilities, lack of gas emissions, lack of moving components, and reverse

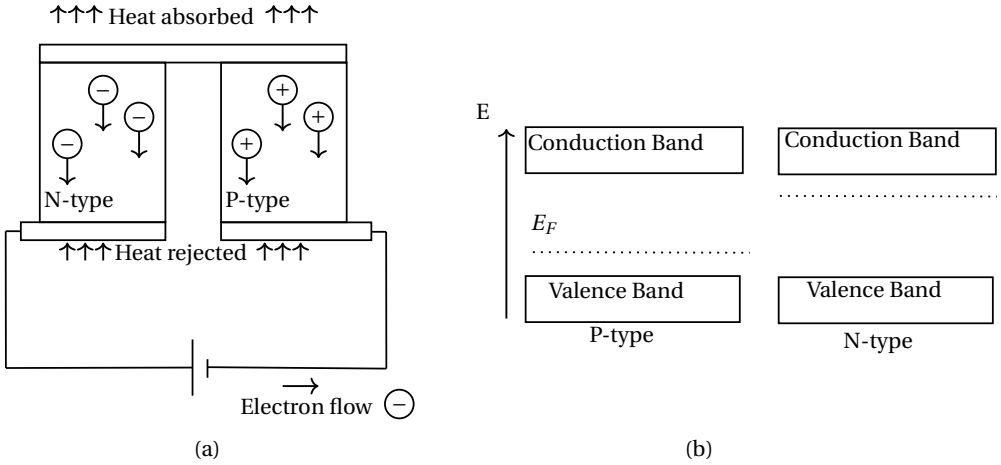

Figure 1.6.: Illustration of a thermoelectric module, consisting of alternating p-type and n-type semiconductor materials. Heat is absorbed on one side of the module, while heat is removed on the opposite side. The directional flow (arrows) of electrons and holes (represented by circles with − and + symbols, respectively) is shown within the n-type and p-type materials, respectively, highlighting the process of thermoelectric cooling or heating. The module is connected to an external electrical circuit.

operation capabilities.

With the SiPMs DCR being one of the main contributors to BTL's loss of timing resolution, actively controlling their temperature provides multiple advantages. These advantages can be summarized as lower operating temperatures that reduce signal noise in SiPMs [29] and annealing procedures that help recover radiation-induced damage [30, 31]. The effect of active control of the temperature of SiPMs is modelled in CMS [13] and represented in Figure 1.7. This plot represents the DCR of the SiPMs on the y axis and the operation year on the x axis, using different nominal temperatures during operation and annealing cycles during shutdown periods. This plot suggests that we can reduce the dark current rate (DCR) of the SiPMs at the end of life for BTL by half for each 10 degrees lower for their operational temperature and with annealing scenarios above 10 °C.

Bornheim *et al.* [34] describes the BTL cooling system, which consists of biphasic CO2 cooling linked to 4 TECs per 16 SiPMs through a copper housing, and provides preliminary results for the system based on a mock-up. Boiling liquid CO2 inside steel pipes embedded in an aluminium plate acts as the primary heat sink, dissipating heat from the detector. However, the CO2 system, shared with the Tracker, operates between −35 °C during use and +10 °C during shutdowns. TECs decouple the SiPM temperatures from the CO2 system, enabling annealing during shutdowns and lower temperatures during operation. Experiments performed in Bornheim *et al.* [34] using a water-cooled aluminium plate and testing two different Phononic TECs [35], achieve a 10 °C temperature reduction with 420 mW injected into the SiPMs and 600 mW into the 4 TECs. The anneal-

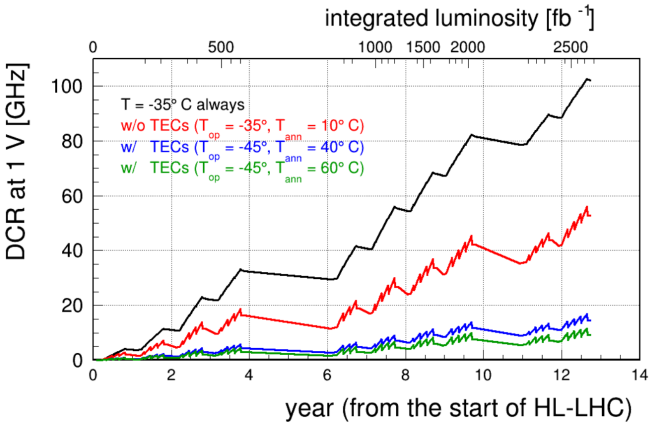

Figure 1.7.: Evolution of dark count rate at fixed operating over-voltage of 1 V throughout the detector operation assuming the current baseline running plan of the HL-LHC [32] and for different scenarios of SiPM temperature during operation (Top) and during technical stops (Tann) when annealing can be accelerated. This figure and caption is taken from Heering *et al.* [33].

ing procedure up to 40 °C shows a need of 1W for each 4 TECs. The design of the current BTL system is then based on experimental testing, which is time-consuming and expensive. Thermoelectric simulations can streamline this process by allowing comparisons of more configurations at a lower cost and a faster pace. Standard TECs use simple rectangular semiconductor blocks connected electrically in series and thermally in parallel. However, the TEC performance depends on semiconductor geometry, not just semiconductor volume or their connections [36]. Recent research applies topology optimization through finite element methods (FEM) to optimize the shape and distribution of the pellets in simplified 2D models for specific thermoelectric applications [37].

1.3. Research aim and scope

The main research question of this thesis is formulated as

Can numerical design optimization techniques be applied to improve the timing precision of minimum ionizing particle detectors?

This central question is addressed from the point of view of the overall detector. To narrow down the question, we focus on the largest components from Equation (1.1) to the overall time resolution, namely the photonic and DCR influences. In this manner, we can achieve lower timing resolutions through more efficient active-temperature controls of the photomultipliers to reduce the ensuing electrical noise and higher light collection values from the coupled scintillators to increase the overall signal.

Looking first at the σ^{DCR} component, we develop a first subquestion as

- *Can a topology optimization formulation for thermoelectric devices improve cooling performance accounting for material cost and specific operational factors, including electrical working points and nonlinear Joule heating?*

Using topology optimization, we postulate that we can improve the efficiency of the TECs attached to the SiPMs. These TECs provide active thermal regulation to the SiPMs, providing a lower operating temperature and a lower σ^{DCR}. Given the limitations of the power source, if we can provide higher temperature differences across the TECs for the same power consumption, we can improve the detector timing resolution. However, to develop this procedure, we first need to understand the convergence of the thermoelectrical topology optimization problem under multiple operational points and constraints. Knowing that the thermoelectrical problem is non-linear due to the Joule heating, the problem can lead to nonconvexities and a lack of convergence to feasible design regions during the optimization. Furthermore, we notice that, for cooling approaches, we have a power limitation but freedom to operate the voltage gradient across the device within limits.

Answering the previous question can provide an approach to improving the BTL time resolution. However, thermoelectrical devices are also subject to mechanical loads that need to be supported by the devices. This leads to the second subquestion of this dissertation,

- *Can numerical methods optimize coupled thermoelectric-mechanical systems while considering mechanical and thermoelectrical loads?*

Answering this question can prevent the loss of efficiency within the TECs with successive loading and unloading during thermal cycles, reduce stresses during installation procedures, and increase their overall reliability.

The SiPM temperature is not the only factor affecting the timing resolution; the properties of the scintillators can also modify it. In this manner, we approach the reduction of the second largest component to the timing resolution, being σ^{phot}, with the subquestion

- *Can shape optimization of scintillation crystal surfaces reduce light re-absorption and improve performance at the photodetector interface, considering the stochastic nature of the optimization process?*

This question poses the challenge of using the numerical optimization procedures to scintillator crystals, with the challenge of the stochastic nature of the particle-matter interaction simulation software associated with these processes. This realization leads to a final subquestion

- *Can deterministic modelling approaches, such as FEM and FDTD, enhance scintillation efficiency through improved photon generation and detection while reducing the computational demands associated with Monte Carlo methods?*

In this last question, we pose the challenge of changing the modelling of the Monte Carlo-based particle interactions to a deterministic approach to accelerate the optimization procedure of scintillation crystals.

Overall, providing a satisfactory answer to each one of these questions is bound to provide an optimization procedure to improve the timing resolution of BTL. The results are then based on its most significant components, namely the DCR of the SiPMs governed by their temperature control and the signal level determined by the properties and geometry of the scintillators.

1.4. Main contributions and outline

This thesis is created over the compendium of papers already published in journal papers (including Chapter 2 and Chapter 4) or are expected to be published in the coming months after the submission of this document. This document is organized regarding the order of the sub-questions stated in Section 1.3.

In particular, the content and main contributions of each chapter are summarized as follows:

- Chapter 2 studies the design space of thermoelectric devices for cooling applications, focusing on nonconvex topology optimization of thermoelectric elements. This framework includes power budget constraints to improve thermal gradients across the thermocouples. The approach maintains an optimal power-to-heat extraction ratio by integrating the voltage gradient across the thermocouple as a design variable. Given the non-linearities present in the problem, we develop a simplified analytical model to examine how penalization coefficients affect optimization convergence. The chapter concludes with topology optimizations of thermocouples based on the commercial TEC 1MC10-031. The results show that this method achieves temperature reductions of up to 10 degrees while using 60% less semiconductor material, with temperature-constant properties that enhance the correlation with the analytical model. The analysis also verifies the impact of temperature non-linear material properties on each optimized result.

  Chapter 3 expands on Chapter 2 by introducing mechanical degrees of freedom. The formulation decouples thermoelectric and mechanical calculations, significantly reducing memory usage. The topology optimization aims to minimize temperature while accounting for the electrical working point, using voltage as a design variable and non-linear temperature-dependent materials. We describe a polynomial fitting method to model the nonlinear materials. Additionally, the formulation includes power and stress constraints. Stress and temperature objectives are aggregated to prevent hot spots and stress singularities in the optimized topologies. The section concludes with 2D and 3D optimized thermocouple examples based on loads present on the thermoelectrical devices during the operation of a thermocouple. Helmholtz filtering is finally applied to address checkerboarding, preventing porous materials that arise when mechanical degrees of freedom are included in the optimization. The results include a study on the effect of grey elements, nonlinear temperature-dependent material properties, and air conductance on the optimized designs.

- Chapter 4 demonstrates how to apply stochastic data from particle-matter interaction software with nongradient-based genetic optimizers. The goal is to es-

tablish a Pareto front that balances the amount of scintillation material in the detector, influencing costs, against the number of photons detected by the photodetectors. This research models a scintillator and silicon photomultiplier package assembly using GEANT4, an open-source software for particle-matter interactions. We describe a method to simplify the modelling process of the BTL modules within GEANT4 and assess computational requirements for accurate light collection calculations. The study includes two geometries compatible with BTL. The model's geometry employs parameterized splines for smooth results and is meshed using GMSH, facilitating genetic numerical optimization through NSGAII (non-dominated sorting genetic algorithm). This approach generates optimized scintillator geometries and evaluates trade-offs among various objective functions based on the resulting stochastic data. The Pareto results, whose convergence is studied using the hypervolume indicator, compare favourably to the original design, leading to a recommendation to prioritize light collection per energy deposition and track path length. The findings indicate potential relative improvements to the original designs of up to 18% for a constant volume in geometries suitable for the BTL detector design.

- Chapter 5 presents a formulation that transitions scintillator optimization from nongradient methods to a framework that accommodates derivative-based optimizers. This chapter details the implementation of finite element method (FEM) techniques to scintillators, which enhance computational efficiency compared to the use of GEANT4. The chapter introduces boundary condition translation for scintillation phenomena, converting them into energy pulses in a transient electromagnetic framework. This translation facilitates the comparison of energy deposition calculations in different photodetectors and scintillator assemblies. The chapter also examines a frequency domain problem, fitting its wavelength and energy losses to fit the GEANT4 model design space depending on the crystal shape. Validation occurs through comparison with a GEANT4 model, accounting for geometry and material properties. The findings highlight the significance of self-absorption and boundary conditions in modelling scintillators through FEM. The frequency domain model serves as the basis for numerical shape optimization, using energy deposition as an objective function while adhering to multiple geometric constraints. The chapter concludes with validation results that demonstrate a 7% improvement in the median light collection distribution, achieved in a fraction of the time compared to traditional GEANT4 or transient modelling methods.

Finally, Chapter 6 contains a discussion of the results of all previous chapters, including further numerical optimization opportunities in the field of particle detectors and the use of these techniques in fields where there is still no extensive literature and there is potential for higher time resolution or cooling capabilities. Furthermore, this chapter discusses how the overall optimization procedures have been able to improve the performance of the BTL detector and future recommendations are provided.

References

[1] H. Kolanoski and N. Wermes. *Particle Detectors: Fundamentals and Applications*. Oxford University Press, June 2020. ISBN: 9780198858362. DOI: 10.1093/oso/9780198858362.001.0001. eprint: https://academic.oup.com/book/43645/book-pdf/50609306/9780191899232_web.pdf. URL: https://doi.org/10.1093/oso/9780198858362.001.0001.

[2] P. G. Martin, Y. Verbelen, E. Sciama Bandel, M. Andrews, and T. B. Scott. "Project Gatekeeper: An Entrance Control System Embedded Radiation Detection Capability for Security Applications". In: *Sensors* 20.10 (2020). ISSN: 1424-8220. DOI: 10.3390/s20102957. URL: https://www.mdpi.com/1424-8220/20/10/2957.

[3] D. Vukadinovic, D. Anderson, and European Commission. Joint Research Centre. *X-ray baggage screening and artificial intelligence (AI) : a technical review of machine learning techniques for X-ray baggage screening*. 2022, p. 50. ISBN: 9789276534945. DOI: 10.2760/46363.

[4] A. Alavi, T. J. Werner, E. Ł. Stępień, and P. Moskal. In: *Bio-Algorithms and Med-Systems* 17.4 (2021), pp. 203–212. DOI: doi:10.1515/bams-2021-0186. URL: https://doi.org/10.1515/bams-2021-0186.

[5] "Two decades of SPECT/CT – the coming of age of a technology: An updated review of literature evidence". In: *European Journal of Nuclear Medicine and Molecular Imaging* 46.10 (2019), pp. 1990–2012. ISSN: 16197089. DOI: 10.1007/s00259-019-04404-6.

[6] R. Kaiser and R. Kaiser. "Muography : overview and future directions Subject Areas : Author for correspondence :" in: *Philosophical Transactions of the Royal Society A: Mathematical, Physical and Engineering Sciences* 377 (2019).

[7] S. Paranjpe. "Neutron Imaging: A Non-Destructive Tool for Materials Testing". In: *IAEA-TECDOC-1604: Neutron Imaging: A Non-Destructive Tool for Materials Testing (IAEA-TECDOC Series)* September (2008). DOI: 978âĂŞ92âĂŞ0âĂŞ110308âĂŞ6. URL: http://www.amazon.com/Neutron-Imaging-Non-destructive-Materials-IAEA-TECDOC/dp/9201103085.

[8] C. Grupen and I. Buvat. *Handbook of particle detection and imaging; 1st ed.* Heidelberg: Springer, 2012. DOI: 10.1007/978-3-642-13271-1. URL: https://cds.cern.ch/record/1431438.

[9] G. Aad *et al.* "Observation of a new particle in the search for the Standard Model Higgs boson with the ATLAS detector at the LHC". In: *Physics Letters B* 716.1 (2012), pp. 1–29. ISSN: 0370-2693. DOI: https://doi.org/10.1016/j.physletb.2012.08.020. URL: https://www.sciencedirect.com/science/article/pii/S037026931200857X.

[10] A. G., B. A. I., B. O., F. P., L. M., R. L., and T. L. *High-Luminosity Large Hadron Collider (HL-LHC): Technical Design Report V. 0.1*. CERN Yellow Reports: Monographs. Geneva: CERN, 2017. DOI: 10.23731/CYRM-2017-004. URL: https://cds.cern.ch/record/2284929.

[11] G. Petrucciani. "The CMS experiment at the CERN LHC". In: *The Search for the Higgs Boson at CMS* 08004 (2013), pp. 15–58. DOI: 10.1007/978-88-7642-482-3_2.

[12] David Barney. *CMS Slice*. Accessed: 2024-09-06. 2018. URL: https://cds.cern.ch/record/2628641/files/.

[13] C. CMS. *A MIP Timing Detector for the CMS Phase-2 Upgrade*. Tech. rep. Geneva: CERN, 2019. URL: https://cds.cern.ch/record/2667167.

[14] A. Apresyan, J. Bendavid, A. Bornheim, J. Butler, N. Cartiglia, F. Golf, L. Gray, W. Li, T. Liu, M. T. Lucchini, S. Lusin, W. Lustermann, P. Martinez Ruiz Del Arbol, P. Meridiani, I. Ojalvo, O. Sahin, D. Stuart, T. Tabarelli De Fatis, S. Tkaczyk, J. Varela, S. Cittolin, W. Adam, J. Borg, T. Bose, D. Contardo, K. Gill, F. Hartmann, J. Kieseler, K. Klein, F. Meijers, M. Moll, P. Rumerio, A. Savin, J. Spalding, R. Tenchini, and W. Zeuner. *A MIP Timing Detector for the CMS Phase-2 Upgrade: Technical Design Report*. Tech. rep.

[15] A. Ghezzi. "Precision Timing with LYSO:Ce Crystals and SiPM Sensors in the CMS MTD Barrel Timing Layer". In: *2021 IEEE Nuclear Science Symposium and Medical Imaging Conference (NSS/MIC)*. 2021, pp. 1–4. DOI: 10.1109/NSS/MIC44867.2021.9875613.

[16] A. Heering, Y. Musienko, J. Gonzales, A. Karneyeu, M. Wayne, R. Ruchti, and M. Moll. "Low temperature characteristics of SiPMs after very high neutron irradiation". In: *Nuclear Instruments and Methods in Physics Research Section A: Accelerators, Spectrometers, Detectors and Associated Equipment* 936 (2019). Frontier Detectors for Frontier Physics: 14th Pisa Meeting on Advanced Detectors, pp. 671–673. ISSN: 0168-9002. DOI: https://doi.org/10.1016/j.nima.2018.09.111. URL: https://www.sciencedirect.com/science/article/pii/S0168900218312646.

[17] F. Addesa, P. Barria, R. Bianco, M. Campana, F. Cavallari, A. Cemmi, M. Cipriani, I. Dafinei, B. D'Orsi, D. del Re, M. Diemoz, G. D'Imperio, E. Di Marco, I. Di Sarcina, M. Enculescu, E. Longo, M. Lucchini, F. Marchegiani, P. Meridiani, S. Nisi, G. Organtini, F. Pandolfi, R. Paramatti, V. Pettinacci, C. Quaranta, S. Rahatlou, C. Rovelli, F. Santanastasio, L. Soffi, R. Tramontano, and C. Tully. "Comparative characterization study of LYSO:Ce crystals for timing applications". In: *Journal of Instrumentation* 17.08 (Aug. 2022), P08028. DOI: 10.1088/1748-0221/17/08/P08028. URL: https://dx.doi.org/10.1088/1748-0221/17/08/P08028.

[18] M. P. Rauch. "Thermal measurements and characterizations for the CMS phase-1 barrel pixel detector and the CMS phase-2 upgrade tracker 2S module with evaporative CO2 cooling systems". Veröffentlicht auf dem Publikationsserver der RWTH Aachen University; Dissertation, RWTH Aachen University, 2020. Dissertation. Aachen: RWTH Aachen University, 2020, 1 Online–Ressource (173 Seiten) :

Illustrationen, Diagramme. DOI: 10.18154/RWTH-2020-05630. URL: https://publications.rwth-aachen.de/record/791803.

[19] C. Kim, W. Lee, A. Melis, A. Elmughrabi, K. Lee, C. Park, and J.-Y. Yeom. "A Review of Inorganic Scintillation Crystals for Extreme Environments". In: *Crystals* 11.6 (2021). ISSN: 2073-4352. DOI: 10.3390/cryst11060669. URL: https://www.mdpi.com/2073-4352/11/6/669.

[20] H. Fukushima, D. Nakauchi, G. Okada, T. Kato, N. Kawaguchi, and T. Yanagida. "Ce concentration dependence on scintillation properties of SrHfO3 single crystals". In: *Journal of Alloys and Compounds* 934 (2023), p. 167929. ISSN: 0925-8388. DOI: https://doi.org/10.1016/j.jallcom.2022.167929. URL: https://www.sciencedirect.com/science/article/pii/S0925838822043201.

[21] R.-Y. Zhu. *Summary Talk in CEPC Calorimetry Workshop at IHEP, Beijing*. 2019. URL: https://www.its.caltech.edu/~rzhu/.

[22] S. Xie, X. Zhang, Y. Zhang, G. Ying, Q. Huang, J. Xu, and Q. Peng. "Evaluation of various scintillator materials in radiation detector design for positron emission tomography (Pet)". In: *Crystals* 10.10 (2020), pp. 1–15. ISSN: 20734352. DOI: 10.3390/cryst10100869.

[23] C. Bircher and Y. Shao. "Investigation of crystal surface finish and geometry on single LYSO scintillator detector performance for depth-of-interaction measurement with silicon photomultipliers". In: *Nuclear Instruments and Methods in Physics Research Section A: Accelerators, Spectrometers, Detectors and Associated Equipment* 693 (2012), pp. 236–243. ISSN: 0168-9002. DOI: https://doi.org/10.1016/j.nima.2012.07.029. URL: https://www.sciencedirect.com/science/article/pii/S0168900212008042.

[24] N. Ghal-Eh and R. Koohi-Fayegh. "Light collection behaviour of scintillators with different surface coverings". In: *Radiation Measurements* 41.3 (2006), pp. 289–294. ISSN: 1350-4487. DOI: https://doi.org/10.1016/j.radmeas.2005.06.039. URL: https://www.sciencedirect.com/science/article/pii/S1350448705002507.

[25] S. Agostinelli *et al.* "GEANT4 - A simulation toolkit". In: *Nuclear Instruments and Methods in Physics Research, Section A: Accelerators, Spectrometers, Detectors and Associated Equipment* 506.3 (2003), pp. 250–303. ISSN: 01689002. DOI: 10.1016/S0168-9002(03)01368-8.

[26] F. A. Danevich, R. V. Kobychev, V. V. Kobychev, H. Kraus, V. B. Mikhailik, and V. M. Mokina. "Optimization of light collection from crystal scintillators for cryogenic experiments". In: *Nuclear Instruments and Methods in Physics Research, Section A: Accelerators, Spectrometers, Detectors and Associated Equipment* 744 (2014), pp. 41–47. ISSN: 01689002. DOI: 10.1016/j.nima.2014.01.042. URL: http://dx.doi.org/10.1016/j.nima.2014.01.042.

[27] S. Min, Y. Kim, K. H. Ko, B. Seo, J. Cheong, C. Roh, and S. Hong. "Optimization of plastic scintillator for detection of gamma-rays: Simulation and experimental study". In: *Chemosensors* 9.9 (2021). ISSN: 22279040. DOI: 10.3390/chemosensors9090239. URL: https://doi.org/10.3390/chemosensors9090239.

[28] D. Zhao and G. Tan. “A review of thermoelectric cooling: Materials, modeling and applications”. In: *Applied Thermal Engineering* 66.1-2 (2014), pp. 15–24. ISSN: 13594311. DOI: 10.1016/j.applthermaleng.2014.01.074.

[29] V. Puill, C. Bazin, D. Breton, L. Burmistrov, V. Chaumat, N. Dinu, J. Maalmi, J. Vagnucci, and A. Stocchi. “Single photoelectron timing resolution of SiPM as a function of the bias voltage, the wavelength and the temperature”. In: *Nuclear Instruments and Methods in Physics Research Section A: Accelerators, Spectrometers, Detectors and Associated Equipment* 695 (2012). New Developments in Photodetection NDIP11, pp. 354–358. ISSN: 0168-9002. DOI: https://doi.org/10.1016/j.nima.2011.12.039. URL: https://www.sciencedirect.com/science/article/pii/S0168900211022480.

[30] E. Garutti and Y. Musienko. “Radiation damage of SiPMs”. In: *Nuclear Instruments and Methods in Physics Research Section A: Accelerators, Spectrometers, Detectors and Associated Equipment* 926 (2019). Silicon Photomultipliers: Technology, Characterisation and Applications, pp. 69–84. ISSN: 0168-9002. DOI: https://doi.org/10.1016/j.nima.2018.10.191. URL: https://www.sciencedirect.com/science/article/pii/S0168900218315055.

[31] F. Gu, Y. Liu, X. Sun, Y. Xu, D. Zhang, Z. An, K. Gong, X. Li, X. Wen, S. Xiong, F. Zhang, C. Wang, and G. Qu. “Achieving significant performance recovery of SiPMs’ irradiation damage with in-situ current annealing”. In: *Nuclear Instruments and Methods in Physics Research Section A: Accelerators, Spectrometers, Detectors and Associated Equipment* 1053 (2023), p. 168381. ISSN: 0168-9002. DOI: https://doi.org/10.1016/j.nima.2023.168381. URL: https://www.sciencedirect.com/science/article/pii/S0168900223003716.

[32] CERN LHC Commissioning Group. *LHC Long Term Schedule*. https://lhc-commissioning.web.cern.ch/schedule/LHC-long-term.htm. [Accessed: 02-Oct-2024]. 2024.

[33] A. Heering, Y. Musienko, J. Gonzales, A. Karneyeu, M. Wayne, R. Ruchti, and M. Moll. “Low temperature characteristics of SiPMs after very high neutron irradiation”. In: *Nuclear Instruments and Methods in Physics Research, Section A: Accelerators, Spectrometers, Detectors and Associated Equipment* 936.September 2018 (2019), pp. 671–673. ISSN: 01689002. DOI: 10.1016/j.nima.2018.09.111. URL: https://doi.org/10.1016/j.nima.2018.09.111.

[34] A. Bornheim, W. Lustermann, K. Stachon, G. Reales Gutiérrez, A. Benaglia, F. De Guio, A. Ghezzi, M. T. Lucchini, M. Malberti, S. Palluotto, T. Tabarelli De Fatis, M. Benettoni, R. Carlin, M. Tosi, R. Rossin, P. Meridiani, R. Paramatti, F. Santanastasio, J. C. Silva, J. Varela, A. Heering, A. Karneyeu, Y. Musienko, M. Wayne, T. Anderson, B. Cox, C. E. Perez Lara, A. Ledovskoy, S. White, and I. Schmidt. “Integration of thermo-electric coolers into the CMS MTD SiPM arrays for operation under high neutron fluence”. In: *Journal of Instrumentation* 18.8 (2023). ISSN: 17480221. DOI: 10.1088/1748-0221/18/08/P08020. arXiv: 2306.00818.

[35] Phononic. *Solid State Cooling Solutions & Technology*. https://phononic.com/. Accessed: 2024-09-30. 2024.

[36] A. Fabián-Mijangos, G. Min, and J. Alvarez-Quintana. “Enhanced performance thermoelectric module having asymmetrical legs”. In: *Energy Conversion and Management* 148 (2017), pp. 1372–1381. ISSN: 01968904. DOI: 10.1016/j.enconman.2017.06.087.

[37] C. Lundgaard and O. Sigmund. “A density-based topology optimization methodology for thermoelectric energy conversion problems”. In: *Structural and Multidisciplinary Optimization* 57.4 (2018), pp. 1427–1442. ISSN: 16151488. DOI: 10.1007/s00158-018-1919-1.

2

Enhancing the cooling performance of thermocouples: a power-constrained topology optimization procedure

Heat pumping through thermoelectric devices has many advantages over traditional cooling. However, their current efficiency is a limiting factor in their implementation. In this paper [1], we formulate and solve the nonconvex topology optimization problem of thermoelectric cooling elements using the Method of Moving Asymptotes (MMA), with the objective of maximizing cooling effectiveness per unit power input. The optimization problem is defined for a given power budget, aiming for the minimum temperature with a known heat pumping need. The introduction of power as a constraint justifies the introduction of the voltage gradient across the thermocouple as a design variable to maintain the thermoelectrical device in its optimum power-to-heat extraction ratio. To better understand the convergence of this nonconvex problem, we present a two-variable analytical thermoelectric optimization model. We use this example to select the material penalty coefficients involved in the SIMP problem through a combinatorial study of the design spaces of each objective and constraint. Finally, we test the combination of penalty coefficients given by $k_p = \sigma_p > \alpha_p$ through numerical optimizations of a model based on the commercial thermoelectric cooler (TEC) 1MC10-031 using the finite element method (FEM). We perform these optimizations using constant material properties with temperature to better correlate with the analytical model and simplify the computational complexity. The results of these optimizations are studied to understand the effect of multiple design parameters on the optimized designs found. We show that these optimizations

This chapter has been published as the Structural and Multidisciplinary Optimization Journal, 189 (2024) [1]

can provide temperatures lower than those of the original design at volumes lower than those of the imposed constraints. With postprocessing, we can also show that the gains remain true using nonlinear material properties. Given the test cases studied, we find designs that achieve temperatures close to 10 degrees lower for 60% *less volume of semiconductor material using thermocouple FEM models.*

2.1. Introduction

The energy consumption for cooling and heating accounts for half of the global energy consumption and 40% of global energy-related CO_2 emissions, respectively [2]. Most heat-transfer-related activities are carried out through compressor- and refrigerant-based systems for active thermal management. Conversely, thermoelectric modules offer an alternative thermal management solution with simpler static systems, higher reliability, lower maintenance cost, refrigerant-free operation [3], miniaturization possibilities, and reverse heat-pumping capabilities [4]. These advantages make thermoelectric-coolers (TECs) ideal for niche applications such as sustainable self-cooling, cryogenic applications, medical, food or building refrigeration, thermal cycling and electronic cooling of sensors, lasers and chips [5]. Despite their advantages over conventional systems, TECs have yet to see a significant adoption in applications where they compete against turbomachinery-based cooling systems due to their low energy conversion efficiency and high system cost (approximately $75/W [6] per TEC against $7/W for liquid electronic cooling systems [7].

The static behaviour and miniaturization possibilities of TECs arise from using the Peltier effect. First observed in 1834 [8], the Peltier effect dictates that when a current is passed through two dissimilar conductors, such as a p-n semiconductor junction, heat absorption occurs at the interface, arising from the elevation of the energy levels of electrical current electrons from the p-type to the n-type semiconductor. The Seebeck effect can also be harnessed through dissimilar conductor connections, called thermocouples, to generate an electrical potential gradient, which can be harnessed for applications such as heat recovery and power generation in remote or hard-to-reach locations. Peltier and Seebeck effects exist within the same thermoelectric device architecture based on thermocouples.

As the smallest unit of thermoelectric device architecture, the thermocouple has captured significant attention in endeavours aimed at improving the efficiency of thermoelectric devices. On the one hand, these efforts focus on reconciling the conflicting material properties of the often-used semiconductor materials. To have high efficiency, we require high electrical conductivity, low thermal conductivity, and large Seebeck coefficient gradients – related by the Wiedemann-Franz law – to maximize the figure of merit or ZT, directly associated with the device's efficiency. These properties can be modified through the nanoscale constituents of semiconductors; however, the procedures required are limited by the available material composition and manufacturing technologies, with the largest ZT obtained being in the range of 1–3 [5]. On the other hand, the electrical and thermal conductivities of the entire device also depend on the thermocouple topology.

Numerical simulations show that thermocouples with variable cross-sections can provide higher efficiencies and lower stresses than conventional constant-section thermocouples [9]. In particular, thermocouple design is highly interesting for the standard thermoelectrical module architecture (flat-bulk) [10]. Fabián-Mijangos, Min, and Alvarez-Quintana [11] experimentally tested multiple thermocouple designs, showing efficiency increases using asymmetric thermocouples for power recovery.

Topology optimization (TO) is a powerful tool for enhancing the efficiency of thermocouples without the need for extensive experimental testing and its associated costs. Since its inception with Bendsøe and Kikuchi [12], the method has promoted different variations such as the commonly used solid isotropic material with penalization (SIMP) or level set (LS) approaches, among others [13, 14]. TO is practical for designing thermoelectrical compliant microactuators, showing promise with both SIMP and LS approaches [15–17]. Additionally, TO can increase the efficiency of heat recovery devices using novel thermocouple designs [18] and multi-material optimizations [19]. Finally, Soprani *et al.* [20] delve into the optimization of thermal coupling materials for TECs, and Lundgaard and Sigmund [21] looks into the topology optimization of multi-material thermoelectrical devices for multiple objective criteria.

Despite research on TO applied to thermoelectric-compliant mechanisms and heat recovery, current formulations fall short regarding cooling applications and specific working points. A more tailored TO formulation that takes TEC design considerations into account can provide a reduction of bulk-material costs (representing approximately 1/3 of the system cost according to Leblanc *et al.* [6]) and improved cooling performance. Furthermore, previous formulations have overlooked important operational factors, such as the working points for electrical and power consumption and their limitations. The lack of attention to these factors often leads to postprocessing at different operational points to understand the device's actual performance [21]. Furthermore, the lack of study of the multiple electrical working points neglects the effect of the nonlinear Joule heating over the topology of the device, which can induce higher local current densities and subsequent hot spots. Previous results for heat recovery also tend to use volume constraints, which can reduce material costs, but that can also reduce the performance of the designs studied, missing optima at higher volumes, depending on the ratio of thermal conductivity to electrical conductivity of the device [18, 22]. Furthermore, in thermoelectrical devices, increasing the volumes of semiconductor material in the design does not necessarily lead to better performances [23]. This fact raises doubts about the optima found using volume constraints. Additionally, the absence of thermoelectrical optimization results based on 3D geometries in the literature raises questions about the influence of intricate geometries on the design of each semiconductor leg, or pellet, in a thermocouple.

This paper [1] presents a novel approach to optimize three-dimensional TEC thermocouples using TO. First, we propose an analytical model with two design variables to study the design space and understand its non-convexity. This model is studied concerning the material scaling used in SIMP to predict the optimization parameters to improve the convergence of an optimization problem with a larger

number of design variables. Secondly, we apply TO to a finite element model of a thermocouple based on a commercial product, validating the insights from the lower-dimensionality problem. These models are studied with constant material properties to compare with the analytical solution of the thermoelectrical equations. Using constant material properties further reduces the computational complexity and cost of the models. We later study the error introduced by these assumptions in the results section. Furthermore, the design considerations of TECs are integrated into the optimization through the selection of a temperature objective function subject to power consumption limitations. In this model, the power consumption can be modified through the density design variables and the voltage gradient through the thermocouples. This voltage design variable introduces an electrical control over the nonlinear Joule heating in the device. Finally, the results are studied for multiple electrical and thermal working points of the thermocouple.

2.2. Governing Equations

The bulk-flat thermoelectrical architecture depicted in Figure 2.1 uses alternating p- and n-type pellet-shaped thermoelectric materials connected electrically in series and thermally in parallel. Copper layers on the top and bottom of each thermoelectric leg serve as electrical contacts, and two ceramic plates provide thermal contacts. Although all the materials in the thermoelectrical modelling should account for all three elements, the Seebeck coefficients of the copper layers are often neglected due to symmetry conditions (meaning copper segments generate equal and opposite voltages that cancel out), with only thermal degrees of freedom. However, the bulk properties of the semiconductors are subject to nonlinear thermoelectric coupling.

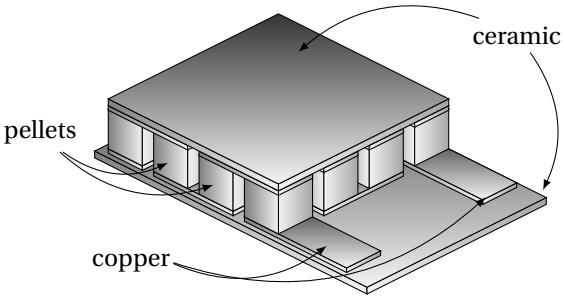

Figure 2.1.: Flat-bulk thermoelectric cooler (TEC) schematic exemplifying the electrical contacts between the semiconductor pellets and the thermal contact plates.

Goupil *et al.* [24] provides the balance and constitutive equations representing the thermoelectrical coupling. We can write down the balance equations in stationary conditions for the electric charge and energy flux as

$$\begin{aligned} \nabla \cdot \mathbf{j} &= 0\,, \\ \nabla \cdot \mathbf{q} + \mathbf{j} \cdot \nabla \phi &= q_\Omega\,, \end{aligned} \tag{2.1}$$

where $\mathbf{j}$ is the current density, $\mathbf{q}$ is the heat flow, q_Ω is the heat generated in the volume and ϕ is the electrical potential across the semiconductor material. These equations then express – within a given volume – the conservation of internal charge and energy given their flow through the volume boundary without magnetic fields.

The Ohm and Fourier equations,

$$\mathbf{j} = -\sigma(\nabla\phi + \alpha\nabla T), \tag{2.2}$$

$$\mathbf{q} = \alpha T\mathbf{j} - k\nabla T, \tag{2.3}$$

complete the thermoelectrical coupling. Where σ is the electrical conductivity, α is the Seebeck coefficient, k is the thermal conductivity of the semiconductor material, and T is its temperature. Equations (3.3) and (3.4) provide the constitutive equations and a relation between the temperature, heat flux, electrical potential and current flow. Although we can analytically solve these equations for simple configurations, complex geometries or nonlinear material properties can only be solved numerically.

2.2.1. Finite Element Modeling

The thermoelectric equations' finite element formulation makes it possible to solve the thermoelectric fields in complex semiconductor geometries through discretized equations and meshing algorithms. With Equations (3.1), (3.3) and (3.4) as the strong formulation of the thermoelectric problem, we need to introduce the required boundary conditions to solve it. We can write these boundary conditions as

$$\begin{aligned} V &= V_{\Gamma_V} \text{ in } \Gamma_V, & T &= T_{\Gamma_V} \text{ in } \Gamma_V, \\ \mathbf{j}\cdot\mathbf{n} &= j_c \text{ in } \Gamma_j, & \mathbf{q}\cdot\mathbf{n} &= q_c \text{ in } \Gamma_q, \end{aligned} \tag{2.4}$$

where V_{Γ_V} and T_{Γ_V} define the prescribed boundary conditions in the domain, and q_c and j_c represent the externally prescribed heat flows and current densities, respectively. The defined boundaries satisfy the conditions $\Gamma_V \cup \Gamma_j = \Gamma, \Gamma_V \cap \Gamma_j = 0$ where Γ represents the entire boundary. Similarly, the thermal boundaries satisfy $\Gamma_T \cup \Gamma_q = \Gamma, \Gamma_T \cap \Gamma_q = 0$.

The thermoelectrical system can now be transformed into the weak form of the Equations (3.1), (3.3) and (3.4), using an approximation function ω and the divergence theorem,

$$\begin{aligned} &-\int_\Omega \omega\nabla\cdot\mathbf{q}\,\mathrm{d}\Omega + \int_\Omega \omega\mathbf{j}\cdot\nabla\phi\,\mathrm{d}\Omega + \int_{\Gamma_q} \omega q_c\,\mathrm{d}\Gamma \\ &= \int_\Omega \omega q_\Omega\,\mathrm{d}\Omega, \\ &-\int_\Omega \nabla\omega\cdot\mathbf{j}\,\mathrm{d}\Omega + \int_{\Gamma_j} \omega\cdot\mathbf{j_c}\,\mathrm{d}\Gamma = 0. \end{aligned} \tag{2.5}$$

We can now discretize Equation (2.5) to reach the Garlekin formulation using the approximation shape functions as

$$\begin{aligned} T &= \mathbf{N}^\intercal\mathbf{T}, \\ \phi &= \mathbf{N}^\intercal\mathbf{V}, \end{aligned} \tag{2.6}$$

where $\mathbf{V}$ and $\mathbf{T}$ are the temperature and voltage degrees of freedom and $\mathbf{N}$ contains the shape functions. Combining Equation (3.10) with Equation (2.5) and creating a homogeneous equation system, we obtain the residual $\mathbf{R}$ for a given nodal value solution,

$$\begin{aligned}
\mathbf{R} &= \begin{bmatrix} \mathbf{R_A} \\ \mathbf{R_B} \end{bmatrix}, \\
\mathbf{R_A} &= -\int_\Omega \mathbf{N}\boldsymbol{\nabla}\cdot\mathbf{q}\,\mathrm{d}\Omega + \int_\Omega \mathbf{N}\mathbf{j}\cdot\boldsymbol{\nabla}\mathbf{N}^\intercal\mathbf{V}\,\mathrm{d}\Omega + \\
&\int_{\Gamma_q} \mathbf{N}q_c\,\mathrm{d}\Gamma - \int_\Omega \mathbf{N}q_\Omega\,\mathrm{d}\Omega = \mathbf{0}, \\
\mathbf{R_B} &= -\int_\Omega \boldsymbol{\nabla}\mathbf{N}\cdot\mathbf{j}\,\mathrm{d}\Omega + \int_{\Gamma_j} \mathbf{N}\cdot\mathbf{j_c}\,\mathrm{d}\Gamma = \mathbf{0}.
\end{aligned} \tag{2.7}$$

We can separate this residual into its components related to the temperature, $\mathbf{R_A}$, and voltage, $\mathbf{R_B}$, degrees of freedom. Pérez-Aparicio, Taylor, and Gavela [25] provides a more detailed development of the thermoelectric finite element method (FEM) equations with benchmark tests concerning analytical solutions and nonlinear material properties.

To obtain the solution of this system, we use the Newton-Raphson (NR) algorithm with the tangent system matrix, $\mathbf{K^k}$, calculated for each iteration and equal to the derivative of the residual concerning the problem degrees-of-freedom;

$$\mathbf{K^k} = \begin{bmatrix} \frac{\partial \mathbf{R^k}}{\partial \mathbf{T}} & \frac{\partial \mathbf{R^k}}{\partial \mathbf{V}} \end{bmatrix} = \begin{bmatrix} \frac{\partial \mathbf{R_A^k}}{\partial \mathbf{T}} & \frac{\partial \mathbf{R_A^k}}{\partial \mathbf{V}} \\ \frac{\partial \mathbf{R_B^k}}{\partial \mathbf{T}} & \frac{\partial \mathbf{R_B^k}}{\partial \mathbf{V}} \end{bmatrix}. \tag{2.8}$$

We can expand the derivatives of the residual to an integral form for any given iteration,

$$\begin{aligned}
\frac{\partial \mathbf{R_A}}{\partial \mathbf{T}} &= -\int_\Omega \boldsymbol{\nabla}\mathbf{N}\frac{\partial \mathbf{q}}{\partial \mathbf{T}}^\intercal \mathrm{d}\Omega + \int_\Omega \mathbf{N}(\frac{\partial \mathbf{j}}{\partial \mathbf{T}}^\intercal \boldsymbol{\nabla}\mathbf{N}^\intercal\mathbf{V})^\intercal\,\mathrm{d}\Omega, \\
\frac{\partial \mathbf{R_A}}{\partial \mathbf{V}} &= -\int_\Omega \boldsymbol{\nabla}\mathbf{N}\frac{\partial \mathbf{q}}{\partial \mathbf{V}}^\intercal \mathrm{d}\Omega + \int_\Omega \mathbf{N}(\frac{\partial \mathbf{j}}{\partial \mathbf{V}}^\intercal \boldsymbol{\nabla}\mathbf{N}^\intercal\mathbf{V})^\intercal\,\mathrm{d}\Omega \\
&\quad + \int_\Omega \mathbf{N}(\mathbf{j}^\intercal\boldsymbol{\nabla}\mathbf{N})^\intercal\,\mathrm{d}\Omega, \\
\frac{\partial \mathbf{R_B}}{\partial \mathbf{T}} &= -\int_\Omega \boldsymbol{\nabla}\mathbf{N}\frac{\partial \mathbf{j}}{\partial \mathbf{T}}^\intercal \mathrm{d}\Omega, \\
\frac{\partial \mathbf{R_B}}{\partial \mathbf{V}} &= -\int_\Omega \boldsymbol{\nabla}\mathbf{N}\frac{\partial \mathbf{j}}{\partial \mathbf{V}}^\intercal \mathrm{d}\Omega,
\end{aligned} \tag{2.9}$$

These equations depend on the heat and current flow derivatives. Using constant

material properties with the temperature, we can write the equations as follows:

$$\begin{aligned}
\frac{\partial \mathbf{j}}{\partial \mathbf{V}} &= -\sigma \nabla \mathbf{N}^{\mathsf{T}}, \\
\frac{\partial \mathbf{j}}{\partial \mathbf{T}} &= -\alpha\sigma \nabla \mathbf{N}^{\mathsf{T}}, \\
\frac{\partial \mathbf{q}}{\partial \mathbf{V}} &= \alpha(\mathbf{N}^{\mathsf{T}}\mathbf{T})\frac{\partial \mathbf{j}}{\partial \mathbf{V}}, \\
\frac{\partial \mathbf{q}}{\partial \mathbf{T}} &= \alpha(\mathbf{N}^{\mathsf{T}}\mathbf{T})\frac{\partial \mathbf{j}}{\partial \mathbf{V}} + \alpha \mathbf{j}\mathbf{N}^{\mathsf{T}} - k\nabla \mathbf{N}^{\mathsf{T}}.
\end{aligned} \tag{2.10}$$

Notice that simplifying the material description using non-temperature-dependent material properties reduces the complexity of the TO. However, the lack of material nonlinearities disregards the Thomson effect. The Thomson effect relates to the gradient of the Seebeck coefficient with temperature and induces an extra component in the electrical current flow. However, this effect is small compared to the other thermoelectric effects and can be ignored [26]. Disregarding the Thomson effect implies that the results are inaccurate for large temperature deviations from the temperature point used to measure the material properties [27].

The nonlinearities in the problem, arising from the strong coupling of the thermoelectrical equations and subsequent Joule heating, can produce convergence issues within the NR. Higher-order elements provide exact results for the second-order thermoelectric equations within each element, improving convergence. Using higher-order elements also increases the overall computational complexity of the problem. However, the nanometer validity limit for the thermoelectrical equations and manufacturability limitations to micrometre level [28] reduce the element and system size we need to solve. Using a filter to set a characteristic length scale could also mitigate these effects at the cost of higher complexity. To reduce the computational cost of the higher-order element, we use 20-node serendipity elements and a 14-point integration scheme based on integration locations in the corners and faces of a hexahedron internal to the element. Hoit and Krishnamurthy [29] describes the advantages and development of this integration scheme with benchmark examples, and the whole element and integration implementation can be found in Appendix A.

2.3. Optimization Formulation

The optimization problem formulation employed in this work follows that proposed first by Bendsøe and Kikuchi [12]. The design variable x_e represents a variation of the density of the element associated with it,

$$\rho_e(x_e) = x_e \rho_0, \tag{2.11}$$

where ρ_e is the density of element e dependent on its design variable, ρ_0 is the nominal density of the material associated with that element, and x_e is comprised between 0 and 1. We define the rest of the material properties with respect to the

design variable x_e with a penalty coefficient as

$$\begin{aligned} \alpha_e &= \alpha_{\min} + x_e^{p_\alpha}(\alpha_0 - \alpha_{\min}), \\ k_e &= k_{\min} + x_e^{p_k}(k_0 - k_{\min}), \\ \sigma_e &= \sigma_{\min} + x_e^{p_\sigma}(\sigma_0 - \sigma_{\min}), \end{aligned} \tag{2.12}$$

where we interpolate between the minimum allowed value, denoted by the subindex min, and the nominal value of the semiconductor material, denoted by the subindex 0. This interpolation helps to avoid numerical singularities at each linear solve of the NR iterations. Furthermore, the penalization coefficient p_i for each material property helps to avoid intermediate density results, rapidly decreasing the influence of each variable at lower densities if the volume constraints are active or the optimum is found at lower material quantities than the initial design.

Once we have defined the material properties concerning our design variables, we can define the objectives and constraints of our optimization from the problem's governing equations. Traditionally, the objective function for thermoelectric devices is their efficiency, which involves the ratio of the heat extracted against the power consumption, defined as the coefficient-of-performance (COP) for a heat pumping device,

$$\mathrm{COP} = \frac{Q[\mathrm{W}]}{P[\mathrm{W}]}, \tag{2.13}$$

where Q is the heat extracted by the TEC and P is its power consumption, whose ratio can be higher than 1. Knowing the power dissipation of the electronic system we want to cool down, we know the heat extracted Q. Fixing Q limits a COP maximization objective to reduce power consumption and increase device efficiency. However, reducing power consumption for a known heat extraction does not necessarily correlate to a lower temperature in our electronics, which is critical for specific applications [30]. Defining the electronics temperature as our optimization objective means that we must include the power limitation – or power budget – of the thermoelectric system as a constraint, as it is no longer present in our objective function.

As we can easily modify the power consumption by external operational inputs – applied voltage or current through the device – to work on more efficient states, we must include this operation in the optimization to compare to the initial design. For this purpose, we introduce an externally applied voltage boundary condition as a design variable. This voltage allows us to compare the optimum working point of the non-optimized designs without postprocessing. Furthermore, the voltage gradient design variable considers the system's nonlinear behaviour concerning the applied electrical load.

In some cases, reducing the volume does not improve the TEC's performance. If we still want to limit the material used and associated costs, we must introduce a volume constraint to the problem.

The optimization shall take into account the objective and constraints as

$$\mathbf{x} = \underset{\mathbf{x}}{\arg\min}: \qquad T_{avg}(\mathbf{x},\mathbf{T}) = \frac{1}{n_n}\sum_{i=1}^{n_n}(T_i) = \mathbf{L}^\intercal\mathbf{T}, \tag{2.14a}$$

$$\text{subject to:} \qquad \mathbf{R}^k = \mathbf{0}, \tag{2.14b}$$

$$c_v = \sum_{e=1}^{n_e}\frac{v_e x_e}{v_0 v_{obj}} - 1 \leq 0, \tag{2.14c}$$

$$c_P = \frac{P}{P_{obj}} - 1 < 0, \tag{2.14d}$$

$$V_f = V_{\min} + x_{n_e+1}(V_{\max} - V_{\min}), \tag{2.14e}$$

where the objective function, T_{avg}, is defined as the average temperature value of the specified nodal values. Only the nodal values of the surface of the thermocouple in contact with the device to cool down – in this case, one of the copper interfaces – need to be taken into account for the objective value, with n_n being the total number of nodes in this surface. This summation can then be represented as a matrix product of a vector of constant values ($\mathbf{L}$) – equal to $\frac{1}{n_n}$ for the nodal temperature values within the surface to cool down and zero otherwise – by the vector $\mathbf{U}$ that contains the nodal degrees of freedom (DOFs). For this calculation to be accurate, after the optimization has converged, we need to ensure that the temperature DOFs at the copper surface temperature have a uniform value.

Furthermore, the established limit volume for optimization, v_{obj}, and design variables, $\mathbf{x}$, are scaled between 0 and 1. The volume constraint, Equation (3.25d), is calculated dependent on each element design variable, x_e, related to the total initial design volume, v_0, and the desired maximum volume percentage, v_{obj}. While the power consumption constraint, Equation (3.25c), can surpass a value of 1, it is made dimensionless with the limiting power budget, P_{obj}. If both values are of the same order of magnitude, the optimization should not be affected.

To calculate the overall power consumption, we need to define the power differential as the current density multiplied by the differential of the voltage gradient at a given point. We can calculate the total power consumption of the thermocouple through the sum of the volume integral of this power differential for each element as

$$P = \sum_{e=1}^{n_e} P_e = \sum_{e=1}^{n_e}\left(-\int_{\Omega_e}\mathbf{j}^\intercal\boldsymbol{\nabla}\mathbf{N}^\intercal\mathbf{V_e}\,\mathrm{d}\Omega_e\right), \tag{2.15}$$

where n_e is the total number of elements in the FEM model, Ω_e the volume associated with a given element with e denoting element-based properties, and the minus sign takes into account the opposite sense of the current and voltage differentials.

To be able to maintain the optimized power consumption for any x_e density design space, within our power budget limitations, we introduce an extra design variable x_{n_e+1} stored in the last index of the design variable vector $\mathbf{x}$ of size n_e+1. This variable is related to the voltage boundary condition (V_f) through a linear interpolation, Equation (3.25e), between user-selected voltage values ($V_{\max}, V_{\min}$).

As stated in the objective and design variable discussion, this variable introduces the nonlinear dependency of the power consumption and Joule heating into the problem. Using x_{n_e+1} as a design variable allows the thermoelectrical pellet to operate at an electrically favourable load within the optimization framework, reducing the postprocessing needs to study different working points and avoiding lower efficiencies due to high current density concentrations at higher electrical loading.

We can now solve this problem with the method of moving asymptotes (MMA) [31] optimization algorithm. MMA is popular in the structural optimization field due to its robustness, flexibility and ability to handle multiple constraints, even if other optimization algorithms provide better computational efficiency [32, 33]. MMA is based on the local approximation of specific convex functions to the nonlinear problem. These approximations require the derivative of the objective and constraint equations concerning the design variables x_e that are calculated in each iteration of MMA.

Subsequently, each MMA step needs to recalculate the FEM solution running an NR algorithm from a given initial point. Using the linearized equations concerning the nodal degrees of freedom, Equations (3.15), (7.22) and (7.23), we find that certain conditions for the NR initial point can improve the convergence of the method:

- For the first step of the MMA algorithm, without information on previous NR solutions,

$$\begin{aligned} \mathbf{T} &= \mathbf{0}, \\ \mathbf{V} &= \mathbf{0}, \end{aligned} \tag{2.16}$$

  provides convergent solutions if the boundary conditions are not electrically or thermally disconnected.

- Having a solution from a previous MMA step, we can improve the NR convergence rate using the initial point,

$$\begin{aligned} \mathbf{T}^{t+1} &= \mathbf{T}^{t}, \\ \mathbf{V}^{t+1} &= \mathbf{V}^{t} \frac{V_f^{t+1}}{V_f^{t}}, \end{aligned} \tag{2.17}$$

  where t represents the ith step of the MMA procedure.

2.3.1. Sensitivity calculation

In this section, we separate the problem, Equation (4.12), into each of its objectives and constraints to calculate their derivatives concerning the design variables. We can use these sensitivities to find an optimum thermocouple design through gradient descent optimization algorithms. We calculate these sensitivities through the adjoint method due to its efficiency for a large number of design variables. A development of the adjoint method for structures optimization is developed in [34, 35].

Objective Function

The objective function defined in Equation (3.25a) defines the average temperature from the surface of the thermocouple in charge of extracting heat from the environment. From this equation, we can apply the adjoint theorem to calculate its derivatives using an equivalent objective defined as

$$T^*_{avg} = \mathbf{L}^\intercal \mathbf{U} + \Lambda^\intercal \mathbf{R}^k,$$

where we include the residuals from the thermoelectric system solution, which tends to zero for convergence conditions of the Newton-Raphson algorithm, multiplied by a vector of unknown constants Λ. We can write the derivative of this new expression of the objective function concerning the design variables as

$$\frac{\mathrm{d}T^*_{avg}}{\mathrm{d}\mathbf{x}} = \mathbf{L}^\intercal \frac{\mathrm{d}\mathbf{U}}{\mathrm{d}\mathbf{x}} + \Lambda^\intercal \left(\frac{\mathrm{d}\mathbf{R}^k}{\mathrm{d}\mathbf{x}} \right). \tag{2.18}$$

Considering the dependencies of each variable and the values of the prescribed degrees of freedom ($\bar{\mathbf{U}}$), we can write

$$\begin{aligned} &\mathbf{R}^k = \mathbf{R}(\mathbf{U}, \bar{\mathbf{U}}, \mathbf{x}), \\ &\mathbf{U} = \mathbf{U}(\mathbf{x}, V_f); \bar{\mathbf{U}} = \bar{\mathbf{U}}(V_f), \\ &V_f = V_f(x_{n_e+1}), \end{aligned} \tag{2.19}$$

and applying the chain rule to the residual derivative, we get

$$\frac{\mathrm{d}\mathbf{R}^k}{\mathrm{d}\mathbf{x}} = \frac{\partial \mathbf{R}^k}{\partial \mathbf{x}} + \mathbf{K}^\mathbf{k} \left(\frac{\partial \bar{\mathbf{U}}}{\partial V_f} \frac{\mathrm{d}V_f}{\mathrm{d}\mathbf{x}} + \frac{\mathrm{d}\mathbf{U}}{\mathrm{d}\mathbf{x}} \right). \tag{2.20}$$

We can then write the derivative of the average temperature as

$$\begin{aligned} \frac{\mathrm{d}T^*_{avg}}{\mathrm{d}\mathbf{x}} =& (\mathbf{L}^\intercal + \Lambda^\intercal \mathbf{K}^\mathbf{k}) \frac{\mathrm{d}\mathbf{U}}{\mathrm{d}\mathbf{x}} \\ &+ \Lambda^\intercal \left(\frac{\partial \mathbf{R}^k}{\partial \mathbf{x}} + \mathbf{K}^\mathbf{k} \frac{\partial \bar{\mathbf{U}}}{\partial V_f} \frac{\mathrm{d}V_f}{\mathrm{d}\mathbf{x}} \right), \end{aligned} \tag{2.21}$$

and we obtain the adjoint equation so that the components multiplying a derivative of $\mathbf{U}$ concerning a design variable is zero,

$$\Lambda = -(\mathbf{K}^\mathbf{k})^{-\intercal} \mathbf{L}. \tag{2.22}$$

Substituting Equation (2.22) into Equation (2.21), we can now calculate the derivatives concerning the design variables,

$$\frac{\mathrm{d}T^*_{avg}}{\mathrm{d}\mathbf{x}} = +\Lambda^\intercal \left(\frac{\partial \mathbf{R}^\intercal}{\partial \mathbf{x}} + \mathbf{K}^\mathbf{k} \frac{\partial \bar{\mathbf{U}}}{\partial V_f} \frac{\mathrm{d}V_f}{\mathrm{d}\mathbf{x}} \right), \tag{2.23}$$

where this solution can be reduced to the element level, taking into account that each element depends only on each density design variable x_e, and we can treat x_{n_e+1}, which modifies the voltage boundary conditions separately. We can calculate the sensitivity concerning a x_e density design variable as

$$\frac{\mathrm{d}T^*_{avg}}{\mathrm{d}x_e} = \Lambda_e^{\intercal} \frac{\partial \mathbf{R}^k}{\partial x_e}, \tag{2.24}$$

where the derivatives of the residual can be written in an integral form using the element densities,

$$\begin{aligned} \frac{\partial \mathbf{R}^{\mathbf{k}}_{\mathbf{A}}}{\partial x_e} &= -\int_{\Omega_e} \boldsymbol{\nabla}\mathbf{N} \frac{\partial \mathbf{q}}{\partial x_e}^{\intercal} \mathrm{d}\Omega_e + \int_{\Omega_e} \mathbf{N} (\frac{\partial \mathbf{j}}{\partial x_e}^{\intercal} \boldsymbol{\nabla}\mathbf{N}^{\intercal}\mathbf{V})^{\intercal} \mathrm{d}\Omega_e, \\ \frac{\partial \mathbf{R}^{\mathbf{k}}_{\mathbf{B}}}{\partial x_e} &= -\int_{\Omega_e} \boldsymbol{\nabla}\mathbf{N} \frac{\partial \mathbf{j}}{\partial x_e}^{\intercal} \mathrm{d}\Omega_e. \end{aligned} \tag{2.25}$$

We can also reduce the derivatives of the heat and current densities to the element level as

$$\begin{aligned} \frac{\partial \mathbf{j}}{\partial x_e} &= -\frac{\partial \sigma_e}{\partial x_e} \left(\boldsymbol{\nabla}\mathbf{N}^{\intercal}\mathbf{V_e} + \alpha_e \boldsymbol{\nabla}\mathbf{N}^{\intercal}\mathbf{T_e} \right) + \sigma \frac{\partial \alpha_e}{\partial x_e} \boldsymbol{\nabla}\mathbf{N}^{\intercal}\mathbf{T_e}, \\ \frac{\partial \mathbf{q}}{\partial x_e} &= \frac{\partial \alpha_e}{\partial x_e} \left(\mathbf{N}^{\intercal}\mathbf{T_e} \right) \mathbf{j} + \alpha_e \left(\mathbf{N}^{\intercal}\mathbf{T_e} \right) \frac{\partial \mathbf{j}}{\partial x_e} - \frac{\partial k_e}{\partial x_e} \boldsymbol{\nabla}\mathbf{N}^{\intercal}\mathbf{T_e}, \end{aligned} \tag{2.26}$$

where V_e and T_e refer to the nodal values relative to the associated element. To conclude the formulation, we can write the dependence of the material properties on the density variables (Equation (3.24)),

$$\begin{aligned} \frac{\partial \alpha_e}{\partial x_e} &= p_\alpha x_e^{p_\alpha - 1} (\alpha_0 - \alpha_{\min}), \\ \frac{\partial k_e}{\partial x_e} &= p_k x_e^{p_k - 1} (k_0 - k_{\min}), \\ \frac{\partial \sigma_e}{\partial x_e} &= p_\sigma x_e^{p_\sigma - 1} (\sigma_0 - \sigma_{\min}), \end{aligned} \tag{2.27}$$

for the SIMP method.

Remembering we still have an extra design variable controlling the voltage across the thermocouple that is not considered in the previous density derivatives, x_e. We store this design variable in the same vector that stores the density design variables with index $n_e + 1$. If we do not apply the boundary conditions to any element with an associated x_e, we can calculate its sensitivity as the matrix product

$$\frac{\mathrm{d}T^*_{avg}}{\mathrm{d}x_{n_e+1}} = +\Lambda^{\intercal}\mathbf{K}^{\mathbf{k}} \frac{\partial \bar{\mathbf{U}}}{\partial V_f} \frac{\mathrm{d}V_f}{\mathrm{d}x_{n_e+1}}, \tag{2.28}$$

and the derivative of $\mathbf{R}^k$ with respect to the vector of prescribed nodal values $\bar{\mathbf{U}}$ is equal to the rows of the $\mathbf{R}^k$ matrix corresponding to the fixed degrees of freedom in $\bar{\mathbf{U}}$. Now, the partial derivative of the prescribed degrees of freedom concerning V_f

equals one in the prescribed values and zero otherwise. Given the interpolation of the voltage boundary condition, Equation (3.25e), its derivative with respect to the n_e+1 design variable is

$$\frac{\mathrm{d}V_f}{\mathrm{d}x_{n_e+1}} = V_{\max} - V_{\min}\,, \tag{2.29}$$

which provides all the information needed to calculate the derivative of the objective function.

Volume Constraint

For an isotropic material, we calculate the derivative of the volume constraint element-wise using the volume of each element. Starting from the formulation in Equation (3.25d), the derivative of the constraint concerning each density variable is,

$$\frac{\mathrm{d}c_v}{\mathrm{d}x_e} = \frac{\partial \sum_{e=1}^{n_e}\left(\frac{x_e v_e}{v_0 v_{obj}}\right)}{\partial x_e} = \frac{v_e}{v_0 v_{obj}}\,. \tag{2.30}$$

From this formulation, we can also appreciate that the derivative from any external boundary condition, including voltage, V_f, will be zero,

$$\frac{\mathrm{d}c_{vol}}{\mathrm{d}V_f} = 0. \tag{2.31}$$

Power Constraint

Using the definition of the power consumption in Equation (3.58), we can calculate its derivative concerning the density design variable x_e with $e \leq n_e$,

$$\frac{\mathrm{d}P_e}{\mathrm{d}x_e} = -\int_\Omega \left(\frac{\mathrm{d}\mathbf{j}}{\mathrm{d}x_e}\right)^\intercal \boldsymbol{\nabla}\mathbf{N}^\intercal \mathbf{V_e}\,\mathrm{d}\Omega - \int_\Omega \mathbf{j}^\intercal \boldsymbol{\nabla}\mathbf{N}^\intercal \frac{\mathrm{d}\mathbf{V_e}}{\mathrm{d}x_e}\,\mathrm{d}\Omega\,. \tag{2.32}$$

The current density in the previous equation depends on the nodal voltages and temperature values given by Equation (3.3). The derivative of the current density can be written as

$$\begin{aligned}\frac{\mathrm{d}\mathbf{j}}{\mathrm{d}x_e} =& -\frac{\partial\sigma}{\partial x_e}\left(\boldsymbol{\nabla}\mathbf{N}^\intercal \mathbf{V_e} + \alpha \boldsymbol{\nabla}\mathbf{N}^\intercal \mathbf{T_e}\right) \\ & -\sigma\left(\boldsymbol{\nabla}\mathbf{N}^\intercal \frac{\mathrm{d}\mathbf{V_e}}{\mathrm{d}x_e} + \frac{\partial\alpha}{\partial x_e}\boldsymbol{\nabla}\mathbf{N}^\intercal \mathbf{T_e} + \alpha\boldsymbol{\nabla}\mathbf{N}^\intercal \frac{\mathrm{d}\mathbf{T_e}}{\mathrm{d}x_e}\right).\end{aligned} \tag{2.33}$$

In this equation, we can separate the components that multiply the derivatives of the system nodal degrees of freedom, $\mathbf{L_{dUe}}$, from the rest of the integrator, L_{Ue}, element-wise,

$$\begin{aligned}L_{Ue} =& \mathbf{V_e}^\intercal \boldsymbol{\nabla}\mathbf{N}\frac{\partial\sigma}{\partial x_e}\boldsymbol{\nabla}\mathbf{N}^\intercal \mathbf{V_e} + \\ & \mathbf{V_e}^\intercal \boldsymbol{\nabla}\mathbf{N}\left(\frac{\partial\alpha}{\partial x_e}\sigma + \alpha\frac{\partial\sigma}{\partial x_e}\right)\boldsymbol{\nabla}\mathbf{N}^\intercal \mathbf{T_e}\,, \\ \mathbf{L_{dUe}} =& \begin{bmatrix} \mathbf{V_e}^\intercal \boldsymbol{\nabla}\mathbf{N}\sigma\alpha\boldsymbol{\nabla}\mathbf{N}^\intercal \\ \mathbf{V_e}^\intercal \boldsymbol{\nabla}\mathbf{N}\sigma\boldsymbol{\nabla}\mathbf{N}^\intercal - \mathbf{j}^\intercal\boldsymbol{\nabla}\mathbf{N}^\intercal \end{bmatrix},\end{aligned} \tag{2.34}$$

We can observe that the first term L_{Ue} is a constant value within the element, and we can extract this term outside the integral,

$$\frac{\mathrm{d}P_e}{\mathrm{d}x_e} = L_{Ue}v_e + \int_\Omega \left(\mathbf{L_{dUe}}^\intercal \frac{\mathrm{d}\mathbf{U_e}}{\mathrm{d}x_e}\right) \mathrm{d}\Omega. \tag{2.35}$$

Applying the summation from Equation (3.58) and Equation (2.35) we can assemble both terms, L_{Ue} and $\mathbf{L_{dUe}}$, for the full system nodal values into $\mathbf{L_U}$ and $\mathbf{L_{dU}}$ respectively. The result of taking the derivative for all density values, x_e with $e \leq n_e$ is,

$$\begin{aligned} \frac{\mathrm{d}P}{\mathrm{d}\mathbf{x}} &= \mathbf{L_U} + \mathbf{L_{dU}}^\intercal \frac{\mathrm{d}\mathbf{U}}{\mathrm{d}\mathbf{x}}, \\ \mathbf{L_U} &= \begin{bmatrix} L_{U1}v_1 & L_{U2}v_2 & \dots & L_{UN}v_N \end{bmatrix}. \end{aligned} \tag{2.36}$$

Introducing the derivative of the power, Equation (2.36), in the constraint derived in Equation (3.25c) and using an equivalent formulation with an adjoint vector, $\Lambda_\mathbf{P}$, multiplied by the residuals we obtain,

$$c^*_{pow} = \frac{P}{P_{obj}} - 1 + \Lambda_\mathbf{P}{}^\intercal \mathbf{R}^k. \tag{2.37}$$

The derivative of this new c^*_{pow} can be re-written as

$$\frac{\mathrm{d}c^*_{pow}}{\mathrm{d}\mathbf{x}} = \frac{\frac{\mathrm{d}P}{\mathrm{d}\mathbf{x}}}{P_{obj}} + \Lambda_\mathbf{P}{}^\intercal \frac{\mathrm{d}\mathbf{R}^k}{\mathrm{d}\mathbf{x}}, \tag{2.38}$$

where we can substitute Equation (2.36),

$$\begin{aligned} \frac{\mathrm{d}c^*_{pow}}{\mathrm{d}\mathbf{x}} = &\frac{1}{P_{obj}} \left(\mathbf{L_U} + \mathbf{L_{dU}}^\intercal \frac{\mathrm{d}\mathbf{U}}{\mathrm{d}\mathbf{x}}\right) \\ &+ \Lambda_\mathbf{P}{}^\intercal \left(\frac{\partial \mathbf{R}^k}{\partial \mathbf{x}} + \mathbf{K^k}\frac{\mathrm{d}\mathbf{U}}{\mathrm{d}\mathbf{x}} + \frac{\partial \mathbf{R^k}}{\partial \bar{\mathbf{U}}}\frac{\partial \bar{\mathbf{U}}}{\partial V_f}\frac{\mathrm{d}V_f}{\mathrm{d}\mathbf{x}}\right). \end{aligned} \tag{2.39}$$

Finally, we can select the adjoint vector $\Lambda_\mathbf{P}$ imposing that the components of the derivative of the system nodal degrees of freedom, $\frac{\mathrm{d}\mathbf{U}}{\mathrm{d}\mathbf{x}}$, are removed from the equation as

$$\Lambda_\mathbf{P} = -(\mathbf{K^k})^{-\intercal} \left(\frac{1}{P_{obj}}\mathbf{L_{dU}}\right). \tag{2.40}$$

Equation (2.40) can now be used with Equation (2.39) to calculate the derivatives concerning the density variables, reducing it to the element level as

$$\frac{\mathrm{d}c^*_{pow}}{\mathrm{d}x_e} = \frac{1}{P_{obj}} L_{Ue}\mathbf{V_e} + \Lambda_\mathbf{Pe}{}^\intercal \frac{\partial \mathbf{R}^k}{\partial x_e}, \tag{2.41}$$

where Equation (7.24) provides the derivative of the residual concerning the element density.

The calculation of the derivative concerning the x_{n_e+1} design variable controlling the voltage gradient across the thermocouple, Equation (3.25e), can be calculated by noticing that the material properties do not depend on the voltage ($\alpha, \sigma, k \neq f(V_f)$), $L_{Ue} = 0$. We can calculate the derivative as

$$\frac{\mathrm{d}c^*_{pow}}{\mathrm{d}x_{n+1}} = +\Lambda_{\mathbf{P}}{}^{\intercal} \frac{\partial \mathbf{R}^k}{\partial \bar{\mathbf{U}}} \frac{\partial \bar{\mathbf{U}}}{\partial V_f} \frac{\mathrm{d}V_f}{\mathrm{d}x_{n+1}}. \tag{2.42}$$

where the conclusion and procedure from Equation (2.28) can still be applied with the new adjoint vector, Λ_P.

2.4. Results

The use of SIMP provides a simple integration with FEM and flexibility with modifications using filtering techniques. SIMP shows excellent results in mechanical problems with penalty factors, p_i, higher than 1 and usually equal to 3. However, for high nonlinear or *multi-physics* problems, these coefficients might need to be re-evaluated empirically to improve the convergence of TO [36].

In this section, we study the use of an analytical problem of low dimension that can help to provide insight into the larger FEM problem. Notably, we want to understand the influence of the parameters introduced in the optimization – material penalty coefficients – and the starting points of the MMA algorithm over the optimized designs.

Finally, the proposed method in Section 2.4.2 is applied to a FEM thermocouple model using the insight obtained from the analytical model and with the application of different heat extraction and power consumption requirements, studying their effects over the optimized designs.

2.4.1. Landscape study through analytical models

For a thermocouple optimization, a parallel semiconductor problem with two pillars per thermoelectric leg and two design variables, x_1 and x_2 – associated with each one of the two pillars of each thermoelectric leg, see Figure 2.2 – provides one of the smallest problems that we can solve analytically, providing insights into the problem and avoiding electrical and thermal disconnections.

The schematic in Figure 2.2 describes a problem with two legs for each pellet with two different density variables, x_1 and x_2, in each electrical connection to the copper layers – elements shaded in grey – to avoid disconnected designs unless both density variables are equal to zero. The heat injection, q_{in}, ground voltage level, V_0, with the voltage gradient V_f and constant temperature sink T_0 represent the boundary conditions for the problem. Finally, A and L provide each column's cross-sectional area and height, with z representing a certain height along the legs starting from the heat sink.

Notice that we apply the boundary conditions at the bottom and top of each leg or semiconductor column in the copper layers connections, providing the compatibility equations between the legs, which we can write using Equations (3.1), (3.3) and (3.4)

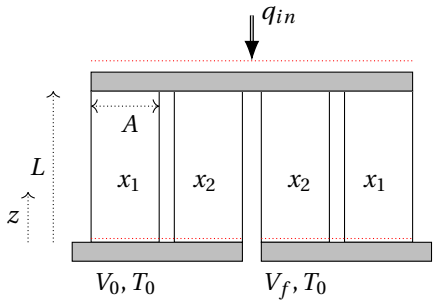

Figure 2.2.: Thermocouple analytical problem schematic with 4 columns and 2 density design variables, x_1 and x_2. The geometry of the design is defined through a constant cross-section area A, and height of L, with the height dimension being represented by the z coordinate. The boundary conditions are represented by a heat injection q_{in}, a heat sink temperature T_0 and 2 voltages, V_0 and V_f.

and Figure 2.2 as

$$\begin{aligned}
\sum_{xi} q_{p,xi}(L) + \sum_{xi} q_{n,xi}(L) &= -\frac{q_{in}}{A}, \\
\sum_{xi} j_{p,xi}(L) + \sum_{xi} j_{n,xi}(L) &= 0, \\
T_{p,xi}(L) &= T_{n,xi}(L) = T_c, \\
\phi_{p,xi}(L) &= \phi_{n,xi}(L) = V_c, \\
T_{p,xi}(0) &= T_{n,xi}(0) = T_0, \\
\phi_{p,xi}(0) &= V_0 = 0, \\
\phi_{n,xi}(0) &= V_f,
\end{aligned} \tag{2.43}$$

where p and n indices refer to the p or n-type semiconductors – positioned in series through a copper connection – and xi to the design variable associated with each parallel leg, Figure 2.2. Finally, T_c and V_c represent the unknown values in the top cold connection at location $z == L$ according to Figure 2.2.

The solution of the integration of Equations (3.1), (3.3) and (3.4) along the length, z, of a constant cross-section leg provides,

$$\begin{aligned}
T(z) &= -\frac{j^2}{k\sigma}\frac{z^2}{2} + C_1 z + C_2, \\
\phi(z) &= +\frac{\alpha j}{\sigma k}\frac{z^2}{2} - \frac{j}{\sigma} z + \alpha C_3 z + C_4,
\end{aligned} \tag{2.44}$$

where the C_i are constants that need to be solved using the boundary conditions Equation (2.43). The voltage and temperature distributions of Equation (2.44) are quadratic functions across the bulk material with constant material coefficients. The

semiconductor material properties for each of the $p-Bi_2Te_3$ and $n-Bi_2Te_3$ pellets are available from the manufacturer and taken from Hu *et al.* [37], where the data from ULVAC-Riko Co. Ltd is fit to polynomials of the form,

$$\begin{aligned}
\alpha_p &= 8.33e-12T^3 - 1.32e-8T^2 + 6.3e-6T - 7.04e-4, \\
\rho_p &= -7.36e-13T^3 + 6.14e-10T^2 - 6.35e-8T - 1.78e-6, \\
k_p &= 1.59e-8T^3 - 3.32e-6T^2 - 2.177e-3T + 1.5775, \\
\alpha_n &= -3.98e-12T^3 + 7.34e-9T^2 - 3.82e-6T + 3.95e-4, \\
\rho_n &= -6.83e-13T^3 + 6.66e-10T^2 - 1.55e-7T + 1.81e-5, \\
k_n &= 2.19e-8T^3 - 4.60e-6T^2 - 4.51e-3T + 2.48,
\end{aligned} \tag{2.45}$$

where each subindex refers to p-type or n-type semiconductors, respectively. We ignore the copper Seebeck coefficient due to symmetry, with its effects counteracted

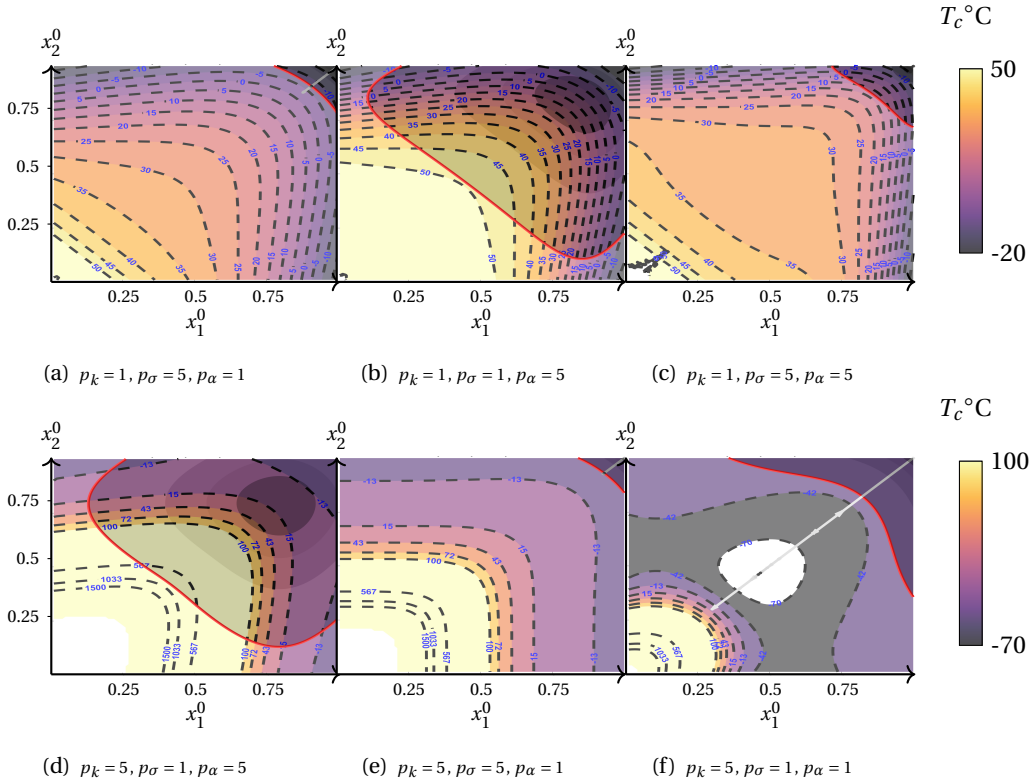

(a) $p_k = 1, p_\sigma = 5, p_\alpha = 1$ (b) $p_k = 1, p_\sigma = 1, p_\alpha = 5$ (c) $p_k = 1, p_\sigma = 5, p_\alpha = 5$

(d) $p_k = 5, p_\sigma = 1, p_\alpha = 5$ (e) $p_k = 5, p_\sigma = 5, p_\alpha = 1$ (f) $p_k = 5, p_\sigma = 1, p_\alpha = 1$

Figure 2.3.: Material penalization coefficient cold temperature isolines for a 4 column TEC problem with 2 design variables and a power constraint, shadowed in black. The MMA optimization starting with the point (1,1) is reflected with grey to black lines turning darker until convergence.

in the full thermoelectric circuit. To simplify the problem to constant material properties, we fix the values at 300 K as summarized in Table 2.1.

	ρ (Ω m)	k (W/K)	α (V/K)
$p-Bi_2Te_3$	$1.45e-05$	1.054963	$2.17e-04$
$n-Bi_2Te_3$	$1.30e-05$	1.305023	$-1.99e-4$
Cu	$1.67e-08$	385	0

Table 2.1.: TEC Semiconductor Material Properties at 300 K.

To solve the system, we require the C_i constants for four different legs, leading to a system of 11 equations, plus an additional equation for the power,

$$P = -A\left(\sum j_{li}(V_c - V_0) + \sum j_{ri}(V_f - V_c)\right), \tag{2.46}$$

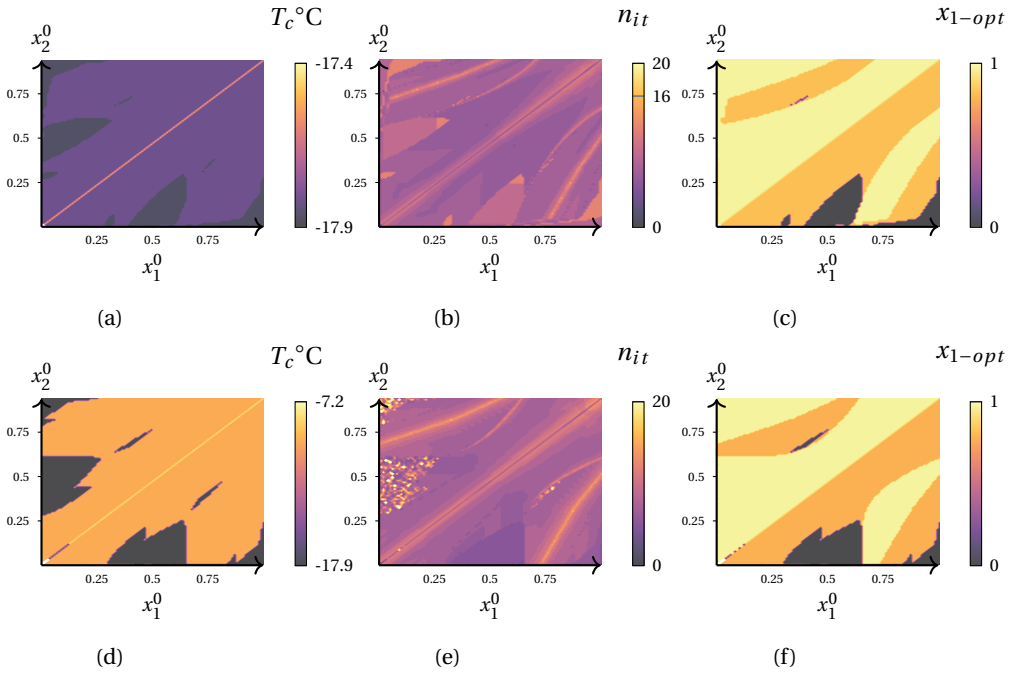

Figure 2.4.: Graphs exemplifying the final convergence values of a cold temperature T_c MMA optimization of a 2D analytical thermocouple with a power constraint of 0.065 W for different initial design variables in the horizontal and vertical axis. The top figures represent the results of T_c, total iterations until convergence and the optimized x_1 found (x_{1-opt}) for a combination of penalty coefficients of $p_k = p_\sigma = 5, p_\alpha = 1$ while the bottom row uses the penalty coefficients $p_k = p_\alpha = 1, p_\sigma = 5$.

for constant values of the material coefficients (α, σ, k).

To solve the system, we select a given operational point, defined by all the parameters needed to solve the problem, given by,

$$T_0 = 298.15\,\text{K}\ , \qquad q_{in} = 0.01\,\text{W/m}^2\ ,$$
$$L = 1.2\,\text{mm}\,, \qquad A = 1\,\text{mm}^2\,, \qquad V_f = 0.05\,\text{V}\ ,$$

and the parametric solution to Equations (2.43) and (2.44) found in Appendix B. Notice that in this solution, we set all minimum material properties – α_{min}, k_{min} and σ_{min} from Equation (3.24) – to zero for simplification purposes.

The quadratic nature of the system provides two different solutions. We look for a solution with temperatures above absolute zero to evaluate which one has a physical meaning. For the material properties, we use the values of the p-semiconductor from Table 2.1. Notice that, to account for an n-type semiconductor using a given direction of the current and a constant positive α, we need to provide a negative sign to the Seebeck coefficients using Equation (2.44).

In Figure 2.3, we represent the objective temperature, T_c, for multiple combinations of the material penalty coefficients. The infeasible region of the power constraint, given by Equation (2.46), is superimposed to T_c as a grey-shadowed region limited by a red line. We represent this power consumption with a darker grey colour the higher the power consumption to visualize its landscape. The path followed by the MMA optimizer, drawn with grey arrows that grow darker with successive iterations, starting from a full density design – $x_i = 1$ for both design variables – provides information on the convergence of the problem.

We find 3 different possible landscapes depending on the material penalty coefficients, which will affect the convergence of the problem. Except for Figure 2.3f, all penalty coefficients present an objective temperature global minima in the full density design point, and local minima at the locations with one single design variable with full density, *i.e.* $x_1 = 0$ and $x_2 = 1$ or $x_1 = 1$ and $x_2 = 0$. With regards to the power constraint, it can either present a negative slope in all the infeasible design regions (Figures 2.3a, 2.3e and 2.3f) or set the full density design point in a valley region, having a maximum within the infeasible region (Figures 2.3b to 2.3d).

These landscapes affect the convergence of MMA. The landscapes where the power presents a maximum in the infeasible design space do not move from the initial point, chosen as the full-density design, as all directions increase the constraint value. This non-convexity leads to results within the infeasible design space in the cases in Figures 2.3b to 2.3d. From the remaining cases, we want to avoid global minima in grey design areas that lead to equivalent non-manufacturable porous materials, such as Figure 2.3f.

To further identify the best combination of penalty coefficients for this problem, we look into the convergence properties and final results of Figures 2.3a and 2.3e, which show convergence from the full density design to local minima in the feasible design space. Between both cases, Figure 2.3e shows a steeper design space and lower achieved objective values. However, different initial design points might influence these results. Figure 2.4 studies these two cases for multiple initial points, x_i^0, represented on the horizontal and vertical axis, and plotting in colour the final

temperature values, number of iterations until convergence, n_{it}, and x_{1-opt} or optimized x_1 design variable. We do not represent the design variable x_{2-opt} due to the symmetry of the problem.

Figures 2.4a and 2.4d shows that both penalty coefficients can reach similar values for T_c depending on the initial chosen point. However, the case $p_k = 5, p_\sigma = 5, \alpha = 1$ shows a lower dispersion in the results from different initial points. There is no better configuration regarding the number of iterations until convergence. Still, it does suggest that values slightly off the full-density design might reduce the number of iterations until convergence. Both combinations of penalty coefficients show numerical errors at low initial density values for both design variables due to the disconnection between the boundary conditions, which leads to values close to infinity in T_c.

The previous study only considered the power constraint. We now introduce the volume constraint through the definitions in Equation (3.25d) and Equation (2.30) to study the entire landscape. The new landscape in Figure 2.5 uses a power constraint of 0.05 W in addition to a volume constraint of 85 %. This volume constraint appears as a straight line at 135°, and its location gives rise to 3 distinct cases depending on the constraint limit. We can find that both constraints, volume and power, cross each other Figure 2.5, with the possibility of either of them being active at convergence or finding one of them being the most limiting, in which case it will be the only constraint to be active at convergence.

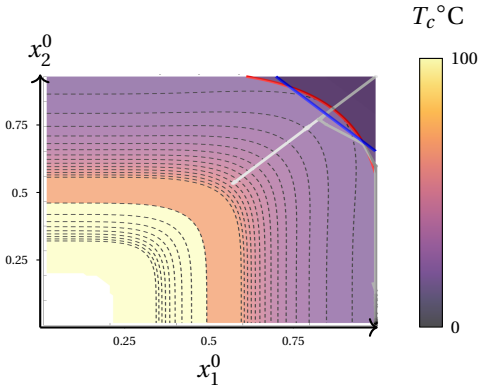

Figure 2.5.: Temperature landscape for a 2D analytical thermocouple optimization with a power constraint of 0.05 W and 85 % initial volume with the non-allowed design space shadowed in gray.

Figure 2.6 represents the value for the optimized x_1 design variable found, x_{1-opt}, for a maximum of 85 iterations with respect the initial design variables, x_1^0 and x_2^0, represented in the horizontal and vertical axis using the previously defined problem, with power and volume constraints. Compared to Figure 2.4, this graph shows that the algorithm removes intermediate density values from the converged results, and only 2 solutions remain. These remaining solutions are the local minima with one of

both design variables equal to one and the other one equal to zero.

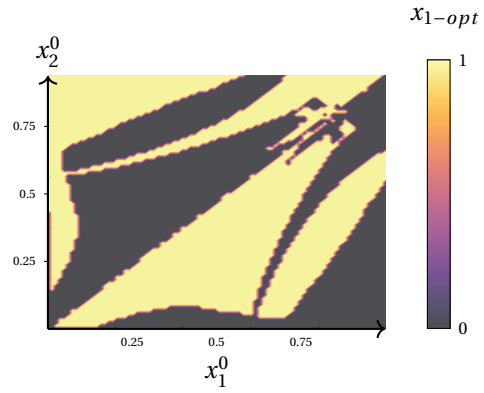

Figure 2.6.: Design variable , x_{1-opt}, of the obtained local minima in the analytical problem for 85 MMA iterations of a 2D analytical thermocouple optimization with a power constraint of 0.05 W and 85 % initial volume.

As a last consideration, Figure 2.7 shows the convergence of the objective function for different penalty values for the case $p_\alpha < p_\sigma = p_k$ starting from a full density design. While higher values of $p_k = p_\sigma$ provide lower objective values, the higher these values, the higher the nonlinearities introduced in the problem. The case with a nonlinear penalty coefficient for p_α shows worse convergence and final results and should be avoided.

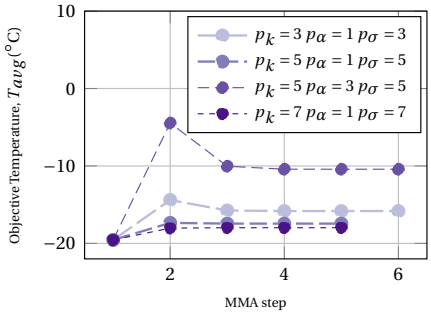

Figure 2.7.: Convergence of the objective function for several penalty coefficients in a thermocouple analytical model.

Notice that Figures 2.3b to 2.3c cases did not converge starting from a full-density design. However, these study cases might converge from different initial design locations. Nevertheless, lacking information on the optimized design, a homogeneous density equal to the full density as a starting point is desirable for larger problems.

The results and reasoning in this section lead to the recommendation of penalty coefficients of $p_k = p_\sigma > p_\alpha = 1$ and initial density values of $x_e = 1$.

2.4.2. Thermocouple optimization examples through FEM

This section showcases optimization examples using the proposed TO methodology based on the 1MC10-031 TEC from RMT Ltd. The data sheet of the 1MC10-031 TEC provides the dimensions of $1.2 \times 1 \times 1\,\text{mm}^3$ separated by an air-gap of 0.4 mm which we reduce in 0.1 mm to have a larger feasible semiconductor design volume.

In this model, we assume a uniformly distributed heat input along the top surface of the thermocouple. We also model the heat sink as having a constant temperature at its bottom. We consider the TEC to consist of 32 pairs of pellets, N_p, considered for the calculation of the boundary conditions as,

$$q_{in} = q_T / N_p\,,$$
$$P_c = P_T / N_p\,,$$

where P_T and P_c represent the TEC's total heat extraction and power consumption, assuming each pair extracts equal heat. Additionally, a voltage gradient is imposed between both copper slabs, with a value of 0 close to the p-type semiconductor and the desired electrical potential, V_f, at the other electrical contact, see Figure 2.8. This $V_f = 0.05\,\text{V}$ is modified through the design variable x_{n_e+1} with limits between $0.5V_f$ and $2V_f$, equivalent to V_{min} and V_{max} in Equation (3.25e).

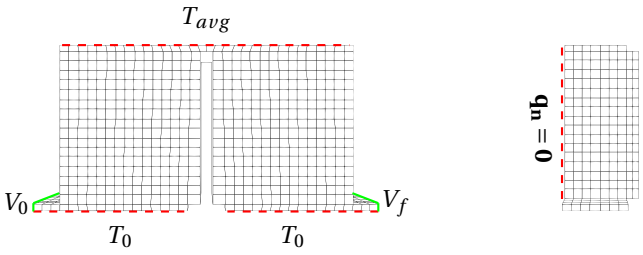

Figure 2.8.: Front and side view of the thermocouple mesh with the applied boundary and symmetry conditions.

We represent the mesh and boundary conditions in Figure 2.8 where we use symmetry boundary conditions, simplifying the thermocouple model and imposing no heat or current fluxes through this surface. The copper is a non-design domain used to apply the surface boundary conditions. We should consider additional terms to the previously calculated sensitivities if the copper is within the design domain.

We can now run the FEM optimization with multiple boundary conditions and constraints using the material properties specified in Table 2.1. To avoid numerical

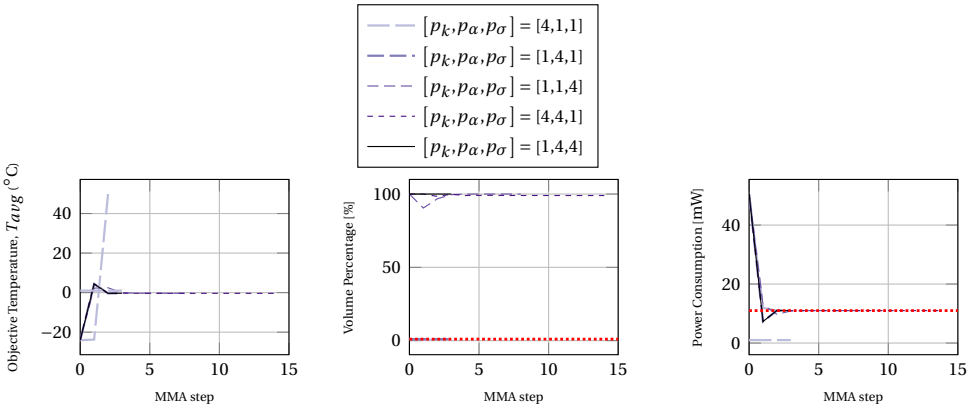

Figure 2.9.: Convergence of the objective and constraint functions – constrained limit in red – for discarded penalization coefficients combinations following the development in section 2.4.1, starting with a full density design.

singularities, following Equation (3.24), all material properties have a minimum scaling value of $1e-9$. To compare to the analytical model, we first select a constant value of $5333\,\mathrm{W/m^2}$ as heat injection and $0.011\,\mathrm{W}$ as power constraint with different penalty coefficients.

In the previous Section 2.4.1, we predicted the behaviour of the thermoelectrical optimization problem for multiple penalization coefficients. In particular, the combination $p_k = p_\sigma > p_\alpha$ shows the most promise, while the rest of the combinations lead to higher minima values and infeasible results. If we repeat this study with the unsatisfactory penalty coefficients using the FEM problem, we obtain Figure 2.9. In this figure, we observe the convergence of the objective value and constraints using the rejected penalization coefficients. In all these cases, we observe that, while there is no volume constraint – it is set to 100% of the original volume – most optimizations get stuck at full volume. We can correlate this issue to the cases studied in analytical form, where we find a maximum value in the power constraint close to the full volume, which makes it difficult to achieve convergence in MMA. Furthermore, we can also appreciate that the combination $p_k > p_\sigma = p_\alpha$ leads to a disconnection of the electrical circuit, leading to heating of the objective surface and an eventual non-convergence of the Newton-Raphson FEM solver. The prediction from the analytical model also leads us to think that the combination $p_k = p_\sigma > p_\alpha$ can remove the convergence issues found with the other combinations.

Figure 2.10 shows the convergence history of three different configurations of penalty coefficients with the objective and constraint values using the penalization coefficient format, $p_k = p_\sigma > p_\alpha$. Furthermore, the limiting values in both constraint plots, v_{obj} and P_{obj}, are drawn as red dotted lines. In Figure 2.10, we observe from the temperature objective path that higher penalty factors with a unity p_α lead to large oscillations until the algorithm provides a solution close to the minima. Furthermore, the model with a higher value p_α demonstrated a smoother

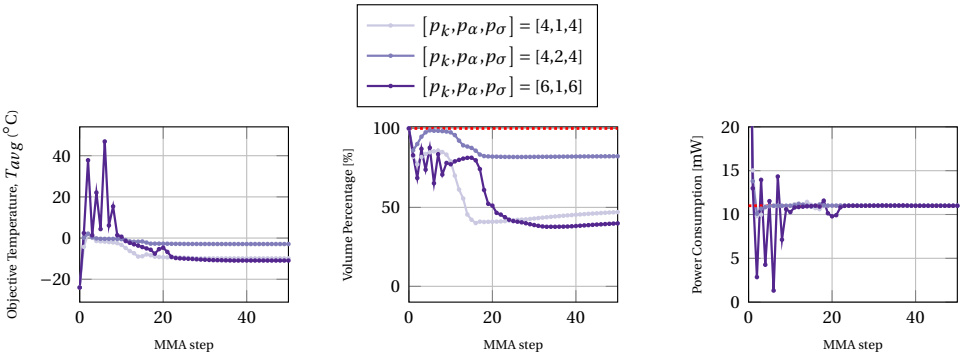

Figure 2.10.: Convergence of the objective and constraint functions – constrained limit in red – for 3 combinations of penalization coefficients following the approach that showed good convergence in section 2.4.1, $p_k = p_\sigma > p_\alpha$, starting with a full density design.

convergence, but the final result was 8 °C higher compared to the unity penalty coefficient case. Finally, the increased $p_\alpha = p_k = 6$ model only achieved a 1 °C improvement compared to $p_\alpha = p_k = 4$. These results imply that larger coefficients can lead to improved designs, but the gains might not compensate for the convergence deterioration. Nevertheless, all combinations of penalty coefficients using $p_k = p_\sigma > p_\alpha$ converge to optimized values volumes with lower minima than all other tested combinations as predicted in Section 2.4.1.

Looking at the constraint convergence results, we further observe that while the power constraint always becomes active – the TEC uses all available power – the volume constraint does not always remain active, with a total volume under the imposed v_{obj}. Furthermore, the volume continues to increase after the convergence of the objective temperature value, which remains constant with less than 0.001 °C variation from the 20th iteration. This increase in volume after the objective convergence introduces low intermediate density values electrically disconnected from the rest of the system and, as such, are not relevant for the final manufacturable design and are visualized in the resulting design in Figure 2.11.

Figure 2.11 shows the result of an optimization where each element is coloured from white to black depending on its associated density. We can appreciate that we obtained column-like structures with surrounding grey or intermediate-density regions in this plot. These grey regions are disconnected from the rest of the design, with densities under 2 %. However, these grey elements do not transmit heat or electrical current, as we do not appreciate any effect on the objective function.

Maintaining a constant value for the penalty coefficient of $p_k = p_\sigma = 4$ and $p_\alpha = 1$, we can run the optimization for different heat injection, power, and volume constraint values to understand the effect of the boundary conditions and constraints on the final converged designs.

Figure 2.12 shows the effect, over the objective value, of the change in the heat injection and power constraint in successive blue lines. Furthermore, since we use

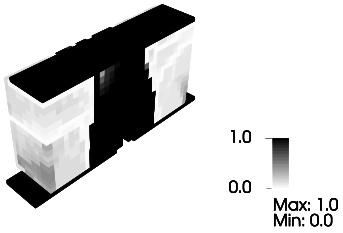

Figure 2.11.: Element density, x_e, for a converged thermocouple TO with for boundary conditions and constraints $q_{in} = 5333\,\mathrm{W}^2/\mathrm{m}, P_{obj} = 11\,\mathrm{mW}$ and $v_{obj} = 0.3$.

the voltage as a design variable, we can compare it with the lowest temperature value achievable in the full-density design for the same power consumption, seen as purple lines in the same plot. The different curves show that a higher power constraint provides lower temperature values. However, there seems to be an asymptotic behaviour with smaller gains for higher power constraint values. Furthermore, an increase in heat injection results in a vertical translation of the objective function towards higher temperature values, with smaller gains with respect to the initial design. This effect can be taken to the limit, where the optimized solution results in the full volume design at high enough heat injections. The overlap in the purple and blue lines in Figure 2.12 confirms this statement.

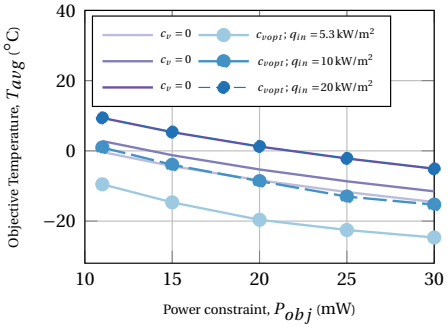

Figure 2.12.: Change in the final average temperature, T_{avg}, with respect to the heat injection and power constraint. The figure further compares the lowest temperature achievable for each power in the full density design, $c_v = 0$, to the optimized designs, c_{vopt}. The results are given for multiple heat injections detailed in the figure legend.

As we obtain the optimization results using constant material properties with temperature, it is convenient to post-process them using a nonlinear material property formulation following Pérez-Aparicio, Taylor, and Gavela [25]. The results plotted in Figure 2.13 show the optimized designs found with constant material properties, run using the material properties in Equation (2.45). This plot shows

the full density results for nonlinear material properties in purple for comparison purposes. These results show that, while the results differ from the constant material properties, in all cases, the optimized still performs better than the original design at a lower computational cost and there is a limited effect of the non-convexity on the problem.

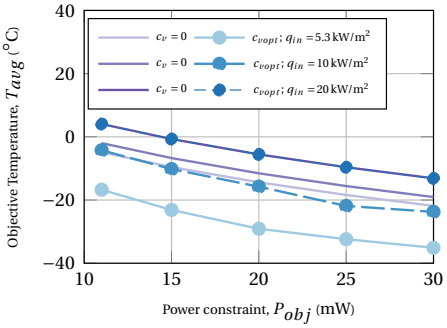

Figure 2.13.: Postprocessing of the optimized designs in Figure 2.12 using a full nonlinear material formulation following Equation (2.45) plotted in blue. In violet, we compare the optimized results to the full-density designs, $c_v = 0$, using nonlinear material properties in both cases.

We can also appreciate the effect of the loading conditions on the optimized thermocouple volume. Figure 2.14 shows the final volume of the designs against the power constraint and heat injection values, calculated as,

$$v_{\%} = \frac{\sum_e^{n_{x>0.9}} x_e}{v_0}, \tag{2.47}$$

where $n_{x>0.9}$ denotes only the elements with densities higher than 0.9, to account for the resulting intermediate density elements. The higher the heat injection in Figure 2.14, the higher the amount of semiconductor volume for the optimized geometry of the thermocouple. Indeed, at the highest studied heat injection values, the optimizer does not move from the initial full-density design. The optimizer can converge at lower thermocouple volumes for lower heat injection values, achieving a minimum objective value at a given power constraint.

While in the previously studied scenarios, the volume constraint was set to full volume and always satisfied, activating the constraint to limit the amount of semiconductor material and reduce material costs is interesting. Figure 2.15 shows in blue lines the effect of lower volume constraints for the largest heat input studied of 20000 W/m^2 – whose converged design is always at full density – and increased power constraints relative to the obtained optimized temperature. This plot shows that for small volume reductions, there are small decreases in the objective function value, which is evidence that the design space is flat in this region of the landscape. However, Figure 2.15 presents a critical value of the volume constraint – around 70% volume – where the objective value increases rapidly. This behaviour is still present

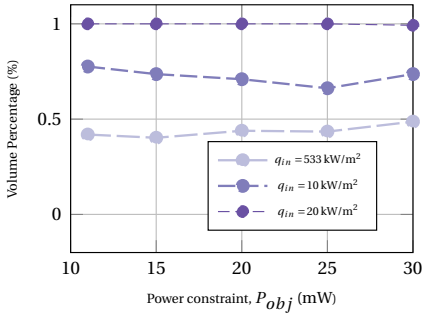

Figure 2.14.: Change in the final design volume percentage over the total initial volume with respect to the heat injection and power constraint.

if we post-process the results with nonlinear material properties Equation (2.45), plotted as purple lines in Figure 2.15. However, nonlinear material properties slightly decrease the objective function for lower volumes, in the order of 2 degrees, compared to the full volume design optimum. This result means that while the optimizations performed with constant material properties provide better designs with lower computational nonlinearities, the problem can present better minima when running with nonlinear material properties.

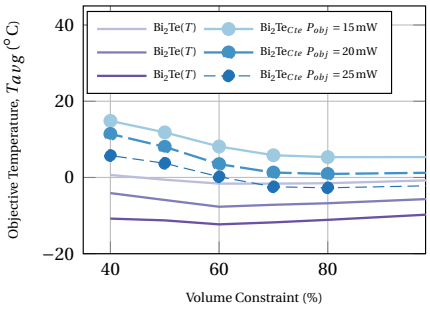

Figure 2.15.: Change in the final average temperature, T_{avg}, with respect to the volume constraint v_{obj} and the power constraint, P_{obj} for a constant heat injection. The results plotted include the temperature-dependent postprocessing of the optimizations following Equation (2.45) in purple.

All these simulations use an averaged temperature objective, taking as a hypothesis that there are no hot spots on the cold surface. In all the resulting optimized designs, the change in the temperature distribution in the thermocouple cold side surface is lower than 0.2 °C. These results remain valid after postprocessing the optimized results using nonlinear material properties. This temperature change along the objective surface is small enough to accept the initial hypothesis taken, stating that the temperature of this surface is homogeneous. If this difference were larger, an aggregation function rather than the average temperature of the surface would need

to be incorporated to take into account the higher sensitivity of the hot spots.

Once we understand the effect of the different parameters on the optimization, we can look into the resulting designs. Figure 2.16 shows the geometry and temperature field of the converged optimization for different boundary conditions and constraints with the penalty factors of $p_k = p_\sigma = 4$ and $p_\alpha = 1$.

The results in Figure 2.16 show a preference towards combinations of column-like results for the lowest heat injection studied. These columns grow and merge with higher power constraints and heat injections. These shapes are related to the constant Peltier effect, which only depends on the material Seebeck coefficient gradient in the p-n connections and the decrease in overall thermal and electrical conductivity with lower volume percentage. This ratio can be quantified through the figure-of-merit ($ZT = \frac{\alpha^2\sigma}{k}T$), related to the efficiency of TEC devices.

The power constraint effect on the design is not so evident, as it can either increase or decrease the final volume percentage, see Figure 2.14. This can be explained through the competing desired effects of low thermal and high electrical conductivity. For low power consumption, the Joule self-heating is not as important as providing good insulation to the warmer heat sink, resulting in lower volume designs. At the same time, at higher current flows, the optimizer minimizes the electrical resistance to reduce the device self-heating.

Finally, we can look at the case in Figure 2.16 where the volume constraint becomes active for a volume constraint of 40 % and a power constraint of 30 mW. This result is dissimilar to the previous ones, finding internal cavities, lower contact surface, and an acute difference between both leg's thermal profiles, with the p-type leg noticeably warmer than its counterpart, given the worse electrical to thermal conductivity ratio of the p-type semiconductor.

2.5. Conclusions

This paper describes a procedure for the computational design of thermocouples for cooling applications using TO. We also use power constraints to maintain optimized operational conditions and volume constraints to limit the material used in the final design.

The problem results in a non-convex design space influenced by the nonlinear thermoelectric equations, the power constraint and the material penalty coefficients. We propose an analytical model which allows us to visualize and understand the effect of different variables on the problem convergence with lower computational expense than FEM models. This study leads to the definition and recommendation of material penalty coefficients for SIMP TO of thermoelectrical devices. The penalty coefficients chosen, $k_p = \sigma_p > \alpha_p = 1$, allow for convergence under non-active volume constraints and with the smallest dispersion of objective values depending on the starting point using MMA between the penalty coefficients studied. Higher values for $k_p = \sigma_p$ lead to better final objective values. However, these higher values also increase the non-linearities affecting the problem convergence. We also show that some combinations of initial designs and operational conditions can lead to unfeasible high or low non-physical temperatures with thermoelectrical

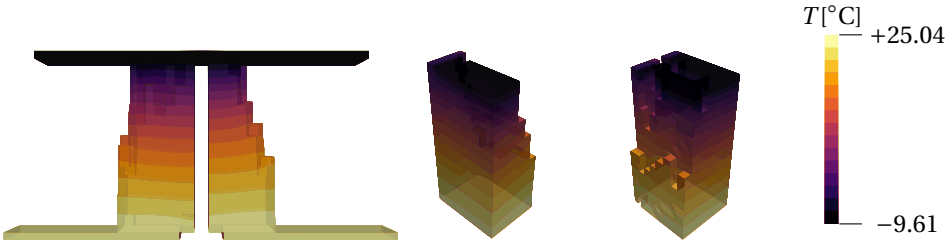

(a) $q_{in} = 5333\,\mathrm{W}^2/\mathrm{m}, P_{obj} = 11\,\mathrm{mW}, v_{obj} = 1$

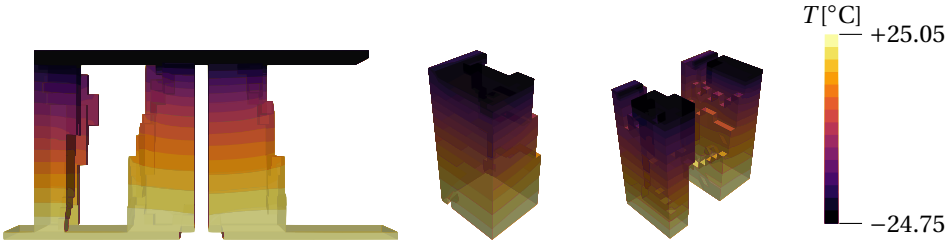

(b) $q_{in} = 5333\,\mathrm{W}^2/\mathrm{m}, P_{obj} = 30\,\mathrm{mW}, v_{obj} = 1$

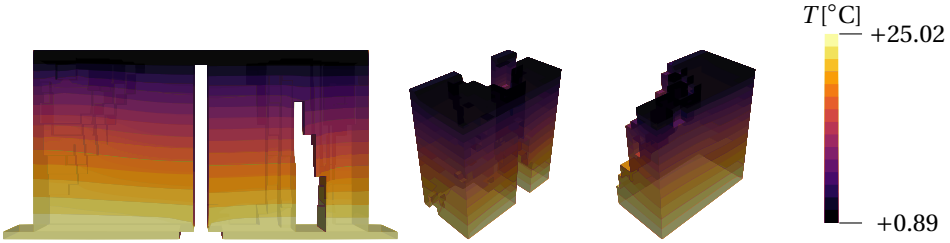

(c) $q_{in} = 10000\,\mathrm{W}^2/\mathrm{m}, P_{obj} = 11\,\mathrm{mW}, v_{obj} = 1$

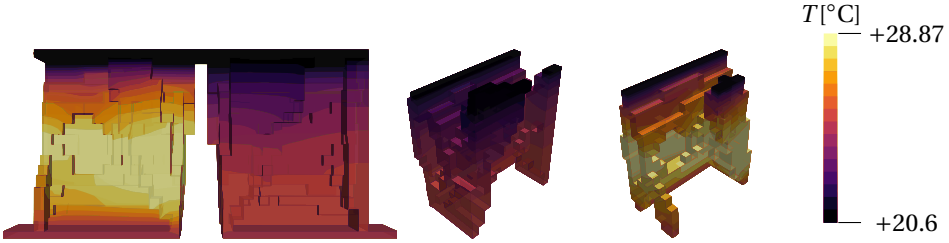

(d) $q_{in} = 20000\,\mathrm{W}^2/\mathrm{m}, P_{obj} = 11\,\mathrm{mW}, v_{obj} = 0.4$

Figure 2.16.: Elements with densities $x_e > 0.99$ resulting from TO of a thermocouple following section 2.4.2 for several boundary conditions and constraints. The temperature plots comprise, from left to right, the side view of the entire thermocouple and isometric views of each n- and p+ semiconductors.

disconnections and intermediate densities.

The use of quadratic elements in combination with the selected penalty coefficients reduces the need for TO filtering techniques in mechanical problems [38], which could also apply to thermoelectrical problems. The use of quadratic elements also improves the nonlinear solver's FEM convergence for the thermoelectric equations at the cost of higher computational complexity. While filtering is not required, it could be helpful to introduce a length scale to remove the optimizer's tendency to create electrically and thermally disconnected regions with intermediate densities.

While the final converged solution results in full-density elements and disregards isolated material regions, we are still subject to manufacturing constraints. Historically, thermoelectric pellets are manufactured through sintering, limiting the complexity of the inner structures in thermoelectric pellets. However, new technologies, such as emerging trends in thermoelectric additive manufacturing, could alleviate these limitations. Nevertheless, manufacturability constraints are crucial to streamline the geometry and mitigate stress concentrations that negatively impact the reliability of the bulk-TEC design.

The initial geometry for the optimization also carries importance in the final optimized results. This study focuses on the bulk-TEC geometries due to their common use and previous experimental testing of the significance of their pellet geometry. However, this formulation could also benefit other current designs, including cylindrical, flat or wearable TEC designs with direct pn electrical connections without copper layers; see He, Schierning, and Nielsch [10]. In some of these designs, introducing mechanical degrees of freedom can limit stresses due to differences in thermal expansion coefficients and allow for the design of elastic modules for wearable technologies. The use of multi-material formulations can also be helpful for the design of stacked semiconductors or metamaterials. Furthermore, the rise in porous thermoelectric materials can improve TEC properties through microstructure optimization.

While microstructures might play a large part in future thermoelectric modules, the material coefficients assume a homogeneous medium that might no longer be valid at small feature scales. Another reason for revising the discrete thermoelectric equations is the case of TEC use under magnetic fields, which are known to modify thermoelectric coefficients. Furthermore, the material models used in this study keep the material coefficients constant with temperature to better understand the equivalent analytical problem. The results obtained with fixed material properties at a given temperature are only accurate for small temperature variations from this reference point.

This paper [1] provides solutions to convergence issues when attaining lower temperatures for TEC at lower volume geometries using TO. However, the material modelling and mechanical studies on the bulk- and other TEC designs should still be studied in further detail.

References

[1] G. Reales Gutiérrez, F. v. Keulen, J. F. L. Goosen, A. M. Aragón, and A. Bornheim. "Enhancing the cooling performance of thermocouples: a power-constrained topology optimization procedure". In: *Structural and Multidisciplinary Optimization* 67.11 (Nov. 2024), p. 189. ISSN: 1615-1488. DOI: 10.1007/s00158-024-03897-6. URL: https://doi.org/10.1007/s00158-024-03897-6.

[2] IRENA, IEA, and REN21. *Renewable Energy-Heating and Cooling*. IRENA, OECD/IEA and REN21, 2020, pp. 1–112. ISBN: 9789292600617.

[3] Q. Liu, F. Wei, G. Li, Z. Kan, J. Yang, H. Zhu, B. Wang, and H. Zhao. "Highly efficient thermoelectric air conditioner with kilowatt capacity realized by ground source heat-exchanging system". In: *iScience* 25.5 (2022), p. 104296. ISSN: 25890042. DOI: 10.1016/j.isci.2022.104296.

[4] S. B. Riffat and X. Ma. "Thermoelectrics: A review of present and potential applications". In: *Applied Thermal Engineering* 23.8 (2003), pp. 913–935. ISSN: 13594311. DOI: 10.1016/S1359-4311(03)00012-7.

[5] D. Zhao and G. Tan. "A review of thermoelectric cooling: Materials, modeling and applications". In: *Applied Thermal Engineering* 66.1-2 (2014), pp. 15–24. ISSN: 13594311. DOI: 10.1016/j.applthermaleng.2014.01.074.

[6] S. Leblanc, S. K. Yee, M. L. Scullin, C. Dames, and K. E. Goodson. "Material and manufacturing cost considerations for thermoelectrics". In: *Renewable and Sustainable Energy Reviews* 32 (2014), pp. 313–327. ISSN: 13640321. DOI: 10.1016/j.rser.2013.12.030. URL: http://dx.doi.org/10.1016/j.rser.2013.12.030.

[7] E. S. Maurya. "Liquid Cooling System and Air Cooling System in Data Center: A Comparison". In: *International Journal for Research in Applied Science and Engineering Technology* 8.11 (2020), pp. 548–550. DOI: 10.22214/ijraset.2020.32226.

[8] J. C. A. Peltier. " Nouvelles experiences sur la caloricite des courants electriques ". In: *Annales de Chimie et de Physique, LVI, LVI (pp: 371-386)* 8 (1834).

[9] O. I. Ibeagwu. "Modelling and comprehensive analysis of TEGs with diverse variable leg geometry". In: *Energy* 180 (2019), pp. 90–106. ISSN: 03605442. DOI: 10.1016/j.energy.2019.05.088.

[10] R. He, G. Schierning, and K. Nielsch. "Thermoelectric Devices: A Review of Devices, Architectures, and Contact Optimization". In: *Advanced Materials Technologies* 3.4 (2018). ISSN: 2365709X. DOI: 10.1002/admt.201700256.

[11] A. Fabián-Mijangos, G. Min, and J. Alvarez-Quintana. “Enhanced performance thermoelectric module having asymmetrical legs”. In: *Energy Conversion and Management* 148 (2017), pp. 1372–1381. ISSN: 01968904. DOI: 10.1016/j.enconman.2017.06.087.

[12] M. P. Bendsøe and N. Kikuchi. “Generating optimal topologies in structural design using a homogenization method”. In: *Computer Methods in Applied Mechanics and Engineering* 71.2 (1988), pp. 197–224. ISSN: 00457825. DOI: 10.1016/0045-7825(88)90086-2.

[13] D. Yago, J. Cante, O. Lloberas-Valls, and J. Oliver. “Topology Optimization Methods for 3D Structural Problems: A Comparative Study”. In: *Archives of Computational Methods in Engineering* 29.3 (May 2022), pp. 1525–1567. ISSN: 1886-1784. DOI: 10.1007/s11831-021-09626-2. URL: https://doi.org/10.1007/s11831-021-09626-2.

[14] O. Sigmund and K. Maute. “Topology optimization approaches: A comparative review”. In: *Structural and Multidisciplinary Optimization* 48.6 (2013), pp. 1031–1055. ISSN: 1615147X. DOI: 10.1007/s00158-013-0978-6.

[15] “Development of Compliant Thermoelectric Generators (TEGs) in Aerospace Applications Using Topology Optimization”. In: *Energy Harvesting and Systems* 4.2 (2019). ISSN: 23298766. DOI: 10.1515/ehs-2016-0017.

[16] K. Furuta, K. Izui, K. Yaji, T. Yamada, and S. Nishiwaki. “Level set-based topology optimization for the design of a peltier effect thermoelectric actuator”. In: *Structural and Multidisciplinary Optimization* 55.5 (2017), pp. 1671–1683. ISSN: 16151488. DOI: 10.1007/s00158-016-1609-9.

[17] O. Sardan, D. H. Petersen, K. Mølhave, O. Sigmund, and P. Bøggild. “Topology optimized electrothermal polysilicon microgrippers”. In: *Microelectronic Engineering* 85.5-6 (2008), pp. 1096–1099. ISSN: 01679317. DOI: 10.1016/j.mee.2008.01.049.

[18] A. Takezawa and M. Kitamura. “Geometrical design of thermoelectric generators based on topology optimization”. In: *International Journal for Numerical Methods in Engineering* February (2012), pp. 1102–1119. DOI: 10.1002/nme.3375.

[19] X. Xu, Y. Wu, L. Zuo, and S. Chen. “Multimaterial topology optimization of thermoelectric generators”. In: *Proceedings of the ASME Design Engineering Technical Conference* 2A-2019.September 2021 (2019). DOI: 10.1115/DETC2019-97934.

[20] S. Soprani, J. H. Haertel, B. S. Lazarov, O. Sigmund, and K. Engelbrecht. “A design approach for integrating thermoelectric devices using topology optimization”. In: *Applied Energy* 176.June (2016), pp. 49–64. ISSN: 03062619. DOI: 10.1016/j.apenergy.2016.05.024.

[21] C. Lundgaard and O. Sigmund. “A density-based topology optimization methodology for thermoelectric energy conversion problems”. In: *Structural and Multidisciplinary Optimization* 57.4 (2018), pp. 1427–1442. ISSN: 16151488. DOI: 10.1007/s00158-018-1919-1.

[22] J. Mativo, K. Hallinan, U. George, G. Reich, and R. Steininger. “Topology optimized thermoelectric generator: A parametric study”. In: *Energy Harvesting and Systems* 7.2 (2020), pp. 33–53. ISSN: 23298766. DOI: 10.1515/ehs-2021-0002.

[23] S. Shittu, G. Li, X. Zhao, and X. Ma. “Review of thermoelectric geometry and structure optimization for performance enhancement”. In: *Applied Energy* 268.December 2019 (2020), p. 115075. ISSN: 03062619. DOI: 10.1016/j.apenergy.2020.115075.

[24] C. Goupil, W. Seifert, K. Zabrocki, E. Müller, and G. J. Snyder. “Thermodynamics of thermoelectric phenomena and applications”. In: *Entropy* 13.8 (2011), pp. 1481–1517. ISSN: 10994300. DOI: 10.3390/e13081481.

[25] J. L. Pérez-Aparicio, R. L. Taylor, and D. Gavela. “Finite element analysis of nonlinear fully coupled thermoelectric materials”. In: *Computational Mechanics* 40.1 (2007), pp. 35–45. ISSN: 01787675. DOI: 10.1007/s00466-006-0080-7.

[26] H. S. Lee. “The Thomson effect and the ideal equation on thermoelectric coolers”. In: *Energy* 56 (2013), pp. 61–69. ISSN: 03605442. DOI: 10.1016/j.energy.2013.04.049.

[27] E. J. Sandoz-Rosado, S. J. Weinstein, and R. J. Stevens. “On the Thomson effect in thermoelectric power devices”. In: *International Journal of Thermal Sciences* 66 (2013), pp. 1–7. ISSN: 12900729. DOI: 10.1016/j.ijthermalsci.2012.10.018.

[28] Q. Liu, G. Li, H. Zhu, and H. Zhao. “Micro thermoelectric devices: From principles to innovative applications”. In: *Chinese Physics B* 31.4 (2022). ISSN: 20583834. DOI: 10.1088/1674-1056/ac5609.

[29] M. Hoit and K. Krishnamurthy. “A 14-Point reduced integration scheme for solid elements”. In: *Computers and Structures* 54.4 (1995), pp. 725–730. ISSN: 00457949. DOI: 10.1016/0045-7949(94)00360-F.

[30] A. Bornheim, W. Lustermann, K. Stachon, G. Reales Gutiérrez, A. Benaglia, F. De Guio, A. Ghezzi, M. T. Lucchini, M. Malberti, S. Palluotto, T. Tabarelli De Fatis, M. Benettoni, R. Carlin, M. Tosi, R. Rossin, P. Meridiani, R. Paramatti, F. Santanastasio, J. C. Silva, J. Varela, A. Heering, A. Karneyeu, Y. Musienko, M. Wayne, T. Anderson, B. Cox, C. E. Perez Lara, A. Ledovskoy, S. White, and I. Schmidt. “Integration of thermo-electric coolers into the CMS MTD SiPM arrays for operation under high neutron fluence”. In: *Journal of Instrumentation* 18.8 (2023). ISSN: 17480221. DOI: 10.1088/1748-0221/18/08/P08020. arXiv: 2306.00818.

[31] K. Svanberg. “The method of moving asymptotes - a new method for structural optimization”. In: *International Journal for Numerical Methods in Engineering*. 24.October 1985 (1987), pp. 359–373.

[32] D. Yang and P. Yang. “Numerical instabilities and convergence control for convex approximation methods”. In: *Nonlinear Dynamics* 61.4 (2010), pp. 605–622. ISSN: 0924090X. DOI: 10.1007/s11071-010-9674-x.

[33] M. Fanni, M. N. Shabara, and M. G. Alkalla. “A Comparison between Different Topology Optimization Methods”. In: *Egyptian Knowledge Bank* (2013). DOI: 10.21608/BFEMU.2020.103788.

[34] G. Allaire. *Conception optimale de structures*. 1st ed. Mathématiques et Applications. Published: 02 November 2006 (softcover), eBook published: 12 October 2006. Springer Berlin Heidelberg, 2007. ISBN: 978-3-540-36710-9. DOI: 10.1007/978-3-540-36856-4. URL: https://doi.org/10.1007/978-3-540-36856-4.

[35] G. Allaire. “A review of adjoint methods for sensitivity analysis, uncertainty quantification and optimization in numerical codes”. In: *Ingénieurs de l’Automobile* 836 (July 2015), pp. 33–36. URL: https://hal.science/hal-01242950.

[36] M. P. Bendsøe and O. Sigmund. “Material interpolation schemes in topology optimization”. In: *Archive of Applied Mechanics* 69.9-10 (1999), pp. 635–654. ISSN: 09391533. DOI: 10.1007/s004190050248.

[37] X. Hu, H. Takazawa, K. Nagase, M. Ohta, and A. Yamamoto. “Three-Dimensional Finite-Element Simulation for a Thermoelectric Generator Module”. In: *Journal of Electronic Materials* 44.10 (2015), pp. 3637–3645. ISSN: 03615235. DOI: 10.1007/s11664-015-3898-y.

[38] M. V. O. Araujo, E. N. Lages, and M. A. A. Cavalcante. “Checkerboard free topology optimization for compliance minimization applying the finite-volume theory”. In: *Mechanics Research Communications* 108 (2020), p. 103581. ISSN: 0093-6413. DOI: https://doi.org/10.1016/j.mechrescom.2020.103581. URL: https://www.sciencedirect.com/science/article/pii/S0093641320301099.

3

Mechanical considerations in thermoelectric topology optimization, a stress-constraint approach for higher reliability

This paper addresses the topology optimization of thermocouples for cooling applications, considering stress constraints to enhance reliability under service loads. We provide a first approach to derive sensitivities using SIMP (solid isotropic material with penalization) for thermo-electro-mechanical systems with temperature-dependent material properties. The proposed formulation decouples the thermoelectrical system from the mechanical degrees of freedom, reducing computational memory usage from a fully coupled approach. The study focuses on the formulation of thermocouples for cooling applications using the Peltier effect, which considers electrical power limits, electrical working points, and material stress thresholds. Furthermore, while the thermoelectrical problem does not show the need for filtering techniques, including the mechanical degrees of freedom, we show that we recover undesirable porous optimized designs. We provide 2D thermocouple example optimizations with geometries and boundary conditions based on a practical case for the implementation of thermoelectric coolers in the Minimum Ionizing Particle Timing Detector (MTD) at CERN. The optimizations are performed with increased complexity, including the unfiltered thermoelectrical and thermo-electro-mechanical problems and a Helmholtz-filtered example. The optimizations are compared with constant and nonlinear material properties with temperature and with respect the consideration of air-conductance losses within the devices. Although more efficient topologies can be achieved without the need for volume constraints, we include an example with a constraint of 60%

[*] Parts of this chapter have been submitted to the Structural and Multidisciplinary Optimization Journal

volume to understand its effect on the design and provide a methodology to reduce semiconductor-associated costs at lower efficiency costs. Finally, we explore the same formulation in 3D. The results provide guidelines for manufacturing compliant thermocouples, increasing their reliability without decreasing efficiency.

3.1. Introduction

Thermoelectric coolers utilize the Peltier effect to induce a heat flux by connecting dissimilar semiconductor materials. Compared to traditional vapour compression refrigeration, thermoelectric cooling offers static operation, miniaturization, subambient temperature capability, high reliability, absence of gaseous emissions, and noiseless operation. These benefits have led to the application of Thermoelectric Coolers (TECs) in diverse fields such as cryogenics [1], on-chip thermal management [2], laser and fibre optics with precise temperature regulation requirements [3, 4], medical devices [5], and localized cooling in space vehicles [6]. Despite ongoing research on its large-scale implementation, such as building refrigeration [7], cost-effectiveness remains a challenge due to its lower efficiencies compared to vapour compression systems. These lower efficiencies are due to the need to balance the properties of the thermoelectric material within the semiconductor components [8].

The material composition of a TEC determines its intrinsic properties. However, the arrangement of materials in each semiconductor leg can also modify the device's overall characteristics. The impact of the semiconductor leg shape was investigated in Fabián-Mijangos, Min, and Alvarez-Quintana [9], who provided a manufacturing method and demonstrated a higher efficiency for asymmetric pyramidal or trapezoidal thermocouple shapes compared to regular cubic shapes. In Sun *et al.* [10], these shapes are combined with segmented legs containing more than a single semiconductor material to train a neural network to provide an optimized combination of geometric parameters and output power. Additionally, topology optimization (TO) through the SIMP (solid isotropic material with penalization) method with volume constraints can be employed to improve the efficiency of heat recovery thermoelectric devices. Takezawa and Kitamura [11] introduce this methodology for thermoelectric generators with all material penalization coefficients equal to unity and a 1D model to validate the sensitivities. In Xu *et al.* [12], the previous method is extended to segmented semiconductor legs using multimaterial TO. There is also literature on the system integration of thermoelectrical devices with Soprani *et al.* [13] optimizing the thermal coupling material from the TECs to its thermal contacts, with simplifications of the thermoelectrical module as a single material block for a downhole oil well intervention tool. Finally, Lundgaard and Sigmund [14] examine the TO formulation for different thermoelectrical objectives and problem formulations, including power output, conversion efficiency, temperature, heat flux and coefficient of performance using two different materials in direct contact. Together, these studies highlight the importance of material arrangement and leg optimization in shaping TEC performance.

TO algorithms can reduce semiconductor materials' volume and material costs – up to a third of the system cost [15] – maintaining efficiency. However, the topology shapes that arise can compromise their mechanical reliability. Mechanical ageing, which occurs from the dissimilar materials in the thermocouple composition, introduces efficiency losses. A single thermocouple involves a solder and an electrode with thermoelastic properties different from the semiconductor's, leading to mechanical loading. Additionally, these devices experience temperature variations through their thickness, influencing the properties of the semiconductor material and the fatigue conditions. This ageing process, which increases electrical resistivity and decreases Seebeck coefficients of the affected thermocouples, decreases efficiency over time. Due to the importance of this efficiency loss, multiple approaches have been proposed to predict it. For instance, Merienne *et al.* [16] and Williams *et al.* [17] highlight the effect of thermal cycling on commercial thermoelectric generators, revealing the increased resistance due to material cracking over time. Wang *et al.* [18] use digital image correlation to experimentally identify the cracking spot at the copper-Bi_2Te_3 interface to provide a diagnostic method. Gong *et al.* [19] present a model to estimate thermal loads and proposes improvements over previous models considering copper and ceramic layers. The electrical operation also impacts the ageing process, as demonstrated by Fan, Rezania, and Gao [20], who showed that pulse operation could reduce thermally induced stresses. The effect of the shape of the thermoelectric semiconductor is highlighted in the literature through FEM (finite element method) models. Erturun, Erermis, and Mossi [21] look into the effect of the shape of the pellets on the thermo-electro-mechanical performance of thermoelectric generators in ANSYS, and Zhang *et al.* [22] use COMSOL to perform similar measures within a thermoelectric cooler and a parametric analysis of the dimensions of the design. Finally, Suhir and Shakouri [23] develop an analytical model to estimate the shear stress along the bonded layers of a TEC and compares it to an ANSYS model. The results from these works emphasize the higher induced thermal stresses at the edges of the legs and their contact with the solder layer. Different leg designs, including truncated cones or trapezoidal shapes with variable cross-sections, show promise in reducing stress at material interfaces [24–26].

TO can alleviate local stresses, with formulations dating back to Yang and Chen [27]. Verbart [28] and Yvonnet and Da [29] summarize recent advances in fracture TO, which presents commonly used stress aggregations to mitigate fatigue and crack initiation in materials. Verbart, Langelaar, and van Keulen [30] outline various options for structural stress aggregation, highlighting their distinct impacts on optimized outcomes. Lastly, Meng *et al.* [31] explore the thermoelastic stress-based TO. These techniques are readily applicable to thermoelectric devices, and their thermoelastic behaviour is incorporated to minimize induced thermal stresses and enhance operational reliability. In Mativo *et al.* [32], a simplified thermomechanical model using SIMP is further used to reduce shear loading-induced stresses. Another example of designs of thermo-electro-mechanical compliant mechanisms through the level set method can be found in Furuta *et al.* [33] with linear material properties with temperature. In essence, TO methods offer a versatile approach to reducing stress and optimizing thermoelectric device performance and reliability.

There are limited examples of multiphysics thermo-electro-mechanical optimizations considering the Peltier effect in the literature. Some of the relevant work in the field includes Furuta *et al.* [33], which provides a level-set optimization formulation for thermoelectric mechanical actuators based on the Peltier effect or Xing *et al.* [34], which uses a Kriging optimization and COMSOL to optimize a flexible thermoelectric generator without the use of sensitivities. Pérez-Aparicio, Moreno-Navarro, and Gómez-Hernández [35] perform shape optimization using simulated annealing for transient pulse shapes and associated temperature profiles with limits to the induced stresses using linear elasticity. Chen *et al.* [36] use ANSYS and multi-objective genetic optimization algorithms to reduce stresses in a full thermoelectric module through the parameterization of the cooling fin distribution. Maduabuchi [37] shows the use of deep learning network techniques trained through ANSYS simulations for parametric optimization of thermoelectrical for faster calculations using power, efficiency, and induced stresses as objectives.

The numerical implementation and performance of fully coupled thermo-electro-mechanical topology optimization remains largely unexplored compared to parametric analysis on these structures. Particularly, the SIMP method — widely adopted in structural optimization — has seen little application in this field. Despite the critical impact of stresses on device reliability and failure, the influence of optimization parameters on the resulting designs has not been studied in detail. Current optimization approaches for thermo-electro-mechanical problems lack sensitivity formulations to account for stress concentrations in these devices. Furthermore, existing studies rely on idealized fixed boundary conditions and neglect thermal losses to the environment, limiting the accuracy of the optimized designs.

This work presents a topology optimization framework for thermoelectric devices that incorporates mechanical stress considerations using the SIMP method, an approach not seen in the literature for this class of multiphysics problems. Unlike existing studies that focus solely on thermal and electrical behaviour, this method introduces mechanical degrees of freedom into the optimization process, enabling the inclusion of stress constraints critical to device reliability. We explore decoupled thermoelectrical and mechanical equations for the FEM simulations, examining their optimization convergence and optimized designs. A simplified model is proposed to simulate the electrical operating conditions of TECs using its voltage gradient across a thermocouple. We use this model to analyze the optimization results with and without stress constraints, addressing the impact of length scale on optimized designs through filtering techniques. We evaluate the effect of the results of Heaviside and Helmholtz filters and the need for filtering techniques due to the addition of stress constraints. This further contemplates studying the effect of grey regions in optimized thermo-electro-mechanical designs as opposed to pure thermoelectrical optimization. The examples consider both vacuum and air-filled environments to capture realistic thermal losses during operation. Prior work shows that air conduction dominates while convection is negligible and radiation contributions depend on leg geometry with less than 10% effect for the device efficiency with leg gaps under 1 mm [38]. A detailed study by Cai *et al.* [39] confirms the limited impact of radiation at low temperatures, particularly on power output rather than

conversion efficiency. Additionally, we present illustrative 2D and 3D results for a thermocouple under various constraint conditions, demonstrating convergence to lower semiconductor volumes with larger efficiencies and compliance compared to the initial design.

3.2. Governing Equations

The physics of thermoelectric coolers in steady-state conditions is governed by the thermoelectric coupling given by the electric charge and energy balance or equilibrium equations, i. e.,

$$\begin{aligned} \nabla \cdot \mathbf{j} &= 0\,, \\ \nabla \cdot \mathbf{q} + \mathbf{j} \cdot \nabla \phi &= q_\Omega\,. \end{aligned} \tag{3.1}$$

In these equations, we find the balance of current density $\mathbf{j}$ and heat flow $\mathbf{q}$ within our material depending on the applied electric field ϕ and the internal heat generation q_Ω. Furthermore, to study the induced stress, we also need to consider the mechanical static equilibrium

$$\nabla \cdot \boldsymbol{\sigma} + \mathbf{b} = \mathbf{0}\,, \tag{3.2}$$

with $\boldsymbol{\sigma}$ being the Cauchy stress tensor, $\mathbf{b}$ the body forces.

The constitutive equations in this problem rely on Ohm's equation, i. e.,

$$\mathbf{j} = -\gamma(\nabla \phi + \alpha \nabla T)\,. \tag{3.3}$$

This equation relates the current density $\mathbf{j}$ with the electric potential ϕ, the electrical conductivity γ, with the thermoelectric coupling to the temperature field T, through the Seebeck coefficient α. The coupling of the thermoelectric equations also involves Fourier's equation

$$\mathbf{q} = \alpha T \mathbf{j} - \kappa \nabla T\,, \tag{3.4}$$

which represents the contributions to the total energy flow of the current flow and the heat conduction. From Equation (3.4), we see that the thermal conduction term depends on the temperature gradient and thermal conductivity κ, while the heat due to the current flow depends on the Seebeck coupling and current flow. Finally, the generalized Hooke equation or the isotropic linear thermoelastic constitutive equation for small displacements assumption in a 2D plane stress situation using the Voigt notation is

$$\hat{\boldsymbol{\sigma}} = \mathbf{C}\boldsymbol{\varepsilon} - \boldsymbol{\beta}_T \theta\,, \tag{3.5}$$

$$\theta = (T - T_{ref})\,, \tag{3.6}$$

$$\boldsymbol{\beta}_T = \frac{E}{1-2\nu}\begin{bmatrix} 1 & 1 & 0 \end{bmatrix}^\intercal \alpha_T = \mathbf{C}\mathbf{e}_{\mathrm{tr}}\alpha_T\,, \tag{3.7}$$

where the isotropic coefficient of expansion α_T affects the normal stresses through a trace operator $\mathbf{e}_{\mathrm{tr}}$. This equation relates the stresses with the material properties

considering the thermoelastic problem where we define E as the Young's modulus of the material, and ν the Poisson's ratio, the reference temperature T_{ref}, the temperature at which there are no thermally induced stresses, $\boldsymbol{\epsilon}$ is the strains tensor, and $\mathbf{C}$ is the constitutive relation between the mechanical strain and stresses without thermal stresses. In a 2D plane stress problem, we define this constitutive relation as

$$\mathbf{C} = E\mathbf{C}_0 = \frac{E}{1-\nu^2}\begin{bmatrix} 1 & \nu & 0 \\ \nu & 1 & 0 \\ 0 & 0 & \frac{1-\nu}{2} \end{bmatrix}.$$

The strong form of the problem is completed by the boundary conditions

$$\begin{aligned} V &= V_\Gamma \text{ on } \Gamma_V, & T &= T_\Gamma \text{ on } \Gamma_T, & \boldsymbol{U_p} &= \boldsymbol{U}_\Gamma \text{ on } \Gamma_U, \\ \mathbf{j}\cdot\mathbf{n} &= j_c \text{ on } \Gamma_j, & \mathbf{q}\cdot\mathbf{n} &= q_c \text{ on } \Gamma_q, & \boldsymbol{\sigma}\cdot\mathbf{n} &= \boldsymbol{t}_c \text{ on } \Gamma_t. \end{aligned} \tag{3.8}$$

In these boundary conditions, we impose fixed DOFs in the form of voltages V_Γ, temperatures T_Γ, and displacements $\boldsymbol{U}_\Gamma$, and external loads along their respective boundaries Γ_V, Γ_T and Γ_U. The boundaries that prescribe primal and dual variables must be disjoint, i.e., , $\Gamma = \Gamma_V \bar{\cup} \Gamma_j$ and $\Gamma_V \cap \Gamma_j = \emptyset$ for the electrical problem. Similarly, for the thermal problem we have $\Gamma = \Gamma_T \bar{\cup} \Gamma_q$ and $\Gamma_T \cap \Gamma_q = \emptyset$ and for the mechanical equilibrium $\Gamma = \Gamma_U \bar{\cup} \Gamma_t$ and $\Gamma_U \cap \Gamma_t = \emptyset$.

We approach the nonlinear thermoelectric problem previously presented through numerical procedures to overcome the challenge posed by an analytical solution.

3.2.1. Finite element modelling

To solve the coupled thermo-electro-mechanical through FEM, we reformulate the equations in weak form and discretize them by approximation functions. Using the residual, Garlekin's, and the divergence theorems, we get

$$\begin{aligned} &-\int_\Omega \omega \boldsymbol{\nabla}\cdot\mathbf{q}\,\mathrm{d}\Omega + \int_\Omega \omega \mathbf{j}\cdot\boldsymbol{\nabla}\phi\,\mathrm{d}\Omega + \int_{\Gamma_q} \omega q_c\,\mathrm{d}\Gamma \\ &\qquad = \int_\Omega \omega q_\Omega\,\mathrm{d}\Omega, \\ &-\int_\Omega \boldsymbol{\nabla}\omega\cdot\mathbf{j}\,\mathrm{d}\Omega + \int_{\Gamma_j} \omega\cdot\mathbf{j_c}\,\mathrm{d}\Gamma = 0, \\ &\int_\Gamma \omega\cdot\boldsymbol{\sigma}\,\mathrm{d}\Gamma - \int_\Omega \boldsymbol{\sigma}\cdot\boldsymbol{\nabla}\omega = 0, \end{aligned} \tag{3.9}$$

where ω is the weight function.

To discretize the weak forms in Equation (3.9), we use standard bilinear shape functions. For the thermoelectric problem, temperature T and electric potential ϕ are interpolated using $\mathbf{N}$. For the mechanical problem, the displacement field $\boldsymbol{U_p}$ is interpolated using $\mathbf{N_U}$. All these vectors are represented in column form. This interpolation is written as

$$T = \mathbf{N}^\intercal\mathbf{t},\ \phi = \mathbf{N}^\intercal\mathbf{v},\ \boldsymbol{U_p} = \mathbf{N_U}^\intercal\mathbf{u},\ \theta = \mathbf{N}^\intercal\left(\boldsymbol{t} - \boldsymbol{T_{ref}}\right), \tag{3.10}$$

where vectors **t**, **v** and **u** are the temperature, electric potential, and displacement DOFs at element level, respectively. We use these shape functions and discretized displacements to define the strain-displacement matrix **B** as

$$\boldsymbol{\varepsilon} = \mathbf{B}\mathbf{u}. \tag{3.11}$$

The strain-displacement matrix can be introduced into the mechanical weak-form equation and using the Hooke thermoelastic relation, Equation (3.5), to obtain the residual from the mechanical coupling $\mathbf{r_u}$

$$\begin{aligned}
\mathbf{r_u} &= \int_\Gamma \mathbf{N_U}^\intercal \boldsymbol{\sigma}\, \mathrm{d}\Gamma - \mathbf{k_u}\mathbf{u} + \mathbf{k}_\Theta \boldsymbol{\theta} = \mathbf{0}, \\
\mathbf{k_u} &= \int_\Omega \mathbf{B}^\intercal \mathbf{C}\mathbf{B}\, \mathrm{d}\Omega, \\
\mathbf{k}_\Theta &= \int_\Omega \mathbf{B}^\intercal \boldsymbol{\beta}_T \mathbf{N}^\intercal\, \mathrm{d}\Omega.
\end{aligned} \tag{3.12}$$

The residuals of the remaining thermoelectrical coupling given by Equation (3.9) are

$$\begin{aligned}
\mathbf{r_t} = &- \int_\Omega \mathbf{N}\nabla\cdot\mathbf{q}\, \mathrm{d}\Omega + \int_\Omega \mathbf{N}\mathbf{j}\cdot\nabla\mathbf{N}^\intercal\mathbf{v}\, \mathrm{d}\Omega + \\
&\int_{\Gamma_q} \mathbf{N} q_c\, \mathrm{d}\Gamma - \int_\Omega \mathbf{N} q_\Omega\, \mathrm{d}\Omega = \mathbf{0}, \\
\mathbf{r_v} = &- \int_\Omega \nabla\mathbf{N}\cdot\mathbf{j}\, \mathrm{d}\Omega + \int_{\Gamma_j} \mathbf{N}\cdot\mathbf{j_c}\, \mathrm{d}\Gamma = \mathbf{0}.
\end{aligned} \tag{3.13}$$

The residual and element-level state vector are assembled into

$$\begin{aligned}
\mathbf{r} &= \begin{bmatrix} \mathbf{r_u} & \mathbf{r_t} & \mathbf{r_v} \end{bmatrix}^\intercal \text{ and} \\
\mathbf{s} &= \begin{bmatrix} \mathbf{u} & \mathbf{t} & \mathbf{v} \end{bmatrix}^\intercal.
\end{aligned} \tag{3.14}$$

The derivative of this residual concerning the unknown DOFs is the tangent matrix **K**. Considering the null derivatives of the residual, this matrix can be written at the element level as

$$\mathbf{k}^{(k)} = \frac{\mathrm{d}\mathbf{r}}{\mathrm{d}\mathbf{s}} = \begin{bmatrix} \frac{\partial \mathbf{r}_\mathbf{u}^{(k)}}{\partial \mathbf{u}} & \frac{\partial \mathbf{r}_\mathbf{u}^{(k)}}{\partial \mathbf{t}} & \mathbf{0} \\ \mathbf{0} & \frac{\partial \mathbf{r}_\mathbf{t}^{(k)}}{\partial \mathbf{t}} & \frac{\partial \mathbf{r}_\mathbf{t}^{(k)}}{\partial \mathbf{v}} \\ \mathbf{0} & \frac{\partial \mathbf{r}_\mathbf{v}^{(k)}}{\partial \mathbf{t}} & \frac{\partial \mathbf{r}_\mathbf{v}^{(k)}}{\partial \mathbf{v}} \end{bmatrix}, \tag{3.15}$$

where the development of each derivative of the residual can be found in Appendix C. The global stiffness matrix can be obtained through the standard FEM assembly procedure

$$\mathbf{K}^{(k)} = \frac{\mathrm{d}\mathbf{R}^{(k)}}{\mathrm{d}\mathbf{S}} = \sum_{e=1}^{n_e} \mathbf{k}^{(k)}, \tag{3.16}$$

with **R** and **S** the global residual and state vectors arising from the assembly of **k** and for all elements e.

From the definition in Equation (3.15), we see that the thermoelectrical DOFs, are decoupled from the mechanical DOFs **u**. This decoupling allows us to use the reduced thermoelectrical tangent stiffness

$$\mathbf{K}_{\mathbf{TV}}^{(k)} = \begin{bmatrix} \frac{\partial \mathbf{R}_{\mathbf{T}}^{(k)}}{\partial \mathbf{T}} & \frac{\partial \mathbf{R}_{\mathbf{T}}^{(k)}}{\partial \mathbf{V}} \\ \frac{\partial \mathbf{R}_{\mathbf{V}}^{(k)}}{\partial \mathbf{T}} & \frac{\partial \mathbf{R}_{\mathbf{V}}^{(k)}}{\partial \mathbf{V}} \end{bmatrix}, \tag{3.17}$$

to compute the global thermal and electrical DOFs $\begin{bmatrix}\mathbf{T} & \mathbf{V}\end{bmatrix}$ using the Newton-Raphson method, starting with $\begin{bmatrix}\mathbf{T} & \mathbf{V}\end{bmatrix} = \mathbf{0}$ as an initial solution. Each system is solved using MATLAB's direct sparse linear solver. Subsequently, global displacements **U** are determined in a second step, incorporating the computed temperature field into the thermoelastic equation Equation (3.12). Notably, in this formulation, the solution step of the thermoelastic equation is only nonlinear in scenarios featuring a Young's modulus or coefficient of thermal expansion that is temperature-dependent.

To validate the MATLAB implementation, a test routine was developed using analytical benchmarks from Pérez-Aparicio, Taylor, and Gavela [40], supplemented with analytically calculated thermoelastic deformations. Matrix dimensions and implementation details are provided in Appendix C. For a fully coupled FEM formulation including thermoelectricity, displacement, and magnetic flux, see Pérez-Aparicio, Palma, and Taylor [41].

3.3. Problem formulation

With the finite element formulation of the coupled thermo-electro-mechanical problem in place, we define our design optimization procedure. We use a density-based TO formulation, following the three-field-density formulation from Lazarov, Wang, and Sigmund [42]. In this material representation, we use three density fields $(\bar{\boldsymbol{x}}_\rho, \tilde{\boldsymbol{x}}_\rho, \boldsymbol{x}_\rho)$. Each one represents the density design variables used by the optimizer $\boldsymbol{x}_\rho$, the filtered density design variables $\tilde{\boldsymbol{x}}_\rho$, and the physical density design variables $\bar{\mathbf{x}}_\rho$.

The filtered density field is obtained through the Helmholtz equation B. S. Lazarov [43]

$$-d_r^2 \nabla^2 \tilde{x}_\rho + \tilde{x}_\rho = x_\rho \,, \tag{3.18}$$

where $\tilde{x}_\rho$ and x_ρ represent filtered density design variables and the density variables used by MMA at the element level. In the equation, d_r is a characteristic radius that introduces a length scale in the optimization.

We discretize the Helmholtz equation using standard linear interpolation functions $\mathbf{N}_h$ at the element level, based on standard 8-node hexahedral elements (in 3D) or 4-node quadrilateral elements (in 2D). We use the relation $x_\rho = \mathbf{N}_h^\mathsf{T} \boldsymbol{x}_e$ and $\tilde{x}_\rho = \mathbf{N}_h^\mathsf{T} \tilde{\boldsymbol{x}}_e$. In these relations, $\boldsymbol{x}_e$ and $\tilde{\boldsymbol{x}}_e$ are the nodal density values for each field at the

element level. The discretized Helmholtz equation is written as

$$\begin{aligned} &-\int \mathbf{N}_h d_r^2 \nabla^2 (\mathbf{N}_h^\intercal \tilde{\boldsymbol{x}}_e) \mathrm{d}\Omega + \int \mathbf{N}_h \mathbf{N}_h^\intercal \tilde{\boldsymbol{x}}_e \mathrm{d}\Omega \\ &= \int \mathbf{N}_h^\intercal \boldsymbol{x}_e \mathrm{d}\Omega \,. \end{aligned} \tag{3.19}$$

Applying the divergence theorem and Neumann boundary conditions, we obtain

$$\int \nabla \mathbf{N}_h d_r^2 \nabla (\mathbf{N}_h^\intercal \tilde{\boldsymbol{x}}_e) \mathrm{d}\Omega + \int \mathbf{N}_h \mathbf{N}_h^\intercal \tilde{\boldsymbol{x}}_e d\Omega = \int \mathbf{N}_h^\intercal \boldsymbol{x}_e \mathrm{d}\Omega \,. \tag{3.20}$$

We can write the previous equation as a system of linear equations using a filtering stiffness matrix $\mathbf{K}_h$ using our design variables $\boldsymbol{x}_\rho$ and an assembly procedure, i. e.,

$$\begin{aligned} &\mathbf{K}_h \tilde{\boldsymbol{x}}_\rho = \mathbf{H} \boldsymbol{x}_\rho \,, \text{ where} \\ &\mathbf{K}_h = \sum_e^{n_e} \left(\int \left(\nabla \mathbf{N}_h^\intercal d_r^2 \nabla \mathbf{N}_h + \mathbf{N}_h^\intercal \mathbf{N}_h \right) \mathrm{d}\Omega \right) . \end{aligned} \tag{3.21}$$

In this formulation, $\mathbf{H}$ is a matrix whose column i contains the element level integration $\int \mathbf{N}_h d\Omega$ for the nodes of the element $e == i$.

The preconditioned conjugate gradients method provides the solution to this system. As this $\mathbf{K}_h$ matrix only depends on the mesh, we use a single preconditioning and store it throughout the optimization procedure, reducing the computational cost of filtering the design space [14]. Finally, to recover the element density after filtering, we use the approximation function for the centroid of each element $\mathbf{N}_h(0,0,0)$.

To provide a sharp change between void and solid material, we apply a Heaviside projection to the filtered design that provides the physical density design variable

$$\bar{x}_\rho = \frac{\tanh\left(\beta\mu\right) + \tanh\left(\beta(\tilde{x}_\rho - \mu)\right)}{\tanh\left(\beta\mu\right) + \tanh\left(\beta(1-\mu)\right)} \,. \tag{3.22}$$

The β variable determines the sharpness of the projection, and μ the step location.

The physical density design variable provides the relation

$$\rho_e = \bar{x}_\rho \rho_s \,, \tag{3.23}$$

where the physical density design variable of the e-th design element is directly related to the density of the eth element ρ_e, with respect to its solid density ρ_s.

The rest of the material properties can be written for each element using a power law following a modified SIMP approach [44, 45], as follows:

$$\begin{aligned} \alpha &= \alpha_v + \bar{x}_\rho^{p_\alpha} (\alpha_s(T) - \alpha_v) \,, \\ \kappa &= \kappa_v + \bar{x}_\rho^{p_\kappa} (\kappa_s(T) - \kappa_v) \,, \\ \gamma &= \gamma_v + \bar{x}_\rho^{p_\gamma} (\gamma_s(T) - \gamma_v) \,, \\ E &= E_v + \bar{x}_\rho^{p_E} (E_s(T) - E_v) \,. \end{aligned} \tag{3.24}$$

The properties of the solid material are indicated by the subscript $\square_s$ in Equation (3.24), and we define them according to experimental data. Minimum material properties for void elements are imposed to avoid the singularity in the tangent matrices with a user-defined value $\square_v$. p_S, p_κ, p_γ and p_E are the penalization coefficients for their corresponding material property. Intermediary densities in the optimized design are equivalent to non-manufacturable porous materials. For this reason, the penalization coefficient tries to ensure the optimized results lead to a fully black-and-white design.

Furthermore, we use nonlinear temperature-dependent properties for each material. We modelled the properties of the semiconductors following the measurements for Bi_2Te_3 by Witting *et al.* [46], using the lowest doping values for each semiconductor. The provided values are fitted to a continuous polynomial as detailed in Appendix E within the measured temperature range. We enforce constant material properties for temperatures outside of this range. If the outcome from the optimization falls within this constant material property range, their results should be reevaluated, or the material properties extended to accommodate a broader range. In addition to semiconductor material, we need to define the properties of copper for electrical terminals, aluminium nitride (AlN) for the thermal ceramic contacts, and SAC 305 (tin-silver-copper) as solder. These material properties are kept constant with temperature to avoid further nonlinear effects added to the optimization procedure. We summarize all temperature-constant material properties used in this model in Table 7.5.

3.3.1. Topology optimization formulation

With the density design variables and filtering techniques established, we need to define the optimization problem that will guide the design variables. We can define this problem for cooling applications through a temperature-based objective, power constraints and voltage design variables to limit the electrical working point, stress constraints for reliability, and volume fraction limits to reduce costs. We can describe this formulation as:

$$\mathbf{x}_\Phi^* = \underset{\mathbf{x}_\Phi}{\arg\min} \quad \Phi = \Psi(\mathbf{T}_\Phi), \tag{3.25a}$$

$$\text{such that} \quad c_\sigma = \Psi\left(\frac{\boldsymbol{\sigma}_{VM}}{\sigma_0}\right) - 1 \leq 0, \tag{3.25b}$$

$$c_P = \frac{P}{P_0} - 1 \leq 0, \tag{3.25c}$$

$$c_v = \sum_{e=1}^{n_e} \frac{v_e x_\rho}{v_0 v_{obj}} - 1 \leq 0, \tag{3.25d}$$

$$V_\Gamma = V_{\min} + x_S(V_{\max} - V_{\min}), \tag{3.25e}$$

$$\mathbf{R} = \mathbf{0}, \tag{3.25f}$$

where we look for the design variables $\boldsymbol{x}_\Phi$ that minimize an objective function Φ submitted to several constraints. For this optimization we define a vector of design

variables $\mathbf{x}_\Phi = \begin{bmatrix} \boldsymbol{x}_\rho & \boldsymbol{x}_S \end{bmatrix}^\intercal$, containing the density design variables $\boldsymbol{x}_\rho$ and the design variables controlling the voltage Dirichlet imposed boundary conditions $\boldsymbol{x}_S$ which for our model can be reduced to a single boundary condition V_Γ between a given minimum and maximum voltages defined as $V_{\min}$ as $V_{\max}$.This allows us to take into account the optimum efficiency of thermocouples with respect to the current flow across the device for all geometries, which is a nonlinear effect. The overall objective of our optimization is then the temperature of our heat injection surface, considering a power limit and controlling the power consumption of the system. Furthermore, we limit the stresses to which the device is submitted and incorporate a volume constraint to reduce semiconductor material volume and associated costs. The objective function depends on a temperature field $\mathbf{T}_\Phi$ on Γ_Φ and an aggregation function Ψ. The problem is subjected to various constraints, including a stress constraint c_σ, a power constraint c_P and a volume constraint c_v. The stress constraint is based on limiting stress σ_0 and a field of von Mises stresses aggregated through the same function as the objective function. The power constraint requires a ratio between the overall power consumption of the device P and a limit power P_0. The volume constraint depends on the summation of the volume of each element v_e compared to the total volume of the original design v_0 and a limiting volume v_{obj}.

As an aggregation function Ψ, we use the P-mean, which increases the influence on the function of the values that deviate most from the mean of the input values using a penalization factor p_Ψ. The P-mean is defined as,

$$\Psi(\mathbf{f}) = \left(\frac{1}{n_i} \sum_{i=1}^{n_i} f_i^{p_\Psi} \right)^{\frac{1}{p_\Psi}}, \tag{3.26}$$

with $\mathbf{f}$ a vector field and n_i its size. Ψ provides a lower-bound of the maximum value stored in $\mathbf{f}$,

$$\Psi(\mathbf{f}) \leq \max(f_1, f_2, ..., f_{n_i}), \tag{3.27}$$

leading to an underpenalization of the constraints or maximum values in the field Fernández *et al.* [47]. This function has an asymptotic behaviour towards the maximum in the distribution with increasing p_Ψ values [30]. This means its behaviour will also lead to higher nonlinearities, the larger the penalization coefficient p_Ψ. The stress constraint and the objective functions use this formulation to avoid stress concentrations and hot spots in the optimized designs. The values used within the exponential aggregation function must be rescaled to values close to unity to avoid singularities in the numerical calculation. This can be done in each case through a reference temperature, where we use the initial device temperature of 25 °C, and the limiting stress σ_0.

We also rescale the other constraints to maximum values between 1 and 100 using the objective volume and power to improve the convergence of the MMA optimizer [48]. This algorithm, proposed by Svanberg [49], uses a local convex approximation function in successive iterations to find local minima. MMA has been repeatedly tested in TO problems with success in finding minima. The stopping criteria of

the algorithm used is based on a total number of iterations or the relative change between the design variables $\bar{\mathbf{x}}_\Phi$,

$$\text{Stop if} \quad \frac{1}{\dim(\bar{\mathbf{x}}_\Phi)} \left\| \left(\bar{\mathbf{x}}_\Phi^{(i-2)} - \bar{\mathbf{x}}_\Phi^{(i)} \right) \oslash \bar{\mathbf{x}}_\Phi^{(i)} \right\|_2 < \varepsilon_{\text{KKT}}$$

$$\text{or} \quad i \geq i_{\max}.$$

Because MMA is a gradient descent algorithm, we must formulate the sensitivities for the objective and constraint functions.

3.3.2. Sensitivity calculation

To apply a gradient-based optimization algorithm, we need analytical expressions for the sensitivities of each objective and constraint function concerning the design variables and validate them against finite differences methods according to Appendix D. We calculate these sensitivities for the filtered field, $\bar{\boldsymbol{x}}_\Phi = \begin{bmatrix} \bar{\boldsymbol{x}}_\rho & x_S \end{bmatrix}^\intercal$, although these can be easily extended to any number of boundary condition control variables. Given the use of $\boldsymbol{x}_\rho$ by the optimizer and the $\bar{\boldsymbol{x}}_\rho$ by our FEM, to recover the sensitivities of a function ψ, with respect to the density design variables we need to follow the chain rule

$$\frac{\partial \psi}{\partial \boldsymbol{x}_\rho} = \frac{\partial \psi}{\partial \bar{\boldsymbol{x}}_\rho} \cdot \frac{\partial \bar{\boldsymbol{x}}_\rho}{\partial \tilde{\boldsymbol{x}}_\rho} \cdot \frac{\partial \tilde{\boldsymbol{x}}_\rho}{\partial \boldsymbol{x}_\rho}. \tag{3.28}$$

We can express the derivative of the filtered design space relative to the density values as

$$\frac{\partial \tilde{\boldsymbol{x}}_\rho}{\partial \boldsymbol{x}_\rho} = \mathbf{K}_h^{-1} \mathbf{H}. \tag{3.29}$$

We can recalculate the result of the modified sensitivities through the vector containing the sensitivities to the filtered design variables and a single calculation using the conjugate gradients method. The nodal sensitivities can then be recovered as the mean of each element, as we do for the filtered densities.

The derivative of the physical field concerning the filtered field is given by:

$$\frac{\partial \bar{x}_\rho}{\partial \tilde{x}_\rho} = \frac{\beta\left(\tanh^2\left(\beta(\mu - \tilde{x}_\rho)\right) - 1\right)}{\tanh\left(\beta(\mu - 1)\right) - \tanh(\beta\mu)}. \tag{3.30}$$

The sensitivities with respect to the physical density field are then solved through the *adjoint method* through the definition of the Lagrangian

$$L = \boldsymbol{\psi} + \boldsymbol{\Lambda}^\intercal \mathbf{R}. \tag{3.31}$$

In this definition, L represents the Lagrangian, $\boldsymbol{\Lambda}$ is the adjoint vector, and ψ is the objective or constraint function. The general solution to the total derivative of any Lagrangian functional can be solved through the definition of a $\boldsymbol{\Lambda}$ constant vector

that removes from the equation the derivative of the state vector $\mathbf{S}$ concerning our design variables $\boldsymbol{x}$. The general equation that solves $\boldsymbol{\Lambda}$ looks like

$$-\left(\frac{\partial \mathbf{R}}{\partial \mathbf{S}}\right)^{\mathsf{T}} \boldsymbol{\Lambda} = \left(\frac{\partial \psi}{\partial \mathbf{S}}\right)^{\mathsf{T}}. \tag{3.32}$$

Given that the first component of the equation is the tangent stiffness matrix, we can decompose this calculation as we do for the Newton-Raphson iterative procedure, reducing memory allocation. The solution can then be the following 2 steps:

$$-\left(\frac{\partial \mathbf{R_U}}{\partial \mathbf{U}}\right)^{\mathsf{T}} \boldsymbol{\Lambda}_U = \left(\frac{\partial \psi}{\partial \mathbf{U}}\right)^{\mathsf{T}}, \tag{3.33}$$

$$-\left(\mathbf{K_{TV}}\right)^{\mathsf{T}} \boldsymbol{\Lambda}_{TV} = \begin{bmatrix} \frac{\partial \psi}{\partial \mathbf{T}} & \frac{\partial \psi}{\partial \mathbf{V}} \end{bmatrix}^{\mathsf{T}} + \left(\frac{\partial \mathbf{R}_U}{\partial \mathbf{T}}\right)^{\mathsf{T}} \boldsymbol{\Lambda}_U. \tag{3.34}$$

In the previous separation of the mechanical and thermoelectric solutions of the adjoint vector, we separate it as

$$\boldsymbol{\Lambda}^{\mathsf{T}} = \begin{bmatrix} \boldsymbol{\Lambda_U} & \boldsymbol{\Lambda_T} & \boldsymbol{\Lambda_V} \end{bmatrix} = \begin{bmatrix} \boldsymbol{\Lambda_U} & \boldsymbol{\Lambda_{TV}} \end{bmatrix}. \tag{3.35}$$

Substituting these solutions into the Lagrangian derivative, we can calculate the derivatives of the function ψ as

$$\frac{\mathrm{d}L}{\mathrm{d}\bar{\boldsymbol{x}}_\Phi} = \frac{\mathrm{d}\psi}{\mathrm{d}\bar{\boldsymbol{x}}_\Phi} = \frac{\partial \psi}{\partial \bar{\boldsymbol{x}}_\Phi} + \boldsymbol{\Lambda}^{\mathsf{T}} \left(\frac{\partial \mathbf{R}}{\partial \bar{\boldsymbol{x}}_\Phi}\right). \tag{3.36}$$

This solution still requires the derivative of the residual and the function ψ concerning each design variable in $\boldsymbol{x}$. This $\bar{\boldsymbol{x}}_\Phi$ comprises filtered density design variables and boundary condition control variables. We can identify two different cases. In the case of the derivatives concerning a density variable $\bar{x}_\rho$, the calculation can be taken to the element level as:

$$\frac{\mathrm{d}\psi}{\mathrm{d}\bar{x}_\rho} = \frac{\partial \psi}{\partial \bar{x}_\rho} + \boldsymbol{\Lambda}_e^{\mathsf{T}} \left(\frac{\partial \mathbf{r}}{\partial \bar{x}_\rho}\right). \tag{3.37}$$

In the previous equation, $\boldsymbol{\Lambda}_e$ represents the adjoint solution for the DOFs associated with element e and $\bar{x}_\rho$ its associated density design variable. The second case refers to the sensitivity concerning a boundary condition. In this case, we can use the chain rule as

$$\frac{\mathrm{d}\psi}{\mathrm{d}x_S} = \frac{\partial \psi}{\partial \mathbf{S}} \frac{\partial \mathbf{S}}{\partial S_\Gamma} \frac{\partial S_\Gamma}{\partial x_S} - \boldsymbol{\Lambda}^{\mathsf{T}} \left(\frac{\partial \mathbf{R}}{\partial \mathbf{S}} \frac{\partial \mathbf{S}}{\partial S_\Gamma} \frac{\partial S_\Gamma}{\partial x_S}\right). \tag{3.38}$$

In this equation, we require the derivative of ψ concerning the state vector, already calculated for the adjoint vector system. Now, we need to define the derivative of the state vector concerning the fixed value used in our boundary condition S_Γ. While this is a general formulation that can be applied to Dirichlet boundary conditions in U, T or V as expressed in Equation (3.8), we particularize it for a voltage boundary condition V_Γ as

$$\frac{\partial \mathbf{U}}{\partial V_\Gamma} = \mathbf{0}, \tag{3.39}$$

$$\frac{\partial \mathbf{T}}{\partial V_\Gamma} = \mathbf{0}, \tag{3.40}$$

$$\frac{\partial V_i}{\partial V_\Gamma} = \begin{cases} 1 & \text{if } \mathbf{x}(i) \in \Gamma_V; \\ 0 & \text{otherwise,} \end{cases} \tag{3.41}$$

where Γ_V is the location of the boundary condition we control through x_S and $\mathbf{x}$ is the coordinates of node i.

The last component needed is the derivative of the value associated with the boundary condition concerning its control variable, following the description in Equation (3.25e). The derivative of the voltage boundary condition concerning the control variable can be expressed as

$$\frac{\partial V_\Gamma}{\partial x_S} = V_{max} - V_{min}, \tag{3.42}$$

where V_{max} and V_{min} define the minimum and maximum voltage that we apply across our thermoelectrical device.

Given the previous formulation, we can observe that the derivative of the ψ function concerning a design variable controlling boundary condition is only different from zero if the domain that the objective or constraint affects contains the nodes from the boundary condition. We can state this fact for our voltage boundary condition as

$$\frac{\partial \psi}{\partial \mathbf{S}} \frac{\partial \mathbf{S}}{\partial V_\Gamma} = \frac{\partial \psi}{\partial V_\Gamma} = 0 \text{ if } \Gamma_\psi \cap \Gamma_V = \emptyset, \tag{3.43}$$

where Γ_ψ are the DOFs used by ψ.

These equations provide all the quantities that need to be defined to calculate for each objective and constraint. In the following subsections, we provide the derivatives of each ψ function with respect to S and $\tilde{\boldsymbol{x}}_\Phi$. The common derivatives for all functions of $\mathbf{r}$ and material properties are provided in the Appendix C.

Objective Function

We use the P-mean of the nodal temperature values in the cold surface of the thermocouple as our objective, Γ_Φ. This equation is written in Equation (4.12).

To calculate its derivative with respect to the state vector, we can rewrite it in terms of the of all DOFs using a vector $\mathbf{L}_\Phi$ which stores the components of $\mathbf{T}$ present in Γ_Φ, and performs the division concerning the number of elements in the summation. This multiplier $\mathbf{L}_\Phi$ contains

$$\mathbf{L}_\Phi(i) = \begin{cases} \frac{1}{n_\Phi} & \text{if } \mathbf{x}(i) \in \Gamma_\Phi; \\ 0 & \text{otherwise.} \end{cases}, \tag{3.44}$$

with n_Φ is the number of DOFs used to summate the P-mean function and $\mathbf{x}$ are the coordinates of node i. The objective function can then be written as

$$\Psi(\mathbf{T}_\Phi) = \left(\mathbf{L}_\Phi^\intercal \mathbf{T}^{\circ p_\Psi}\right)^{\frac{1}{p_\Psi}}. \tag{3.45}$$

The derivative of this objective with respect to the global temperature DOFs can now be written as

$$\frac{\partial \Phi}{\partial \mathbf{T}} = \mathbf{L}_\Phi \circ \mathbf{T}^{\circ(p_\Phi - 1)} \left(\mathbf{L}_\Phi^\intercal \mathbf{T}^{\circ p_\Phi}\right)^{\left(\frac{1}{p_\Phi} - 1\right)}. \tag{3.46}$$

This can be rewritten in terms of the global state vector $\mathbf{S}$ as

$$\frac{\partial \Phi}{\partial \mathbf{S}} = \begin{bmatrix} \frac{\partial \Phi}{\partial \mathbf{U}} \\ \frac{\partial \Phi}{\partial \mathbf{T}} \\ \frac{\partial \Phi}{\partial \mathbf{V}} \end{bmatrix} = \begin{bmatrix} \mathbf{0} \\ \frac{\partial \Phi}{\partial \mathbf{T}} \\ \mathbf{0} \end{bmatrix}. \tag{3.47}$$

The partial derivative of the objective function with respect to any density design variable is zero

$$\frac{\partial \Phi}{\partial \tilde{\boldsymbol{x}}_{\boldsymbol{\rho}}} = \mathbf{0}. \tag{3.48}$$

Notice that these equations do not depend on the mechanical DOFs. Therefore, the two-step adjoint equation calculation can be simplified with

$$\boldsymbol{\Lambda}_U = \mathbf{0}. \tag{3.49}$$

Stress constraint

For each element, we consider a single $\hat{\boldsymbol{\sigma}}$ value calculated at its centroid – equivalent to a zero value for its local coordinates $\boldsymbol{\xi} = \mathbf{0}$. The space of these centroids makes up Γ_Φ. The centroid reference for the stresses provides an exact value for hexahedral serendipity elements (H20) without the need for extrapolation for Gauss integration schemes if $\boldsymbol{\xi} = \mathbf{0}$ is used as an integration point [50]. The lack of extrapolation and use of a single evaluation point per element simplifies the calculation of this constraint at the cost of a lower number of evaluation points for the stress constraint. Given these assumptions, we can reduce the derivative of the von Mises stress with respect to each one of the stresses stored in the Voigt notation to the element level.

The partial derivative of the P-mean function of the stress within the design domain requires the calculation of a summation along all nodes n_σ included in the design domain. Following the chain rule, we have

$$\frac{\partial c_\sigma}{\partial \mathbf{S}} = k_\sigma \sum_{e=1}^{n_\sigma} \left(\left(\frac{\sigma_{VM}^{(e)}}{\sigma_0} \right)^{p_\Psi - 1} \begin{bmatrix} \frac{\partial \sigma_{VM}^{(e)}}{\partial \hat{\boldsymbol{\sigma}}} \frac{\partial \hat{\boldsymbol{\sigma}}}{\partial \mathbf{u}} \\ \frac{\partial \sigma_{VM}^{(e)}}{\partial \hat{\boldsymbol{\sigma}}} \frac{\partial \hat{\boldsymbol{\sigma}}}{\partial \mathbf{t}} \\ \frac{\partial \sigma_{VM}^{(e)}}{\partial \hat{\boldsymbol{\sigma}}} \frac{\partial \hat{\boldsymbol{\sigma}}}{\partial \mathbf{v}} \end{bmatrix} \right). \tag{3.50}$$

In this equation, we have a k_σ constant arising from the derivative of the P-mean function and defined as

$$k_\sigma = \frac{1}{n_\sigma \sigma_0} \left(\frac{1}{n_\sigma} \sum_{e=1}^{n_\sigma} \left(\frac{\sigma_{VM}^{(e)}}{\sigma_0} \right)^{p_\Psi} \right)^{\frac{1}{p_\Psi} - 1}. \tag{3.51}$$

Each derivative of a single von Mises stress value with respect to the local stresses is given by

$$\frac{\partial \sigma_{VM}^{(e)}}{\partial \hat{\boldsymbol{\sigma}}} = \frac{1}{2\sigma_{VM}^{(e)}} \begin{bmatrix} (2\sigma_x - \sigma_y - \sigma_z) \\ (2\sigma_y - \sigma_x - \sigma_z) \\ (2\sigma_z - \sigma_y - \sigma_x) \\ 6\tau_{yz} \\ 6\tau_{xz} \\ 6\tau_{xy} \end{bmatrix}^{\mathsf{T}}, \tag{3.52}$$

and the derivative of the local stress vector with respect to the element-level DOFs are

$$\frac{\partial \hat{\boldsymbol{\sigma}}}{\partial \mathbf{u}} = \mathbf{CB}, \tag{3.53}$$

$$\frac{\partial \hat{\boldsymbol{\sigma}}}{\partial \mathbf{t}} = \frac{\partial \mathbf{C}}{\partial T}\mathbf{B}\mathbf{u}\mathbf{N}^{\mathsf{T}} - \frac{\partial \beta_T}{\partial T}\boldsymbol{\theta}\mathbf{N}^{\mathsf{T}} - \beta_T \mathbf{N}^{\mathsf{T}}, \tag{3.54}$$

$$\frac{\partial \hat{\boldsymbol{\sigma}}}{\partial \mathbf{v}} = \mathbf{0}. \tag{3.55}$$

The derivative of the stress constraint with respect to the density design variables can be calculated at the element is

$$\frac{\partial c_\sigma}{\partial \bar{\boldsymbol{x}}_{\boldsymbol{\rho}}} = k_\sigma \left(\sum_{e=1}^{n_\sigma} \left(\frac{\sigma_{VM}^{(e)}}{\sigma_0} \right)^{p_\Psi - 1} \frac{\partial \sigma_{VM}^{(e)}}{\partial \hat{\boldsymbol{\sigma}}} \frac{\partial \hat{\boldsymbol{\sigma}}}{\partial \bar{x}_\rho} \right), \tag{3.56}$$

where the element-level derivative of the Voigt notation stress of each element is

$$\frac{\partial \hat{\boldsymbol{\sigma}}}{\partial \bar{x}_\rho} = \frac{\partial \mathbf{C}}{\partial \bar{x}_\rho}\mathbf{B}\mathbf{u} - \frac{\partial \mathbf{C}}{\partial \bar{x}_\rho}\alpha_T \boldsymbol{\theta}. \tag{3.57}$$

Power constraint

We calculate the thermocouple power through the summation of the integration of the current density multiplied by the voltage gradient within each one of the elements in the mesh used for the power calculation n_P, i. e.,

$$P = \sum_{e=1}^{n_P} P_e = \sum_{e=1}^{n_P} \left(-\int_\Omega \mathbf{j}^{\mathsf{T}} \boldsymbol{\nabla} \mathbf{N}^{\mathsf{T}} \mathbf{v} \, \mathrm{d}\Omega \right). \tag{3.58}$$

The integral is performed at the element level, so the derivative can also be calculated at the element level and assembled through the summation of each

element's component. The derivative of this function with respect to the state vector can be written as,

$$\frac{\partial c_p}{\partial \mathbf{S}} = \frac{1}{P_0}\sum_{e=1}^{n_p}\int_\Omega \begin{bmatrix} \mathbf{0} \\ -\frac{\partial \mathbf{j}}{\partial \mathbf{t}}^\intercal \nabla \mathbf{N}^\intercal \mathbf{v} \\ -\frac{\partial \mathbf{j}}{\partial \mathbf{v}}^\intercal \nabla \mathbf{N}^\intercal \mathbf{v} - \nabla \mathbf{N}\mathbf{j} \end{bmatrix} d\Omega. \tag{3.59}$$

The derivative of the power with respect to the density design variables can also be reduced to the element-level as

$$\frac{\partial c_p}{\partial \bar{x}_\rho} = \frac{-1}{P_0}\int_\Omega \left(\frac{\partial \mathbf{j}}{\partial \bar{x}_\rho}\right)^\intercal \nabla \mathbf{N}^\intercal \mathbf{v}\, d\Omega. \tag{3.60}$$

The partial derivatives of the current density with respect to the density design variables and element-level DOFs are provided in Appendix C.

As in the case of the temperature objective, the mechanical adjoint vector is zero. This can simplify the calculation of these derivatives.

Volume constraint

This constraint does not depend on the state vector or the boundary conditions, leading to the values:

$$\frac{\partial c_v}{\partial \mathbf{S}} = \mathbf{0}. \tag{3.61}$$

Nevertheless, this equation does depend on the element-level densities

$$\frac{\partial c_v}{\partial \bar{x}_\rho} = \frac{v_e}{v_0 v_{obj}}. \tag{3.62}$$

Given the previous equations, this solution does not require the calculation of the adjoint as the solution to the system Equation (3.32) provides the trivial solution.

3.4. Results

This section provides examples of how we apply our formulation to the standard thermoelectrical element mechanical assembly. This is commonly done by introducing the TEC between two plates that can be tightened together using fasteners, adding a compression force into the thermoelectric device. These two plates act as cooling surfaces and heat sinks, respectively. After assembly, the entire thermocouple is under compression loading and cannot expand through its thickness.

3.4.1. 2D results

Each TEC usually consists of multiple thermocouples, with each thermocouple being an in-series connection between dissimilar semiconductors. For our model, we

simplify it to a single thermocouple, considering they are all submitted to the same loads. A $2D$ cross-section of a single thermocouple is depicted in Figure 3.1. In this figure, we can appreciate a cross-section of the yz plane of a thermoelectrical pellet composed of a $p+$ and $n-$ semiconductor pellets joined together by a solder (white blocks) and a copper layer (solid grey blocks). Two ceramic layers (hatched blocks) act as the thermal contacts in this assembly. This figure also shows the boundary conditions at each of the outer edges. The mechanical boundary conditions include a zero displacement in the heat sink and cooling surface along the z axis to simulate the mechanical assembly and at the connection with the surrounding thermocouples with zero displacements along the ceramic and copper connections to the surrounding material in the x direction. The thermoelectrical model imposes a heat flux q_{in} at the cold surface of the TEC and a heat sink with a prescribed temperature T_0 on the opposite surface. Both these thermal boundary conditions are imposed in the ceramic layers. Electrical boundary conditions are applied to each copper electrode, i. e., a voltage $V_f > 0$ at one end and $V_0 = 0$ in the opposite one, according to the definition of the $p+$ and $n-$ materials. Reversing this definition would warm the objective surface instead of cooling it. Finally, as ceramic materials are not electrically conductive, we fix the voltage value of these solids to zero to avoid numerical instabilities. The nodes in contact between both solids, the copper and the ceramic layer, are not fixed and are solved in each iteration.

With our 2D model, we now set the optimization parameters. The TO computational domain within the design in Figure 3.1 is set only to the thermoelectrical elements, i. e., Bi_2Te_3 material regions. While the copper, ceramic, and solder layers can impact the objective and constraint functions, we do not include their topology in the design space. We create the mesh of Bi_2Te_3 using a regular 60×60 grid, totalling 3600 serendipity 8-node elements (Q8) per semiconductor leg. The dimensions of the default thermoelectrical pellet are based on standard thermoelectrical devices and are equal to $1\,\text{mm} \times 1.2\,\text{mm}$. The solder, copper, and ceramic layers measure 0.05, 0.1, and 0.2 mm, respectively, and the gap between two pellets is 0.2 mm. We set the limits of the voltage gradient across the thermocouple defined by the x_S design variable to 0.01 V and 0.06 V and equal to V_f. The initial value imposed to x_S during the optimization is 0, providing the smallest voltage possible according to Equation (3.25e).

For subsequent optimizations without any filtering scheme, we start from the full density design, $\tilde{\boldsymbol{x}}_{\boldsymbol{\Phi}} = \boldsymbol{x}_{\boldsymbol{\Phi}} = \mathbf{0.5}$, given the lack of information on a better initialization design and the need for a fully-connected design. The minimum material property value for all materials according to Equation (3.24) is set to 10^{-6} to avoid numerical instabilities. Furthermore, we fix the heat flux to $7500\,\text{W/m}^2$ and the power consumption to 15 mW per thermocouple. We can translate this power consumption limit for the $2D$ case to 15 W/m, considering a thickness of 1 mm for the thermocouple. Finally, the MMA algorithm requires the definition of some parameters, including a hyperparameter c_m, to penalize the problem for infeasible design spaces. All c_m values are set to 20000 and the optimization is run for a number of iterations i_m of 150. Notice that we obtain these values by trial and error, and if set too low, we might end up with an infeasible design. The penalization

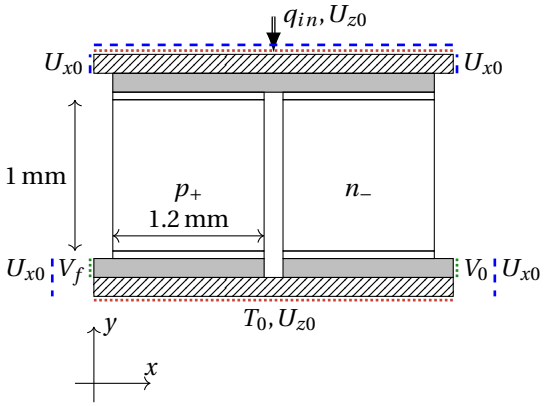

Figure 3.1.: Thermocouple FEM simplified model. The figure includes the heat injection q_{in} and temperature boundary conditions T_0 in red, voltages (V_0, V_f) in green and displacements in blue U_{x0}. The different layers include a grey copper connection, a hashed ceramic layer, and two thermoelectrical pellets soldered to the copper through a solder layer.

coefficient for each material property involved in the optimization has been selected by combinatorial analysis from an analytical model in Reales Gutiérrez *et al.* [51] to achieve convergence. For all optimizations, we use the set of penalization coefficients satisfying

$$p_S < p_k = p_\gamma < p_E \,. \tag{3.63}$$

We summarize all parameters required for the optimizations in Table 3.1 following the methodology in Section 3.3.

Parameter	Value	Parameter	Value
$V_{\min}$	0.01 V	c_m	20000
$V_{\max}$	0.06 V	d_r	0.11 mm
p_E	5	P_{obj}	15 mW/mm
p_S	1	σ_0	10E6
p_σ	3	T_{ref}	298.15 K
p_k	3	T_h	350 K
q_{in}	7500 W/m^2	ε_{KKT}	10^{-8}
β	64	$x_S^{(i=0)}$	0.5
μ	0.4	i_m	150

Table 3.1.: MMA optimization parameter summary according to Equation (4.12), Equation (3.18), and Equation (3.24) for the optimization results in Figure 3.2.

We increase the complexity through multiple optimizations to better understand the problem and the successive nonlinearities introduced. For this reason, we successively add stress constraints and filtering techniques to a pure thermoelectrical optimization with power constraints. Furthermore, we repeat this analysis for different material conditions for the model, from constant material properties at 350 K, to nonlinear material properties with temperature, to the introduction of air material in the void regions and in between the thermocouple legs. The results from these successive optimizations are represented in Figure 3.2 with an increased number of constraints and filtering techniques toward the right and increased model and material complexity further down. Each plot in this figure represents the density field for the 150^{th} iteration or convergence conditions for each optimization with a linear colour scale, with white representing void material and black full-density material.

The pure thermoelectrical TO with power constraints but without stress or volume constraints are shown in Figures 3.2a, 3.2e and 3.2i. These plots show an asymmetry between each pellet, given their different thermoelectrical properties of p+ and n-type semiconductors. Notice that the Peltier effect is based on the change of energy of the electrons moving between different outer valence energy levels between two dissimilar semiconductors. Therefore, the effect only requires contact between dissimilar semiconductors. The optimization objective tries to reach an optimized configuration between decreasing the thermal conductivity and increasing the electrical conductivity of each semiconductor. Given the material properties used, see Appendix E, we use the same thermal conductivity for both semiconductors and the optimization should leave the largest amount of the material with the lowest electrical conductivity at each operational temperature to compensate for it. Indeed, we observe that the electrical conductivity provided in Appendix E decreases with temperature; with the highest temperature located at the bottom surface of the thermocouple, the heat sink, the optimized pellets present the largest amount of material at this location, with the lowest amount of material at the cold top surface contact with the higher electrical conductivity. The optimizer also tries to reduce Joule heating concentrations by creating multiple electrical paths, avoiding hot spots and distributing the Peltier effect through multiple contacts along the cold surface.

A second set of optimizations include a stress constraint to 10 MPa (Figures 3.2b, 3.2f and 3.2j). These optimizations maintain features of the pure thermoelectrical TO, such as continuous paths for the electrical and thermal flow, but also present joints and smaller contacts to the top and bottom surfaces to reduce the thermally induced stresses in the thermocouple. These joints are made through features of a single element and porous material. This is an undesirable and difficult-to-manufacture topology. A Hemlholtz filter can introduce a length scale, removing all single-element features and providing mesh independence to the results. A third set of optimizations using a filter radius $d_r = 0.11$ mm is showed in Figures 3.2c, 3.2g and 3.2k. A larger feature size increases the overall stresses in the structure, and the use of the same mechanical properties under an active stress constraint for both semiconductors leads to an increased symmetry between both legs. However, these results maintain intermediate density elements between the solid and void material.

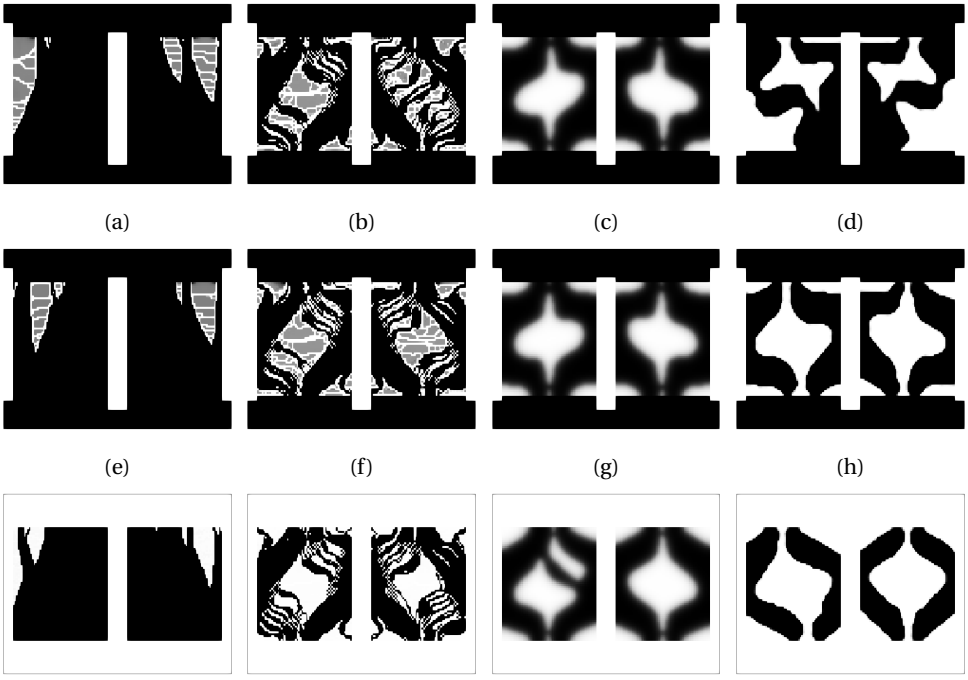

Figure 3.2.: Physical density field for 2D thermocouple optimizations, ranging from full-density elements (in black) to full-void elements (white). Grey elements represent regions with intermediate density values. ubfigures Figures 3.2a to 3.2d use constant material properties at 350 K. Subfigures Figures 3.2e to 3.2h apply nonlinear properties with temperature. The nonlinear material properties and their values at 350 K are described in Appendix E. Subfigures Figures 3.2i to 3.2l also include air as a material in voids and between pellets. Figures 3.2a, 3.2e and 3.2i show results from pure thermoelectric optimizations under power constraints, without filtering or stress constraints. Figures 3.2b, 3.2f and 3.2j include stress and power constraints without filtering. Figures 3.2c, 3.2g and 3.2k apply a Helmholtz filter in addition to stress and power constraints. Figures 3.2d, 3.2h and 3.2l combine stress and power constraints with both Helmholtz and Heaviside filters. The values for each constraint and filtering technique are summarized in Table 3.1.

These intermediate densities can introduce thermoelectric artefacts due to changes in Seebeck's coefficient, the Thompson's effect, and temperature gradients.

To remove these intermediate densities, we introduce a Heaviside projection after the Helmholtz filtering to obtain a sharper transition between the void and solid material in Figures 3.2d, 3.2h and 3.2l. We use a Heaviside projection with $\mu = 0.4$ and a $\beta = 64$. This optimization requires modifying the initial $\boldsymbol{x}_\rho = 0.4$ and default parameters of MMA to obtain convergence and avoid a thermoelectric disconnection of the design. We reduce the movement of the asymptotes in MMA using a move limit, an increase and decrease of the asymptotes, and an initial asymptote of 2%. The results maintain previously found design characteristics, with a crisp transition between solid and void material. We can see that each electrical path develops a rotational joint to accommodate thermal deformation. Between each joint, the algorithm increases the material amount to compensate for the reduced electrical conductance at the joints with smaller cross-sections.

To justify the Heaviside filtering and the impact of grey regions in Helmholtz filtering, the optimized configuration in Figures 3.2f to 3.2h was modified by retaining elements with $x_e > 0.85$. These elements were assigned full density, while others were set to $x_e = 1e-6$. Figure 3.3 compares the new black-and-white designs with the original optimized geometry as $\Delta\Xi = \Xi_{\text{BW}} - \Xi_{\text{opt}}$, where Ξ represents the respective objective or constraint. The black design is colored based on its temperature difference from the optimized design and deformed according to the displacement field difference, scaled by 1000. In Figure 3.3a, grey areas are electrically disconnected, causing minimal thermal variation, with a total deviation of 0.38 °C in localized areas localized at the smallest electrical path contact to the cold surface. In contrast, Figure 3.3b shows larger temperature changes up to 1.4 °C, particularly near the device centre along z. Figure 3.3c improves on the behaviour of Figure 3.3b, with temperature differences of 0.38 °C in localized areas compared to the optimized design, without single element joints. Table 3.2 presents the final values of the objectives and constraints for each black-and-white design, along with the differences from the optimized designs. The grey areas in Figure 3.3a have minimal impact on the metrics compared to the filtered designs. The filtered designs show similar corrected objectives, differing only in the second decimal for the black-and-white designs. However, the objective difference from the optimized designs is two orders of magnitude larger in the design with only the Helmholtz filter. Finally, the stress constraint is not satisfied in all black-and-white designs, with the largest difference found in the design with only the Helmholtz filter.

Although the material properties are nonlinear, the study focuses on the range from 333 to 350 K, where nonlinear effects are moderate compared to the full temperature range, as shown in Appendix E. This suggests that approximating the material properties at a fixed temperature may yield a sufficiently accurate geometry without requiring full nonlinear modelling. Therefore, optimization is performed using properties evaluated at 350 K, as shown in Figures 3.2a to 3.2d. The resulting density fields are then reevaluated using nonlinear material properties and the same voltage gradient. Table 3.3 presents the results, comparing the constant-property-based optimized design to the nonlinear case using $\Delta\Xi = \Xi_{\text{nonlin}} - \Xi_{\text{cte}}$. These results show

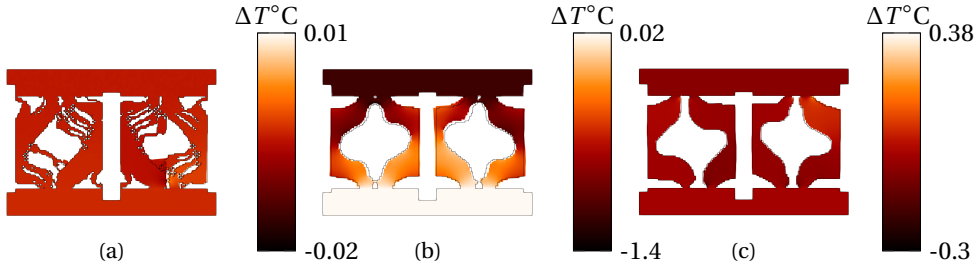

Figure 3.3.: Difference in the thermomechanical response between the black-and-white design (thresholded with $x_e > 0.85$ assigned full density and $x_e = 0.001$ otherwise) and the corresponding optimized design. Field differences are computed for Figures 3.2f to 3.2h in Figures 3.3a to 3.3c, respectively. The colored map shows the temperature field difference, $\Delta\Xi_T = \Xi_{T,\mathrm{BW}} - \Xi_{T,\mathrm{opt}}$. The displacement field difference is depicted as $\Delta\Xi_u = \Xi_{u,\mathrm{BW}} - \Xi_{u,\mathrm{opt}}$, scaled 1000× for visualization, with respect to the original edges of the undeformed design.

	Figure 3.3a	Figure 3.3b	Figure 3.3c
Φ	333.484419	334.142404	333.239808
C_p	5.9×10^{-5}	-8.3961×10^{-2}	-2.072×10^{-3}
C_σ	1.0×10^{-6}	2.10919×10^{-1}	1.9486×10^{-2}
$\Delta\Phi$	-1.129×10^{-3}	-1.153401	-4.6457×10^{-2}
ΔC_p	5.9×10^{-5}	-8.3961×10^{-2}	-1.974×10^{-3}
ΔC_σ	4.0×10^{-6}	2.1092×10^{-1}	2.003×10^{-2}

Table 3.2.: Comparison between the optimized design results (shown in Figures 3.2e to 3.2g) and the corresponding black-and-white design, obtained by thresholding elements with $x_\rho > 0.85$ to full material and the rest to void. The values for Φ, C_p, and C_σ correspond to the black-and-white design, and the differences are computed as: $\Delta\Xi = \Xi_{\mathrm{BW}} - \Xi_{\mathrm{opt}}$, where Ξ denotes any of the considered objective or constraints, with subscripts BW and opt indicating the black-and-white design and the optimized design, respectively.

lower objective and stress values but fail to meet the power constraint. The power deviation corresponds to a maximum increase of 0.7 mW per thermocouple in the design shown in Figure 3.2d. In this case, grey elements in Figure 3.2c appear to limit both the increase in power and the reduction in stress. Nonlinear evaluation leads to temperatures up to 0.46 °C lower than those from constant-property models.

To account for conduction losses, an air model is introduced between the thermoelectric legs. This model uses a void thermal conductivity κ_v of 0.033 W/(Km) and assigns the minimum value for the Young's modulus, electrical conductivity,

	Figure 3.2a	Figure 3.2b	Figure 3.2c	Figure 3.2d
Φ	335.53	333.10	334.91	332.81
C_p	4.14×10^{-2}	4.69×10^{-2}	3.99×10^{-2}	4.57×10^{-2}
C_σ	–	-3.72×10^{-3}	-3.10×10^{-3}	-4.98×10^{-3}
$\Delta\Phi$	-2.40×10^{-1}	-3.93×10^{-1}	-3.61×10^{-1}	-4.59×10^{-1}
ΔC_p	4.14×10^{-2}	4.69×10^{-2}	3.99×10^{-2}	4.58×10^{-2}
ΔC_σ	–	-1.04×10^{-2}	-9.49×10^{-3}	-1.17×10^{-2}

Table 3.3.: Comparison between the results obtained using constant material properties defined at 350 K and those obtained from the same optimized designs using nonlinear material optimization (Figures 3.2e to 3.2h). The values of Φ, C_p, and C_σ correspond to the results obtained using constant material properties, while the differences are computed as $\Delta\Xi = \Xi_{\text{nonlin}} - \Xi_{\text{cte}}$, where $\Xi \in \{\Phi, C_p, C_\sigma\}$.

and the Seebeck coefficient. The resulting density fields are shown in Figures 3.2i to 3.2l. These fields resemble previous designs but show greater separation between solid regions near the cold and hot surfaces due to the increased thermal resistance through the air. Grey regions vanish in these designs, as higher densities in those areas would worsen performance due to non-negligible thermal conductivity. Table 3.4 summarizes the objectives and constraints, comparing the air model designs to those with void materials Figures 3.2e to 3.2h using $\Delta\Xi = \Xi_{\text{air}} - \Xi_{\text{void}}$. These optimizations show a temperature increase of up to 0.84 °C in the optimized geometries. The lowest difference arises in the pure thermoelectric optimization due to the larger optimized volume of semiconductors compared to stress-constrained optimizations. Air inclusion also raises stress levels, as the optimizer increases semiconductor material to counteract heat flux, expanding the contact area with mismatched α_T values. Compared to constant property assumptions, these losses have a more pronounced impact, making them significant for accurate optimization.

	Figure 3.2i	Figure 3.2j	Figure 3.2k	Figure 3.2l
Φ	336.41	334.20	336.14	334.06
$\Delta\Phi$	0.24	0.71	0.84	0.77

Table 3.4.: Comparison of optimized results considering two modelling approaches for void regions: treated as true void and as air. The values of Φ correspond to the results where void is modeled as air (shown in Figures 3.2i to 3.2l), while the differences are computed as $\Delta\Xi = \Xi_{\text{air}} - \Xi_{\text{void}}$.

We perform one last optimization with all filters, considering air-conduction losses, and a volume constraint of 50%, close to 10% lower than the obtained volume for the Figure 3.2l optimization. We show the deformation field of the physical density

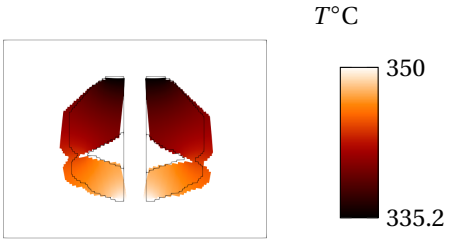

Figure 3.4.: Thermomechanical response of the optimized thermo-electro-mechanical design after 150 iterations with the power and stress constraints defined in Table 3.1 and a volume constraint of 50%. The figure shows all elements with $x_\rho > 0.1$, the mechanical deformation is shown in a colored map that represents the temperature range. The displacements are introduced with a scale of 90 times their nominal value.

field in Figure 3.4 with a scale 90 times the actual deformation superimposed to the undeformed edges. This figure shows the elements in the mesh with $x_\rho > 0.1$. The colour plot shows the temperature of this design for the maximum power allocation allowed of $P = 15\,\mathrm{mW/mm}$. In these results, we can observe a contraction in the middle of the thermocouple and an expansion towards its outer edges, pivoting around the joint in each leg. The temperature field shows a similar profile to that of the previous optimization, with losses in the order of $1.15\,^\circ\mathrm{C}$.

The values of the objective function and all constraints for the first 150 MMA iterations for all optimizations are shown in Figure 3.5. This figure includes the values for the objective aggregated temperature $\Psi(\mathbf{T}_\Phi)$ (Figure 3.5a), the power consumption (Figure 3.5b), the stress aggregated value $\Psi(\boldsymbol{\sigma}_{VM})$ (Figure 3.5c), the voltage gradient across the thermocouple (Figure 3.5d), and percentage of the original semiconductor volume (Figure 3.5e). The objective for the filtered and volume constraint optimization, Figure 3.4, is the one with the highest moving rate by the end of the 150 iterations. Even for this case, the change in the objective is lower than 0.2% between the last ten iterations. The delay in convergence for the Heaviside-filtered designs arises from the slow-moving limits imposed on the MMA optimizer. The temperature objective remains stable after 50 iterations for the rest of optimizations. There is also an initial jump in temperature caused by the excessive power consumption of the initial designs and by its subsequent lowering by MMA. The power constraint is satisfied for all optimizations and is equal to the maximum available. The oscillation present for its value can also be correlated to the stress constraint. In the unfiltered and Helmholtz-filtered designs, there is a peak in the stress constraint that induces a lower voltage and power consumption, reducing the current and joule heating along the device and thermal deformations to satisfy it. These peaks are not present when we reduce the moving limits for MMA or in pure thermoelectrical optimization. While the stress constraint increases the complexity of the problem, it is active for all final results. It can reduce the stresses compared to the pure thermoelectrical optimization to a fifth of its initial

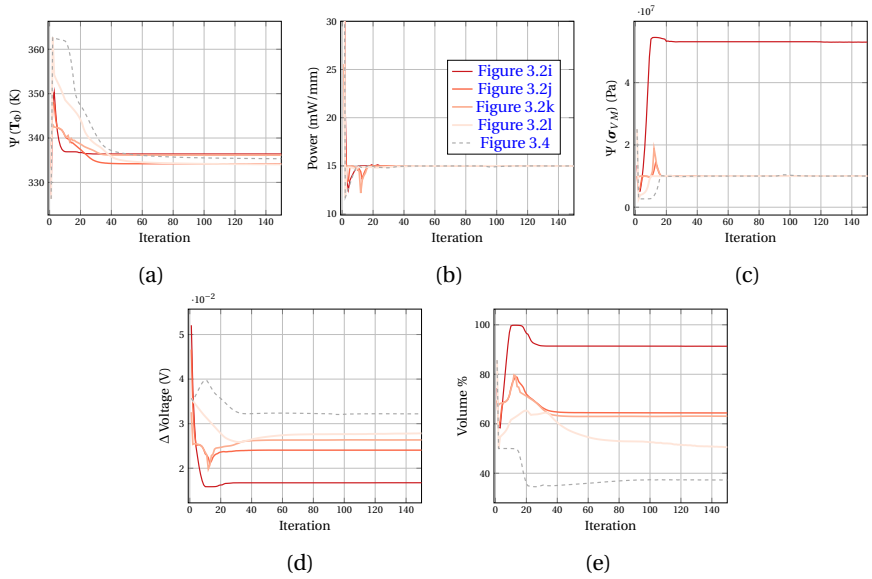

Figure 3.5.: Convergence results for the 2D TO for the 4 different cases summarized in Figure 3.2. Each plot shows the evolution of a different variable, including: Figure 3.5a the objective temperature; Figure 3.5b power; Figure 3.5c stress; Figure 3.5d voltage gradient; and Figure 3.5e volume constraints.

value without compromising the temperature achieved.

We can observe the complexity of the design space field from the multiple designs obtained in Figure 3.2, which can provide similar temperature profiles according to Figure 3.5a. This can partly be achieved through the different final x_S shown in Figure 3.5d. This plot shows that no design shares the same voltage gradient for the optimized temperature profile. Furthermore, the fact that the temperature obtained for the pure thermoelectrical optimization is higher than for the rest of the optimizations, with a difference of $\approx$2.5 °C implies that there are multiple local optima and the stress constraint steers the optimizer towards new optima not reachable by MMA with the imposed parameters from the initial optimization. Furthermore, while the stress-constrained optimization provides one of the lowest temperature profiles and the Helmholtz filter decreases these gains due to the introduced intermediate densities, the Heaviside filter can recover these results with a more manufacturable design.

The higher sensitivity to the voltage design variable compared to the density design variables can be seen as the overall volume of the design keeps changing. Still, the impact on the objective temperature is lower than 1% of its value. In particular, for the volume unconstrained and unfiltered models, there is an increase in the volume of disconnected areas in the latter iterations of the optimizer. Furthermore, the convergence to lower design volumes without volume constraints due to the search for low thermal conductivity reduces the semiconductor material we need to use in these designs. We can see that while we converge to lower volumes for stress-constrained optimisations, this does not lead to worse objective performance. In all cases, the lower volume is compensated by a higher voltage gradient across the thermocouple, leading to multiple local minima present, dependent on this design variable. The intermediate densities are also considered adverse for the objective, as the design obtained by only using the Helmholtz filter increases its value compared to the other stress-constrained designs. Regarding convergence, we show the first 100 MMA iterations, enough to provide convergence for all objective functions. However, in the case of the Heaviside filtered optimizations, the lower bounds for the MMA parameters, lead to larger movements of the density design variables when we reach the maximum iteration value.

3.4.2. 3D results

The 3D model dimensions are the same as those of the 2D model. However, we extend the design space outside the contact area. The parameters of the model's yz plane are shown in Figure 3.6. The square cross section across z is of 0.5 mm with a symmetry condition is at $z = 0$. Given this symmetry condition, we use a power constraint of 7.5 mW. l_1 =0.2 mm and l_2 =0.05 mm delineate the extra design space along the third dimension. Each semiconductor leg is meshed with a $24 \times 24 \times 13$ and regular grid, with a total of 7488 serendipity 20-node elements (H20) per leg.

We perform two 3D optimizations without air modelling between pellets to reduce DOFs, including a thermal conductivity of κ_v =0.033 W/(Km) . Each optimization is run with either no volume constraint or 40% volume constraint. Both optimizations use Helmholtz and Heaviside filters. The same power and stress constraints, filtering,

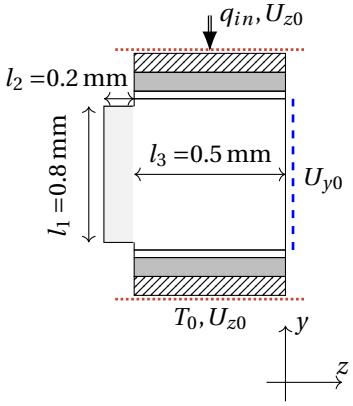

Figure 3.6.: 3D thermocouple FEM model modifications to Figure 3.1. The figure shows the lateral view of Figure 3.1 for a 3D TO model with an increase in material along the z direction and a symmetry boundary condition for the mechanical DOFs.

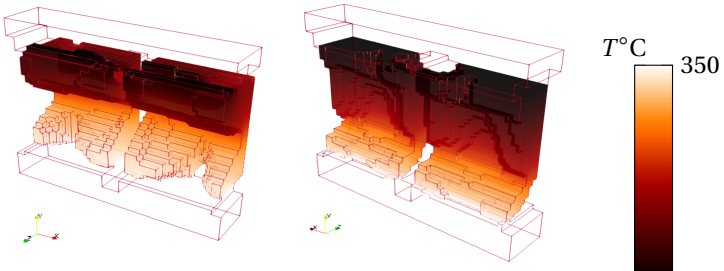

(a) (b)

Figure 3.7.: Results of a 3D TO of a thermocouple with stress constraints using no volume constraint Figure 3.7a or a volume constraint of 40% of the original volume Figure 3.7b. We plot the topology results either for convergence conditions or the 150^{th} iteration. The figure shows the resulting elements with more than 10% density in the design domain and the axis system for each figure. The colour plot shows the temperature gradient of the semiconductor material.

density and voltage design variables and limits, and MMA parameters as in the 2D optimizations are applied, as summarized in Table 1. The filtering parameters are $\mu = 0.4$, $\beta = 64$, an initial semiconductor density of 0.4, and MMA moving limits of 2%.

We show the physical density design variables with values $\mathbf{x}_\rho > 0.1$ for an optimization of the 3D geometry following the values in Table 3.1, using the Helmholtz and Heaviside filter in Figure 3.7, and the MMA parameters are those used for the results in Figure 3.2h. This plot includes the non-semiconductor materials as a transparent volume and the semiconductor material as a colour plot representing its temperature. The two results represent an optimized design with no volume constraint in Figure 3.7a and an optimized design with a volume constraint of 40% in Figure 3.7b. These plots lead to a quasi-symmetrical design for both pellets. As with the 2D results, the mechanical stress constraint dominates the problem. The volume-constrained model leads to a *tuning fork* or *U*-shaped geometry featuring a central contact line along x on the heat sink surface aligned with the middle of the z axis. This central contact then branches into two separate contacts located at the edges in z of the heat injection surface. The unconstrained volume optimization leads to a structure with larger changes along the x axis and a rhomboid hole in the yz plane cross-section. turning around the y axis. In both cases, the resulting topology accommodates the deformations with a topology focused on the yz cross-section.

The convergence history is plotted in Figure 3.8 for the temperature and volume. The volume constrained optimization has found a 35% original volume design compared to the original design with temperature objectives with less that 0.1 °C difference with a voltage up to 4 times higher than in the volume unconstrained optimization. This indicates the presence of non-convex local minima dependent on the voltage that can be reached through the volume constraint.We can further compare the 2D and 3D results by extruding the 2D design into the third dimension (i. e., 2.5D) to the equivalent 3D dimension. The equivalent final volumes of the optimized designs in the 3D configuration are lower than in the 2.5D case. The 3D model also provides a lower optimized temperature of 326 K compared to the 334 K obtained by the 2.5D design, given its larger design space freedom.

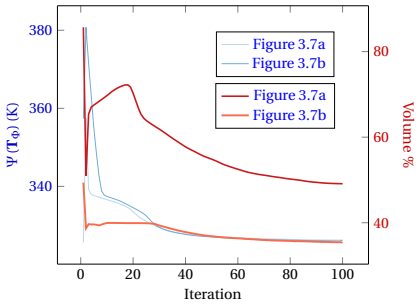

Figure 3.8.: Temperature objective in blue and volume percentage in reds for both results in Figure 3.7 along each iteration of the optimizer.

3.5. Summmary and conclusions

This paper deals with the thermo-electro-mechanical optimization of thermocouples. We do so by linearizing and decoupling the mechanical and thermoelectric DOFs. This approach reduces the memory required to solve the thermo-electro-mechanical problem and is valid for problems with small thermal deformations. As a result, this approach can provide designs that minimize stress concentrations and increase their expected lifetime for thermoelectrical devices.

In the model proposed, we consider a single pellet, and the resulting TEC could be built, making all pellets follow it. However, in reality, some effects are not taken into account when we model the entire device. In particular, the edges and inner regions of the TEC will not absorb the same amounts of heat. This could be considered through homogenization techniques, where each thermocouple can be a unit cell of the final design. The optimization could also incorporate the orientation, location, and number of thermocouples. However, the use of homogenization may increase the number of FEM solves. Neglecting Joule heating in the device can convert the nonlinear thermoelectric equations into a linear system without needing a Newton-Raphson solver for temperature-constant material properties [52]. If these simplifications are taken, the optima found must be post-processed to verify their accuracy compared to the nonlinear models. Future studies could also be conducted on the effect of the overall dimensions of the initial thermocouple design and surrounding materials to optimize the design further. This could also involve the integration of the optimization procedure with boundary-dependent radiation thermal loads, as these are shown by Bjørk *et al.* [38] to have a significant contribution to their efficiency, the larger the internal spacing between thermoelectric legs. Onodera and Yamada [53] already show a methodology to integrate these loads in thermomechanical level-set TO problems, and a simple boundary identification algorithm could also be adapted to environment radiation loading [54].

Even with our simplifying assumptions, the optimizations led to multiple optima with similar objective values and different geometries. This seems to be related to the use of the voltage as a design variable, allowing further flexibility in the design space. However, this flexibility over the electric working point can flatten the design space, hindering convergence. Although the volume constraint can steer the algorithm towards a new solution, this is not ideal as, we do not know the optimized volume for a given working point. Techniques for exploring the overall design space, such as genetic algorithms, could be helpful in understanding the location of these multiple minimum values. Deflation, relaxation, or preconditioning techniques could be used to find other minima [55]. Furthermore, the effect of penalization coefficients on the material properties and their relative ranges has already been shown to affect the overall nonconvexity and the convergence of the problem objective and constraints. In the past, heuristic algorithms have been used to study the effects of optimization parameters [56]. However, heuristics are computationally expensive and must be applied to each problem studied separately. While analytical models help understand the physics behind the problem, techniques to evaluate the fitness of an objective or constraint in higher dimensionality should be explored. New high-dimensionality

projection techniques could be used for this purpose, allowing the selection between different initial parameter values [57].

We also see the need for a length scale filter to avoid single-element features in thermo-electro-mechanical optimizations and to decouple the solution from the mesh resolution in problems involving material nonlinearities. We find that the Helmholtz filter can introduce this length scale. Still, a Heaviside filtering is also needed to provide a sharp design and avoid the intermediate densities from the Helmholtz filter that provides worse optimized objective values. Convergence to lower objectives is also achieved without the need to reinitialize the optimization to gradually increase the filter sharpness. We find that a $\mu \geq 64$ is enough provide a black and white design with minimal grey regions in the thermo-electro-mechanical optimization problem. Zhou *et al.* [58] provides an alternative approach to introduce a length scale function based on constraints on the filtered fields that could also improve the problem solution without introduction of grey regions. We notice as well the tendency of the pure thermoelectrical TO with air losses to remove grey elements, which itself could act as a filter to provide sharp edges geometries with the cost of a single thermoelectrical calculation per MMA iteration for different problems. Different constraints could also be implemented to prevent small features. In particular, the current flow seems attractive for this purpose. Smaller feature sizes lead to higher electrical resistance and smaller current flows through these features. Constraints over the current flow or the resistance it sees could remove these small features from the optimized designs. Furthermore, the imposed constraints do not limit the possibility of dangerous or fatal situations during dynamic situations regarding current flow concentrations or thermal shocks, which should be considered.

The use of stress constraints, while reducing stresses within the assembly that elongate the device's lifespan, further increases the complexity of the problem. Note that we use no contact formulation, and the small size of these devices and the more flexible designs can lead to short circuits that must be avoided. This could be considered a displacement constraint in our optimization or the addition of material between the legs in our model. To simplify the problem formulation further, we could also consider only the most critical solder regions as defined in Awrejcewicz *et al.* [59]. Another further simplification could be reducing the design space of the mechanical constraints to a single pellet, given the dominance of the stress constraint over the thermoelectric variables. This would require special mesh preconditioning between both pellets and mirroring the sensitivities to each pellet.

In summary, we propose a TO approach that uses stress constraints in thermoelectrical problems for cooling applications. Although the proposed formulation can lower stress concentration measurements – up to 5 times lower compared to regular thermoelectrical optimization in the proposed examples – the non-convexity problem still leads to challenges in finding local minima. Furthermore, manufacturing the optimized thermocouples should still be studied and further implemented in the optimization process.

References

[1] A. Goswami and S. Kanetkar. “Thermoelectrics in cryogenic cooling”. In: *2020 IEEE 22nd Electronics Packaging Technology Conference, EPTC 2020* (2020), pp. 355–358. DOI: 10.1109/EPTC50525.2020.9315047.

[2] W. Y. Chen, X. L. Shi, J. Zou, and Z. G. Chen. “Thermoelectric coolers for on-chip thermal management: Materials, design, and optimization”. In: *Materials Science and Engineering R: Reports* 151.July (2022), p. 100700. ISSN: 0927796X. DOI: 10.1016/j.mser.2022.100700. URL: https://doi.org/10.1016/j.mser.2022.100700.

[3] P. Gupta, A. Tanwar, X. He, K. Gradkowski, K. M. Razeeb, P. E. Morrissey, and P. O. Brien. “Substrate integrated micro-thermoelectric coolers in glass substrate for next-generation photonic packages”. In: *Journal of Optical Microsystems* 4.1 (2024), pp. 1–18. DOI: 10.1117/1.JOM.4.1.011006.

[4] W. Zhang, L. Shen, Y. Yang, and H. Chen. “Thermal management for a micro semiconductor laser based on thermoelectric cooling”. In: *Applied Thermal Engineering* 90 (2015), pp. 664–673. ISSN: 13594311. DOI: 10.1016/j.applthermaleng.2015.07.027. URL: http://dx.doi.org/10.1016/j.applthermaleng.2015.07.027.

[5] S. H. Zaferani, M. W. Sams, R. Ghomashchi, and Z. G. Chen. “Thermoelectric coolers as thermal management systems for medical applications: Design, optimization, and advancement”. In: *Nano Energy* 90.PA (2021), p. 106572. ISSN: 22112855. DOI: 10.1016/j.nanoen.2021.106572. URL: https://doi.org/10.1016/j.nanoen.2021.106572.

[6] V. K. Singh, S. S. Sisodia, A. Patel, T. Shah, P. Das, R. N. Patel, and R. R. Bhavsar. “Thermoelectric cooler (TEC) based thermal control system for space applications: Numerical study”. In: *Applied Thermal Engineering* 224.June 2022 (2023), p. 120101. ISSN: 13594311. DOI: 10.1016/j.applthermaleng.2023.120101. URL: https://doi.org/10.1016/j.applthermaleng.2023.120101.

[7] M. Duan, H. Sun, B. Lin, and Y. Wu. “Evaluation on the applicability of thermoelectric air cooling systems for buildings with thermoelectric material optimization”. In: *Energy* 221 (2021), p. 119723. ISSN: 03605442. DOI: 10.1016/j.energy.2020.119723. URL: https://doi.org/10.1016/j.energy.2020.119723.

[8] M. M. R. Al-Fartoos, A. Roy, T. K. Mallick, and A. A. Tahir. “Advancing Thermoelectric Materials: A Comprehensive Review Exploring the Significance of One-Dimensional Nano Structuring”. In: *Nanomaterials* 13.13 (2023). ISSN: 20794991. DOI: 10.3390/nano13132011.

[9] A. Fabián-Mijangos, G. Min, and J. Alvarez-Quintana. “Enhanced performance thermoelectric module having asymmetrical legs”. In: *Energy Conversion and Management* 148 (2017), pp. 1372–1381. ISSN: 01968904. DOI: 10.1016/j.enconman.2017.06.087.

[10] W. Sun, P. Wen, S. Zhu, and P. Zhai. “Geometrical Optimization of Segmented Thermoelectric Generators (TEGs) Based on Neural Network and Multi-Objective Genetic Algorithm”. In: *Energies* 17.9 (2024). ISSN: 1996-1073. DOI: 10.3390/en17092094. URL: https://www.mdpi.com/1996-1073/17/9/2094.

[11] A. Takezawa and M. Kitamura. “Geometrical design of thermoelectric generators based on topology optimization”. In: *International Journal for Numerical Methods in Engineering* February (2012), pp. 1102–1119. DOI: 10.1002/nme.3375.

[12] X. Xu, Y. Wu, L. Zuo, and S. Chen. “Multimaterial topology optimization of thermoelectric generators”. In: *Proceedings of the ASME Design Engineering Technical Conference* 2A-2019.September 2021 (2019). DOI: 10.1115/DETC2019-97934.

[13] S. Soprani, J. H. Haertel, B. S. Lazarov, O. Sigmund, and K. Engelbrecht. “A design approach for integrating thermoelectric devices using topology optimization”. In: *Applied Energy* 176.June (2016), pp. 49–64. ISSN: 03062619. DOI: 10.1016/j.apenergy.2016.05.024.

[14] C. Lundgaard and O. Sigmund. “A density-based topology optimization methodology for thermoelectric energy conversion problems”. In: *Structural and Multidisciplinary Optimization* 57.4 (2018), pp. 1427–1442. ISSN: 16151488. DOI: 10.1007/s00158-018-1919-1.

[15] S. Leblanc, S. K. Yee, M. L. Scullin, C. Dames, and K. E. Goodson. “Material and manufacturing cost considerations for thermoelectrics”. In: *Renewable and Sustainable Energy Reviews* 32 (2014), pp. 313–327. ISSN: 13640321. DOI: 10.1016/j.rser.2013.12.030. URL: http://dx.doi.org/10.1016/j.rser.2013.12.030.

[16] R. Merienne, J. Lynn, E. McSweeney, and S. M. O’Shaughnessy. “Thermal cycling of thermoelectric generators: The effect of heating rate”. In: *Applied Energy* 237.August 2018 (2019), pp. 671–681. ISSN: 03062619. DOI: 10.1016/j.apenergy.2019.01.041.

[17] N. P. Williams, J. Power, D. Trimble, and S. M. O’Shaughnessy. “An experimental evaluation of thermoelectric generator performance under cyclic heating regimes”. In: *Heat and Mass Transfer/Waerme- und Stoffuebertragung* (2022). ISSN: 14321181. DOI: 10.1007/s00231-022-03280-5. URL: https://doi.org/10.1007/s00231-022-03280-5.

[18] P. Wang, J. E. Li, B. L. Wang, T. Shimada, H. Hirakata, and C. Zhang. “Lifetime prediction of thermoelectric devices under thermal cycling”. In: *Journal of Power Sources* 437.June (2019). ISSN: 03787753. DOI: 10.1016/j.jpowsour.2019.226861.

[19] T. Gong, Y. Wu, L. Gao, L. Zhang, J. Li, and T. Ming. “Thermo-mechanical analysis on a compact thermoelectric cooler”. In: *Energy* 172 (2019), pp. 1211–1224. ISSN: 03605442. DOI: 10.1016/j.energy.2019.02.014. URL: https://doi.org/10.1016/j.energy.2019.02.014.

[20] S. Fan, A. Rezania, and Y. Gao. “Thermal-electric and stress analysis of thermoelectric coolers under continuous pulse input current”. In: *Applied Thermal Engineering* 214.June (2022), p. 118910. ISSN: 13594311. DOI: 10.1016/j.applthermaleng.2022.118910. URL: https://doi.org/10.1016/j.applthermaleng.2022.118910.

[21] U. Erturun, K. Erermis, and K. Mossi. “Influence of leg sizing and spacing on power generation and thermal stresses of thermoelectric devices”. In: *Applied Energy* 159 (2015), pp. 19–27. ISSN: 03062619. DOI: 10.1016/j.apenergy.2015.08.112. URL: http://dx.doi.org/10.1016/j.apenergy.2015.08.112.

[22] J. Zhang, H. Zhao, B. Feng, X. Song, X. Zhang, and R. Zhang. “Numerical simulations and optimized design on the performance and thermal stress of a thermoelectric cooler”. In: *International Journal of Refrigeration* 146.October 2022 (2023), pp. 314–326. ISSN: 01407007. DOI: 10.1016/j.ijrefrig.2022.11.010. URL: https://doi.org/10.1016/j.ijrefrig.2022.11.010.

[23] E. Suhir and A. Shakouri. “Predicted thermal stress in a multileg thermoelectric module (TEM) design”. In: *Journal of Applied Mechanics, Transactions ASME* 80.2 (2013). ISSN: 00218936. DOI: 10.1115/1.4007524.

[24] S. Liu, M. Chen, C. Fu, and T. Zhu. “The Interplay of Magnetism and Thermoelectricity: A Review”. In: *Advanced Physics Research* 2.9 (2023). ISSN: 2751-1200. DOI: 10.1002/apxr.202300015.

[25] A. S. Al-Merbati, B. S. Yilbas, and A. Z. Sahin. “Thermodynamics and thermal stress analysis of thermoelectric power generator: Influence of pin geometry on device performance”. In: *Applied Thermal Engineering* 50.1 (2013), pp. 683–692. ISSN: 13594311. DOI: 10.1016/j.applthermaleng.2012.07.021. URL: http://dx.doi.org/10.1016/j.applthermaleng.2012.07.021.

[26] T. Lu, Y. Li, J. Zhang, P. Ning, and P. Niu. “Cooling and mechanical performance analysis of a trapezoidal thermoelectric cooler with variable cross-section”. In: *Energies* 13.22 (2020). ISSN: 19961073. DOI: 10.3390/en13226070.

[27] R. J. Yang and C. J. Chen. “Stress-based topology optimization”. In: *Structural Optimization* 12.2-3 (1996), pp. 98–105. ISSN: 09344373. DOI: 10.1007/BF01196941.

[28] A. Verbart. *Topology Optimization With Stress Constraints*. 2015. DOI: 10.13140/RG.2.1.3422.0880.

[29] J. Yvonnet and D. Da. “Topology Optimization to Fracture Resistance: A Review and Recent Developments”. In: *Archives of Computational Methods in Engineering* 0123456789 (2024). ISSN: 18861784. DOI: 10.1007/s11831-023-10044-9. URL: https://doi.org/10.1007/s11831-023-10044-9.

[30] A. Verbart, M. Langelaar, and F. van Keulen. “A unified aggregation and relaxation approach for stress-constrained topology optimization”. In: *Structural and Multidisciplinary Optimization* 55.2 (2017), pp. 663–679. ISSN: 16151488. DOI: 10.1007/s00158-016-1524-0.

[31] Q. Meng, B. Xu, C. Wang, and L. Zhao. “Thermo-elastic topology optimization with stress and temperature constraints”. In: *International Journal for Numerical Methods in Engineering* 122.12 (2021), pp. 2919–2944. ISSN: 10970207. DOI: 10.1002/nme.6646.

[32] J. Mativo, K. Hallinan, U. George, G. Reich, and R. Steininger. “Topology optimized thermoelectric generator: A parametric study”. In: *Energy Harvesting and Systems* 7.2 (2020), pp. 33–53. ISSN: 23298766. DOI: 10.1515/ehs-2021-0002.

[33] K. Furuta, K. Izui, K. Yaji, T. Yamada, and S. Nishiwaki. “Level set-based topology optimization for the design of a peltier effect thermoelectric actuator”. In: *Structural and Multidisciplinary Optimization* 55.5 (2017), pp. 1671–1683. ISSN: 16151488. DOI: 10.1007/s00158-016-1609-9.

[34] J. Xing, M. Wu, X. Chen, and J. Zhan. “Topology optimization design for voltage enhancement in variable structure double-layer flexible thermoelectric devices”. In: *Applied Mathematical Modelling* 136 (2024), p. 115646. ISSN: 0307-904X. DOI: https://doi.org/10.1016/j.apm.2024.115646. URL: https://www.sciencedirect.com/science/article/pii/S0307904X24003937.

[35] J. L. Pérez-Aparicio, P. Moreno-Navarro, and J. J. Gómez-Hernández. “Weighted sum optimization for combined thermoelectric geometry and electric pulse using finite elements”. In: *Applied Thermal Engineering* 236 (2024), p. 121599. ISSN: 1359-4311. DOI: 10.1016/j.applthermaleng.2023.121599. URL: https://www.sciencedirect.com/science/article/pii/S1359431123016289.

[36] W.-H. Chen, C.-M. Wang, D.-S. Lee, E. E. Kwon, V. Ashokkumar, and A. B. Culaba. “Optimization design by evolutionary computation for minimizing thermal stress of a thermoelectric generator with varied numbers of square pin fins”. In: *Applied Energy* 314 (2022), p. 118995. ISSN: 0306-2619. DOI: 10.1016/j.apenergy.2022.118995. URL: https://www.sciencedirect.com/science/article/pii/S0306261922004044.

[37] C. Maduabuchi. “Thermo-mechanical optimization of thermoelectric generators using deep learning artificial intelligence algorithms fed with verified finite element simulation data”. In: *Applied Energy* 315 (2022), p. 118943. ISSN: 0306-2619. DOI: 10.1016/j.apenergy.2022.118943. URL: https://www.sciencedirect.com/science/article/pii/S0306261922003622.

[38] R. Bjørk, D. Christensen, D. Eriksen, and N. Pryds. “Analysis of the internal heat losses in a thermoelectric generator”. English. In: *International Journal of Thermal Sciences* 85 (2014), pp. 12–20. ISSN: 1290-0729. DOI: 10.1016/j.ijthermalsci.2014.06.003.

[39] L. Cai, P. Li, Q. Luo, H. Yan, P. Zhai, and P. Gao. “Investigation of thermal radiation effects on thermoelectric module performance by an improved model”. In: *Journal of Power Sources* 477 (2020), p. 228713. ISSN: 0378-7753. DOI: 10.1016/j.jpowsour.2020.228713. URL: https://www.sciencedirect.com/science/article/pii/S037877532031017X.

[40] J. L. Pérez-Aparicio, R. L. Taylor, and D. Gavela. “Finite element analysis of nonlinear fully coupled thermoelectric materials”. In: *Computational Mechanics* 40.1 (2007), pp. 35–45. ISSN: 01787675. DOI: 10.1007/s00466-006-0080-7.

[41] J. L. Pérez-Aparicio, R. Palma, and R. L. Taylor. “Multiphysics and Thermodynamic Formulations for Equilibrium and Non-equilibrium Interactions: Non-linear Finite Elements Applied to Multi-coupled Active Materials”. In: *Archives of Computational Methods in Engineering* 23.3 (Sept. 2016), pp. 535–583. ISSN: 1886-1784. DOI: 10.1007/s11831-015-9149-9. URL: https://doi.org/10.1007/s11831-015-9149-9.

[42] B. S. Lazarov, F. Wang, and O. Sigmund. “Length scale and manufacturability in density-based topology optimization”. In: *Archive of Applied Mechanics* 86.1 (Jan. 2016), pp. 189–218. ISSN: 1432-0681. DOI: 10.1007/s00419-015-1106-4. URL: https://doi.org/10.1007/s00419-015-1106-4.

[43] O. S. B. S. Lazarov. “Filters in topology optimization based on Helmholtz-type differential equation”. In: *International* February (2011), pp. 1102–1119. DOI: 10.1002/nme. URL: http://onlinelibrary.wiley.com/doi/10.1002/nme.3279/full.

[44] M. P. Bendsøe and N. Kikuchi. “Generating optimal topologies in structural design using a homogenization method”. In: *Computer Methods in Applied Mechanics and Engineering* 71.2 (1988), pp. 197–224. ISSN: 00457825. DOI: 10.1016/0045-7825(88)90086-2.

[45] G. I. N. Rozvany, M. Zhou, and T. Birker. “Generalized shape optimization without homogenization”. In: *Structural optimization* 4.3 (Sept. 1992), pp. 250–252. ISSN: 1615-1488. DOI: 10.1007/BF01742754. URL: https://doi.org/10.1007/BF01742754.

[46] I. T. Witting, T. C. Chasapis, F. Ricci, M. Peters, N. A. Heinz, G. Hautier, and G. J. Snyder. “The Thermoelectric Properties of Bismuth Telluride”. In: *Advanced Electronic Materials* 5.6 (2019), pp. 1–20. ISSN: 2199160X. DOI: 10.1002/aelm.201800904.

[47] E. Fernández, M. Collet, P. Alarcón, S. Bauduin, and P. Duysinx. “An aggregation strategy of maximum size constraints in density-based topology optimization”. In: *Structural and Multidisciplinary Optimization* 60.5 (Nov. 2019), pp. 2113–2130. ISSN: 1615-1488. DOI: 10.1007/s00158-019-02313-8. URL: https://doi.org/10.1007/s00158-019-02313-8.

[48] K. Svanberg. “MMA and GCMMA – two methods for nonlinear optimization”. In: 2014. URL: https://api.semanticscholar.org/CorpusID:211105912.

[49] K. Svanberg. “The method of moving asymptotes—a new method for structural optimization”. In: *International Journal for Numerical Methods in Engineering* 24.2 (1987), pp. 359–373. ISSN: 10970207. DOI: 10.1002/nme.1620240207.

[50] R. Sharma. *A stress recovery procedure for 3-D linear finite elements*. 2016, pp. 1–86. URL: http://repository.tudelft.nl/islandora/object/uuid%7B%5C%%7D3A97557770-5fc6-4930-b0d5-7476e2d0e050?collection=education.

[51] G. Reales Gutiérrez, F. v. Keulen, J. F. L. Goosen, A. M. Aragón, and A. Bornheim. “Enhancing the cooling performance of thermocouples: a power-constrained topology optimization procedure”. In: *Structural and Multidisciplinary Optimization* 67.11 (Nov. 2024), p. 189. ISSN: 1615-1488. DOI: 10.1007/s00158-024-03897-6. URL: https://doi.org/10.1007/s00158-024-03897-6.

[52] O. A. Fragoso, F. A. S. Orosco, J. A. González, and L. Georgiy. “Linear theory of the thermoelectric cooling based on the peltier effect”. In: *2nd International Conference on Electrical and Electronics Engineering, ICEEE and XI Conference on Electrical Engineering, CIE 2005* 2005.Cie (2005), pp. 235–238. DOI: 10.1109/ICEEE.2005.1529616.

[53] S. Onodera and T. Yamada. “Topology optimization for coupled thermomechanical problems with approximated thermal radiation boundary conditions depending on design variables”. In: *Applied Mathematical Modelling* 142 (2025), p. 115959. DOI: 10.1016/j.apm.2025.115959. URL: https://doi.org/10.1016/j.apm.2025.115959.

[54] O. Ibhadode, Z. Zhang, P. Rahnama, and P. et al. “Topology optimization of structures under design-dependent pressure loads by a boundary identification-load evolution (BILE) model”. In: *Structural and Multidisciplinary Optimization* 62 (Oct. 2020), pp. 1865–1883. DOI: 10.1007/s00158-020-02582-8. URL: https://doi.org/10.1007/s00158-020-02582-8.

[55] P. E. Farrell, Á. Birkisson, and S. W. Funke. “Deflation Techniques for Finding Distinct Solutions of Nonlinear Partial Differential Equations”. In: *SIAM Journal on Scientific Computing* 37.4 (2015), A2026–A2045. DOI: 10.1137/140984798. eprint: https://doi.org/10.1137/140984798. URL: https://doi.org/10.1137/140984798.

[56] A. Ait Ouchaoui, M. Nassraoui, and B. Radi. “Numerical investigation of the effect of topology optimisation methods parameters in the topology quality, the strength, and the computational cost”. In: *Archives of Materials Science and Engineering* 123.2 (2023), pp. 55–71. ISSN: 18972764. DOI: 10.5604/01.3001.0054.2492.

[57] M. Espadoto, F. C. Rodrigues, N. S. Hirata, and A. C. Telea. “Visualizing High-Dimensional Functions with Dense Maps”. In: *SN Computer Science* 4.3 (2023), pp. 1–18. ISSN: 26618907. DOI: 10.1007/s42979-022-01664-2. URL: https://doi.org/10.1007/s42979-022-01664-2.

[58] M. Zhou, B. S. Lazarov, F. Wang, and O. Sigmund. “Minimum length scale in topology optimization by geometric constraints”. In: *Computer Methods in Applied Mechanics and Engineering* 293 (2015), pp. 266–282. ISSN: 0045-7825. DOI: https://doi.org/10.1016/j.cma.2015.05.003. URL: https://www.sciencedirect.com/science/article/pii/S0045782515001693.

[59] J. Awrejcewicz, S. P. Pavlov, A. V. Krysko, M. V. Zhigalov, K. S. Bodyagina, and V. A. Krysko. “Decreasing shear stresses of the solder joints for mechanical and thermal loads by topological optimization”. In: *Materials* 13.8 (2020). ISSN: 19961944. DOI: 10.3390/MA13081862.

4

Multi-objective scintillator shape optimization for increased photodetector light collection

Inorganic scintillators often use exotic, expensive materials to increase their light yield. Although material chemistry is a valid way to increase the light collection, these methods are expensive and limited to the material properties. As such, alternative methods such as the use of specific reflective coatings and crystal optical shapes are critical for the scintillator crystal design procedure. In this paper, we explore the modelling of a scintillator and SiPM (silicon-photomultiplier) assembly detector using GEANT4. GEANT4, an open-source software for particle-matter interaction based on ray-tracing, allows the modelling of a scintillator-based detector while offering methods to simplify and study the computational requirements for a precise calculation of the light collection. These studies incorporate two different geometries compatible with the BTL (barrel timing layer) particle detector that is being built for the CMS (Compact Muon Solenoid) experiment at CERN. Furthermore, the geometry of our model is parameterized using splines for smoother results and meshed using GMSH to perform genetic numerical optimization on the crystal shape through genetic algorithms, in particular NSGAII (non-dominated sorting genetic algorithm II). Using NSGAII, we provide a series of optimized scintillator geometries and study the trade-offs of multiple possible objective functions, including the light output, light collection, and light collection per energy deposited and track path length. The converged Pareto results according to the hypervolume indicator are compared to the original simplified design, and a recommendation towards the use of the light collection per energy deposition and track path length is given based on the results. The results provide increases in this objective of up to 18% for a constant volume for a geometry compatible with the current design of the BTL detector.

This chapter has been published in the JSON B journal, 41 (2024) [1].

4.1. Introduction

Scintillation materials can absorb energy from ionising radiation and convert it to visible light, making them useful for detecting and measuring radiation in a variety of applications. Scintillator crystals are commonly used in the medical sector [2], radiation safety, and high-energy physics research, among other fields [3, 4]. As components of medical imaging technologies – e.g. positron-emission-tomography (PET) or single-photon-emission-computed-tomography (SPECT) [5] – they are a key material for obtaining high resolution of the body's anatomy and function, allowing for early detection of diseases such as cancer or cardiovascular diseases [6]. Furthermore, in high-energy physics research, scintillator crystals play a key role in the study of fundamental particles and the nature of matter and energy [7]. Lastly, as radiation detectors used in the security sector, they help to monitor the use of radioactive material e. g., in airports, nuclear power plants, and other critical infrastructures [8, 9].

In spite of their importance to the aforementioned industry, solid inorganic scintillation materials are often prohibitively expensive. In particular, LYSO:Ce crystals cost up to $4000/kg, constituting more than 50% of the total production cost for scintillator crystals [10]. The factors that contribute to this high cost are the rare materials used – often these crystals require scarce resources, such as rare earths (e.g. caesium or thallium) – the required manufacturing methods, such as crystal pulling or vapour transport, and specialized tooling and machinery. There is a trend to mitigate these costs by searching for cheap organic and polymeric scintillator materials and new manufacturing techniques. Pla-Dalmau, Bross, and Mellott [11] already shows how the extrusion technique applied to plastic scintillators reduces the cost from $40/kg to the order of $7/kg compared to other techniques.

Even if the future of organic scintillators is promising, plastic materials do not comply with the radiation hardness, high density, and light yield (L_Y) – photons created per energy deposited by ionizing sources – required for their use in high-energy physics experiments, leading to the use of expensive inorganic scintillation crystals [12–14]. The need for inorganic crystals makes their design critical, including their optical coupling materials, assembly to the photodetector, and the crystal geometry to increase the light collection with the lowest amount of material possible, which is directly proportional to the crystal cost. The usual high refractive index of scintillators, such as CsI(Tl) or BaF_2, their surface finish or reflective coatings, can help reflect and redirect light towards the attached photodetector, increasing the overall light collection and the signal-to-noise ratio of the detected signal [15]. However, experimentally testing the light collection of multiple shapes is time-consuming and expensive.

The complexity of the scintillation crystal design and optimization can be seen in the literature, with various optimization examples that include their chemical and design criteria. We can find examples of chemical optimization in Khodyuk *et al.* [16], which provides a combinatorial algorithm to predict the light yield of the crystals depending on the composition of the material. In Berg, Roncali, and Cherry [17], we can find an example of the effect of the surface finish of the crystals on their light collection. This study shows, through simulation and experimentation,

that samples with rougher surfaces can improve light collection. The shape of different crystals can also affect the efficiency of the system. Danevich *et al.* [18] experimentally show that a hexagonal crystal improves the energy resolution compared to a cylindrical shape. Knowing that the shape of these crystals affects their timing and light collection, Min *et al.* [19] perform a parameter study of the thicknesses of the crystals with good correlation with the experimental results and Li *et al.* [20] introduce a first sizing optimization using genetic algorithms for the optimization of three design parameters through the Monte Carlo N-Particle software (MCNP, [21]). Direct experimental testing on multiple shapes of inorganic scintillation crystals is tested in Xie *et al.* [15] without any reflective coatings. The results of the experiments showed a higher precision for the tetrahedral shapes compared to those of the other geometries studied. Zhao *et al.* [22] study the coupling shape between SiPM (silicon-photomultiplier) and scintillator, where a runway-shaped groove in the contact region could improve the non-uniformity with low light output loss. Although the literature already cited uses numerical models to explain and enhance the light collection of the scintillator crystals, much of the research is focused on time-consuming and costly experimental results.

The use of numerical modelling and optimization can reduce experimental time and cost. However, the procedure to perform these modellings and optimizations is not evident. Particle-matter interaction software based on ray-tracing and Monte Carlo, such as GEANT4 [23], deals with results in the form of stochastic data. This leads to difficulties in the available numerical optimization techniques, with the need for gradient-free optimization [24] techniques to numerically model multiple shapes of scintillation crystals and optimize them for improved light collection measurements. These optimization techniques avoid the need for analytical expressions for the objective derivatives concerning the design variables. These optimizers applied to multi-objective optimization can also help to identify trade-offs between conflicting objectives and are well-suited for near-global searches in complex design spaces, depending on the optimizer selected parameters.

Parameterization and optimization of scintillation crystal surfaces can further enhance their efficiency compared to parametric or size optimization. Shape optimization can reduce the light reabsorption within the crystals and take into account the effect of localized higher-energy depositions with regard to the photodetector interface location. While these materials are not easy to machine, through advances in free-form optical manufacturing [25], and numerical optimization techniques, we should reconsider the way scintillation crystals are designed nowadays. Furthermore, the lack of numerical optimization examples in the literature and the stochastic nature of the problem do not provide a clear design objective for numerical optimization algorithms and methods to calculate them in an efficient manner.

In this paper [1], we propose a simulation model for a scintillation-based particle detector and its sensitivity to manufacturing tolerances. We used the state-of-the-art detector from MTD-BTL (Minimum Ionizing Particle Timing Detector- Barrel Timing Layer, [26]) to be installed at CMS-CERN as a configuration reference for our model. Starting from MTD-BTL, we propose simplification approaches and techniques

for faster computational time using GEANT4, which is required for a feasible numerical optimization due to the large computational time of Monte Carlo studies. This paper further proposes a one-dimensional design space to prove the dependence of the detector light collection on the scintillator shapes and compare optimization formulations. Finally, two base geometries considered for MTD-BTL are parameterized to perform shape optimization on the scintillation crystals. The optimization is performed using the non-dominated sorting genetic algorithm II (NSGA-II, [27]) with photon count and volume objectives to understand the trade-off between the contrasting objectives. The algorithm's convergence is studied through the hypervolume of successive generations of the genetic algorithm, and the configurations with the same volume as the initial designs are post-processed to verify the optimization outputs and provide further understanding of the optimization procedure for future scintillation crystal design.

4.2. Methodology

Accurate scintillation modelling involves the use of specialized particle-matter interaction software to calculate track and the energy deposition of the particles within the crystals and the resulting number of generated photons. One such software is GEANT4 [28], an open-source Monte Carlo ray tracing library implemented in C++, which has been extensively tested in various fields such as medical engineering, research in high-energy physics and radiation protection.

This section starts by describing the definition of the detector geometries studied in this paper within GEANT4, continues with the particle event definition for the detector characterization, and finishes with the parameterization and definition of the optimization algorithm to perform shape optimization on scintillating crystals. Although this section provides the information needed to model the scintillation phenomena, all relevant material properties used in this paper are summarized in Appendix F for clarity purposes.

4.2.1. Geometry

The detector geometry studied in this paper is based on the BTL detector [26], specifically designed for the detection of minimum ionizing particles within the Compact Muon Solenoid (CMS) detector at CERN. The BTL current configuration consists of 16 rectangular LYSO:Ce bars with 32 SiPM channels optically glued to both ends of each bar. Figure 4.1 shows the dimensions and tolerances used in the model, closely based on the BTL detector. The drawing represents the LYSO bars with a length of 57 mm with ±0.1mm for the coating thicknesses. In Figure 4.1, we can also see a cut section with the different layers in the optical connection consisting of an adhesive layer and a protective resin layer before the SiPM, supported in an FR4 package. This bar scintillator configuration covers a continuous cylindrical area of radius 1991 mm. This configuration is designed so that it can be stacked and reduce the dead area, the area where the scintillators cannot provide any sensing capabilities. However, the mechanical components and optical interfaces account for the 9.5% dead area relative to the total cylindrical area of the detector. For

any further improvements and changes in the detector, we need to consider the stackability of the scintillator crystals to ensure that this dead area does not increase.

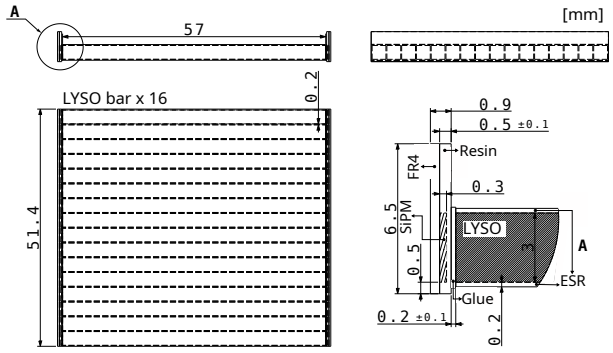

Figure 4.1.: Standard LYSO module schematics for BTL with tolerances used in the GEANT4 model and dimensions in mm.

To maintain this dead area as small as possible, another configuration of interest for the detector is a geometry in which the photodetectors or SiPMs are found in the bottom flat surface of the scintillator. This tile-based configuration can reduce the dead area associated with the SiPM package, maintaining the advantages of the previously described bar configuration. In this geometry, we impose the location of the 2 SiPMs for a single tile along one of its symmetry axes, maintaining the same number of SiPMs and their characteristics to compare to the bar configuration. The sensitive area of each tile must also be comparable to the sensitive area of each scintillator bar in the previous configuration to avoid increasing the total number of channels in the detector. Figure 4.2 shows a lateral view and a cut section for the scintillators in the tile configuration with the respective location of the SiPM.

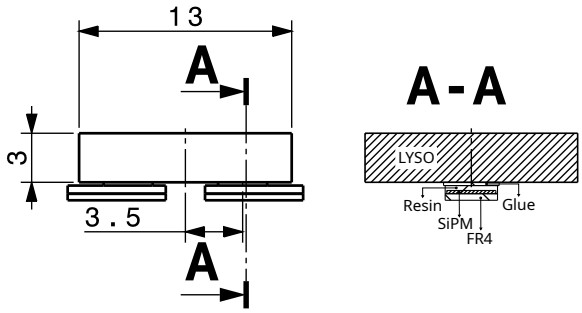

Figure 4.2.: LYSO-SiPM package schematics for BTL tile-configuration with dimensions in mm with a lateral and a cut view.

As the smallest unit of the detector, we focus on these crystal modules for our setup within GEANT4, considering impacts only in a single-crystal sensitive area. The crystal geometry is constructed using a tetrahedral volumetric mesh generated with GMSH [29], and subsequently imported into GEANT4 through the points of each tetrahedral element. Notice that while geometries defined through triangular elements that can be stored in STL format have the advantage of faster loading times in GEANT4, volumetric meshes defined through multiple volumes in the form of tetrahedral elements exhibit computational benefits, particularly when dealing with a large number of events or particle impacts. The resulting lower computational cost of volumetric meshes arises from the reduced cost to determine collision points with the next surface in the model, given a connectivity matrix for the volumetric elements. This is thoroughly tested in Poole *et al.* [30] for complex geometries.

4.2.2. Event definition

To start a particle-matter interaction simulation within GEANT4, we need to define the event interaction that we are going to study. This simulation setup involves defining high-energy particles in a trajectory that impacts our material of interest. For this reason, we differentiate between two different particle impacts of interest. To facilitate direct comparisons with experimental results in the laboratory, we model the particles as 511 keV gamma rays emitted from a ^{22}Na source. By simulating these specific gamma rays, which are commonly used for the characterization of BTL crystals in laboratory settings [31], we ensure that our simulation closely aligns with experimental measurements. In addition to ^{22}Na gamma rays, we also provide the option of setting the ionizing particle as muons with an energy of 2 MeV in our simulations. The use of muons aims to emulate a closer operational condition to CMS. Unlike 511 keV gamma rays, which are locally absorbed within the crystal, higher energies of muons enable them to penetrate the crystal and produce a trace of photons as they cross the scintillator.

The location of the particles' impact also impacts the light collection, and for this reason, two testing scenarios for particle impact positions are implemented. To create a realistic testing scenario that captures the effects of the randomized impact location under radiation sources, we apply a random distribution of the particle impact positions along the x and z coordinates within the crystal's longitudinal-sectional area. This allows us to explore how the particle trajectories influence the generation and propagation of photons within the crystal. To simplify the definition, we consider that the particles fly parallel to the y axis, perpendicular to the crystal $x-z$ plane, which ensures the impact and a full exploration of the entire volume of the crystal with enough impacts. We further incorporate the option to run a uniform pattern impact distribution using symmetry conditions on the assembly, which allows us to simulate a representative subset of impact positions efficiently. Uniform impact distribution locations can reduce the number of simulations required to comprehensively evaluate the scintillator response to particle interactions.

We define a total of $n_I = n_x \times n_z$ impact points arranged uniformly on a two-dimensional grid over the x-z plane. The grid consists of n_x points evenly

spaced along the x-axis and n_z points evenly spaced along the z-axis. The crystal surface extends from 0 to X_1 along the x-axis and from 0 to Z_1 along the z-axis, where X_1 and Z_1 represent the half-lengths of the crystal along their respective axes.

To ensure that impact points are not located exactly on the edges of the crystal surface, a minimum margin $l_{\min}$ is enforced from the boundaries. The coordinates of the impact points are then given by

$$\begin{aligned} x_I(i) &= X_1 - l_{\min} - \frac{X_1}{n_x}(i-1) \quad , \quad i \in \{1, ..., n_x\}, \\ z_I(j) &= Z_1 - l_{\min} - \frac{Z_1}{n_z}(j-1) \quad , \quad j \in \{1, ..., n_z\}, \end{aligned} \tag{4.1}$$

where $x_I(i)$ and $z_I(j)$ denote the coordinates of the i-th and j-th points along the x and z axes, respectively. Each impact point coordinate is then defined as

$$P_I(i,j) = \big(x_I(i), z_I(j)\big).$$

This formulation results in a uniform grid of n_I impact points distributed across the crystal surface, with a consistent margin from the edges.

Figure 4.3 shows a schematic of the Monte Carlo impacts in the bottom left quarter of the crystal and an example of the uniform impact distribution for $n_x = 10$ and $n_z = 5$ on the bottom right quarter. Given the symmetry conditions, only one-quarter of the surface needs to be covered by the events. Figure 4.3 also shows the system of reference for the impact definition, the characteristic half-lengths of the geometry Z_1 and X_1 and the minimum lengths with respect to the edges of the geometry as l_{min}.

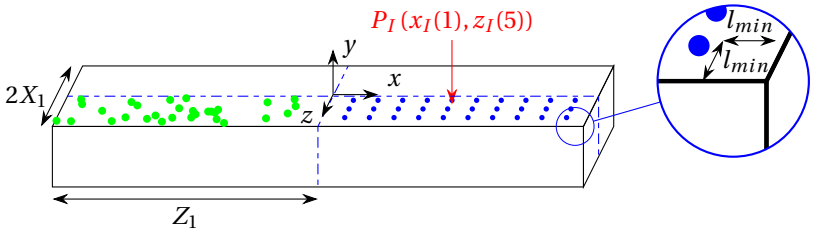

Figure 4.3.: Schematics of a random and uniform pattern of impacts on a crystal represented as green or blue dots respectively within one-quarter of the crystal due to symmetry conditions. The particle is represented by a red arrow showing its perpendicular direction against the top surface of the initial design of the crystals. The symmetry conditions of the crystal are represented as blue dash-dotted lines.

4.2.3. Scintillation

For the model under investigation, we have chosen LYSO:Ce as the scintillator material, with reference to the BTL detector. The selection of LYSO:Ce is motivated

by its widespread use in the industry, its proven radiation hardness, high density, and light yield (L_Y) [26].

To model the scintillation phenomena, we need to calculate the number of photons created within the scintillator (N_γ) in each time step of our ray-tracing algorithm. A Gaussian distribution is used to model the number of photons as,

$$\mu_{N_\gamma} = E \cdot L_Y, \tag{4.2}$$

$$\sigma_{N_\gamma} = r_s \cdot \sqrt{E \cdot L_Y}, \tag{4.3}$$

$$N_\gamma = N(\mu_{N_\gamma}, \sigma_{N_\gamma}), \tag{4.4}$$

In these equations, E represents the energy deposited by an ionizing particle within the crystal during each time step, and r_s represents the resolution scale or possible deviation of the location of the mean value of the distribution. The normal distribution from which we extract N_Y is determined by its standard deviation σ_{N_γ} and mean μ_{N_γ} based on the previously defined L_Y, r_s and E.

While r_s and L_Y are parameters measured experimentally, the mean energy deposited per track length of the impacting particle, $\frac{\partial E}{\partial x}$, is precomputed for the different materials, particles and incident energies and stored in table data [28]. During runtime, $\frac{\partial E}{\partial x}$ values are recovered, interpolated, and used to define the time step size according to an energy loss limit. This energy deposition exhibits stochastic behaviour, following a Landau distribution. The Landau distribution notably leads to tails at large energy-deposition values, caused by possible knock-on electrons turning themselves into ionizing particles, influencing the outcome of the photons detected.

Once the number of photons created is calculated, we need to define their time characteristics. This behaviour can be described by an exponential rise and decay process, i. e.,

$$N_\Gamma(t) = \frac{N_\gamma}{\tau_d - \tau_r}(e^{-\frac{t}{\tau_d}} - e^{-\frac{t}{\tau_r}}), \tag{4.5}$$

where t denotes time, and τ_d and τ_r represent the decay and rise times of the exponential growth and decay of the scintillation process, respectively [32].

The generated photons must also have a given wavelength. This wavelength is calculated through an intensity distribution function from experimental data defined as the spectrum of the scintillator. For our particular LYSO:Ce the spectrum and L_Y measured by Addesa *et al.* [33] and M. Campana and R. Paramatti [34]. These photons propagate through the scintillator, refract, and reflect on the optical surfaces of the detector until they are reabsorbed by the scintillator or arrive at the photodetectors. For the implementation of the scintillation constants and their intensity function within this paper, refer to Appendix F.3.

Although the high refractive index of LYSO:Ce compared to air mitigates the loss of photons to the environment, any escaping photons can create false signals in neighbouring photodetectors. For this reason, it is common practice to coat or cover scintillators with a reflective layer. In our model, we employ an enhanced specular reflector (ESR) that is superimposed on the crystal with an air gap to the LYSO:Ce capitalizing on the substantial refractive index difference between the air-LYSO interface [35], see Appendix F.2. The internal reflections then account for an

optically polished surface for the LYSO-air interface, based on the surface roughness specifications for BTL of $R_a < 15$nm, and a specular reflector for the ESR.

4.2.4. Photon detection

The photons are detected by the SiPMs, which exhibit a photon-detection efficiency (PDE) or probability of detection of the incident photons. These SiPMs are modeled as a silicon block whose PDE depends on the overvoltage (ov), or the voltage across the terminals of the SiPM above its breakdown voltage, and the incident wavelength, λ, given by the expression

$$\text{PDE}(V_{ov}, \lambda) = 0.393(1 - e^{-0.583 V_{ov}}) \cdot F_\lambda(\lambda)\,. \tag{4.6}$$

Although V_{ov} can be modified during operation, we consider a V_{ov} of 3.5 V for comparison purposes in the subsequent simulations. This specific value is utilized in conjunction with the PDE data obtained from the manufacturer's datasheet to scale the function F_λ, see Appendix F.4. This PDE is implemented such that when a photon impacts the SiPM we retrieve a value from a uniform distribution, $U(0,1)$, and the photon is considered detected if this value is higher than its corresponding PDE. The total number of photons detected, or light collection (L_C), can be calculated from each impact and the summation

$$L_C^i = \begin{cases} L_C^{i-1} + 1 & \text{if } u_i \sim U(0,1) > PDE(V_{ov}, \lambda_i) \\ L_C^{i-1} & \text{if } u_i \sim U(0,1) \leq PDE(V_{ov}, \lambda_i) \end{cases}, \tag{4.7}$$

where u_i denotes a value taken from a uniform random distribution, and λ_i represents the wavelength of the impacting photon i. Whether detected or not, all photons that reach the SiPM are subsequently terminated in the next calculation step within GEANT4. This photon-killing procedure simulates their absorption within the SiPM and reduces the computational cost of these traces.

4.2.5. Numerical optimization

Due to the inherently statistical nature of the results obtained from GEANT4, calculating the sensitivities for this problem presents a challenge. As a solution, we turn to the use of genetic algorithms inspired by natural selection, which have demonstrated their effectiveness as heuristic approaches to solve complex problems without the need for exact analytical solutions. In particular, we have chosen to use the Non-dominated Sorting Genetic Algorithm II (NSGA-II, [27]). NSGA-II uses an initial random population of solutions that evolves in successive generations into candidate optimized solutions through crossover, mutation, selection, and non-dominated sorting of each population.

Several indicators assess the quality of populations in multiobjective optimization. Li and Yao [36] surveys various quality indicators, organizing them by the specific aspect of optimization quality they measure. We use the hypervolume indicator [37] which focuses on the convergence of the optimization and the spread of the solution.

This measure is commonly used due to its robustness and practical implementation compared to other indicators. This hypervolume measure can be defined as

$$HV(Q,P_r) = \kappa\left(\bigcup_{q\in Q}\prod_{i=1}^{n_o}[q[i],P_r]\right), \tag{4.8}$$

where κ denotes the Lebesgue measure, Q and q represent a population and each one of its individuals, and n_o is the total number of objective values of each individual. For the calculation of this hypervolume, we need to define a reference point. The selection of this point must be chosen as the nadir point – defined as the worst possible value for all objectives – or the closest approximation to it. In our case, we know the ranges of the volume given the range of the design variables and the light collection, energy deposition, and length paths within the crystal are always higher or equal to zero. Taking this into account, we define the reference point

$$P_r = (H,V) = (0, 4Z_0Y_0l_{max}). \tag{4.9}$$

The hypervolume indicator can be understood as a measure of the area of the Pareto front with respect to this reference point, P_r. Although the hypervolume has limitations due to an increase in the runtime of $O(n_o)$ with each optimization dimension, its sensitivity to any modification in the Pareto front and the fact that it also provides information on the spread of the set make it one of the most common convergence indicators for multiobjective optimizations [38].

Although the hypervolume provides a measure of the change in the ranked population provided by NSGA-II, the randomness inherent in the algorithm does not guarantee that an absence of change in two consecutive generations is indicative of having discovered an optimized design. To address this, the delay parameter n_h compares the hypervolume of the current generation to that of n_h generations prior. The convergence criterion uses this delayed hypervolume normalized by the initial generation's hypervolume, requiring it to fall below a tolerance Tol. This approach reduces the risk of prematurely declaring convergence caused by random fluctuations in the hypervolume, smoothening transient variations and better reflecting when the population quality has stabilized. Nevertheless, this heuristic does not guarantee reaching a global minimum or the true Pareto front. The convergence criteria and the NSGA-II algorithm are represented in Figure 4.4.

Once we have defined the optimization algorithm, we need to provide the design variables and objective functions of the problem. To be able to perform shape optimization on the crystals, we parameterize the shape of the crystal along the $y-z$ cross-section using a series of control points and Catmull-Rom splines. To simplify the definition of control points, we use symmetry conditions along the $x-y$ plane and uniformly distribute control points along the z axis. Figure 4.5a exemplifies this parameterization of the bar-configuration with the original flat design superposed by an optimized design, its splines, and control points. Additionally, we provide one last degree of freedom: the crystals' length or width. To maintain a constant sensitive area in the detector, this degree of freedom is constrained by,

$$Z_1X_1 = Z_0X_0\,, \tag{4.10}$$

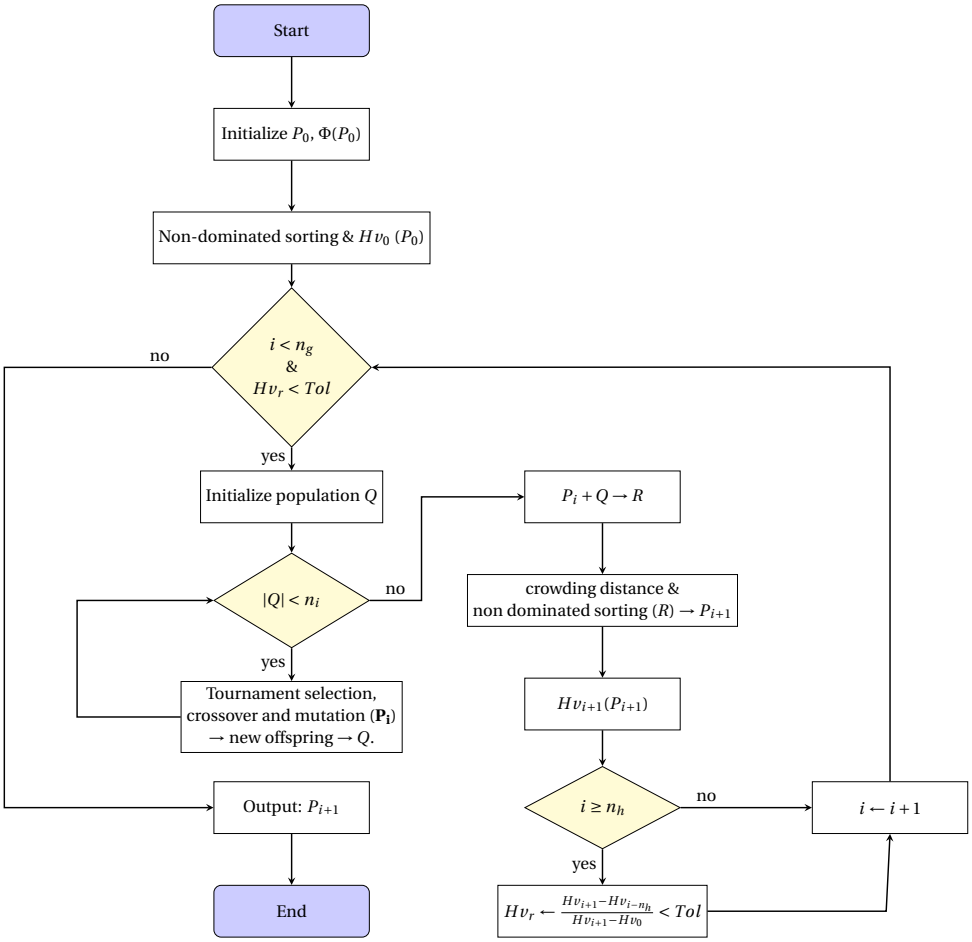

Figure 4.4.: NSGAII formulation flowchart.

where Z_1 and X_1 represent the half-width and half-length, and Z_0 and X_0 are the half-width and half-length of the original configuration. This constraint avoids increasing the number of photodetector channels to cover the same sensitive area as the original detector. The top view of the parameterized crystal shown in Figure 4.5b exemplifies these width and length changes. The SiPM is always maintained at the X_1 location.

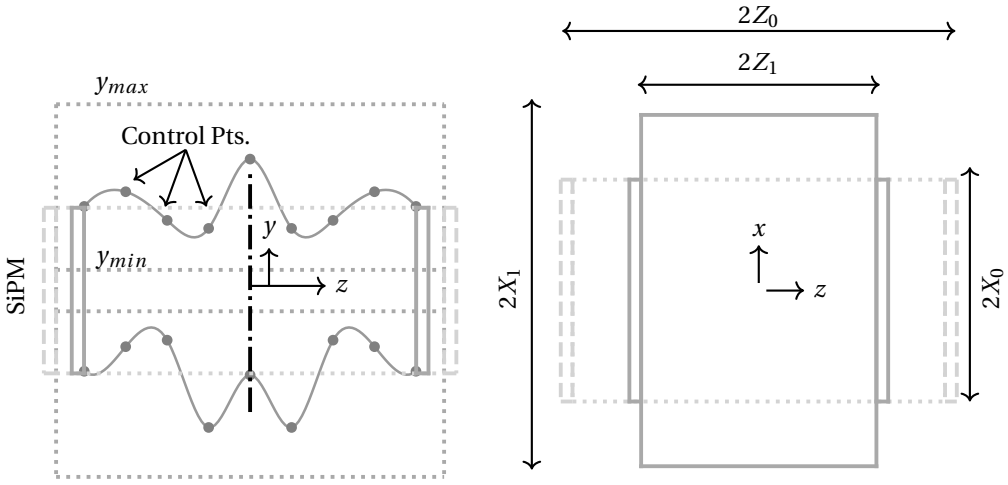

(a) (b)

Figure 4.5.: Lateral and top view of the parameterized bar-shaped crystal. Figure 4.5a shows the $x-y$ plane with control points along z defining the top and bottom surfaces with their maximum and minimum. Figure 4.5b shows the $z-x$ view with changes in width and length according to the constant sensitive area constraint.

Although the splines fully represent the geometry, the mesh must capture its curvature. We recommend a minimum of twice the number of mesh nodes along the splines compared to the number of control points, which should be higher than our number of impacts through the z axis, n_z.

In numerical optimization algorithms, the results are affected by the parameterization of the problem. For this reason, if we want to study a second configuration, we either need to make sure it is attainable with our current parameterization scheme or provide a different one. To study the tile configuration, with the SiPMs in the bottom $x-z$ plane, see Figure 4.2, we parameterize the top $x-z$ plane through nodes along 2 lines in the z direction at locations $x=\{0, X_0\}$. We exemplify this assembly and parameterization in Figure 4.6. The parameterization of this new configuration uses two planes of symmetry along the $z==0$ and $x==0$. This design is no longer possible to extrude, and the bottom surface has a new variable in terms of the location of the SiPMs, the centre of which is imposed in a location z along the

line $x = y = 0$. As we still need to maintain a constant sensitive area for comparison with the original geometry, we define the centre location of the SiPMs with respect to each configuration value Z_1 as

$$c = Z_0 Z_S \, , Z_S \in [0, 1]. \tag{4.11}$$

Equation (4.11) defines the location of the SiPM in z, c, with a new design variable Z_S constrained between a value of 0 and 1.

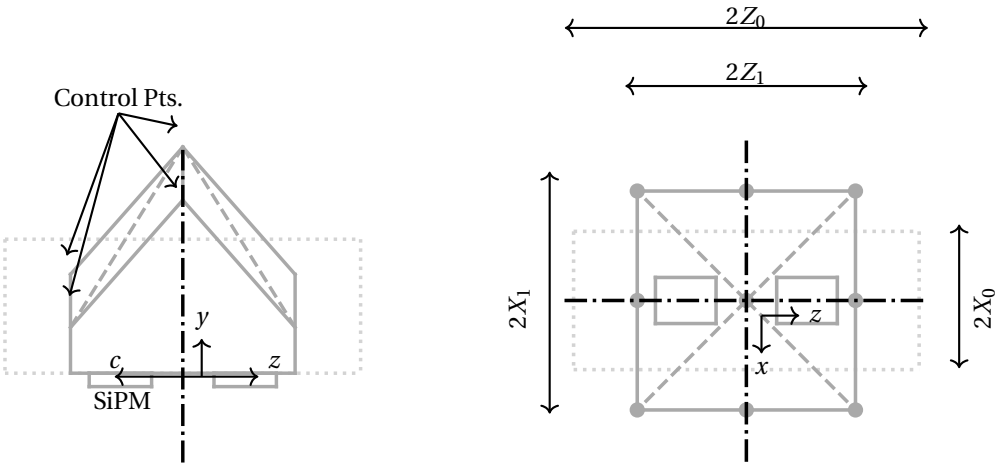

(a) (b)

Figure 4.6.: Lateral and bottom view of the parameterized tile-shaped crystal with 2 nodes per x section. Figure 4.6a shows the $x-y$ plane with control in each vertex. Figure 4.6b shows the $z-x$ view with changes in width and length according to the constant sensitive area constraint.

The optimization formulation for the bar-configuration can then be written as

$$[\Phi, Z_1, Z_s] = \underset{\Phi, V}{\arg\min} \quad \Phi(\boldsymbol{\theta}, Z_1, Z_s) \,\&\, V(\boldsymbol{\theta}, Z_1), \tag{4.12a}$$

$$\text{subject to:} \quad X_1 Z_1 = X_0 Z_0, \tag{4.12b}$$

$$Z_o \in [Z_{min}, Z_{max}], \tag{4.12c}$$

$$\boldsymbol{\theta} \in [y_{min}, y_{max}], \tag{4.12d}$$

$$Z_s \in [zs_{min}, zs_{max}], \tag{4.12e}$$

where the list $\boldsymbol{\theta}$ contains the location along the Y axis of each control point of the top and bottom splines as depicted in Figure 4.5 and Z_1 is the half-length, following symmetry conditions, of the crystal. Furthermore, the design variables $\boldsymbol{\theta}$, Z_s, and Z_1 are limited within a specific range relative to the default design

values. Notice that the variable c is only used in the tile-configuration to displace the SiPM locations. For the bar configuration, the SiPM position can be imposed through $zs_{min} = zs_{max}$ or by removing this design variable from the formulation. The objective values in Equation (4.12a) consist of two functions: the total volume of the crystal V and a measure Φ obtained from the distribution of photons that impact the photodetectors. The total volume V is directly related to the crystal cost and prevents larger volumes, favouring larger energy deposition through longer path lengths within the scintillator. This volume V is calculated by the sum of the volume of each tetrahedral element,

$$V = \sum_{e=1}^{N_e} \mu_e, \tag{4.13}$$

where μ_e represent the volume of the tetrahedron e in a mesh of N_e elements.

The measure Φ is a measure of the distribution of detected photons. In this paper, we study three different ways to define Φ. The first approach is to use L_C, Equation (4.7), or the sum of all detected photons. Another objective distribution worth studying is the light output L_O, or the photons detected per unit of energy deposited in the crystal and SiPM:

$$L_O = \frac{L_C}{E_e}, \tag{4.14}$$

with E_e the energy deposited in the crystal during the event, measured in MeV. Equation (4.14) characterizes the performance of the crystal with respect to different impact particles for a constant cross-sectional area. However, if the impacts have multiple track lengths along the crystal, which is ensured if we modify its thickness, L_O loses information pertinent to the total number of photons created or energy deposited. This loss of information means that we can have a large relative energy deposition in the SiPMs compared to the energy deposited within the crystal, while the total number of photons detected is too small to actually measure.

We define a new objective L_{SP} as the total number of photons detected per unit of energy deposited in the crystal and track path length (which we call pseudo-stopping-power) i. e.,

$$L_{SP} = \frac{L_C}{S_P} = \frac{L_C l_\mu}{E_e},$$

where l_μ represents the total path length of the ionizing particle within the scintillator for the event in which we calculate L_{SP}.

In all cases, all photon count measures have a positive value, and as NSGA-II minimizes the objectives, we need to negate the objective to maximize the light measure received by the detector. Furthermore, these values are not constant per event, and we must consider their behaviour as a distribution. We propose the use of the average and mean as initial values for the optimization of these distributions. The studied objectives can be condensed into

$$\Phi \in \left\{ -\overline{L_C}, -\widetilde{L_C}, -\overline{L_O}, -\widetilde{L_O}, -\overline{L_{SP}}, -\widetilde{L_{SP}} \right\}, \tag{4.15}$$

where the straight line, $\overline{\Phi}$, implies the average of the distribution and the tilde, $\widetilde{\Phi}$, represents the median.

4.3. Results

In this section, we present a summary of the results obtained from the GEANT4 simulations. This includes an evaluation of the default geometry for BTL, possible simplifications and their sources of error, a one-dimensional design space study to understand the effect of the crystal shape on multiple objectives, and numerical optimization results for the two proposed parameterizations in the previous section. The section ends with a verification of the results obtained in the optimization.

4.3.1. Default Geometry

Our initial focus is to characterize the GEANT4 results for the default geometry and explore the impact of different parameters on the simulation. This analysis provides valuable information on the design space, computational time, and the feasibility of numerical optimization for this problem. For these simulations, we employ a Monte Carlo, or random distribution, to define the x and z location of the particles' impacts created, considering both Na^{22} gamma rays with 511 MeV energy and muons with 2 MeV energy. By using both of these event definitions, we can assess the scintillator's performance under different scenarios.

The results depicted in Figure 4.7a show the geometry schematic for the 16 LYSO:Ce bars accompanied by the corresponding light output L_O distributions for both types of particles, muons and gamma rays. On examination of the histograms of L_O from Figure 4.7a, it becomes apparent that muon impacts exhibit a smaller interquartile range (IQR) and smaller means, compared to Na^{22} impacts. In both cases, the difference between the mean and the P_{50} (median) values in these distributions is below 0.2%, indicating a near-symmetric behaviour. The lack of skewness comes from the optical processes occurring within GEANT4, modeled as Gaussians. The influence of the light yield, governed by a Landau distribution, has been considered through the division of energy deposition in Equation (4.14). Due to the slight error between the P_{50} and the mean, we can fit these results to a sum of Gaussian distribution with accurate predictions. This provides a model simplification for the entire GEANT4 model and a comparison between the resulting Monte Carlo studies for different model parameters. The fitting function can be written as

$$N_f(x) = \sum_i^{n_f} a_i \frac{1}{\sqrt{2\pi\sigma_i^2}} \cdot e^{-\frac{(x-\mu_i)^2}{2\sigma_i^2}} \tag{4.16}$$

with μ_i, σ_i and the amplitude, a_i, as the fitting parameters. These parameters represent the mean, standard deviation and amplitude of each normal distribution

up to n_f. The fitting parameters are initialized to

$$\sigma_1 = i \cdot \sigma_{i>1} = \sigma(f), \qquad a_i = max(f),$$
$$\mu_1 = \mu(f), \qquad \mu_{i>1} = \mu(f) + \sigma(f)/i, \tag{4.17}$$

where f refers to the relative frequency – the proportion of observations in a given interval of the histogram compared to the total number of observations – of the subsequent histogram. The fit is performed using a least squares algorithm with all the data from each event in GEANT4.

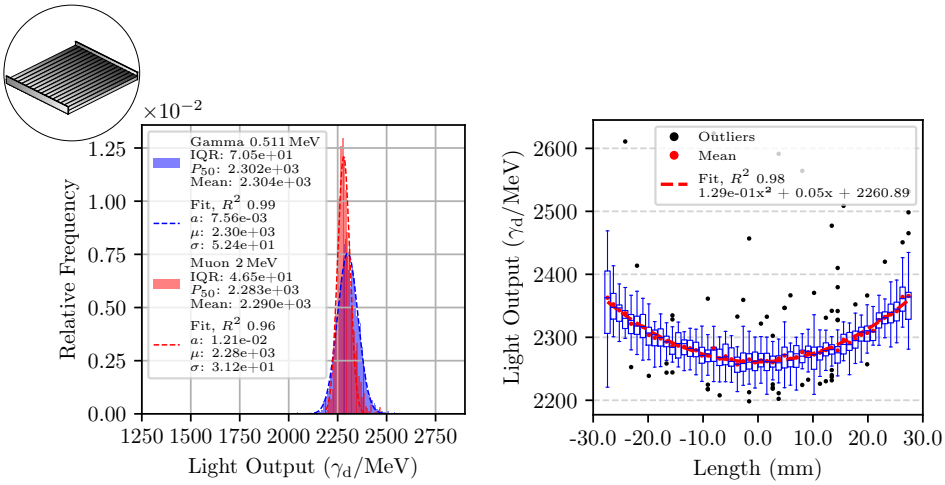

(a) (b)

Figure 4.7.: Light output characteristics of the default geometry with 16 LYSO bars and 32 SiPMs. Figure 4.7a shows the resulting light output distribution per SiPM for muons (μ) and gamma rays of 2 and 0.511 MeV, respectively, with a fit to a linear combination of normal distributions. Figure 4.7b shows a box plot of the averaged light collection between both SiPMs depending on the impact location along the length of the crystal.

The statistical nature of L_O depends on the length of the photon path until detection and its probability of self-absorption within the crystal, see Appendix F.2. Figure 4.7b shows the distribution of L_O as a function of the location of the impact along the crystal in the z axis direction, which can be considered as a measure of the proximity of the impact to each SiPM. This figure shows that the impacts closer to the SiPM in z provide higher light collection for the same energy deposition. However, near the SiPMs, we observe a substantial increase in the L_O interquartile range (IQR). The increased IQR close to the edges of the crystal is attributed to a greater number of photon paths with substantial incidence angles to the glue interface. Despite this local deviation, the relationship between the L_O mean and its dependence on the impact of the location z can be accurately represented by

fitting it to a quadratic polynomial yielding a R^2 of 0.98. This observation highlights the significance of considering the relationship between the impact and the SiPM location when analyzing the scintillator's performance and designing optimized crystal shapes.

Not only can the location of the impact affect the light collection results, but the manufacturing tolerances, see Figure 4.1, can also modify the light output. To estimate the impact of manufacturing uncertainties, we perform simulations following the uniform impact description in Equation (4.1) using a value of n_x and n_z of 4 and 15, respectively. The results of a change in the thickness of the glue layer between 0.1 and 0.3 mm are presented in Figure 4.8a, where each box corresponds to a specific thickness of the glue layer. Following the same procedure for the variation of the resin layer between 0.4 and 0.6 mm, we obtain Figure 4.8b. Both plots show a linear trend for their mean values, with a linear fit of $R^2 = 1$, maintaining a value close to the constant standard deviation within the expected geometric tolerances.

The impact of both the thickness of the glue layer and the thickness of the resin package on the overall light output of the device provides a similar effect; increasing the thickness of any of these elements leads to a decrease in the light output. However, the glue layer has a higher sensitivity in the final light output distribution, exhibiting a steeper slope in the linear fit. These effects can be attributed to the different refractive indices of each material – larger for the glue layer, see Appendix F – which significantly influence photon propagation and collection.

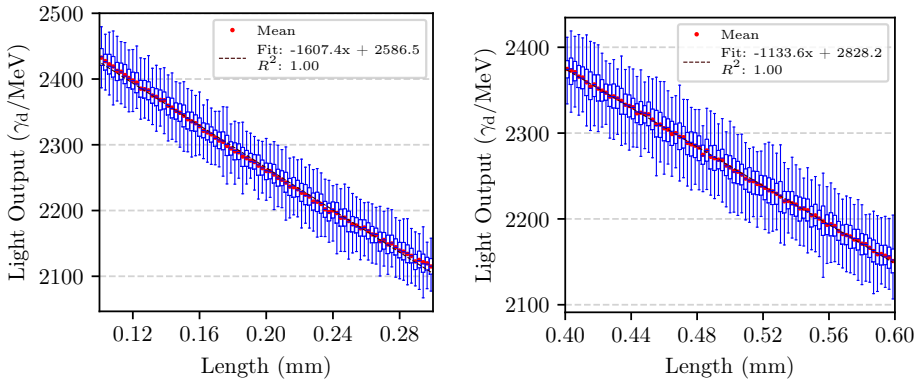

(a) (b)

Figure 4.8.: Effect on the nominal distribution of the manufacturing tolerances in Figure 4.1. Figure 4.8a shows the L_O change for a linear change in the glue layer thicknesses around its nominal value of 0.2 mm. Figure 4.8b shows the L_O change for a linear change in the SiPM resin package thicknesses around its nominal value of 0.5 mm. Both plots include a linear fit using the mean of each boxplot with its formula and R^2.

Notice that even a slight change of 0.2 mm in any of these dimensions can result in up to an 8% variance in the nominal light output. This level of uncertainty can

pose challenges when trying to measure and compare the light output of different geometries and validate the simulation results. As such, it is crucial to account for these variations when studying different scintillator geometries or assembling scintillator devices experimentally. However, these effects only lead to a translation in the objective values for comparison purposes.

4.3.2. 1-dimensional space study

We perform a first design space study of the effect of the shape of the scintillating crystals with a single design variable. Nonetheless, employing the same methodology as in the calculations from the previous Section 4.3.1, where each crystal shape was characterized using over 10000 events for precise Monte Carlo analysis, would require excessive computational time for optimization purposes. Each event can take up to 2 minutes to simulate a 6 mm track of a 2 MeV muon inside the crystal on the CMS TierII Computing Facility.

To reduce computational time, we simplify the geometry, reducing the number of LYSO:Ce crystals, photodetectors, and the number of tetrahedral elements that define the geometry. To investigate the impact of these simplifications on objective functions, we define and compare two configurations against the one studied in the previous section; see Figure 4.7a. In the first simplification, we remove all but one LYSO crystal and its attached SiPMs, while maintaining the original SiPM resin and FR4 package length. In the second configuration, we further reduce the SiPM package to the size of a single SiPM. These simplified geometries allow us to study the impact and sensitivity of internal reflections in the resin package on the L_O.

The results presented in Figure 4.9 illustrate the L_O distributions for the two simplified geometries. The new distributions exhibit a displacement towards higher L_O values, with increases of up to 4.6% and 12% in the nominal and shortened SiPM resin packages, respectively. These improvements can be attributed to the reflections within the simplified resin geometry that would otherwise impact a non-sensitive area, improving the light collection efficiency. This effect could be reproduced through an air gap between neighbouring SiPMs, increasing light collection through internal reflections while minimizing cross-talk between SiPM channels. Although there is a clear difference in the L_O distributions related to the simplified geometries, the difference between muons and the impacts of Na^{22} particles remains consistent with those observed in the default study of the geometry of the 16 LYSO:Ce bars.

From the two simplified cases, we select the nominal resin length with a single LYSO crystal as the most representative model for the optimization process. This choice balances geometry complexity and computational resources, making it a suitable compromise for the more computationally demanding optimization iterative procedure.

The next step is to parameterize the design for the optimization problem. For simplicity, we sought the most straightforward model that maintains a constant volume to allow a direct comparison with the base model. This parameterization involves using two parallelepipeds controlled by a single variable, θ, scaled between 0 and 200. This variable adjusts the thickness in the middle of the crystal while simultaneously compensating its thickness at the edges, maintaining a constant

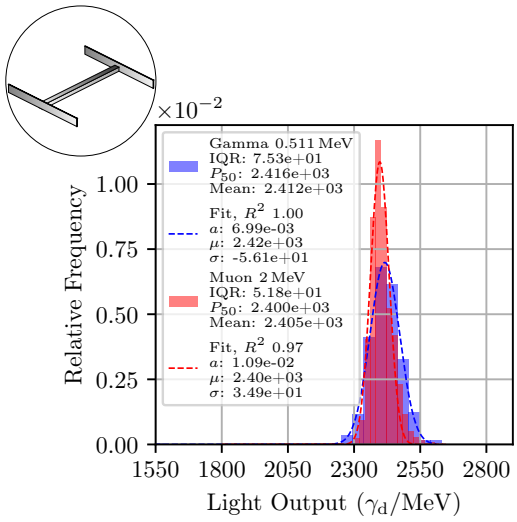

(a)

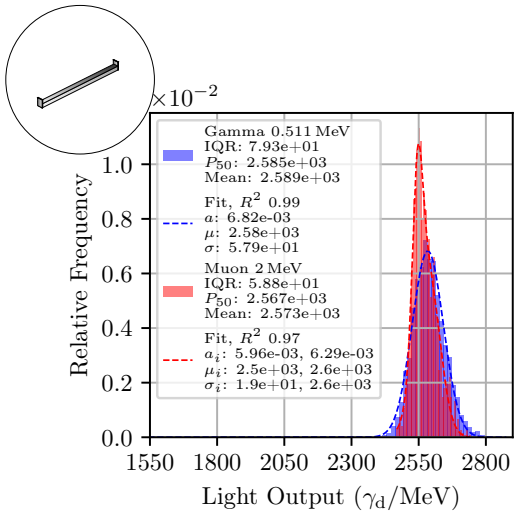

(b)

Figure 4.9.: Simplified LYSO:Ce module geometry L_O distributions. Figure 4.9a shows the geometry and L_O distributions for a SiPM package with a full-length resin layer and a single LYSO:Ce bar. Figure 4.9b shows the geometry and L_O distributions for a SiPM package with a 3 mm wide single SiPM at each end of a single LYSO:Ce bar. Both plots include results for 511 MeV and 2 MeV ^{22}Na and muon impacting particles and a fit for each distribution following Equation (4.17).

volume, as illustrated in Figure 4.10. The limiting values of θ correspond to a zero thickness in the middle or edge of the LYSO:Ce bars and a double thickness, compared to the default geometry, in the opposite location. In this geometry change, the SiPM location and size remain constant, as we are only interested in the effect of the scintillator, and the resin and glue layers are changed to accommodate the size of the edge of the crystals. While these simplifications limit the design space and possible gains, they preserve the influence on the design space of the reflective surfaces and energy depositions of the ionizing particles. This study then provides information on the behaviour of the objective functions concerning these parameters.

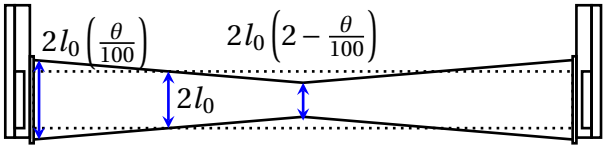

Figure 4.10.: Schematic for the 1D design exploration and optimization with the variable θ modifying the thickness of the crystal in the middle and edge of the crystals with the provided values in the figure, maintaining a constant volume.

In Figure 4.11, we show the mean and median for the distributions L_C, L_O, and L_{SP} obtained from the 10 runs, with the impact distributions $n_x = 4$ and $n_z = 15$, with varying values of θ between 25 and 175. This pattern provides an estimation of a maximum calculation time of two hours per individual. The deviations observed in these distributions correspond to the variability expected in higher-dimensionality studies. In particular, L_C exhibits a larger IQR and more outliers than the other two objectives. This outcome aligns with expectations, as the Landau distributions exhibit tails that can lead to larger deviations than normal distributions for a given number of events.

Furthermore, we observe that when θ is equal to 100, these distributions show symmetric behaviour – the data are balanced around its central point, and the mean, represented in blue, is equal to the median, represented in red – and we appreciate that this corresponds to the original flat configuration, refer to Figure 4.7a. However, at different values of θ, the mean and median are no longer equivalent, indicating non-symmetric behaviour. This characteristic has implications for selecting the appropriate measure for each objective. For optimization L_C, the median value is more suitable, as it reduces the overall deviation in successive evaluations of the function and accounts for the influence of low values on the distribution. On the other hand, for the optimizations L_O and L_{SP}, the mean value is more conservative, being affected by the extreme or outlier values in the distributions.

In particular, we identify an optimized value θ that represents a decrease in thickness between 20% and 40% in the middle of the crystal for all objectives, resulting in a relative increase in the objective between 3 and 8%. This result is correlated with the study by Figure 4.7b in which we observe a lower L_O sensitivity

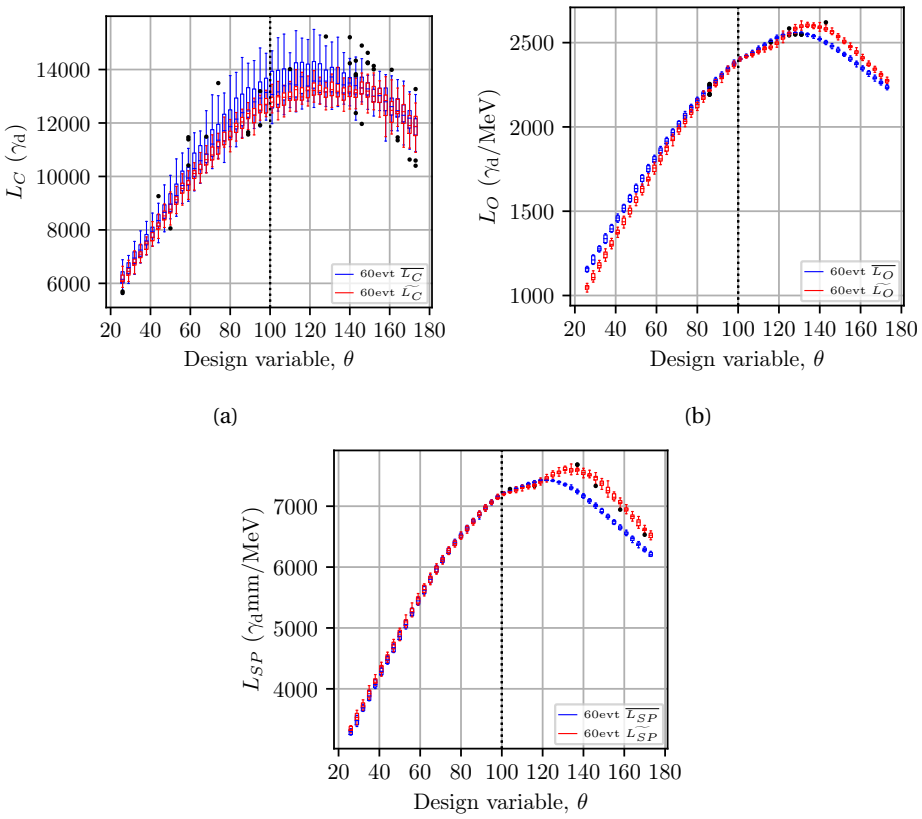

Figure 4.11.: Distributions for multiple objective functions according to 10 runs of 60 – 15 along z and 4 along x – events for each θ value used. Figure 4.11a shows the results for the L_C, Figure 4.11b for the L_O, and Figure 4.11c for the L_{SP} objective. In all cases, we use the P_{50} and an average of each objective for the representation.

to the same energy deposition in the middle of the bar.

These results show a better fitness for the L_O and L_{SP} objectives, with minor design space roughness and stochastic errors. These results can be extrapolated to higher dimensionality spaces which maintain the same dependencies. The only factor not studied through this simplified model, included in the Equation (4.12) formulation, is a volume objective to reduce material costs. This objective is expected to provide a linear design space directly proportional to the overall energy deposition in the crystals. However, the L_O objective is indifferent to the energy deposition in the system and can lead to convergence problems not studied with this simplified model.

4.3.3. Evolutionary optimization

A space study of low dimensionality is useful to understand the problem better and provide simple shape modifications; however, higher-dimensional design spaces allow for more freedom in designs and possibly lower minima. We use NSGA-II following the description in Section 4.2.5 to get close to the Pareto fronts of the optimization problem that relates the volume and a measure of the photon collection in the photodetector.

Bar-configuration

We start by performing the optimization based on the bar configuration, shown in Figure 4.5. Given the definition of NSGA-II in Figure 4.4 and the optimization definition in Equation (4.12) without the design variable Z_s, the values used in the subsequent simulations are summarized in Table 4.1.

Parameter	Value
Maximum Number of Generations , n_g	100
Individuals per Generation, n_i	100
Tournament Participants	2
Selection Probability	90%
Mutation Percentage	5%
Convergence delay, n_h	10
Convergence Tolerance, Tol	1%
$[Z_{min}, Z_{max}]$	[20 mm, 28.5 mm]
$[y_{min}, y_{max}]$	[0.1 mm, 3 mm]
$[n_x, n_z]$	[4, 15]

Table 4.1.: NSGA-II parameters for simulations.

The maximum number of generations (n_g) controls the algorithm's runtime and final population closeness to the Pareto front, where a larger number of generations allows for a more thorough search but increases computational cost. The individuals per generation (n_i) define the population size, affecting the genetic diversity of each population, convergence speed, and the computational cost of each population. Tournament participants determine the selection pressure during the tournament selection process. A selection probability of 90% indicates a high likelihood of selecting superior individuals, promoting faster convergence. A 5% mutation percentage ensures genetic diversity, adding random modifications to each offspring of a maximum of 5%, preventing premature convergence to local optima. A value too high for the mutation percentage can lead to convergence difficulties. The convergence delay (n_h) allows the algorithm to avoid early convergence measurement by avoiding hypervolume changes based on outlier populations with overly small changes in the hypervolume. We select a 10 for n_h as a trade-off between higher

computational time and accuracy in the final converged output. The convergence tolerance (Tol) sets the precision for stopping criteria, ensuring the algorithm halts when improvements between the last n_h generations are marginal compared to the initial Pareto front area or hypervolume set according to the user. The design variable range for Z $[Z_{min}, Z_{max}]$ and $y[y_{min}, y_{max}]$ define the allowable limits for the crystal's half-length and height according to Figure 4.5, ensuring feasible and practical solutions. The limits on these variables are set by the nominal half-length of the crystal of 28.5, and the space allocation for these detector crystals of 6 mm. The lower bound for the half-length of the crystal is set as a compromise so that the crystal can reduce its length and increase the light collection of impacts in $z = 0$, without unnecessarily extending the design space. The lower bound for the y nodal location is set to a small value higher than zero to avoid computational issues if part of the crystal has zero thickness during the random geometry generation by NSGA-II. The grid resolution parameter for the number of impacts as defined in Equation (4.1) $[n_x, n_z]$ dictates the balance of solution accuracy and computational efficiency and is studied in the 1D solution. The values of 4 impacts through the half-x dimension and 15 impact along the z direction showed, in the 1D analysis, to provide an error under 1% for the L_O and L_{SP} objectives for ten different evaluations, reducing computational time for a good result reliability compared to L_C.

Optimizations are performed for the same objectives studied in Section 4.3.1, including the mean and median values of the L_O, L_C, and L_{SP} photon counts. To study the convergence of these optimizations through the hypervolume we use its change concerning the hypervolume of the converged generation, for each generation of L_O and L_{SP}, which is plotted in Figure 4.12a. From this plot, we can further appreciate the difference in convergence rates of different objectives where $\widetilde{L_O}$ is the fastest and $\widetilde{L_{SP}}$ is the slowest in the 43 and 75 generations, respectively. The hypervolume value not only offers insights into the convergence rate but also serves as an indicator of the spatial distribution of the converged Pareto fronts. Specifically, the highest hypervolume of L_O is found to be $3.2e6$, less than half of the smallest L_{SP} hypervolume of $7.8e6$. This difference shows that the optimized designs within L_O are located within a significantly smaller region of the design space than the Pareto of L_{SP}. Due to the metaheuristic nature of NSGA-II, the hypervolume indicates when we are close to the Pareto front, which can be reached for multiple NSGA-II runs. However, we cannot ensure that we obtain the same individuals within the front between multiple runs, and the convergence rate can vary within the same orders of magnitude. These conclusions remain true for the objectives using the mean and median of each photon count distribution.

Figure 4.12 shows individuals close to Pareto fronts for the three different light collection measurements for the last NSGA-II generation run, and the volume value of the default initial configuration in Section 4.3.1 as a dashed horizontal line. In each subplot of the Pareto front depicted in Figure 4.12, there is a cross symbolizing the mean value of the distribution from the corresponding photon count measurement using the simplified geometry of the full resin width; see Figure 4.9a. This plot can provide further information compared to the 513 mm^3 default bar design, and the reference point, or nadir point, used for the hypervolume calculation, represented

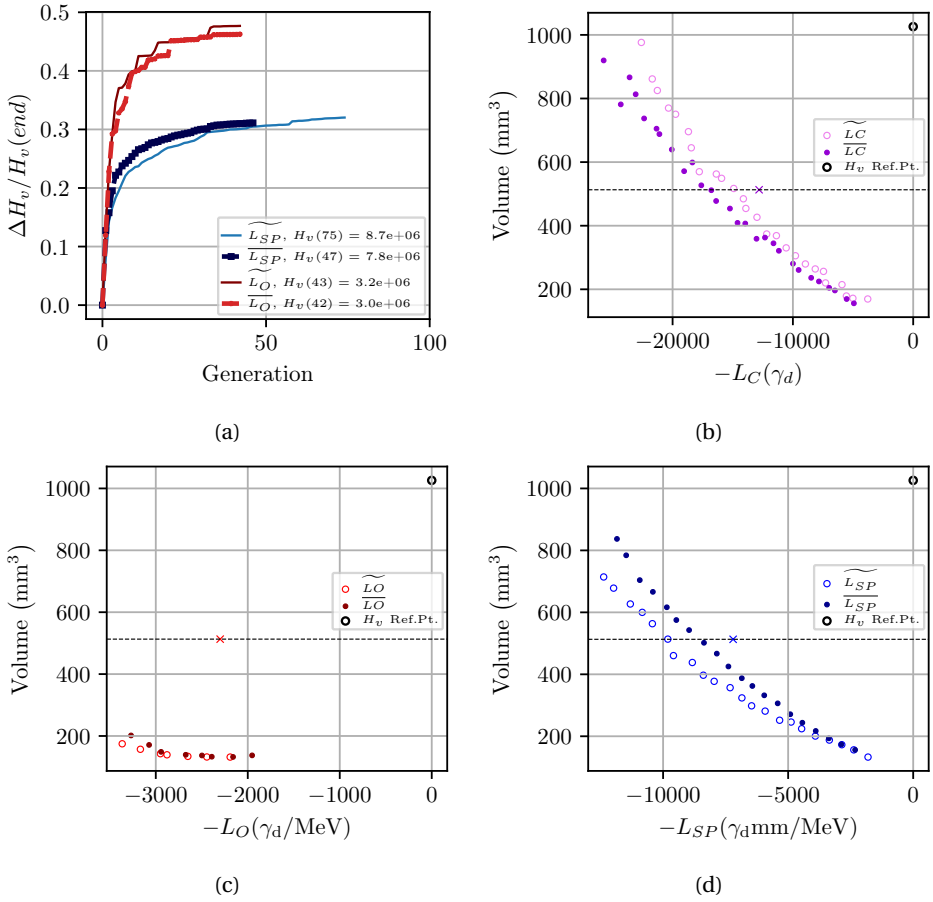

Figure 4.12.: Results for the bar-configuration optimization with NSGA-II. Figure 4.12a shows the hypervolume change with respect to the final calculated value with respect to the generation index, and convergence satisfaction for the L_O and L_{SP} mean and median objectives. The results for a subset of the last NSGA-II generation is plotted in Figure 4.12b, Figure 4.12c and Figure 4.12d for the L_C, L_O and L_{SP} mean and median objectives, respectively. These plots include the original objective value for the bar configuration as a cross, its volume as a dashed horizontal line, and the nadir point as a circle in the top right of each figure.

in the top right corner of each plot. The visually smoothest Pareto is obtained from the L_O optimization. However, the L_O optimizations converge to Pareto fronts at lower volumes compared to the other objectives, leading to subsequent lower photon counts. This observed effect is rectified in both L_C and L_{SP} objectives by incorporating the impacting particle's path length within the scintillator into the objective, either directly within L_{SP} or through the consideration of energy deposition in L_C.

From Figure 4.12, it is evident that the rate of increase in the photon count slows as the values approach the maximum allowed volume. The individual with the maximum value is known and defined as the maximum thickness for all design variables, $\boldsymbol{\theta} == y_{max}$, see Figure 4.5. This maximum volume design results in a design featuring flat parallel surfaces, equivalent to the original design with a larger volume. Therefore, the optimized designs found in larger volumes have an active restriction on their thickness, limiting the design space. Expanding the ranges of θ for design variables that reside in the limits of the Pareto front may reveal better designs at these volumes.

A comparison of optimized results with respect to the default crystal bar volume allows us to discern the effects of the optimization between the P_{50} and mean objectives. When confronted with distributions that show tails at higher values, P_{50} tends to yield the most conservative results, focusing primarily on the lower values of the distribution. In contrast, for objectives such as L_O and L_{SP}, the mean results are more conservative, as P_{50} allows inclusion of lower objective results while maintaining a higher value of P_{50}.

The resulting geometries for the same volume as the original bar, $513\,\mathrm{mm}^3$, are plotted in Figure 4.13. In the case of the objective L_O, the Pareto front does not reach the value of $513\,\mathrm{mm}^3$, and we plot the results for the value of $200\,\mathrm{mm}^3$, close to the highest volume found in the Pareto. These plots use the GMSH library to create the exact same mesh introduced in GEANT4 and are superimposed to the default rectangular section. We can see from Figure 4.13 that while the design is based on a spline, the number of nodes in the mesh affects the design, creating flat surfaces, which also affects the final design and its manufacturing. Furthermore, not all geometries have the same number of tetrahedral elements besides having the same number of nodes. This means that we can have geometries with far more complex meshes due to their shape, deteriorating the computational time.

Figure 4.13 not only gives information on the mesh of the models but also on the results from each different objective. The L_O objectives show a reduced thickness in the middle of the crystal bar that progressively increases toward its edges, ultimately covering a significant portion of the SiPM area at the crystal's end. Likewise, comparable trends are observed between the L_C and L_{SP} objectives for each of the used distribution metrics, median and mean values. This behaviour is similar to the results obtained in the 1D study, where a lower energy deposition in the middle of the crystal is compensated by focusing of the photons into the SiPMs, and a higher sensitivity of the objective to impacts near the SiPMs. Concerning the median metric, both photon count objectives tend to decrease the thickness in the middle section of the crystal, as in the case L_O. This lower thickness results in

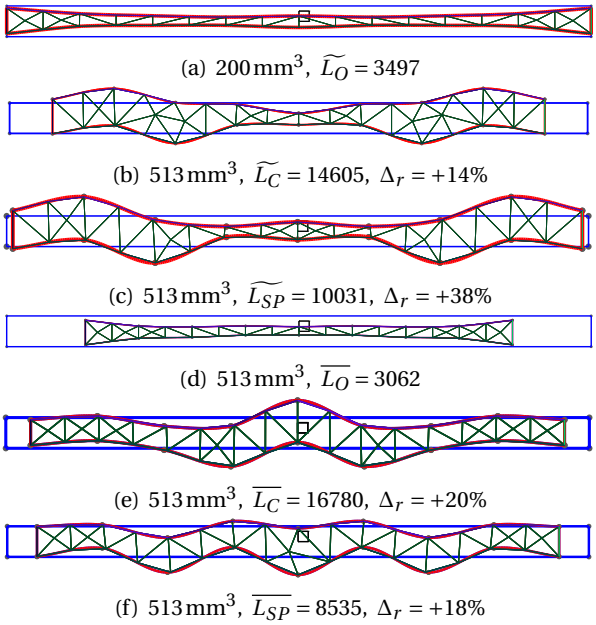

(a) 200 mm^3, $\widetilde{L_O} = 3497$

(b) 513 mm^3, $\widetilde{L_C} = 14605$, $\Delta_r = +14\%$

(c) 513 mm^3, $\widetilde{L_{SP}} = 10031$, $\Delta_r = +38\%$

(d) 513 mm^3, $\overline{L_O} = 3062$

(e) 513 mm^3, $\overline{L_C} = 16780$, $\Delta_r = +20\%$

(f) 513 mm^3, $\overline{L_{SP}} = 8535$, $\Delta_r = +18\%$

Figure 4.13.: Resulting geometries in GMSH for the last converged generation for multiple objectives, in red, superimposed to the mesh used in GEANT4 and the original bar configuration in blue. The comparable geometries with the same volume provide the resulting objectives and their relative difference, Δ_r, to the corresponding values of the original simplified design Figure 4.9.

lower energy deposition in the areas where the light output is the smallest due to a larger path length to the SiPM with a subsequent larger number of self-absorbed photons; see Figure 4.7b. In the case of objectives based on the mean of the distributions, both outcomes yield a wavy design that facilitates photons reaching SiPMs through successive reflections, featuring increased material concentrations in the middle of the crystal. This creates longer path lengths within the scintillator for ionizing particles and larger energy depositions, counteracting the lower light output previously observed in these regions for the default design. Furthermore, in these latest cases, the crystal is optimized to a smaller length and proportionally larger width, maintaining a constant sensitive area. This change reduces the overall photon path to the photodetector while increasing the losses in the SiPM interface – the SiPM size remains constant – to an optimum value. The gains of the optimized design can be obtained from the relative difference of the objectives to the original design,

$$\Delta_r = \frac{\Phi_i - \Phi_0}{\Phi_0}. \tag{4.18}$$

In Equation (4.18), Φ_i is the photon count measure from the optimized design and Φ_0 the values from the original design, see Figure 4.14. From this relative difference, we obtain the highest gains through the $\widetilde{L_{SP}}$ objective with a 38% increase. Other objectives provide more conservative gains between 15 and 20% for the same amount of volume.

While the Pareto fronts and resulting geometries offer insights into the algorithm's objectives, these solutions include errors stemming from the stochastic nature of GEANT4 ray-tracing simulations. Consequently, a thorough examination of each resulting individual is required to validate the accuracy of the photodetector photon counts with respect to the optimization outcomes. In Figure 4.14, the results of each individual illustrated in Figure 4.13, are presented using boxplots for the various light measures employed in this study. Each box plot features the mean of the distribution marked with a red point, while the result obtained from the NSGA-II algorithm is denoted by a dark blue star. For comparative analysis, the distributions for the initial default geometry (Def.) are included alongside the optimized crystal shapes. The NSGA-II results demonstrate a commendable alignment with the detailed light characteristics of each individual, as evidenced by the blue stars in Figure 4.14. An exception to this pattern is observed in the optimization of L_C, where the error committed is approximately ±3% for each objective. In contrast, the error is considerably lower for L_O at 0.5% and for L_{SP} at 0.7%. The 1D model predicted these higher errors for the L_C objectives, see Figure 4.11. These results suggest a higher reliability of the L_O and L_{SP} individuals that result at a comparable computational cost.

However, not all results from a different objective perform equally well in the other photon count metrics. The optimized results for L_O provide the highest L_O values compared to the other metrics, but perform worst in total light collection. This is again due to the lack of impact of the path length of the ionizing particles within the crystal in this measure. We can also appreciate that the optimized results P_{50} displace the distribution toward larger light collections but do not introduce

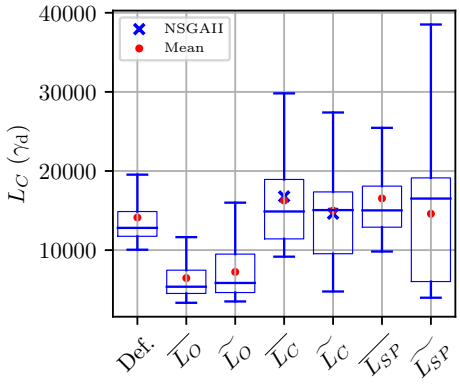

(a)

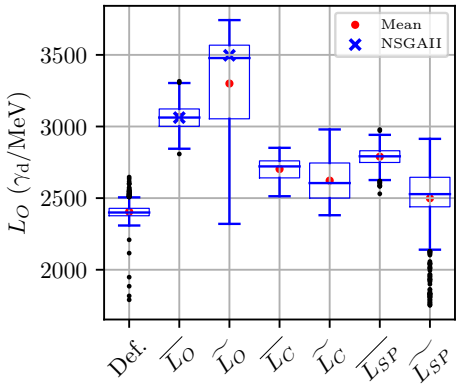

(b)

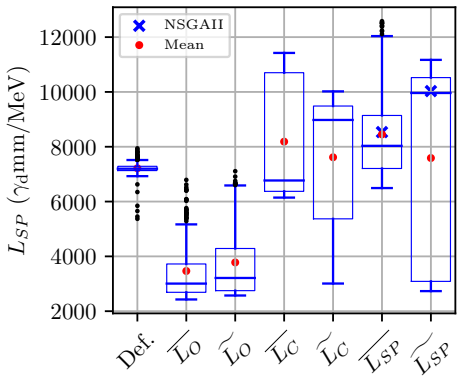

(c)

Figure 4.14.: Resulting light function distributions (L_O,L_C and L_{SP}) as boxplots against the default configuration (Def.) for three different objectives (L_O,L_C and L_{SP}) and two distribution metrics (P_{50} and $\bar{x}$) for a volume of 513 mm^3 together with the corresponding scalar values obtained from the NSGA-II optimization as a blue cross.

larger IQR values into the distributions. In the case of L_C, this more significant deviation is limited by the Landau distribution shape to larger values; however, for other objectives, this can introduce photon counts near to zero for certain impact locations. From these results, it becomes obvious that from the objectives studied, the $\overline{L_{SP}}$ provides a Pareto front with the largest gains in total light collection for any particle without reducing the minimum value of light collected and most accurate results with the same GEANT4 number of events. Using the results of the optimized results $\overline{L_{SP}}$ as a reference, we can further study the optimized result by comparing it with the original design depending on the position of the impact.

Figure 4.15 shows the L_{SP} objective for the original design in red and for the optimized design of the same volume in blue for half of the LYSO bar. This boxplot still shows the expected parabolic profile in the default design; however, the values for the optimized design provide a much higher value for L_{SP} in each of the bumps due to the larger track-path-length of the impacting particles within the scintillator. This can lead to more complex data processing with a larger variation of the photon count depending on the impact location.

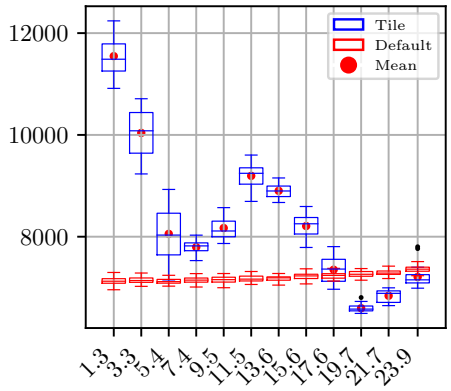

Figure 4.15.: L_{SP} distributions against the impact point along the z half-length of the optimized geometry obtained for the $\overline{L_{SP}}$ objective with 513 mm^3 and the default simplified geometry.

Tile Configuration

The previous optimization, based on Figure 4.5, uses an extrusion of a 2D profile to simplify crystal manufacturing. However, this can lead to lower light collections compared to a full surface optimization. Using the configuration with SiPMs at the bottom of the LYSO crystals or tile-configuration, and the parameterization described in Figure 4.6, we can perform a complete surface shape optimization.

To perform this optimization, we focus on the $\overline{L_{SP}}$ objective given the results in Figure 4.14. Furthermore, this optimization includes the position of the SiPM in the bottom $y == 0$ plane as a variable defined in Equation (4.11). In this case, since we

are only displacing the location of the y nodes from the top surface, rather than the bottom and top as in the bar configuration, we modify the variable limits to

$$[y_{min}, y_{max}] = [0.85\text{mm}, 6\text{mm}]. \tag{4.19}$$

This maintains the maximum height of the scintillator below 6 mm using a single control point for the top surface following Figure 4.6. The only other change from the parameters in Table 4.1 is the pattern of impact points set to

$$[n_x, n_z] = [6, 6], \tag{4.20}$$

using a lower number of impacts compared to the previous simulations. This is helpful in reducing the computational time along the optimization process, as a larger computational complexity is expected of this problem, which has more design freedom than previous ones. This extra computational complexity or computation time arises from the larger number of elements created to define the geometry that needs to be evaluated in the photon paths.

The results of this optimization provide a new Pareto front plotted in Figure 4.16. This figure shows a Pareto front with higher $\overline{L_{SP}}$ for intermediate volume objective values than the previous case, highlighting the influence of initial parameterization and design freedom on the results.

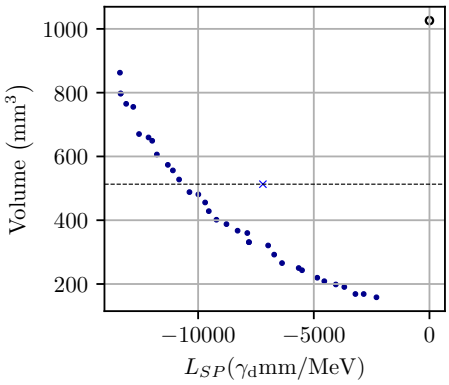

(a)

Figure 4.16.: Pareto front for the tile-configuration, see Figure 4.6. The plot includes the volume objective and the negative $\overline{L_{SP}}$ in the y and x axis, respectively. The plot also includes the reference point H_v in black and the default configuration $\overline{L_{SP}}$ as a blue cross.

In particular, we find that for a volume of 490 mm, we obtain a relative gain with the default bar-configuration of up to 47%, $\overline{L_{SP}} = 10584$, compared to the previous value of 18%. The resulting geometry for this particular individual is represented in Figure 4.17 with two lateral views corresponding to the projections of the plane $x-y$ and $y-z$.

This result has a value of Z_S of 25%, which locates the centre of the SiPM below the first node from the centre of the crystal in z. Furthermore, the optimization creates an inclined top surface with lower thickness towards the edges. This has two effects: firstly, it redirects photons toward the central region of the crystal, precisely where the SiPMs are positioned; secondly, it induces a lower-energy deposition at a greater distance from the SiPMs.

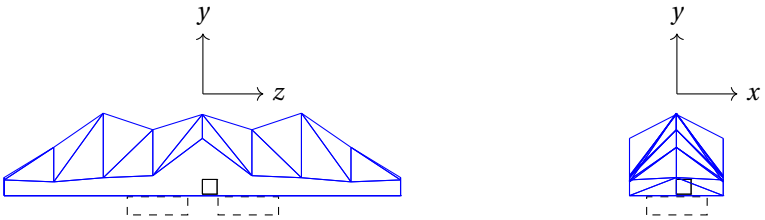

(a) (b)

Figure 4.17.: Front Figure 4.17a and lateral Figure 4.17b view of the resulting geometries from GMSH for the last converged generation for the Tile, see Figure 4.6. The results are obtained from the Pareto front at a volume of 490 mm. The individual has an objective value of $\overline{L_{SP}} = -10588$ with a relative gain of 47%.

This new configuration, while attractive because of a larger light collection, has some disadvantages. In particular, the manufacturing of the optical surfaces becomes more complex, and we have a larger dependence of the light collection on the y impact locations. Furthermore, the discretization of the surface does not ensure a smooth contour as we would obtain with a spline definition.

We still need to verify the results of the NSGA-II algorithm, as the lower number of impacts can impose a greater error on the objective values L_{SP}. Running a Monte Carlo study on the optimized configuration showed in Figure 4.17, we can obtain an accurate prediction of its L_O distributions at the cost of a larger computational complexity, which is not feasible for optimization purposes. Furthermore, we can also try to discern the design criterion that the algorithm applies to the design of these crystals by investigating the dependence of L_{SP} on the impact locations. This verification shows a resulting mean of 8950, with a relative gain of 24% rather than 47% for the optimized design. This means that we have an overestimation of the objective of the photon count in the Pareto front of 18% with respect to the default bar-configuration measure. To better understand the source of these differences and the inner workings of the algorithm, we need to understand the effect of the location of the particle impacts on the geometry.

Figure 4.18 shows the dependence of L_{SP} with the impact locations along z and x based on the verification Monte Carlo analysis. The distributions in Figure 4.18a show the variation of the L_{SP} depending on the z axis impact location while Figure 4.18b shows this effect along the x axis, including each distribution percentiles, mean and outliers. From these figures, we deduce that the algorithm maximizes the light

collection from the central location of the crystal in x and z, disregarding the effects of the edges along x and z. From these plots, we can also see that the use of more than one row of control points along x leads to a clear dependence on the output mean with regard to this axis. This dependence seems to correlate with the overall thickness change in each region linearly. The disregard of the edge locations can be related to the smaller number of impact points, with larger gaps in these regions.

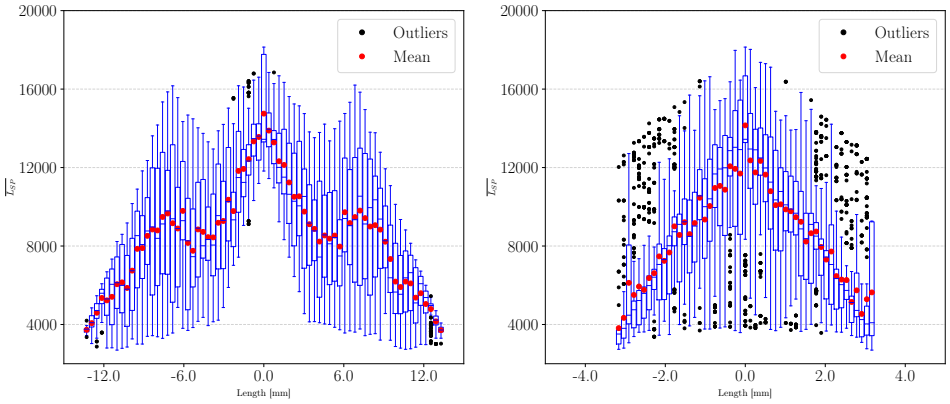

(a) (b)

Figure 4.18.: $\overline{L_{SP}}$ for an optimized LYSO:Ce Tile configuration with respect to the impact location using a random impact pattern. Figure 4.18a shows the distribution effect with respect to the z impact location while Figure 4.18b shows the dependence of the x impact location.

These results suggest that a low number of impacts can provide improved scintillator geometries at a lower computational cost. However, the objective functions for the scintillator optimizer are sensitive to the impact locations studied and should be selected for each particular case so as not to deteriorate the optimization procedure and limit the objective value variability over multiple evaluations.

4.4. Conclusions

In this paper, we have introduced a novel approach that involves design criteria and modelling techniques to increase the light collection of scintillation crystal-based photodetectors with GEANT4. Moreover, we conducted a comprehensive comparison of different optimization objectives capable of modifying the resulting light collection distributions while keeping constant the material-associated costs. Through our research, we have found that neither the light collection nor the light output are adequate indicators of the problem. Instead, we propose a new objective function based on the light collection per pseudo-stopping-power, L_{SP}, which yields improved Pareto fronts, objective distributions, and convergence for this problem. These

studies have been performed through a simplified 1D model to isolate the influence of the reflective surfaces and energy deposition from the material volume and study the problem fitness. The results of this 1D model have then been extrapolated to a multidimensional optimization and compared, obtaining design criteria for the LYSO:Ce crystals. Although this model is capable of predicting the fitness of the problem and expected errors due to the stochastic nature of the problem, the problem could be further studied through landscape analysis at a possible higher computational cost and lower pre-processing required to simplify the problem in question [39].

Compared to the previous literature in the optimisation of scintillator geometries, we provide a shape optimisation capable of higher flexibility and generalizability of the design methodology rather than the commonly used parametric optimisation with predispositions made by the designers [19, 22]. The multiple-objective study looks into the overall light collection using a multiobjective optimizer. The focus on the light collection can be seen to be related to the timing of the detector [40]. However, using the light collection as a single objective can lead to larger widths for the optimized distributions, which is the focus of previous optimizations [20, 22]. The formulation with NSGAII allows for the introduction of multiple objectives that could ensure selecting the shapes with the highest light collection, highest time precision, and smallest distribution width, with the addition of the extra objectives and a higher computational cost. Some proposed objectives to reduce the width of these distributions are the interquartile range (IQR) for non-symmetrical distributions or the minimum values within the distribution. We also notice that the use of normalization techniques could improve the behaviour of some of the objectives in multiobjective optimization, and techniques to deal with the stochastic noise could reduce the objective variability between different runs, such as dynamic sampling rates during the optimization.

Furthermore, our results emphasize the critical role of the SiPM or photodetector model and its location in achieving overall detector efficiency; notice how the ends of the crystals always adapt to the photodetector shape. The impact of SiPMs on the collection area is appropriately recognized, and we underscore the importance of considering the SiPM power needs and its changes with its area under a joint LYSO-SiPM optimization. Additionally, our optimized results reveal that a larger crystal area in contact with the SiPM module may lead to higher losses to the environment. Nevertheless, in the bar configuration, this decrease in performance from a larger contact area can be counteracted by a lower length of the overall crystal.

Not only the photodetector model but also the material models have an impact on the results. Our material models are derived from measured prototypes, which serve as a valuable guide for future designs. However, there is limited information available on scintillating materials, which should be considered when interpreting the model output. However, because the LYSO:Ce crystals have a non-negligible cost, experimental tests are limited. In the case of plastic scintillators, which present lower light yields and refractive indices, the optimization results are speculated to provide lower gains based on the reflective surfaces under a direct air-scintillator interface.

This could be mitigated through directly deposited reflective coatings, increasing the objective sensitivity to these surfaces. The use of non-polished surfaces also shows promise in increasing light collection in scintillator-based detectors [15]. According to our model, we can reduce material costs without losing light collection efficiency. Nevertheless, the resulting shapes might require the use of free-form optics. This manufacturing technology is relatively recent, and there is no current good way to estimate the cost of these intricate shapes derived by optimization. As this complexity increases, careful evaluation of the associated manufacturing cost becomes essential. This paper deals with the optimization of a BTL-based design which limits the variability of surface roughness of the crystals and their coatings. However, the use of localized surface treatments could be introduced as a further design variable, alleviating the manufacturing constraints and potentially modifying the light collection and timing. For experimental testing of the optimized results, plastic scintillators also have an advantage as they can be easily machined and are less expensive.

Despite the potential of our automated design procedure to enhance performance and reduce costs, further investigation and access to cluster computing tools are currently necessary due to the computational demands of genetic algorithms and ray-tracing software, with its associated costs. Nevertheless, our research highlights the potential for numerical optimization in particle detectors, extending its applicability beyond scintillation material modelling to the optical interfaces of the assembly. To further tackle the computational challenges arising from the lack of sensitivities in Monte Carlo-based problems, we suggest exploring methods such as finite element methods (FEM) or finite differences in the time domain (FDTD) to incorporate scintillation models and improve computational efficiency.

As the field of numerical optimization in particle detectors continues to evolve, we anticipate numerous opportunities for improvement and new discoveries, not only in scintillation geometries but also in the optical interfaces of the assembly. Additionally, the recent application of 3D printing technologies to the manufacturing of scintillators opens new avenues for utilizing this optimization approach. Furthermore, the insights obtained from our study can be extrapolated to different detector geometries, such as fibre-based ones, as well as other detector types where shape optimization can increase efficiency. We strongly encourage further exploration in these areas to broaden the scope of this optimization technology.

In conclusion, our work [1] presents valuable insights and guidelines for designing efficient and cost-effective scintillation-crystal-based photodetectors, serving as a foundation for future research and advancements in this domain. By considering the proposed optimization objectives and modelling techniques, researchers can make informed decisions to enhance the performance of particle detectors and drive innovation in the field.

References

[1] G. Reales, F. van Keulen, A. M. Aragón, J. F. L. Goosen, and A. Bornheim. "Multi-objective scintillator shape optimization for increased photodetector light collection". In: *J. Opt. Soc. Am. B* 41.9 (Sept. 2024), pp. 2014–2032. DOI: 10.1364/JOSAB.529434. URL: https://opg.optica.org/josab/abstract.cfm?URI=josab-41-9-2014.

[2] Z. Wang, C. Dujardin, M. S. Freeman, A. E. Gehring, J. F. Hunter, P. Lecoq, W. Liu, C. L. Melcher, C. L. Morris, M. Nikl, G. Pilania, R. Pokharel, D. G. Robertson, D. J. Rutstrom, S. K. Sjue, A. S. Tremsin, S. A. Watson, B. W. Wiggins, N. M. Winch, and M. Zhuravleva. "Needs, Trends, and Advances in Scintillators for Radiographic Imaging and Tomography". In: *IEEE Transactions on Nuclear Science* 70.7 (2023), pp. 1244–1280. DOI: 10.1109/TNS.2023.3290826.

[3] C. Dujardin, E. Auffray, E. Bourret-Courchesne, P. Dorenbos, P. Lecoq, M. Nikl, A. N. Vasil'Ev, A. Yoshikawa, and R. Y. Zhu. "Needs, trends, and advances in inorganic scintillators". In: *IEEE Transactions on Nuclear Science* 65.8 (2018), pp. 1977–1997. ISSN: 00189499. DOI: 10.1109/TNS.2018.2840160. URL: https://doi.org/10.1109/TNS.2018.2840160.

[4] S. Liu, M. Chen, C. Fu, and T. Zhu. "The Interplay of Magnetism and Thermoelectricity: A Review". In: *Advanced Physics Research* 2.9 (2023). ISSN: 2751-1200. DOI: 10.1002/apxr.202300015.

[5] P. Lecoq. "Development of new scintillators for medical applications". In: *Nuclear Instruments and Methods in Physics Research, Section A: Accelerators, Spectrometers, Detectors and Associated Equipment* 809 (2016), pp. 130–139. ISSN: 01689002. DOI: 10.1016/j.nima.2015.08.041. URL: http://dx.doi.org/10.1016/j.nima.2015.08.041.

[6] F.-M. Lu and Z. Yuan. "PET/SPECT molecular imaging in clinical neuroscience: recent advances in the investigation of CNS diseases." In: *Quantitative imaging in medicine and surgery* 5.3 (2015), pp. 433–47. ISSN: 2223-4292. DOI: 10.3978/j.issn.2223-4292.2015.03.16. URL: http://dx.doi.org/10.3978/j.issn.2223-4292.2015.03.16.

[7] K. Yu. "Scintillation Detectors in Modern High Energy Physics Experiments and Prospect of Their use in Future Experiments". In: *Journal of Lasers, Optics & Photonics* 04.01 (2017), pp. 1–9. ISSN: 2469-410X. DOI: 10.4172/2469-410x.1000148.

[8] J. Glodo, Y. Wang, R. Shawgo, C. Brecher, R. H. Hawrami, J. Tower, and K. S. Shah. “New Developments in Scintillators for Security Applications”. In: *Physics Procedia* 90.November 2016 (2017), pp. 285–290. ISSN: 18753892. DOI: 10.1016/j.phpro.2017.09.012. URL: http://dx.doi.org/10.1016/j.phpro.2017.09.012.

[9] C. Kim, W. Lee, A. Melis, A. Elmughrabi, K. Lee, C. Park, and J.-Y. Yeom. “A Review of Inorganic Scintillation Crystals for Extreme Environments”. In: *Crystals* 11.6 (2021). ISSN: 2073-4352. DOI: 10.3390/cryst11060669. URL: https://www.mdpi.com/2073-4352/11/6/669.

[10] R.-Y. Zhu. *Summary Talk in CEPC Calorimetry Workshop at IHEP, Beijing*. 2019. URL: https://www.its.caltech.edu/~rzhu/.

[11] A. Pla-Dalmau, A. D. Bross, and K. L. Mellott. “Low-cost extruded plastic scintillator”. In: *Nuclear Instruments and Methods in Physics Research, Section A: Accelerators, Spectrometers, Detectors and Associated Equipment* 466 (3 2001), pp. 482–491. ISSN: 01689002. DOI: 10.1016/S0168-9002(01)00177-2. URL: http://dx.doi.org/10.1016/S0168-9002(01)00177-2.

[12] R.-Y. Zhu. “Ultrafast and Radiation Hard Inorganic Scintillators for Future HEP Experiments”. In: *Journal of Physics: Conference Series* 1162.1 (2019). ISSN: 17426596. DOI: 10.1088/1742-6596/1162/1/012022. URL: https://doi.org/10.1088/1742-6596/1162/1/012022.

[13] Y. N. Kharzheev. “Radiation Hardness of Scintillation Detectors Based on Organic Plastic Scintillators and Optical Fibers”. In: *Physics of Particles and Nuclei* 50.1 (2019), pp. 42–76. ISSN: 15318559. DOI: 10.1134/S1063779619010027. URL: https://doi.org/10.1134/S1063779619010027.

[14] S. Cherny. “Problems in the use of plastic scintillators in intense radiation fields”. In: *Radiation Physics and Chemistry* 41.1-2 (1993), pp. 181–184. ISSN: 0969806X. DOI: 10.1016/0969-806X(93)90054-X. URL: https://doi.org/10.1016/0969-806X(93)90054-X.

[15] S. Xie, X. Zhang, Y. Zhang, G. Ying, Q. Huang, J. Xu, and Q. Peng. “Evaluation of various scintillator materials in radiation detector design for positron emission tomography (Pet)”. In: *Crystals* 10.10 (2020), pp. 1–15. ISSN: 20734352. DOI: 10.3390/cryst10100869.

[16] I. V. Khodyuk, S. A. Messina, T. J. Hayden, E. D. Bourret, and G. A. Bizarri. “Optimization of scintillation performance via a combinatorial multi-element co-doping strategy: Application to NaI:Tl”. In: *Journal of Applied Physics* 118.8 (2015). ISSN: 10897550. DOI: 10.1063/1.4928771. URL: http://dx.doi.org/10.1063/1.4928771.

[17] E. Berg, E. Roncali, and S. R. Cherry. “Optimizing light transport in scintillation crystals for time-of-flight PET: an experimental and optical Monte Carlo simulation study”. In: *Biomedical Optics Express* 6.6 (2015), p. 2220. ISSN: 2156-7085. DOI: 10.1364/boe.6.002220. URL: https://doi.org/10.1364/boe.6.002220.

[18] F. A. Danevich, R. V. Kobychev, V. V. Kobychev, H. Kraus, V. B. Mikhailik, and V. M. Mokina. "Optimization of light collection from crystal scintillators for cryogenic experiments". In: *Nuclear Instruments and Methods in Physics Research, Section A: Accelerators, Spectrometers, Detectors and Associated Equipment* 744 (2014), pp. 41–47. ISSN: 01689002. DOI: 10.1016/j.nima.2014.01.042. URL: http://dx.doi.org/10.1016/j.nima.2014.01.042.

[19] S. Min, Y. Kim, K. H. Ko, B. Seo, J. Cheong, C. Roh, and S. Hong. "Optimization of plastic scintillator for detection of gamma-rays: Simulation and experimental study". In: *Chemosensors* 9.9 (2021). ISSN: 22279040. DOI: 10.3390/chemosensors9090239. URL: https://doi.org/10.3390/chemosensors9090239.

[20] Z. Li, Z. Pan, G. Hu, W. Sun, and H. Hu. "Optimization for energy response characteristics of plastic scintillators based on genetic algorithm". In: *AIP Advances* 12.11 (2022), p. 115111. ISSN: 21583226. DOI: 10.1063/5.0124131. URL: https://doi.org/10.1063/5.0124131.

[21] J. A. Kulesza, T. R. Adams, J. C. Armstrong, S. R. Bolding, F. B. Brown, J. S. Bull, T. P. Burke, A. R. Clark, R. A. Forster III, J. F. Giron, T. S. Grieve, C. J. Josey, R. L. Martz, G. W. McKinney, E. J. Pearson, M. E. Rising, C. J. Solomon Jr., S. Swaminarayan, T. J. Trahan, S. C. Wilson, and A. J. Zukaitis. "MCNP® Code Version 6.3.0 Theory & User Manual". In: ed. by J. A. Kulesza. LA-UR-22-30006, Rev. 1. Los Alamos, NM, USA, Sept. 2022. DOI: 10.2172/1889957. URL: https://www.osti.gov/biblio/1889957.

[22] B. Zhao, M. Dong, M. Zhou, Z. Wang, H. Zhao, Y. Niu, T. Hu, and S. Zhao. "Optimization of the scintillator units for the CEPC scintillator-tungsten ECAL". In: *Radiation Detection Technology and Methods* 4.1 (2020), pp. 39–45. ISSN: 25099949. DOI: 10.1007/s41605-019-0146-7. URL: https://doi.org/10.1007/s41605-019-0146-7.

[23] S. Agostinelli *et al.* "GEANT4 - A simulation toolkit". In: *Nuclear Instruments and Methods in Physics Research, Section A: Accelerators, Spectrometers, Detectors and Associated Equipment* 506.3 (2003), pp. 250–303. ISSN: 01689002. DOI: 10.1016/S0168-9002(03)01368-8.

[24] L. M. Rios and N. V. Sahinidis. "Derivative-free optimization: A review of algorithms and comparison of software implementations". In: *Journal of Global Optimization* 56.3 (2013), pp. 1247–1293. ISSN: 09255001. DOI: 10.1007/s10898-012-9951-y. URL: http://dx.doi.org/10.1109/4235.996017.

[25] S. Kumar, Z. Tong, and X. Jiang. "Advances in the design and manufacturing of novel freeform optics". In: *International Journal of Extreme Manufacturing* 4.3 (2022). ISSN: 26317990. DOI: 10.1088/2631-7990/ac7617. URL: https://doi.org/10.1088/2631-7990/ac7617.

[26] C. CMS. *A MIP Timing Detector for the CMS Phase-2 Upgrade*. Tech. rep. Geneva: CERN, 2019. URL: https://cds.cern.ch/record/2667167.

[27] K. Deb, A. Pratap, S. Agarwal, and T. Meyarivan. “A fast and elitist multiobjective genetic algorithm: NSGA-II”. In: *IEEE Transactions on Evolutionary Computation* 6.2 (2002), pp. 182–197. ISSN: 1089778X. DOI: 10.1109/4235.996017. URL: http://dx.doi.org/10.1109/4235.996017.

[28] Geant4 Collaboration. *Geant4 Physics Reference Manual*. Version 10.5. CERN. Geneva, Switzerland, 2019. URL: https://geant4-userdoc.web.cern.ch/UsersGuides/PhysicsReferenceManual/.

[29] C. Geuzaine and J.-F. Remacle. “Gmsh: a three-dimensional finite element mesh generator with built-in pre-and post-processing facilities”. In: *INTERNATIONAL JOURNAL FOR NUMERICAL METHODS IN ENGINEERING Int. J. Numer. Meth. Engng* 0 (2009), pp. 1–24. URL: https://doi.org/10.1002/nme.2579.

[30] C. M. Poole, I. Cornelius, J. V. Trapp, and C. M. Langton. “Fast tessellated solid navigation in GEANT4”. In: *IEEE Transactions on Nuclear Science* 59 (4 PART 3 2012), pp. 1695–1701. ISSN: 00189499. DOI: 10.1109/TNS.2012.2197415. URL: https://doi.org/10.1109/TNS.2012.2197415.

[31] E. Sysoeva, V. Tarasov, and O. Zelenskaya. “Comparison of the methods for determination of scintillation light yield”. In: *Nuclear Instruments and Methods in Physics Research, Section A: Accelerators, Spectrometers, Detectors and Associated Equipment* 486.1-2 (2002), pp. 67–73. ISSN: 01689002. DOI: 10.1016/S0168-9002(02)00676-9. URL: http://dx.doi.org/10.1016/S0168-9002(02)00676-9.

[32] S. E. Derenzo, W. S. Choong, and W. W. Moses. “Fundamental limits of scintillation detector timing precision”. In: *Physics in Medicine and Biology* 59.13 (2014), pp. 3261–3286. ISSN: 13616560. DOI: 10.1088/0031-9155/59/13/3261. URL: https://doi.org/10.1088/0031-9155/59/13/3261.

[33] F. Addesa, P. Barria, R. Bianco, M. Campana, F. Cavallari, A. Cemmi, M. Cipriani, I. Dafinei, B. D’Orsi, D. del Re, M. Diemoz, G. D’Imperio, E. Di Marco, I. Di Sarcina, M. Enculescu, E. Longo, M. Lucchini, F. Marchegiani, P. Meridiani, S. Nisi, G. Organtini, F. Pandolfi, R. Paramatti, V. Pettinacci, C. Quaranta, S. Rahatlou, C. Rovelli, F. Santanastasio, L. Soffi, R. Tramontano, and C. Tully. “Comparative characterization study of LYSO:Ce crystals for timing applications”. In: *Journal of Instrumentation* 17.08 (Aug. 2022), P08028. DOI: 10.1088/1748-0221/17/08/P08028. URL: https://dx.doi.org/10.1088/1748-0221/17/08/P08028.

[34] M. Campana and R. Paramatti. *Study of light output and characterization of LYSO crystals for the new timing detector of the CMS experiment*. Tech. rep. 2018.

[35] F. Loignon-Houle, C. M. Pepin, S. A. Charlebois, and R. Lecomte. “Reflectivity quenching of ESR multilayer polymer film reflector in optically bonded scintillator arrays”. In: *Nuclear Instruments and Methods in Physics Research, Section A: Accelerators, Spectrometers, Detectors and Associated Equipment* 851 (Apr. 2017), pp. 62–67. ISSN: 01689002. DOI: 10.1016/j.nima.2017.01.051. URL: http://dx.doi.org/10.1016/j.nima.2017.01.051.

[36] M. Li and X. Yao. *Quality evaluation of solution sets in multiobjective optimisation: A survey*. Vol. 52. 2. 2019. ISBN: 2016112514. DOI: 10.1145/3300148. URL: http://dx.doi.org/10.1145/3300148.

[37] A. Auger, J. Bader, D. Brockhoff, and E. Zitzler. "Hypervolume-based multiobjective optimization: Theoretical foundations and practical implications". In: *Theoretical Computer Science* 425 (2012), pp. 75–103. ISSN: 03043975. DOI: 10.1016/j.tcs.2011.03.012. URL: http://dx.doi.org/10.1016/j.tcs.2011.03.012.

[38] A. P. Guerreiro, C. M. Fonseca, and L. Paquete. "The Hypervolume Indicator: Computational Problems and Algorithms". In: *ACM Comput. Surv.* 54.6 (July 2021). ISSN: 0360-0300. DOI: 10.1145/3453474. URL: https://doi.org/10.1145/3453474.

[39] K. M. Malan. "A Survey of Advances in Landscape Analysis for Optimisation". In: *Algorithms* 14.2 (2021). ISSN: 1999-4893. DOI: 10.3390/a14020040. URL: https://www.mdpi.com/1999-4893/14/2/40.

[40] E. Auffray, B. Frisch, F. Geraci, A. Ghezzi, S. Gundacker, H. Hillemanns, P. Jarron, T. Meyer, M. Paganoni, K. Pauwels, M. Pizzichemi, and P. Lecoq. "A comprehensive & systematic study of coincidence time resolution and light yield using scintillators of different size, wrapping and doping". In: *2011 IEEE Nuclear Science Symposium Conference Record*. 2011, pp. 64–71. DOI: 10.1109/NSSMIC.2011.6154402.

5

An efficient shape optimization of scintillator crystals through deterministic models

In this paper, we provide an alternative formulation to ray-tracing for the optical modelling and analysis of scintillators through an electromagnetic finite element method (FEM) formulation. We provide the required boundary conditions and material properties to translate the scintillation phenomena from a stochastic definition to an energy pulse. We perform this translation using a non-steady electromagnetic formulation that can provide a measure of the photon energy depositions in the photodetectors with time. Furthermore, we study equivalent frequency domain problems as a surrogate model of the effect of the impacts with respect to their location along the crystal. We compare these models with the results obtained for the equivalent GEANT4 model. This comparison is performed through multiple functions based on the energy deposition within the photodetector material blocks in the simulation and a simplified one-degree-of-freedom parameterized geometry. These functions depend on multiple impacts along the crystals to capture their effect and a corresponding adaptive integration scheme. The results show the importance of self-absorption and boundary conditions for modelling the phenomena. The losses of the frequency domain model are tuned with the GEANT4 model obtaining similar dependencies of the objective function with good agreement of a simplified 1D geometry. We parameterize this model and use it to optimize the numerical shape of the scintillation crystals using FEM and a simplex algorithm. To obtain better designs, we incorporate geometric constraints to ensure the manufacturability of the resulting design. The optimized scintillator shape gains are validated within GEANT4 with gains higher than 7% in the median distribution for light collection. Furthermore, the optimized designs are obtained with a fraction of the time that would take using GEANT4 or a FEM transient model.

5.1. Introduction

Scintillation transforms high-energy particles (e. g., X-rays, gamma rays, muons) into photons in the visible spectrum, enabling detection via photodetectors. This process helps detect radioactive materials for security, both passively and actively, e. g., in cargo inspection [1, 2]. In medicine, scintillation detectors are essential for non-invasive imaging instruments such as PET (positron emission tomography), SPECT (single-photon emission computed tomography), and X-ray scanners [3]. The scientific community also uses this technology for spectrometry and crystallographic studies [4]. Finally, in high energy physics, they allow for more precise identification and research of new particles and physical phenomena [5]. Improvements in the capacity of scintillators to provide higher spatial and temporal resolution allow precise imaging with lower doses, which benefits medical patients and improves early diagnosis. Enhancing the number of photons produced per energy deposited in scintillators can reduce material costs and increase sensitivity to radioactive materials for safety applications [6]. In high-energy physics, fast timing measurements are necessary to handle higher pile-ups, or particle collision bunches, in new accelerators and associated particle detectors [7].

Recent advances in understanding the scintillation phenomena have enabled a higher efficiency of engineered scintillating materials through experimental combinatorial strategies to test doping agents and activators [8]. The literature also shows efforts to reduce radiation damage, which can increase the self-absorption of photons within the crystal, reducing its transparency [9], and afterglow, which can avoid detection of successive impacts due to photons still present in the crystal after the initial impact [10]. However, using these scintillators in extreme environments (such as high-energy physics experiments, nuclear facilities, or outer space) [11] limits the use of cheap organic or plastic scintillators. The use of high-end inorganic scintillators increases costs due to the need for rare-earth elements such as Ce and Re [12]. These scintillators can cost up to $4000/kg [13] and are subject to geopolitical constraints. Additionally, these scintillators often require specialized manufacturing techniques, such as the Czochralski method [14] – growth technique for single crystals – and optical polishing [15].

To reduce their cost, there is an ongoing effort to improve the efficiency of scintillators through methods not based on material composition. Liu *et al.* [16] proposes a cheaper manufacturing method through a glass matrix with embedded high-yield scintillator materials. Developments in sintering scintillating materials have also been shown to reduce manufacturing costs [17]. A similar process is carried out in recent advances in 3D-printing of inorganic crystals [18, 19] through stereolithography and powdered ceramic scintillators, where composition and crystal shape can be controlled locally. Another way to improve the spatial resolution is through the pixelization of the scintillator, which reduces the crosstalk between different channels. This pixelization has been achieved in the literature through vapour-deposition [20] and porous Si filling [21]. Similar research into patterned nanophotonic scintillators is theorized to be able to improve the yield and directionality depending on the spatial distribution of its scintillating centres [22]. In this way, we can observe that the shape and size of the crystal can affect

the scintillation yield in bulk designs, as shown in Xie *et al.* [23] with various macro-scintillator shapes and reflective surface angles tested for PET scanners [24]. Studies on the effect of the shape of the scintillating crystal have also been able to enhance the time resolution [25] and the light collection [26]. These experiments also put effort into studying the coupling surface to the photodetector through embedded photodetectors and curved scintillator surfaces. Another design criterion that can improve the light collection without changing the scintillation intrinsic properties is the outer optical surface and coatings. Several texts deal with improving light collection using different surface finishes, from diffuse to polished optical surfaces. Bircher and Shao [27] show how the roughness of the surface finish can impact the light loss within the scintillator and how this effect is more pronounced the larger the cross-section to length ratio of the scintillator. Kilimchuk, Tarasov, and Vlasova [28] provide a study on the effect of the surface roughness of a scintillator on the light output, providing higher photon counts and double peaks for the spectra of CsI:Tl crystals for finer surface polishes. However, Ghal-Eh and Koohi-Fayegh [29] show that a diffuse paint coating can reduce the number of reflections that the photons experience before reaching the photodetectors. Romanchek *et al.* [30] show how optical coupling using grease can affect the overall light collection and how these interfaces respond to temperature changes. Furthermore, current research in photonic crystals has been applied and measured to increase the light output of scintillators and resolution by reducing photon loss, focusing scintillation photons into the photodetector [31]. Surani *et al.* [32] show an example of the design process of photonic crystals (PhCs) applied to scintillators requiring an interface between the FDTD (finite differences in the time domain) and ray-tracing libraries (GEANT4 [33]). Using FDTD Yasar *et al.* [34] study PhCs made of scintillators for a higher spatial resolution X-ray detector. Although the literature shows several paths for improving the efficiency of scintillating crystals, experimental measurements are costly and time-consuming. GEANT4 can be used to improve the efficiency of particle detectors through parameter analysis Binkley [35]. Using particle-matter interaction codes to extract the optical wave pulse and using an FDTD software to simulate it provides a faster and more economical method to test multiple designs before production. Deilami *et al.* [36] use COMSOL to simulate and select the optimized pair of scintillator and photodiode for nine different designs. Elsey *et al.* [37] study the coupling of a scintillator to an optical fibre using an analytical model and a numerical approach for more complex shapes.

While being a particle-matter interaction effect, our primary focus on improving the scintillating efficiency is on photon generation and detection. In this manner, there are deterministic approaches to model electromagnetic waves that are more computationally efficient than Monte Carlo-based particle-matter interaction software that can provide faster optimization procedures and ease of post-processing. Although FDTD has been used in optical modelling and for the coupling of ray-tracing to wave description for the design of photonic crystals [38], it is not well-posed for complex geometries [39]. Furthermore, the use of a finite element method (FEM) or FDTD scintillating model can remove the need to interface the ray-tracing libraries to design photonic crystals and provide analytical derivatives

to move along the design space. These simulations, while faster, should also be compared to the results used within GEANT4 to validate the sensitivity to the results of the different parameters studied.

In this paper, we propose a model through FEM using COMSOL [40] for an ionizing particle impact in a scintillator crystal detector. The detector studied is based on the MTD-BTL (Minimum Ionizing Particle Timing Detector - Barrel Timing Layer) to be installed in the CMS (Compact Muon Solenoid) at CERN. We study a one-degree-of-freedom (1DOF) design space with the energy deposition from an equivalent electromagnetic wave at the point of impact. We compare transient and frequency space models and validate the results obtained through GEANT4. The FEM-based models that agree with the GEANT4 result's objective function shapes provide optimized scintillator geometries. Finally, we compare the optimized shapes with their light collection outputs in GEANT4. This output results in a less computationally costly approach to testing scintillator shapes.

5.2. Methodology

To reduce the calculation cost of modelling and optimizing scintillators using FEM, a unified framework linking particle-matter interactions and FEM calculations is necessary. Establishing this requires a simplified geometry compatible with GEANT4 and COMSOL and a shared metric for comparison. This section outlines the detector geometry and its corresponding models in both software packages, detailing the physical equations used to simulate photon propagation and scintillation in GEANT4 and COMSOL. To integrate these stochastic processes into FEM, the methodology translates them into a continuous electromagnetic pulse. This pulse is implemented in COMSOL as a boundary condition, which is detailed in this section. With the established physics framework, the section defines the optimization objectives and constraints for scintillator shape optimization in COMSOL.

5.2.1. Geometry

This research is based on the BTL detector geometry, comprising a rectangular LYSO:Ce scintillation bar of a rectangular cross-section attached to a silicon photodetector package with sensors at the end of each bar. In GEANT4, it is represented as a horizontal bar along the z-axis with a square cross-section of 3×3 mm and a 57 mm length. The crystal is bonded to a resin package containing two photodetectors per bar. An OpenGL-based rendering in Figure 5.1 shows the assembly submerged within a block made of air, with the coordinate axes displayed for orientation.

This configuration is simplified for a FEM model in COMSOL using a 2D model with the cross-section of the crystal in the $y-z$ plane of GEANT4 Figure 5.2. In this geometry, we can further appreciate the cross-section of the photodetector package. This package is bonded to the scintillator using an optical RTV-45 glue. An optical resin also protects the photodetectors. The muon impact that causes the generation of light within the scintillator is defined in the FEM model as a discontinuity for the application of the corresponding boundary conditions along the y-axis in COMSOL.

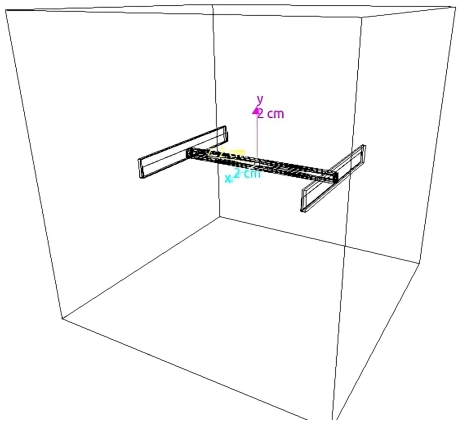

Figure 5.1.: OpenGL rendering of a LYSO bar with square cross-section along the z axis and associated photodetector packages at its ends within GEANT4.

The reference system showed in Figure 5.2 also establishes the zero in the middle of the crystal and a nominal full length of 57 mm. We also introduce a non-dimensional variable I_p representing the location of the impact along x with a transformation over the overall length $I_p = \frac{x}{LYSO_L}$.

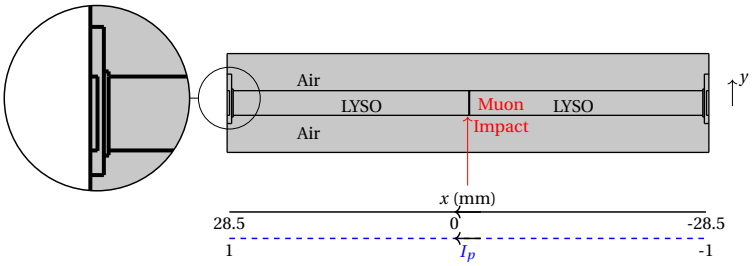

Figure 5.2.: 2D FEM representation of the scintillator detector in COMSOL including a LYSO-Air interface and the photodetector at the end of the scintillator of 57 mm of length in x. This photodetector comprises glue, resin, and silicon layers or blocks, with the silicon block being the sensitive area. The muon impact is represented as a discontinuity in the crystal for applying the boundary conditions, where the muon flies in the positive y axis direction.

The modelling and optimization of the photodetector or silicon photomultipliers (SiPMs) is a separate problem. Because this leads to increased power consumption for the particle detector in higher detection areas, it will not be optimized in the following studies.

5.2.2. Scintillation modeling

The GEANT4 and COMSOL models must provide an equivalent model for light collection from the scintillation process. The physical scintillation process is described in Korzhik, Tamulaitis, and Vasil'ev [41]. The process begins with an ionizing particle that deposits energy into a scintillating material. This energy deposition per unit distance, $\frac{d\mathscr{E}}{dl}$, depends on the material and particle properties and can be obtained from pre-computed tables from the GEANT4 libraries. The deposited energy is converted to a total number of emitted photons N_p, calculated using the experimentally measured light yield of the material Y. This is expressed as

$$N_p = \int_l \frac{d\mathscr{E}}{dl} Y \delta l \approx \frac{d\mathscr{E}}{dl} Y \Delta l, \tag{5.1}$$

where l represents the particle path length through the scintillator.

These photons are generated over time, following an exponential rise and decay, as described by

$$N(t) = N_p \left(\exp\left\{ \frac{t}{t_r} \right\} - \exp\left\{ \frac{t}{t_d} \right\} \right). \tag{5.2}$$

In Equation (5.2), the total number of photons created in time $N(t)$, depends on the rise time t_r and decay time t_d of the scintillator material. The wavelength of these photons arises from an intensity function defined by the user. The scintillation properties for the GEANT4 model have been extracted from Reales *et al.* [42]. The wavelength intensity distribution for LYSO:Ce has a peak at 420 nm that will be used as the nominal wavelength for the emitted photons in the deterministic models.

Finally, the photons are emitted in random directions from the interaction point. Ray-tracing is traditionally used to follow the path of each of these photons until they disappear due to self-absorption within the material involved or leave the space of study.

5.2.3. Finite Element Representation

Rather than using ray tracing within a particle matter interaction software, COMSOL can solve the continuum electromagnetic equations through FEM. Although there is a particle-wave duality description of the photon, the conversion from a ray-tracing simulation algorithm to a continuous description through FEM is not evident. In this section, we detail the equations used within COMSOL in transient- and frequency-domain FEM models to obtain an equivalent description of the previously detailed scintillation process.

Transient Electromagnetic modeling

The electromagnetic equations used by COMSOL depending on time t take the form

$$\mu_0 \sigma \frac{\partial \mathbf{A}}{\partial t} + \mu_0 \epsilon_0 \frac{\partial}{\partial t} \left(\epsilon_r \frac{\partial \mathbf{A}}{\partial t} \right) + \nabla \times \left(\mu_r^{-1} \nabla \times \mathbf{A} \right) = 0 . \tag{5.3}$$

To solve the electromagnetic equations in a given medium, we must define each material's relative magnetic permeability μ_r, electrical relative permittivity ϵ_r, and

electrical conductivity σ. These equations depend on the vacuum permeability and permittivity constants (μ_0, ϵ_0) and are solved for the magnetic potential $\mathbf{A}$ in each time step. This magnetic potential can be related to the electrical and magnetic fields through the relations

$$\mathbf{B} = \nabla \times \mathbf{A}, \tag{5.4}$$

$$\mathbf{E} = -\nabla V - \frac{\partial \mathbf{A}}{\partial t}, \tag{5.5}$$

which provide the fields of interest for the scintillation process. The results of this differential equation require boundary conditions to be solved, which must define the scintillation light pulse.

To simulate the scintillation energy pulse, we introduce, in a cut along the scintillator in the y direction, see Figure 5.2, a scattered electrical wave of a known amplitude $|\mathbf{E}(t)|$. The energy injection of this wave must correlate with the scintillation phenomena in the given material. Given that we work with dielectric isotropic materials, the electrical energy of the wave can be defined as

$$W_e = \int_{\Gamma_I} \left(\int_{t_i(l)}^{T} \frac{1}{2} \epsilon \epsilon_r \mathbf{E} \cdot \mathbf{E} \, dt \right) d\Gamma_I, \tag{5.6}$$

where T is the evaluation time of the simulation, t_i represents the time at which photon generation begins or the time of impact, and Γ_I is the integration domain, equal to the previously defined vertical line used for the boundary condition or impact location for the ionizing particle. The total electrical energy deposited in the scintillation process can also be written as,

$$W_e = \sum_{i=1}^{N_p} \frac{hc}{\lambda_i} \approx \frac{hc}{\lambda_p} N_p, \tag{5.7}$$

where we substitute the wavelength of each photon λ_i created by the peak of the wavelength intensity λ_p of 420 nm and its time evolution is given by Equation (5.2). Given $T >> t_r >> t_i(l) \approx 0$ we consider the electric field independent on the y coordinate along the impact location, $\mathbf{E} = \mathbf{E}(t)$. The equality between Equations (5.6) and (5.7) provides the electric field norm

$$|E| = K^2 \left(\exp\left\{ \frac{t}{2 t_d} \right\} \sqrt{1 - \exp\left\{ \frac{t (t_r - t_d)}{t_d t_r} \right\}} \right). \tag{5.8}$$

In the previous equation, K is a proportionality constant. For $t_d >> t_r$, the term within the square root can be deprecated for the integral calculation leading to a relation between the scintillation and FEM energy deposition of,

$$K^2 \approx \frac{\frac{hc}{\lambda} \frac{d\mathscr{E}}{dl} Y}{\epsilon_r \epsilon_0 t_d \left(-1 + \exp\left\{ \frac{T}{t_d} \right\} \right)}. \tag{5.9}$$

valid for a $T >> t_d$ so that most of the photon energy has been released by the end of the COMSOL scintillation simulation. Finally, to define the electric value by each

one of its components, and considering a polarized wave along $(1,1)$, we remove the absolute value from the electric field with a factor of $\frac{1}{\sqrt{3}}$ in each component of $\mathbf{E}$.

The previous scintillation wave description provides an approximation of energy deposition over time where $T >> t_d >> t_r$ and $T >> t_i(l)$. To consider the ionizing particle characteristic time across the crystal, we can modify this deposition depending on $t_i(l)$, given the speed of the ionizing particle along the crystal. Considering the movement of the impacting particle along the y-axis, t_i can be written as

$$t_i = t - (y - y_{min})/v_\mu = t - t_0(y), \tag{5.10}$$

where t is the absolute simulation time, v_μ is the velocity of the ionizing particle, and y_{min} is the location along the muon path smaller than the minimum y location of the scattering boundary condition that introduces the scintillation wave into the system.

To avoid numerical issues while solving the electromagnetic equations, we add a step function approximated by a Heaviside equation to ensure no energy deposition is introduced in the model before $t_0(y)$,

$$H_{\beta,t_0}(t) = \frac{1}{2}\left[1 + \tanh\left(\frac{t - t_0}{\beta}\right)\right]. \tag{5.11}$$

The steepness of this Heaviside function depends on the β parameter, which needs to be small compared to the characteristic scintillation rise time, $\beta << t_r$. To avoid an intensity source in direct contact with the air, leading to electric energy released in the air medium, we can add two more Heaviside functions dependent on the maximum and minimum y values of the impact surface,

$$H_{\beta_y,y_{min}}(y) = \frac{1}{2}\left[1 + \tanh\left(\frac{y - y_{min}}{\beta_y}\right)\right], \tag{5.12}$$

$$H_{\beta_y,y_{max}}(y) = 1 - \frac{1}{2}\left[1 + \tanh\left(\frac{y - y_{max}}{\beta_y}\right)\right]. \tag{5.13}$$

Finally, the intensity of the input electric wave in each direction takes the form

$$E_i(y) = \frac{K}{\sqrt{3}}\left(\exp\left\{\frac{t - t_0}{2t_d}\right\}\sqrt{1 - \exp\left\{\frac{(t - t_0)(t_r - t_d)}{t_d t_r}\right\}}\right) H_{\beta,t_0} H_{\beta_y,y_{min}} H_{\beta_y,y_{max}}. \tag{5.14}$$

All the remaining boundary conditions to the system are defined as plane wave scattering surfaces to remove as much electrical energy arriving from the system as possible.

Frequency Domain

While a transient solution provides information on the time of arrival of the photons to the photodetector, this leads to a FEM solution per time step. To save computational time, the electromagnetic equations can be rewritten using a known solution for the electric and magnetic fields of sinusoidal shape,

$$\mathbf{E} = \mathbf{E}e^{j\omega t}, \mathbf{H} = \mathbf{H}e^{j\omega t}, \tag{5.15}$$

The equation to solve the electric field then looks like,

$$\nabla \times (\nabla \times \mathbf{E}) - k_0^2 \bar{n}^2 \mathbf{E} = \mathbf{0} \tag{5.16}$$

In this equation, $\bar{n}$ considers the real and imaginary parts of the refractive index,

$$\bar{n} = n - jk, \tag{5.17}$$

with k being the extinction coefficient directly related to the dielectric losses within the material and related to the absorption lengths L and the photon wavelength used by GEANT4 as

$$k = \frac{\lambda}{4\pi L}. \tag{5.18}$$

Finally, the wave number k_0 is defined as

$$k_0 = \frac{\omega}{c_0}, \tag{5.19}$$

with c_0 the speed of light in vacuum and ω the angular frequency of the wave.

The boundary conditions in this model, which introduce the harmonic wave, require an electric field amplitude. For simplification purposes, the amplitude is defined as a constant in all directions, representing the scintillation pulse. This simplified approach assumes a purely harmonic input and response, which does not reflect the actual scintillation process. However, it captures the influence of reflective surfaces and surface-dependent energy deposition when the wavelength is short enough to interact with the scintillator. The rest of the boundary conditions are the same as those of the transient COMSOL model.

This formulation reduces the cost of solving multiple time steps at the expense of requiring a mesh resolution small enough to capture the introduced wavelengths, typically at least ten times lower than the wavelength. This limits how small a wavelength can be accurately modelled for large design spaces in terms of memory requirements.

Numerical Optimization

We not only want to have a numerical model using FEM that can represent the dependence of the light collection of the scintillator depending on its shape but also to numerically optimize its design. For this purpose, we parameterize the scintillator's top and bottom boundaries through splines to study different reflective surfaces of the LYSO crystals. However, the impact location along the x axis of the crystal, its distance to each photodetector, and the energy deposition also play a role in the photodetectors' overall energy absorption.

To take into account the energy deposition at different impacts along x, we use the symmetry conditions at $x = 0$ and evaluate the energy deposition in the Si block over multiple impacts along x. The overall objective function can be written as,

$$\Phi = -\int_{I_0}^{I_1} \Psi\left(|\mathbf{E}|^2\right) \mathrm{d}I_p \tag{5.20}$$

where Ψ is the function depending on the crystal's impact location along I_p, and we integrate over a region $I_0 < I_p < I_1$. This objective function needs to be a measure of the number of photons detected in the photodetectors or, in the case of FEM, the electrical energy deposited. The objective function also introduces a minus sign, as typical optimizers are designed to minimize the objective. At the same time, we look to maximize the absorbed energy, and the energy always provides a value greater than zero.

To avoid unnecessary simulations and computational time and ensure a given tolerance of the result, we use an adaptive Simpson's integration to solve the previous integral over the impact location of the crystals. This adaptive integration decides on the number of evaluation points, comparing the integration values with an s size interval between a and b from a user input preset interval through the error estimation based on the Simpsons' rules given by

$$Q1(s) = \frac{s}{3}\left(\Phi(a) + 4\Phi\left(\frac{a+b}{2}\right) + \Phi(b)\right), \tag{5.21}$$

$$Q2(s/2) = \frac{s}{6}\left(\Phi(a) + 4\Phi\left(a + \frac{b-a}{4}\right) + 2\Phi\left(\frac{a+b}{2}\right) + 4\Phi\left(a + \frac{3(b-a)}{4}\right) + \Phi(b)\right). \tag{5.22}$$

The error for a given interval can be given as,

$$Error = \left|\frac{1}{15}(Q2 - Q1)\right|. \tag{5.23}$$

The Simpsons rule provides fast convergence with a small number of function evaluations for functions well approximated by cubic polynomials. If this were not true, a more sophisticated integration, such as the Kronrod or Chlenshaw-Curtis quadratures, should be used for the objective function.

Besides the objective function, we need to impose a volume constraint on the LYSO material to avoid higher material-associated costs, noticing that a higher material thickness will always provide higher energy deposition by the impacting ionizing particles. This volume constraint can be defined as,

$$c_v = \frac{v_{LYSO}}{v_0} - 1 < 0, \tag{5.24}$$

the value of the constraint c_v must be maintained lower than zero to be satisfied, depending on a maximum volume given as an input v_0 and the current geometry volume v_{LYSO}, depending on the design variables.

The overall optimization for the FEM calculation can be defined as

$$\mathbf{y} = \underset{\mathbf{y}}{\arg\min} \quad \Phi(\Psi(\mathbf{y})) = -\int_{I_0}^{I_1} \Psi\left(|\mathbf{E}|^2\right) \mathrm{d}I_p\,, \tag{5.25a}$$

$$\text{subject to:} \quad c_v = \frac{v_{LYSO}}{v_0} - 1 < 0\,, \tag{5.25b}$$

$$\oint_{\partial V} \mathbf{E} \cdot d\mathbf{A} = \frac{Q}{\epsilon_0}\,, \tag{5.25c}$$

$$\oint_{\partial V} \mathbf{B} \cdot d\mathbf{A} = 0\,, \tag{5.25d}$$

$$\oint_{\partial S} \mathbf{E} \cdot d\mathbf{l} = -\frac{d}{dt}\int_S \mathbf{B} \cdot d\mathbf{A}\,, \tag{5.25e}$$

$$\oint_{\partial S} \mathbf{B} \cdot d\mathbf{l} = \mu_0 I + \mu_0 \epsilon_0 \frac{d}{dt}\int_S \mathbf{E} \cdot d\mathbf{A}\,, \tag{5.25f}$$

where we want to minimize our objective function dependent upon a measure of the electric field norm and the impact location of our particle with respect to a series of design variables $\mathbf{y}$. The Maxwell's equations we need to solve, Equations (5.25c) to (5.25f), can be tailored to either transient or frequency domain FEM calculations.

We use a Simplex exploration algorithm within the 'fminsearchbnd' MATLAB function for the optimization algorithm. This implementation provides a design space pattern search without requiring derivatives and the ability to handle bound constraints on the design variables. With $\boldsymbol{\theta}$ being the vector of variables with bounds according to $\mathbf{L} \leq \boldsymbol{\theta} \leq \mathbf{U}$, the transformation function maps the bounded variables θ to an unbounded space $\boldsymbol{\theta}'$ where the simplex search algorithm can be applied. This transformation is defined mathematically as

$$\theta_i' = \begin{cases} \log(\theta_i - L_i) & \text{if } \theta_i \text{ is bounded below only,} \\ \log(U_i - \theta_i) & \text{if } \theta_i \text{ is bounded above only,} \\ \log\left(\frac{\theta_i - L_i}{U_i - \theta_i}\right) & \text{if } \theta_i \text{ is bounded both below and above.} \end{cases} \tag{5.26}$$

The inverse transformation provides the objective design variables.

5.3. Results

This section summarises the results obtained from the developed COMSOL model defined in the previous section. These results include a comparison with the scintillation results from GEANT4 for both the transient- and frequency-domain FEM models. This study consists of the transient model's pulse shape and the transient model's absolute energy deposition. For both FEM approaches, we study a simplified 1D parameterized model with constant volume and its design space. An agreement of this 1D model between GEANT4 and COMSOL ensures that the shape and influence of the objective function have an equivalent behaviour depending on the design variables.

The material properties for the scintillation in GEANT4 are summarized in Appendix F and those used for the COMSOL models in Appendix G. The

physics-controlled mesh in COMSOL automatically adapts the mesh element size based on the physics involved and the material properties. For electromagnetic simulations, we use standard triangular linear elements and the mesh element size is scaled relative to the wavelength in each medium, typically set to about one-fifth of the vacuum wavelength in 3D with quadratic elements. This approach ensures accurate resolution of wave behaviour while maintaining computational efficiency. Additionally, the mesh refines near material interfaces and sources, providing a balanced and reliable discretization for all simulations.

5.3.1. Comparison of scintillation models

The methodology section defines boundary conditions to replicate the energy deposition from scintillation in the FEM transient simulation (Equation (5.8)). To evaluate the processes in GEANT4 and COMSOL, the number of photons reaching the photodetectors is analyzed. This metric is derived from the overall energy deposition, as done for photons generated through scintillation (Equation (5.6)). This approach measures the scintillation shape's efficiency, correlating the total photons created with those detected for physical measurements. We can first compare the GEANT4 and COMSOL models in terms of the overall electric energy collection per unit of time. Figure 5.3a shows a histogram of the total number of photons arriving at the photodetector N_a per unit of time and width of the SiPMs – as the GEANT4 simulation is performed in 3D against a 2D simulation in COMSOL – with respect to the total number of photons created in the scintillation process N_p. Assuming minor wavelength deviations, the photon ratio is proportional to the energy ratio of created to absorbed photons (Equation (5.6)). We plot the results from COMSOL in Figure 5.3a, a line representing the energy deposition in the Si block surface W_a with respect to the total electric energy deposited in the boundary condition for the entire simulation time W_i. Figure 5.3b shows for both of these plots the total integrated ratio in time.

The results show that both plots have the same temporal behaviour. These plots follow the exponential rise and decay of the energy introduced into the system. The rise time in these plots is so fast compared to the design study time that the overall pulse is barely perceptible, validating the assumption $T >> t_d >> t_r$. The absolute values depend on the representation and width of the GEANT4 histogram. However, the COMSOL simulation does not include losses within the material, and the FEM model simplification implies an infinite crystal along the z axis, disregarding the effect of the impacts along this direction on the energy deposition. Overall, the total energy deposition is expected to be higher in COMSOL. Figure 5.3b shows that the ratio of energy deposition in the COMSOL model is more than twice that obtained in GEANT4.

Although the absolute values do not correspond between COMSOL and GEANT4, we only need to obtain the same relative effect of the design variables to obtain designs that improve our objective function through numerical optimization. For this reason, we study a simple design space of a simplified geometrical tapered configuration with a single design variable. This simplified configuration is represented in Figure 5.4. This geometry uses symmetry in the location $x = 0$

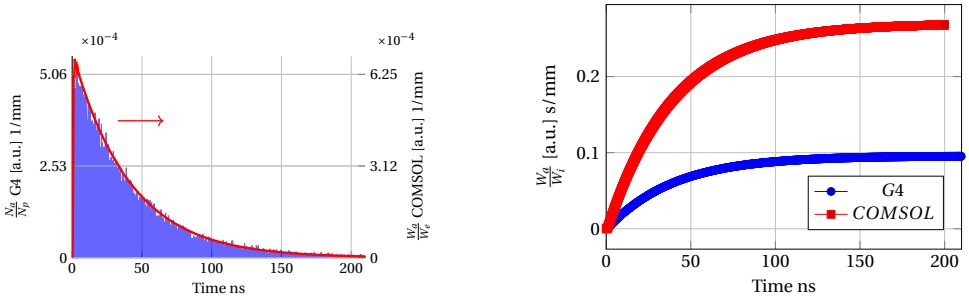

(a) (b)

Figure 5.3.: Comparison for the energy deposition using GEANT4 and a transient COMSOL model for an impact at $I_p = 0$. Figure 5.3a shows the histogram of the number of photons obtained in G4 per number of photons created and unit of width of the SiPM compared to the energy intensity received in the photodetector using COMSOL per total energy introduced. Figure 5.3b shows the integration in time of the functions used in Figure 5.3a.

5

and $y = 0$ and a reference half-thickness of $y_0 = 1.5\,\text{mm}$. The design is further parameterized through a single degree of freedom (DOF) $\Theta \in (0,2)$. The result is a geometric parameterization of a constant volume. This allows us to compare the light collection without an overall increase in material in the design. This geometry simplification is represented in Figure 5.4.

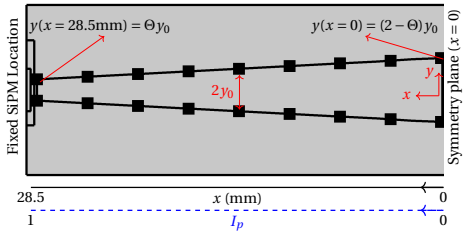

Figure 5.4.: 1DOF tapered geometric model simplification of the scintillator geometry through an extra symmetry axis along $x = 0$ and $y = 0$ defined through the variable Θ using a default thickness of $y_0 = 1.5\,\text{mm}$.

1DOF geometric model base response in GEANT4

With the previous geometry for the crystals, we use GEANT4 to study the effect of Θ with a sweep from 0.25 to 1.75 over a measurement of the number of impacting photons. For this measurement, we use the light collection per energy deposited in

the scintillator $\mathscr{E}$ and path length within the crystal Δl,

$$L_{SP} = \frac{N_a}{\mathscr{E}} \Delta l, \tag{5.27}$$

where N_a is the number of photons that arrived at the photodetector. This function provides information on the energy deposition within the photodetectors. The advantage of this function is the removal of the tails from the energy deposition of the ionizing particle, associated with a Landau function, while maintaining its information through the particle track length within the crystal. Figure 5.5a shows the L_{SP} distributions for five geometries according to Figure 5.4 and increasing values of Θ. For each one of these tapered geometries, 60 events or particle impacts are run for an increased value of I_p between zero and one and the corresponding boxplot is represented. For each Θ, the average L_{SP} for each I_p is used to plot a quadratic fit through a dashed red line. The results show the dependence of L_{SP} on the impact across the length of the crystal. If we start from a configuration of $\Theta = 0.5$, we can see that until we reach a value of $\Theta = 1$, the L_{SP} suffers a vertical translation to higher values for a higher Θ.

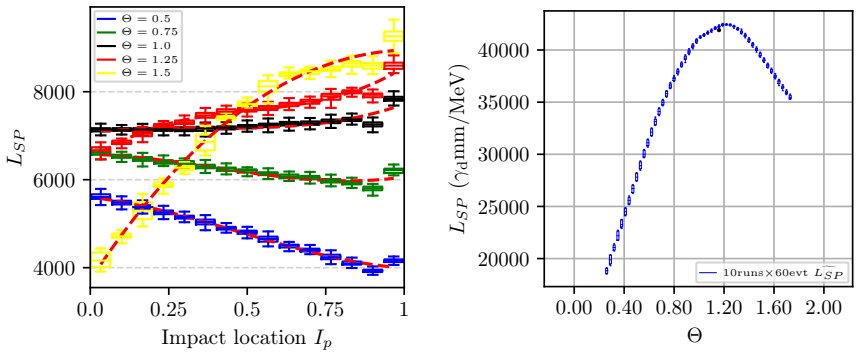

(a) (b)

Figure 5.5.: Figure 5.5a shows the dependence of light collection per energy deposition and track length on the impact point for five different Θ values and a dashed quadratic fit (red dashed lines) to their mean following the 1DOF model description in GEANT4. Figure 5.5b shows the design space of the GEANT4 simulation of the averaged L_{SP} for 10 runs, each one of 60 events equally spaced in the x axis, depending on Θ.

As in this case, the crystal is smaller than the photodetector, and most of these losses arise from self-absorption in the crystal. After we reach a value of $\Theta = 1$, increasing the taper leads to a smaller thickness in the middle of the crystal, with lower L_{SP} from impacts at this location. This configuration also leads to higher photon losses to the environment with a crystal larger than the photodetector in the contact region. However, the larger sensitivity of the L_{SP} to the material close to the photodetector can keep increasing its value for small values of Θ over one. This

leads to an optimum value for the taper depending on the material arrangement and environmental losses. The overall design space is shown in Figure 5.5b. This plot shows the boxplot representation of the average L_{SP} from 10 different simulations using 60 impacts uniformly distributed along the length of the crystal for each one. The average value of L_{SP}, which we call $\widetilde{L_{SP}}$, shows a maximum for Θ close to the value of 1.2.

In Figure 5.5a, we also observe discontinuities near the end of the crystal, $I_0 \approx 0.9$, because of the proximity to the optical surface. The edge of the crystals should be discounted from the region of interest for the scintillator, given the outlier effect over the distribution.

To obtain a satisfactory characterization of scintillation crystals through other models, we should be able to replicate the dependencies on Θ observed in Figure 5.5a and Figure 5.5b.

1DOF geometric model response in the Transient Pulse Design Space

A transient model for scintillation is most beneficial in obtaining the arrival distribution of the photons into the photodetectors, as shown in Figure 5.3a. However, this formulation's lack of material self-absorption causes significant differences in the energy deposition in the SiPMs as seen in Figure 5.3b. To compare against the design space depending on Θ in this model, we use the function

$$\Phi_t = \Phi(\Psi_t(\phi(\Theta))) = -\int_{I_0}^{I_1}\int_0^T\int_{\Gamma_w} \phi \mathrm{d}\Gamma_w \mathrm{d}t\,\mathrm{d}I_p = -\int_{I_0}^{I_1}\int_0^T\int_{\Gamma_w} \frac{1}{2}\epsilon\epsilon_r \mathbf{E}\cdot\mathbf{E}\mathrm{d}\Gamma_w \mathrm{d}t\,\mathrm{d}I_p\,, \tag{5.28}$$

which calculates the total electrical energy deposition of the scintillation electromagnetic wave into the SiPM area Γ_w during a simulation time T with the same importance for all impact points between I_0 and I_1. These two points are selected according to the GEANT4 results as $I_p \in [I_0, I_1] = [0.05, 0.9]$. This range avoids possible discontinuities at $I_p = 0$ and close distance to the SiPMs. Figure 5.6a provides the dependence of the electric energy deposition Ψ_t with respect to the impact location for multiple Θ values. This plot leads to a design space where there is no vertical translation of the light collection dependent on the impact location as in Figure 5.5a. All geometries depending on Θ provide an energy deposition that crosses at $I_p = 0.5$ while maintaining a discontinuity close to the edge of the crystal, $Ip \approx 1$, with an exponential increase in energy deposition. Looking into the design space for the 1DOF model, the lack of material self-absorption translates into a higher light collection for a Θ smaller than 1 where a larger number of photons are created in the middle of the crystal and which reach the photodetector through a larger path length than in GEANT4.

This lack of self-absorption for these dielectric materials can be remedied by adding electrical losses through an electrical conductivity value greater than zero. However, the definition of this electrical conductivity is not evident for an equivalent model. The provided formulation is based on the relative permittivity and electrical conductivity in COMSOL. The permittivity can be written as,

$$\bar{\epsilon} = \epsilon + \epsilon' = \bar{n}^2 = n^2 - k^2 - 2nkj\,, \tag{5.29}$$

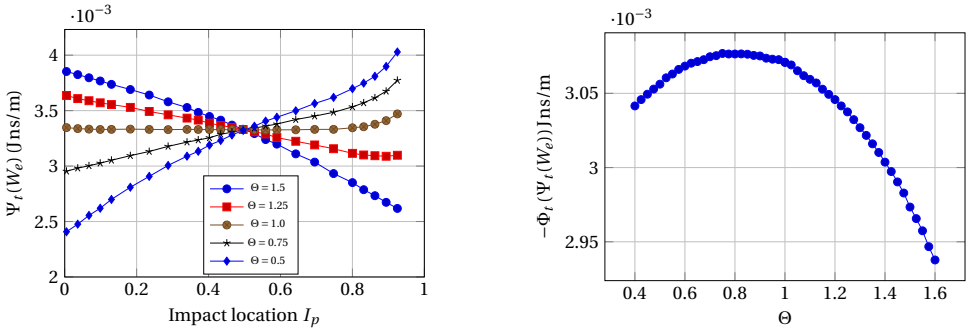

(a) (b)

Figure 5.6.: Figure 5.6a shows the dependence of light collection per energy deposition and track length on the impact point for five different Θ values following the 1D model description in COMSOL. Figure 5.6b shows the design space of the transient COMSOL simulation of the $-\Phi_t(\Psi_t(W_e))$ Jns/m function depending on Θ.

5

where the complex part of the permittivity can be related to the losses due to the electrical conductivity of the material σ. This relation is given by the respective angular frequency ω,

$$\epsilon_0 \epsilon' \frac{2\pi c}{\lambda} = \sigma \,. \tag{5.30}$$

This relation can be used to calculate ϵ' from the electrical conductivity and solve Equation (5.16) considering these losses. However, the scintillation decay process lacks a defined angular frequency. The model relies on determining a λ that replicates the expected losses.

1DOF geometric model response in the Frequency Domain Design Space

In the steady results in the frequency domain, we simplify the integral of the objective function to an integral over the impact location and over the SiPM surface of the electric field as

$$\Phi_f = \Phi(\Psi_f(\phi(\Theta))) = -\int_{I_0}^{I_1}\int_{\Gamma_w} \phi \mathrm{d}\Gamma_w \,\mathrm{d}I_p = -\int_{I_0}^{I_1}\int_{\Gamma_w} \left(|\mathbf{E}|^2\right) \mathrm{d}\Gamma_w \,\mathrm{d}I_p \,. \tag{5.31}$$

The value in the surface integral is proportional to the energy deposition per surface area W_e and can save computational time.

For this model, we must select a given wavelength for the input sinusoidal wave at the impact location. For this reason, we need to strike a balance between the higher memory for the FEM calculation due to mesh refinement needed for smaller wavelength and the computational complexity of the simulation while maintaining the losses expected from the GEANT4 model. These losses mainly arise from self-absorption and the confinement factor within the scintillator. The losses can

be modelled as an exponential decay of the field amplitude from the origin of the source

$$|\mathbf{E}(\mathbf{x})| = |\mathbf{E}_0| e^{-\alpha|\mathbf{x}|},$$

with the attenuation constant

$$\alpha = \alpha_L + \alpha_\Gamma = \frac{2\pi k}{\lambda} + \alpha_\Gamma(\lambda).$$

The first source of losses α_L is due to the material losses. The second source of losses α_Γ arises from radiation losses. We can have a measure of the radiation losses for leaky modes through the confinement factor. These radiation losses for leaky modes can be expressed as the ratio of the power of the confinement factor. This measurement is a ratio between the power that escapes to the surrounding environment in the form of evanescent waves compared to the guided power along a waveguide. According to Saleh and Teich [43], for the fundamental TE mode in a symmetrical slab waveguide, the confinement factor can be estimated as

$$\Gamma = \frac{P_{\text{core}}}{P} = \frac{\int_{-d}^{+d} \varepsilon(x)|\mathbf{E}(x)|^2\, dx}{\int_{-\infty}^{+\infty} \varepsilon(x)|\mathbf{E}(x)|^2\, dx} \approx \frac{1}{1 + \frac{2}{V^2}}, \tag{5.32}$$

where, V is the normalized frequency

$$V = \frac{2\pi}{\lambda} \cdot \frac{d}{2} \cdot \sqrt{n_1^2 - n_2^2}. \tag{5.33}$$

In this equation, d is the core width, n_1 is the core refractive index, and n_2 is the surrounding material refractive index. Hu and Menyuk [44] studies in detail radiation losses in leaky modes for slab waveguides.

For a higher wavelength, we can see that the confinement decreases, leading to higher power losses, being the main cause of losses up to the photodetector, while for lower wavelengths, self-absorption becomes important. As we want to reach an equilibrium between mesh size and accurate losses within the crystals, we estimate the highest wavelength we can study before the wave becomes evanescent. This frequency can be estimated through the cutoff wavelength for each mode m, which can be calculated through

$$\lambda_{\text{cutoff},m} = \frac{2d}{m}\sqrt{n_1^2 - n_2^2}, \tag{5.34}$$

where m is the integer defining the mode. Only modes with $\lambda < \lambda_{\text{cutoff},m}$ remain confined in the core of a waveguide. For the first mode we get a cutoff wavelength of approximate 9.34 mm for a width of 3 mm of the LYSO and of 14 mm for a width of 4.5 mm. Given the tapered shape of the benchmark, we start testing the simulation results at an intermediate value of 12 mm wavelengths. For this purpose, we study a mesh convergence of the different settings of the physics-informed mesh creation from COMSOL. The results of this mesh convergence are shown in Figure 5.7 with

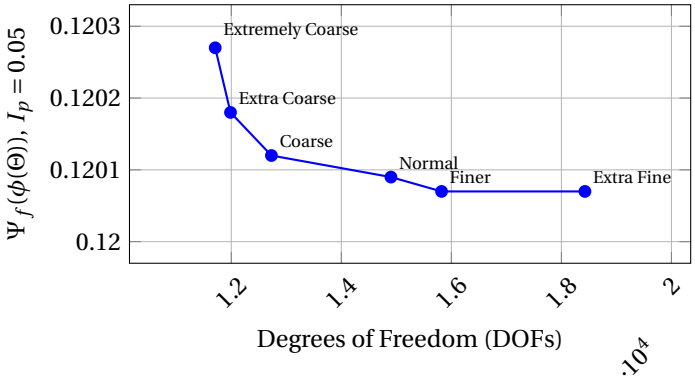

Figure 5.7.: Mesh convergence of $\Psi_f(\phi(\Theta))$ for $I_p = 0.05$ versus the number of degrees of freedom created by each physics-controlled mesh in COMSOL.

respect to the settings used, the number of degrees of freedom and the resulting objective for an impact point at the middle of the crystals, $I_p = 0.05$. In the rest of the studies, a *Normal* setting for meshing is used.

In Figure 5.8, the design space for the wavelength of 12 mm is shown concerning the design variable Θ. Comparing Figure 5.8a to the results in GEANT4 for energy deposition concerning the location of the impact, we can identify a similar trend in the relative location of each curve concerning the variable Θ, except for its sinusoidal nature. Higher values of Θ provide higher energy depositions closer to the photodetector, whereas impacts close to the middle of the crystal for these Θ provide smaller objective values due to the smaller energy introduced into the system. For $\Theta < 1$, the optical surfaces lead to higher self-absorption of the electric wave within the scintillator, displacing these curves to smaller objective values. This leads to a design space comparable to that shown in Figure 5.5b with a maximum found for $\Theta > 1$.

Notice that to capture the shape of the sinusoidal nature of $W_a(I_p)$ in this case, the adaptive integration must add a larger number of points along the impact location compared to the transient study case. Taking into account the time taken to solve the system using an i7-12700H processor and ten cores, we find that the transient calculation takes an average of 10 evaluations 57 s, while each evaluation in the frequency domain takes 8 s each for the same number of evaluations and $\Theta = 1$ for a number of degrees of freedom close to 15000 in each remeshing procedure for the frequency analysis and close to 36000 for the transient case. The frequency domain has an advantage in computational complexity over the transient model for the same number of function evaluations.

We conclude that this wavelength of 12 mm can replicate the behaviours we observe in GEANT4 with a lower confinement factor, reducing the higher energy collection in the photodetector in relation to the energy deposited within the crystal. Lowering this wavelength decreases these losses, moving the Figure 5.8b plot to the right while increasing the self-absorption that eventually should move the plot back

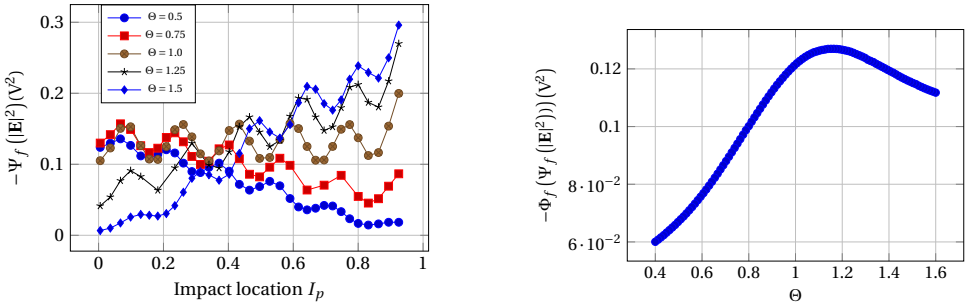

(a) (b)

Figure 5.8.: Figure 5.8a shows the dependence of light collection per energy deposition and track length on the impact point for five different Θ values following the 1D model description in COMSOL. Figure 5.8b shows the design space of the frequency domain COMSOL simulation of the $-\Phi_f\left(\Psi_f\left(|\mathbf{E}|^2\right)\right)\left(\mathrm{V}^2\right)$ function depending on Θ.

towards the left at wavelengths close to the 420nm. Higher wavelengths end up with an unconfined wave with similar distributions of the objective function as the transient model. This study shows that for specific problems, we can replicate the energy loss of electromagnetic fields at higher wavelengths, reducing the required mesh size, given their nonlinear behaviour, using the frequency domain simulation in COMSOL.

5.3.2. Scintillator numerical optimization through frequency domain FEM

Having found in the frequency domain model a solution that correlates to the results obtained from GEANT4, we can run an optimization over the Θ variable for the design in Figure 5.4 using a simplex algorithm with bounded design variables using a wavelength of 1.5 mm. The results of this optimization are plotted in Figure 5.9.

The optimization of the 1DOF design space provides an optimum at Θ = 1.15 with 14 iterations of the simplex algorithm. Although there is a correlation between the COMSOL and GEANT4 models, the location of the optimum is 5% lower compared to the value of Θ = 1.2. The lack of study of multiple wavelengths in COMSOL and possible differences in the treatments of the reflections and material interfaces can lead to differences in the output, even if the effect of the different variables remains comparable. The output of the optimization leads to a design with gains in L_{SP} compared to the analysis shown in Figure 5.5b. This optimization indicates that the optimization procedure is viable and can also provide gains in GEANT4. However, this is still a model with a single design variable and an optimization with a larger number of design variables is expected to provide higher gains.

The geometry of the crystals can be parameterized with a larger number of design variables through interpolation curves defined as shown in Figure 5.10. This figure

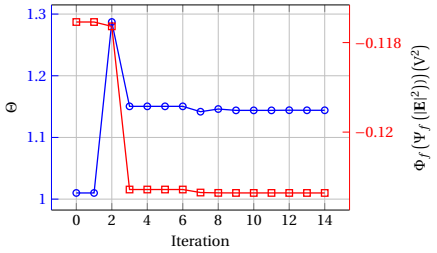

Figure 5.9.: Results for a numerical optimization using a bounded simplex algorithm of the COMSOL 2D scintillation model in the frequency domain. The x axis of this plot shows the iteration number within the algorithm, while the left axis shows the change of the Θ design variable, and the right axis shows the value of the objective function $-\Phi_f\left(\Psi_f\left(|\mathbf{E}|^2\right)\right)\left(\mathrm{V}^2\right)$.

shows the top and bottom surfaces of the LYSO in COMSOL generated through 9 points each. The points for the top surface are named p_i, and the ones at the bottom m_i. These points are uniformly distributed through the half-length of the crystals along x. These points define two splines that can be modified through the absolute y distance of the points to $y = 0$. This can be written as

$$y(p_i) = y_0 * y_{pi}\,, \tag{5.35}$$

$$y(m_i) = -y_0 * y_{mi}\,, \tag{5.36}$$

where the y_0 is the original half-thickness of the crystals of 1.5 mm and y_{pi} and y_{mi} are the design variables associated to the y location of each point along the splines. All design variables are collected in a vector as $\boldsymbol{y} = [\boldsymbol{y_p}, \boldsymbol{y_m}]$. A symmetry plane is defined at x equal to zero for the crystal geometry, and the top and bottom surfaces can be modified independently.

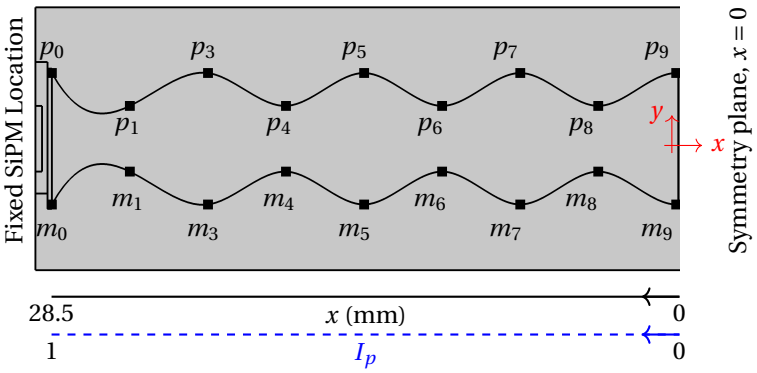

Figure 5.10.: Half-crystal parameterized through 18 points using its top (p_i) and bottom (m_i) surface from COMSOL.

Using the frequency domain COMSOL model, we now run two optimizations using the same objective as in the $1DOF$ optimization and a new objective considering the length of the impact location,

$$\Phi = \Phi_f\left(\Psi_f(\phi(\mathbf{y}))\right) = \Phi_f\left(\Psi_f\left(\frac{|\mathbf{E}|^2}{\Delta l}\right)\right). \tag{5.37}$$

Given that the ionizing particle's energy deposition in the crystals can be considered proportional to the length it travels within it, this measurement can be viewed as a measure of the energy deposition in the photodetectors by the energy deposition in the crystal.

We now impose the volume constraint defined in Equation (5.25b) to compare two geometries with the same amount of scintillating material. The volume constraint is set to a value equal to the original scintillator area calculated with a total thickness of 3 mm and length of 57 mm. The starting point for the following optimizations is defined as the geometry with all design variables equal to 0.99 to avoid a non-satisfied constraint for the initial design. The range of the $\boldsymbol{y}$ design variables is set to $[0.1, 2]$. The final shape of the crystals and the convergence of the objective function for both optimizations are shown in Figure 5.11 for a run of 200 iterations of the simplex algorithm.

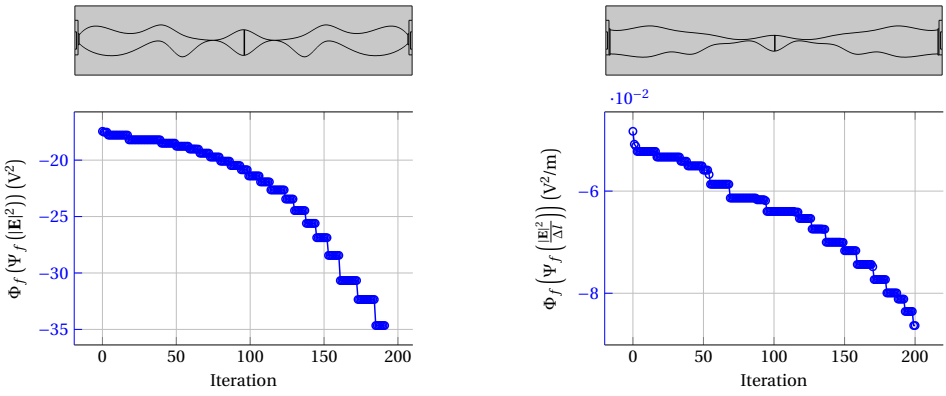

(a) (b)

Figure 5.11.: Convergence for $\Phi_f\left(\Psi_f\left(\phi\right)\right)\left(\mathrm{V}^2\right)$ with $\phi = |\mathbf{E}|^2$ (Figure 5.11b) and $\phi = \frac{|\mathbf{E}|^2}{\Delta l}$ (Figure 5.11a) objective values according to Equation (5.25) and geometries for the last iteration of each optimization.

The results for both objectives show a gains. However, none of them show convergence under 200 iterations. The results from the crystals in both cases show curved surfaces to direct the photons towards the photodetector. These shapes also show a minor influence on the thickness or material close to the middle of the crystal compared to the material close to the photodetectors. The smaller thickness near the centre of the crystal also focuses the photons created in a single

photodetector rather than trying to divide the detection between them. This can be counterproductive for timing detection, where using both photodetectors can increase the timing precision by $\sqrt{2}$ [45].

To avoid small thickness along the crystal, we introduce an extra constraint related to the minimum $\Psi_f(\phi)$ depending on the impact location I_p,

$$c_\Psi = -\frac{\min\left(\Psi_f(\phi)\right)}{J_{min}} + 1 < 0, \tag{5.38}$$

with J_{min} the minimum value required. Another option is to impose the constraint over the minimum thickness of the crystal, directly related to the energy deposited in the crystal,

$$c_t = -\frac{y_0(y_{pi} - y_{mi})}{t_{min}} + 1 < 0, \tag{5.39}$$

applied to each couple of points p_i and m_i with a minimum thickness t_{min}. This formulation limits the smallest thickness of the crystal while allowing any shape within the design limits of each p_i and m_i point rather than using the design variables' bounds. Another possibility of introducing this constraint is to reparameterize the design with the points m_i or p_i referenced to their counterpart p_i or m_i, avoiding the definition of the constraint. However, this means a reformulation of the parameterization proposed in this paper.

Rerunning the optimization using the same starting point and iteration limit, the objective function $-\Phi_f\left(\Psi_f\left(|\mathbf{E}|^2\right)\right)$ with the same volume constraint as the previous ones, a minimum thickness constraint of 1 mm and a minimum value of $\Psi_f\left(|\mathbf{E}|^2\right)$ of $0.02\,\mathrm{V}^2$ we obtain the final shape and convergence plotted in Figure 5.12.

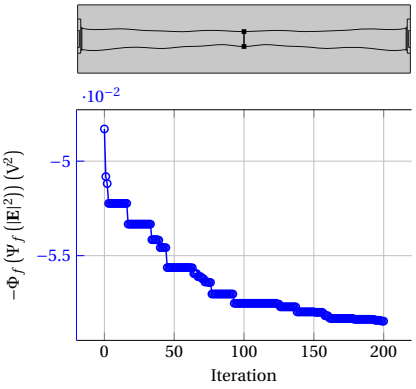

Figure 5.12.: Convergence for the $|\mathbf{E}|^2$ objective values according to Equation (5.25) with a geometry constrained to 1 mm thickness (t_{min}) and a minimum energy deposition of $0.02\,\mathrm{V}^2$ (J_{min}). The resulting geometry is plotted for the last iteration.

This optimization provides a wavy design with a softer slope across both splines, the same common traits as in the previous cases, and a smaller thickness in the

middle than next to the photodetectors. In this case, the final iterations' objective function is much flatter, indicating a faster convergence than without the thickness constraints, although the gains seem to be smaller.

These results need to be validated and compared with the results within GEANT4. Although the interpolation for GEANT4 does not use the same spline definitions, the representation is considered close enough to verify the optimum geometry objective value. Section 5.3.2 shows the histograms of light output $L_O = \frac{N_a}{\mathscr{E}}$ within GEANT4 for the default geometry with constant crystal thickness and parallel surfaces in red and the crystal with the optimized shape from Figure 5.12 in blue. This plot shows how the light collection per energy deposited in the crystal for the optimized geometry found also provides gains in GEANT4. In particular, the optimized geometry raises the average L_O from a median of the distribution of 2400 ph/MeV to a value of 2585 ph/MeV with a relative gain of 7.7% and with a similar bottom value close to 2200 ph/MeV.

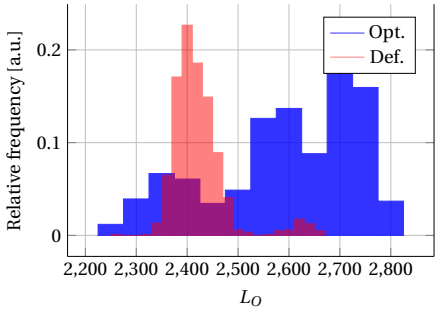

Figure 5.13.: Light output or photons per energy deposited in the crystal detected in the GEANT4 model for the default geometry with flat surfaces in red and optimized geometry found in COMSOL reevaluated in GEANT4 in blue.

5.4. Conclusions

In this document, we provide an approach to translate the scintillation pulse to an electrical wave boundary condition for the transient continuum electromagnetic equations solved through FEM. The resulting FEM model provides a proportional energy deposition in the photodetectors in time to the GEANT4 model. However, the absolute values of both simulations did not reach an agreement. This is expected to arise from the different electromagnetic losses within the materials between the two models. Other effects that could affect the different results are the reflection treatment between different materials and the lack of internal dielectric losses within COMSOL for the transient electromagnetic simulations, taking the refractive index as input. While through the wave-particle duality of light, an agreement between the ray-tracing and FEM continuous description is feasible, the parameters must be tuned between both simulations.

Although absolute correlation in this chapter is not achieved between both simulations, we only require the same trend in the design space or the same influence of the different design variables involved to compare and optimize multiple designs. We show that with COMSOL's frequency domain solution to the Maxwell equations, we can maintain the relevant effect on the light collection objectives of the energy input and energy deposition within the photodetector. The optimization shape results provide gains in the light output once retested within GEANT4. Furthermore, this process avoids the use of stochastic processes in the calculation of the efficiency measure of the scintillating crystals. This also means that the error arising from the stochastic processes in GEANT4 is not dealt with for calculating the objective functions, providing a deterministic and repeatable approach to the optimization process and an advantage in computational complexity. Using FEM, obtaining the deviation from the light collection measurements through multiple wavelengths and material properties can provide further information about the scintillating system.

Not only is the reproducibility of the numerical optimization achieved, but these models also provide a much lower computational cost than the requirements of a Monte Carlo study for each scintillator configuration. This computational complexity is further reduced using a static surrogate model to solve the problem within the frequency domain. Although static solutions cannot represent one-by-one the energy pulse generated within a scintillation process, they maintain the influence of the reflecting surfaces, energy deposition in the scintillator, and material properties on the output. This model also shows the importance of the internal material losses in the scintillation process in relation to the design space in GEANT4 for sufficiently small wavelength inputs. Notice that the wavelength used within this paper has been found experimentally to solve a trade-off problem between a small enough wavelength to capture the design geometry and a large enough one to capture the energy function oscillations through the Simpson's adaptive quadrature and reduce the computational time through coarser meshes.

The use of simplified models can accelerate the optimization of scintillation crystals. However, once we validate a scintillation model in FEM, there are multiple ways to decrease the complexity of optimization further. The need to change the surface to introduce the electrical wave boundary condition leads to a re-meshing for each impact location. This could be avoided with boundary conditions applied within the design domain and mesh-morphing approaches, potentially reducing the computational cost of re-meshing multiple times for each objective value. Another way to further accelerate the convergence of the optimization algorithm is through derivative-based optimizers such as the typically used method of moving asymptotes. However, derivatives are often challenging to evaluate from commercial software without full access to their solvers and related linear systems used during FEM calculations. Using derivative-based optimizers could also facilitate the introduction of topology optimization for scintillators.

Not only is the calculation time essential, but so is the precision of the results. The precision of the objective value is defined through a tolerance introduced into the adaptive Simpson's routine. Although this method converges fast for functions

close to cubic polynomials, the possibility of discontinuities could benefit from other approaches, such as Clenshaw-Curtis or spline-based quadrature procedures. The number of evaluations required for this numerical integration is also a large part of the overall computational cost of the optimization procedure. Fitting procedures or approximations through a lower number of evaluation points with a better understanding of the shape of the light collection concerning the impact location have the potential to reduce the computational cost of this problem further. Extended degrees of freedom through the defined impact location could provide these benefits without more precise meshing through the impact surface. In all cases, the results of the optimization still need to be retested within GEANT4 for validation of the gains achieved. For a more accurate optimized design, the solutions obtained through FEM surrogate models could be re-optimized within GEANT4 using these optima as starting point. This can lead to a more accurate and precise output with a fraction of the computational time than if all the optimization iterations are calculated in GEANT4.

Finally, taking into account that 3D-printing is becoming a new tool also in scintillation manufacturing, faster scintillation simulation and its optimization procedure must mature at the same time. Topology optimization of scintillators typically requires the evaluation of many design variables and their design sensitivities, for which non-derivative-based optimizers often lead to unbearable calculation times. The use of FEM and topology optimization for scintillation could lead to scintillators with properties not otherwise available and specific doping locations for higher light yields.

In summary, we validate a first approach to tackle the simulation of scintillators through FEM using a transient formulation and a simplified model in the frequency domain that maintains the sensitivity to the geometric design variables from GEANT4. Although the design of the scintillator shape to improve its efficiency is still in its infancy, we believe it has the potential to improve its performance with the rise of new manufacturing techniques.

References

[1] J. Glodo, Y. Wang, R. Shawgo, C. Brecher, R. H. Hawrami, J. Tower, and K. S. Shah. "New Developments in Scintillators for Security Applications". In: *Physics Procedia* 90 (2017). Conference on the Application of Accelerators in Research and Industry, CAARI 2016, 30 October – 4 November 2016, Ft. Worth, TX, USA, pp. 285–290. ISSN: 1875-3892. DOI: https://doi.org/10.1016/j.phpro.2017.09.012. URL: https://www.sciencedirect.com/science/article/pii/S1875389217301712.

[2] M. Belousov, M. Gromyko, and O. V. Ignatyev. "Scintillation γ spectrometers for use at nuclear power plants (review)". In: *Instruments and Experimental Techniques* 60 (Jan. 2017), pp. 1–19. DOI: 10.1134/S0020441217010171.

[3] P. Lecoq. "Development of new scintillators for medical applications". In: *Nuclear Instruments and Methods in Physics Research Section A: Accelerators, Spectrometers, Detectors and Associated Equipment* 809 (2016). Advances in detectors and applications for medicine, pp. 130–139. ISSN: 0168-9002. DOI: https://doi.org/10.1016/j.nima.2015.08.041. URL: https://www.sciencedirect.com/science/article/pii/S0168900215009754.

[4] Z. Wang, C. Dujardin, M. S. Freeman, A. E. Gehring, J. F. Hunter, P. Lecoq, W. Liu, C. L. Melcher, C. L. Morris, M. Nikl, G. Pilania, R. Pokharel, D. G. Robertson, D. J. Rutstrom, S. K. Sjue, A. S. Tremsin, S. A. Watson, B. W. Wiggins, N. M. Winch, and M. Zhuravleva. "Needs, Trends, and Advances in Scintillators for Radiographic Imaging and Tomography". In: *IEEE Transactions on Nuclear Science* 70.7 (2023), pp. 1244–1280. DOI: 10.1109/TNS.2023.3290826.

[5] B. A. Shwartz. "Scintillation Detectors in Experiments on High Energy Physics". In: ed. by M. Korzhik and A. Gektin. Vol. 200. 2017, pp. 211–230. DOI: 10.1007/978-3-319-68465-9_13.

[6] L. Lu, M. Sun, Q. Lu, T. Wu, and B. Huang. "High energy X-ray radiation sensitive scintillating materials for medical imaging, cancer diagnosis and therapy". In: *Nano Energy* 79 (2021), p. 105437. ISSN: 2211-2855. DOI: https://doi.org/10.1016/j.nanoen.2020.105437. URL: https://www.sciencedirect.com/science/article/pii/S2211285520310132.

[7] C. H. Peña, I. Dutta, and C. Collaboration. "Precision Timing with the CMS MIP Timing Detector". In: *Journal of Physics: Conference Series* 1162.1 (ene 2019), Art. No. 012035. ISSN: 1742-6596. DOI: 10.1088/1742-6596/1162/1/012035.

[8] I. V. Khodyuk, S. A. Messina, T. J. Hayden, E. D. Bourret, and G. A. Bizarri. “Optimization of scintillation performance via a combinatorial multi-element co-doping strategy: Application to NaI:Tl”. In: *Journal of Applied Physics* 118.8 (2015). ISSN: 10897550. DOI: 10.1063/1.4928771. URL: http://dx.doi.org/10.1063/1.4928771.

[9] R.-y. Zhu. “Radiation damage in scintillating crystals”. In: *Nuclear Instruments and Methods in Physics Research Section A: Accelerators, Spectrometers, Detectors and Associated Equipment* 413.2 (1998), pp. 297–311. ISSN: 0168-9002. DOI: https://doi.org/10.1016/S0168-9002(98)00498-7. URL: https://www.sciencedirect.com/science/article/pii/S0168900298004987.

[10] C. Luo, Y. Jing, Z. Hua, Z. Sui, C. Wang, P. Hu, L. Zheng, S. Qian, L. Yang, X. Sun, G. Tang, H. Cai, Y. Zhu, H. Ban, J. Han, Z. Wang, X. Qiao, J. Ren, and J. Zhang. “Band Gap and Defect Engineering Enhanced Scintillation from Ce3+-Doped Nanoglass Containing Mixed-Type Fluoride Nanocrystals”. In: *ACS Applied Materials and Interfaces* 15.39 (2023), pp. 46226–46235. ISSN: 19448252. DOI: 10.1021/acsami.3c09230.

[11] C. Kim, W. Lee, A. Melis, A. Elmughrabi, K. Lee, C. Park, and J.-Y. Yeom. “A Review of Inorganic Scintillation Crystals for Extreme Environments”. In: *Crystals* 11.6 (2021). ISSN: 2073-4352. DOI: 10.3390/cryst11060669. URL: https://www.mdpi.com/2073-4352/11/6/669.

[12] “Study of rare-earth-doped scintillators”. In: *Optical Materials* 35.11 (2013), pp. 1987–1992. ISSN: 09253467. DOI: 10.1016/j.optmat.2012.11.002. URL: http://dx.doi.org/10.1016/j.optmat.2012.11.002.

[13] R.-Y. Zhu. *Summary Talk in CEPC Calorimetry Workshop at IHEP, Beijing*. 2019. URL: https://www.its.caltech.edu/~rzhu/.

[14] M. Nikl and A. Yoshikawa. “Recent R&D Trends in Inorganic Single-Crystal Scintillator Materials for Radiation Detection”. In: *Advanced Optical Materials* 3.4 (2015), pp. 463–481. DOI: https://doi.org/10.1002/adom.201400571. eprint: https://onlinelibrary.wiley.com/doi/pdf/10.1002/adom.201400571. URL: https://onlinelibrary.wiley.com/doi/abs/10.1002/adom.201400571.

[15] S. Xie, Q. Sun, G. Ying, L. Guo, Q. Huang, Q. Peng, and J. Xu. “Ultra-precise surface processing of LYSO scintillator crystals for Positron Emission Tomography”. In: *Applied Surface Science* 469 (2019), pp. 573–581. ISSN: 0169-4332. DOI: https://doi.org/10.1016/j.apsusc.2018.11.024. URL: https://www.sciencedirect.com/science/article/pii/S0169433218330927.

[16] J. Liu, X. Zhao, Y. Xu, H. Wu, X. Xu, P. Lu, X. Zhang, X. Zhao, M. Xia, J. Tang, and G. Niu. “All-Inorganic Glass Scintillators: Scintillation Mechanism, Materials, and Applications”. In: *Laser and Photonics Reviews* (2023), p. 2300006. DOI: 10.1002/lpor.202300006. URL: https://hal.science/hal-04115685.

[17] J. Shen, R. Jia, Y. Hu, W. Zhu, K. Yang, M. Li, D. Zhao, J. Shi, and J. Lian. “Cold-Sintered All-Inorganic Perovskite Bulk Composite Scintillators for Efficient X-ray Imaging”. In: *ACS Applied Materials & Interfaces* 16.19 (May 2024), pp. 24703–24711. ISSN: 1944-8244. DOI: 10.1021/acsami.4c03124. URL: https://doi.org/10.1021/acsami.4c03124.

[18] G. A. Dosovitskiy, P. V. Karpyuk, P. V. Evdokimov, D. E. Kuznetsova, V. A. Mechinsky, A. E. Borisevich, A. A. Fedorov, V. I. Putlayev, A. E. Dosovitskiy, and M. V. Korjik. “First 3D-printed complex inorganic polycrystalline scintillator”. In: *CrystEngComm* 19.30 (2017), pp. 4260–4264. ISSN: 14668033. DOI: 10.1039/c7ce00541e.

[19] T. Sibilieva, V. Alekseev, S. Barsuk, S. Berns, E. Boillat, I. Boiaryntseva, A. Boyarintsev, A. Carbone, A. De Roeck, S. Dolan, T. Driuk, A. Gendotti, I. Gerasymov, B. Grynyov, S. Hugon, U. Kose, O. Opolonin, A. Rubbia, D. Sgalaberna, M. Sibilyev, S. Tretyak, T. Weber, J. Wuthrich, and X. Y. Zhao. “3D printing of inorganic scintillator-based particle detectors”. In: *Journal of Instrumentation* 18.3 (2023). ISSN: 17480221. DOI: 10.1088/1748-0221/18/03/P03007.

[20] I. Shestakova, V. Gaysinskiy, J. Antal, L. Bobek, and V. V. Nagarkar. “A new scintillator structure for thermal neutron imaging”. In: *Nuclear Instruments and Methods in Physics Research, Section B: Beam Interactions with Materials and Atoms* 263.1 SPEC. ISS. (2007), pp. 234–238. ISSN: 0168583X. DOI: 10.1016/j.nimb.2007.04.092.

[21] M. Simon, K. J. Engel, B. Menser, X. Badel, and J. Linnros. “X-ray imaging performance of scintillator-filled silicon pore arrays”. In: *Medical Physics* 35.3 (2008), pp. 968–981. DOI: https://doi.org/10.1118/1.2839441. eprint: https://aapm.onlinelibrary.wiley.com/doi/pdf/10.1118/1.2839441. URL: https://aapm.onlinelibrary.wiley.com/doi/abs/10.1118/1.2839441.

[22] C. Roques-Carmes, N. Rivera, A. Ghorashi, S. E. Kooi, Y. Yang, Z. Lin, J. Beroz, A. Massuda, J. Sloan, N. Romeo, Y. Yu, J. D. Joannopoulos, I. Kaminer, S. G. Johnson, and M. Soljačić. “A framework for scintillation in nanophotonics”. In: *Science* 375.6583 (2022), eabm9293. DOI: 10.1126/science.abm9293. eprint: https://www.science.org/doi/pdf/10.1126/science.abm9293. URL: https://www.science.org/doi/abs/10.1126/science.abm9293.

[23] S. Xie, X. Zhang, Y. Zhang, G. Ying, Q. Huang, J. Xu, and Q. Peng. “Evaluation of various scintillator materials in radiation detector design for positron emission tomography (Pet)”. In: *Crystals* 10.10 (2020), pp. 1–15. ISSN: 20734352. DOI: 10.3390/cryst10100869.

[24] Y. Valenciaga, D. L. Prout, R. Taschereau, and A. F. Chatziioannou. “Feasibility of Using Crystal Geometry for a DOI Scintillation Detector”. In: *IEEE Transactions on Radiation and Plasma Medical Sciences* 2.3 (2018), pp. 161–169. ISSN: 24697311. DOI: 10.1109/TRPMS.2017.2760857.

[25] V. Vedia, M. Carmona-Gallardo, L. M. Fraile, H. Mach, and J. M. Udías. "Performance evaluation of novel LaBr3(Ce) scintillator geometries for fast-timing applications". In: *Nuclear Instruments and Methods in Physics Research, Section A: Accelerators, Spectrometers, Detectors and Associated Equipment* 857.March (2017), pp. 98–105. ISSN: 01689002. DOI: 10.1016/j.nima.2017.03.030. URL: http://dx.doi.org/10.1016/j.nima.2017.03.030.

[26] F. A. Danevich, R. V. Kobychev, V. V. Kobychev, H. Kraus, V. B. Mikhailik, and V. M. Mokina. "Optimization of light collection from crystal scintillators for cryogenic experiments". In: *Nuclear Instruments and Methods in Physics Research, Section A: Accelerators, Spectrometers, Detectors and Associated Equipment* 744 (2014), pp. 41–47. ISSN: 01689002. DOI: 10.1016/j.nima.2014.01.042. URL: http://dx.doi.org/10.1016/j.nima.2014.01.042.

[27] C. Bircher and Y. Shao. "Investigation of crystal surface finish and geometry on single LYSO scintillator detector performance for depth-of-interaction measurement with silicon photomultipliers". In: *Nuclear Instruments and Methods in Physics Research Section A: Accelerators, Spectrometers, Detectors and Associated Equipment* 693 (2012), pp. 236–243. ISSN: 0168-9002. DOI: https://doi.org/10.1016/j.nima.2012.07.029. URL: https://www.sciencedirect.com/science/article/pii/S0168900212008042.

[28] I. Kilimchuk, V. Tarasov, and I. Vlasova. "Study of light collection as a function of scintillator surface roughness". In: *Radiation Measurements* 45.3 (2010). Proceedings of the 7th European Conference on Luminescent Detectors and Transformers of Ionizing Radiation (LUMDETR 2009), pp. 383–385. ISSN: 1350-4487. DOI: https://doi.org/10.1016/j.radmeas.2010.01.027. URL: https://www.sciencedirect.com/science/article/pii/S1350448710000284.

[29] N. Ghal-Eh and R. Koohi-Fayegh. "Light collection behaviour of scintillators with different surface coverings". In: *Radiation Measurements* 41.3 (2006), pp. 289–294. ISSN: 1350-4487. DOI: https://doi.org/10.1016/j.radmeas.2005.06.039. URL: https://www.sciencedirect.com/science/article/pii/S1350448705002507.

[30] G. Romanchek, Y. Wang, H. Marupudi, and S. Abbaszadeh. "Performance of Optical Coupling Materials in Scintillation Detectors Post Temperature Exposure". In: *Sensors* 20.21 (2020). ISSN: 1424-8220. DOI: 10.3390/s20216092. URL: https://www.mdpi.com/1424-8220/20/21/6092.

[31] A. Knapitsch and P. Lecoq. "Review on photonic crystal coatings for scintillators". In: *International Journal of Modern Physics A* 29.30 (2014), p. 1430070. DOI: 10.1142/S0217751X14300701. eprint: https://doi.org/10.1142/S0217751X14300701. URL: https://doi.org/10.1142/S0217751X14300701.

[32] S. Surani, F. Logoglu, P. Albert, D. Wolfe, and M. Flaska. “Inorganic scintillator surface enhancements with 2-D photonic crystals to improve light collection”. In: *EPJ Web of Conferences* 288 (Nov. 2023), p. 10014. DOI: 10.1051/epjconf/202328810014.

[33] S. Agostinelli *et al.* “GEANT4 - A simulation toolkit”. In: *Nuclear Instruments and Methods in Physics Research, Section A: Accelerators, Spectrometers, Detectors and Associated Equipment* 506.3 (2003), pp. 250–303. ISSN: 01689002. DOI: 10.1016/S0168-9002(03)01368-8.

[34] F. Yasar, M. Kilin, S. Dehdashti, Z. Yu, Z. Ma, and Z. Wang. “Spatially resolved x-ray detection with photonic crystal scintillators”. In: *Journal of Applied Physics* 130.4 (July 2021), p. 043101. ISSN: 0021-8979. DOI: 10.1063/5.0050380. eprint: https://pubs.aip.org/aip/jap/article-pdf/doi/10.1063/5.0050380/15263998/043101_1_online.pdf. URL: https://doi.org/10.1063/5.0050380.

[35] D. M. Binkley. “Optimization Of Scintillation-Detector Timing Systems Using Monte Carlo Analysis”. In: *IEEE Transactions on Nuclear Science* 41.1 (1994), pp. 386–393. ISSN: 15581578. DOI: 10.1109/23.281528.

[36] S. Deilami, K. Abbasi, A. Houshyar, H. Izadneshan, and H. Mortazavy Beni. “A numerical study attitude of compatibility in scintillator detectors through matching pair scintillator-photodiode materials”. In: *Results in Engineering* 21 (2024), p. 101924. ISSN: 2590-1230. DOI: https://doi.org/10.1016/j.rineng.2024.101924. URL: https://www.sciencedirect.com/science/article/pii/S2590123024001774.

[37] J. Elsey, D. R. McKenzie, J. Lambert, N. Suchowerska, S. L. Law, and S. C. Fleming. “Optimal coupling of light from a cylindrical scintillator into an optical fiber”. In: *Applied Optics* 46.3 (2007), pp. 397–404. ISSN: 15394522. DOI: 10.1364/AO.46.000397.

[38] M.-R. Mohammadian-Behbahani, S. Saramad, and M. Mohammadi. “Combined FDTD-Monte Carlo analysis and a novel design for ZnO scintillator rods in polycarbonate membrane for X-ray imaging”. In: *Nuclear Instruments and Methods in Physics Research Section A: Accelerators, Spectrometers, Detectors and Associated Equipment* 853 (2017), pp. 78–84. ISSN: 0168-9002. DOI: https://doi.org/10.1016/j.nima.2017.02.027. URL: https://www.sciencedirect.com/science/article/pii/S0168900217302115.

[39] T. Grosges, A. Vial, and D. Barchiesi. “Models of near-field spectroscopic studies: comparison between Finite-Element and Finite-Difference methods”. In: *Opt. Express* 13.21 (Oct. 2005), pp. 8483–8497. DOI: 10.1364/OPEX.13.008483. URL: https://opg.optica.org/oe/abstract.cfm?URI=oe-13-21-8483.

[40] C. Multiphysics. “Introduction to COMSOL multiphysics®”. In: *COMSOL Multiphysics, Burlington, MA, accessed Feb* (2022). Accessed May 2025.

[41] M. Korzhik, G. Tamulaitis, and A. Vasil’ev. *Physics of Fast Processes in Scintillators*. Jan. 2020. ISBN: 978-3-030-21965-9. DOI: 10.1007/978-3-030-21966-6.

[42] G. Reales, F. van Keulen, A. M. Aragón, J. F. L. Goosen, and A. Bornheim. “Multi-objective scintillator shape optimization for increased photodetector light collection”. In: *J. Opt. Soc. Am. B* 41.9 (Sept. 2024), pp. 2014–2032. DOI: 10.1364/JOSAB.529434. URL: https://opg.optica.org/josab/abstract.cfm?URI=josab-41-9-2014.

[43] B. E. A. Saleh and M. C. Teich. *Fundamentals of Photonics*. 2nd. New York, NY: Wiley, 2007. ISBN: 9780471358329.

[44] J. Hu and C. R. Menyuk. “Understanding leaky modes: slab waveguide revisited”. In: *Adv. Opt. Photon.* 1.1 (Jan. 2009), pp. 58–106. DOI: 10.1364/AOP.1.000058. URL: https://opg.optica.org/aop/abstract.cfm?URI=aop-1-1-58.

[45] C. CMS. *A MIP Timing Detector for the CMS Phase-2 Upgrade*. Tech. rep. Geneva: CERN, 2019. URL: https://cds.cern.ch/record/2667167.

6

Conclusions and recommendations

This thesis demonstrated the use of topology and shape numerical optimization to increase the photon-collection efficiency, the cooling capabilities, and the reliability of thermoelectrical elements based on the design of the BTL particle detector. Unlike experimental research, the simulation-based methods developed provide a faster and more cost-efficient approach for testing and selecting preliminary designs for particle detectors and related applications. The research also leads to recommendations for future particle detectors with specific scintillator and thermocouple designs. The core research question,

Can numerical design optimization techniques be applied to improve the timing precision of minimum ionizing particle detectors?

is addressed affirmatively, with thermal and optical improvements supported by the results of the multiple optimization methods tested. This question has then been divided into smaller subquestions, since it was determined that thermal and optical aspects are the most influential on detector timing precision. In Equation (1.1) the largest component is σ^{DCR}, which can be reduced through active cooling. For this reason we decided to include thermoelectrical elements in the BTL detector system to reduce the radiation damage through thermal cycling. This can reduce the base electrical noise and the one induced by the radiation damage of the photodetectors. However, the design of these devices is not evident, which led to the sub-question:

- Can a topology optimization formulation for thermoelectric devices improve cooling performance accounting for material cost and specific operational factors, including electrical working points and nonlinear Joule heating?

  Throughout Chapter 2, we studied the topology optimization of the semiconductors of a thermocouple to provide lower temperatures under a power constraint. Furthermore, we introduced the electrical operational condition of the TEC as an optimization variable, which allowed us to maintain a favourable electrical working point even if we removed or added material.

The use of an optimized voltage drop for all designs provided designs that were comparable to the initial design. An analytical model with two density design variables was used to understand the non-convexity of the problem and select the optimization parameters, which allowed convergence to lower minima and volumes without the need for volume constraints. The visual inspection of the results shows that we need to use a penalization coefficient for the thermal Seebeck coefficient smaller than for the thermal and electrical conductivities $k_p = \sigma_p > \sigma_\alpha$ to improve convergence using SIMP. This visual inspection also shows how the combination of the power constraint and objective functions causes the non-convexity convergence issues with a local maximum close to the full-density design. However, certain combinations of penalization coefficients can also lead to undesirable intermediate density optima due to manufacturing considerations and possible solutions through an electrical disconnection. We also proposed a particular set of initial points for the Newton-Raphson FEM iterations to accelerate its convergence based on the previous iterations.

The convergence to lower volume quantities for improved performance also reduces material costs, which are estimated to be up to one-third of the thermoelectric cooler costs. Although the optimized device for specific operating ranges is the full-density design, it is also concluded that introducing a volume constraint under this methodology can still remove the material with low-performance loss. The results provide up to 10° lower temperatures for the same power limitations compared to the original design.

The installation of thermoelectrical coolers (TECs) in the BTL detector revealed frequent early failures of TECs shortly after deployment. For this reason, we decided to investigate the mechanical reliability of these devices, which often use fragile ceramic material, glued or soldered between the working surfaces, and suffer from thermal expansion loading.

The following subquestion was then formulated related to the mechanical stability of TEC devices:

- Can numerical methods optimize coupled thermoelectric-mechanical systems while considering mechanical and thermoelectrical loads?

  Following the research in Chapter 2, in Chapter 3 we modify the previous formulation to include mechanical degrees of freedom and the expected loads under operation. We proposed a decoupled approach between the thermoelectrical and mechanical degrees of freedom for lower computational memory requirements and complexity. The mechanical constraints were introduced through a stress constraint and an aggregation function to consider discontinuities in the stress field. This P-mean aggregation function was also introduced in the temperature objectives to include the effect of hot spots in the objective function. Furthermore, we provided a strategy to introduce temperature-dependent material properties as a continuous function within the expected working regimes. This was done through a polynomial fitting and constant values in the unknown temperature regimes.

The results showed that the decoupling could be performed without significant loss of information between the thermoelectrical and mechanical degrees of freedom. Furthermore, the new formulation required filtering techniques to obtain manufacturable designs. This density filtering through the Helmholtz and Heaviside equations introduces a length scale and avoids design with porous regions arising from the stress constraints in the model. The density-optimized field resulted in quasi-symmetrical designs, given that we used the same Young modulus for both semiconductors. However, the dissimilar thermoelectric properties introduced different thermoelectrical paths for each semiconductor. The results showed up to 10 times lower stress measurements while still finding a thermoelectric optimum at lower semiconductor volumes. Furthermore, we show that the air thermal conductivity has an impact on results and can be included in the model without increased cost through the minimum thermal conductivity of the elements. The increased minimum thermal conductivity also leads to a removal of grey elements from the optimized topologies without the need of filters.

The second largest component from Equation (1.1) arises from the optical uncertainties within scintillator crystals. Scintillator design is then a fundamental part of particle detector technology, transforming the energy from ionizing radiation into detectable photons and directing them towards the photodetectors. However, little to no effort has been made to understand the effect of their shape on their light collection and timing uncertainties. This leads to the question:

- Can shape optimization of scintillation crystal surfaces reduce light reabsorption and improve performance at the photodetector interface, considering the stochastic nature of the optimization process?

  We first approached the scintillator light collection in Chapter 4 through the already available particle-matter interaction software GEANT4. This effort led to a model comparison and validation concerning the experimental data available in the literature for the BTL project. These validations allowed us to simplify the geometry to lower computational costs. Given the lack of analytical sensitivities from stochastic simulations, a lower computational complexity was required to perform an exploration of the design space through genetic algorithms. We then performed heuristic optimizations through NSGAII with two objectives: material volume for lower costs and light collection measures. We defined a new objective based on the photon count, energy deposition, and particle tracking to improve the output distributions with the highest precision possible and lowest computational complexity. Compared to the previous two objectives studied, this allowed for a move of the distribution to higher light collection values with higher accuracy in the objective function for the same number of events and taking into account the effect of the energy deposited in the crystal. We also studied two different parameterizations, which showed their importance over the final optimized designs. The results provided gains higher than 30% for certain light collection measurements as compared to the original design.

Due to the computational complexity and the stochastic nature of the problem, the characterization of light collection distributions can lead to high estimation errors during the optimization procedure, which needs to be re-evaluated. This led to the following research focus in Chapter 5 and the last subquestion:

- *Can deterministic modelling approaches, such as FEM and FDTD, enhance scintillation efficiency through improved photon generation and detection while reducing the computational demands associated with Monte Carlo methods?*

  To answer this question, we proposed an FEM procedure to gain insight into the scintillator optical designs. This approach allowed us to compare the scintillator outputs without the need for precise characterization that can be performed in specialized particle-matter software. For this purpose, we translated the scintillation phenomena with information extracted from GEANT4 to boundary conditions in FEM. We used a transient electromagnetic model in COMSOL to obtain the time characteristics of the energy deposition. We also proved that a frequency-based electromagnetic model in COMSOL is enough to replicate the behaviour of the light collection objective functions studied in Chapter 4. We then performed a new design space exploration using a simplex algorithm over a 2D FEM model, which included manufacturing constraints. The resulting shapes were tested using GEANT4, showing lower gains than the optimizations performed with GEANT4, of up to 7%, but at a small fraction of the time previously required.

6.1. Conclusions

While the focus of this thesis is on specific elements, namely thermoelectric coolers and scintillators, the numerical approaches developed apply broadly across particle detector design. Numerical design for such components remains in its infancy, presenting opportunities to enhance efficiency in various applications, including not only high-energy physics but also medicine [1–3], aerospace [4], and security [5]. For example, this thesis's main cohesion point is how SiPMs can provide signal intensity through improved light collection and reduced noise via temperature control. Decoupling the lower temperature and higher luminosity objectives avoids increasing the simulation complexity with an increased number of objectives and constraints. The capabilities of numerical optimization in this thesis underscore the necessity of integrating optimization techniques into the early stages of detector development to ensure higher performance, given current trends towards pico-second timing resolutions. The proposed workflow in this dissertation also lays a foundation for integrating these effects into a unified model for the entire detector. However, the optimization procedures described could also be applied directly to these SiPMs.

Using the proposed methodology to provide active signal control for SiPMs through temperature optimization is relevant in quantum computing technologies [6], where precise photon detection is critical for quantum state measurements. Mitigating radiation damage through optimized thermoelectrical devices can contribute to extending the lifetime of SiPMs [7] and lowering maintenance costs, following sustainability drivers. Lowering the power consumption of thermoelectrical devices

can also lead to lower operational costs and power consumption in the overall system. Considering the power dissipation of SiPMs also depends upon their operational temperature. As society tackles climate change challenges, reducing raw material and energy use, and precision optimization shown in this research can contribute to reducing these effects for particle detector design.

The use of numerical tools for optimization of scintillators can also lead to a reduction in costs, not only in material but also in allowing more compact detectors with similar resolutions. The SiPM size required for a given resolution could also be reduced with a higher focus on the generated photons, leading to lower costs. Reducing the detector size would also lower the cost of associated infrastructures (e. g., shielding and support structures). With a density of 7200 kg/m^3 for LYSO:Ce and a total weight of 1800 kg for BTL, of which more than 50% is comprised of these scintillators, a weight reduction could lead to further gains. We could also select scintillators with lower photon emission or different time characteristics, whose efficiency could be improved by optimizing their shape instead of relying on higher-quality materials. This includes the introduction of scintillator 3D-printing and the mixing of different materials in the same structure to provide different properties to the final design. These numerical tools also enable the design of specific experiments with non-uniform particle fluxes or non-uniform efficiencies across its detection area. The computational cost of these simulations using non-differentiable particle-matter ray-tracing-based software is still computationally expensive. Tailored surrogate models become key for future particle detector optimization. These simplified models would also apply to the previously mentioned medical, aerospace, and security fields. Deterministic models and hybrid approaches could be further refined to replace or complement stochastic simulations, enabling faster iteration in particle detector design.

The research in this thesis further signals how the computational aspects of multiphysics optimizations are still underdeveloped compared to pure mechanical numerical optimization. This often leads to poorly chosen objectives and constraints. One such constraint is the volume constraint, which serves as an optimization objective subject to design criteria, such as timing resolution, light collection, temperature gradient, and heat absorption. While constraints generally add complexity to the objective landscape, a volume constraint can influence the optimization process by guiding it toward different optima, often aiding convergence through altered objective landscapes or hyperparameter tuning.

Furthermore, the computational methodologies developed here and shared with the community, see Appendix H, can serve as training platforms for students and researchers. This becomes of higher importance as we move to more complex optimizations and models, reducing the barrier of entry. These have only been possible thanks to the interdisciplinary research through the multiple expertise of physicists and engineers in a common environment, as is CERN. This emphasizes the importance of open source, public research, and interdisciplinary organizations.

We can summarize that numerical optimization in particle detector design is a field with significant potential for further advancement.

6.2. Recommendations and future research directions

In this section, I provide recommendations under the themes of the thermal and optical optimizations performed in this thesis and the overall application to particle detectors.

6.2.1. Thermoelectrical devices and topology optimization

In this thesis, I have detailed several processes by which we can improve the performance of thermoelectrical coolers through topology optimization. However, the application of TO to thermoelectric devices is still in its initial stages, and multiple options still exist to improve the results which are detailed hereafter.

As shown in this thesis, ***TO optimization convergence needs to be studied for all new multiphysics optimization problems.*** For density-based TO, the penalization coefficients using SIMP should be examined for each objective and constraint. The analytical model we used in this thesis could be extended to similar thermoelectric problems, including mechanical behaviour and other objectives. A summary of the objectives where this methodology could improve the algorithm convergence is provided in Lundgaard and Sigmund [8]. All proposed objectives for thermoelectric TO, including temperatures and heat extraction or injection, could also benefit from the introduction of the optimization of their boundary conditions, as we did in this dissertation. Otherwise, multidimensional projection could be used directly to gain insights into the design space. Malan [9] offers a review of landscape analysis algorithms that could be used for this purpose. A comparison with other methods, such as level set TO, could lead to different results, reducing the influence of material discontinuities and providing different material arrangements.

The convergence to the final topology is also dependent on the initial design. However, ***the bulk thermoelectrical designs are not the only thermoelectrical device configuration***. Previous tests and analytical models have been developed for bulk thermoelectrical modules due to their common use and the previous knowledge of their shape-dependent efficiency [10]. However, the TO approach developed in this thesis could be extended to other configurations with different heat and electrical transport directionalities to gain insights into the different problem landscapes.

Different configurations also lead to different mechanical loading that affects their performance. TECs lose efficiency with cycling loading. We modelled the results for a stress-constrained TEC under thermal loading. Other loading scenarios, such as shearing or bending loads, can affect the final designs and optimizations. The contact region between different layers, such as semiconductor, soldering material, and ceramic, can also affect reliability. Large deformation implementations may further support newer flexible TEC designs or wearable TECs [11].

The thermocouple, the smallest unit of a thermoelectric device, is convenient for optimization models, but clearer benchmark guidelines are needed to solve this thermoelectrical TO problem. However, ***the studied thermocouples are just part of a multiscale problem***. We have studied the use of optimization techniques over a single thermocouple, but 3D effects in the full thermoelectric device should be considered. Given the computational cost of modelling a full TEC, a homogenization or linearization procedure should be implemented to consider 3D

effects. Furthermore, the entire TEC is prone to experiment load concentration in specific locations, such as its corners, rather than in a single thermocouple [12]. This means that homogenization could also be useful for stress-constrained optimization of thermoelectrical devices. The use of multi-scale topology optimization algorithms is another way to include these effects in a full thermoelectrical device comprised of multiple thermocouples. Multi-scale topology optimization algorithms are summarized in Wu, Sigmund, and Groen [13]. Also, the evidence that porous semiconductor materials can improve thermocouples' efficiency makes this research direction interesting [14].

Thermoelectrical devices also need to be able to be manufactured, and there is currently limited experimental testing on results from topology optimization. While an experimental setup exists to test the standard TEC used within BTL, further efforts are needed to test optimized designs. This might require more effort due to a lack of manufacturing constraints. In this thesis, we approached the manufacturing limitations through Helmholtz and Heaviside filtering, limiting feature size. However, other constraints might need to be implemented depending on the manufacturing method. The manufacturing methods available to produce thermoelectrical devices are summarized in Song *et al.* [15], including inkjet printing and extrusion, among others.

The length scale and filtering prevent nanoscale designs where the thermoelectric equations are no longer valid due to size effects [16]. However, miniaturizing thermoelectric devices may require equations that account for nanoscale electronic transport, enabling topology optimization for such designs. However, introducing smaller-sized elements in the simulation could lead to designs with better objective values. Furthermore, the presence of a magnetic field could lead to changes in the material properties not considered in the equations of this thesis [17].

Finally, looking at our particular problem, ***the timing resolution from SiPMs can be tuned through multiple working points of the TECs.*** For the application of SiPM detectors, we are interested in cooling and annealing cycles. However, the results in this thesis focused on the cooling aspects of TECs. A multiobjective optimization could include the efficiency of cooling and heating up the photomultiplier in reverse polarity operation. A multiobjective optimization or an aggregation of multiple electrical points or power consumptions could also increase the range of operation of a single device. This leads to difficulties arising from higher computational costs and the device's opposite requirements between electrical and thermal conductivities for both operational modes.

6.2.2. Scintillation crystal design and optimization

Although the results offered higher light collection, the optical surfaces or geometrical design is a single aspect of the design of these crystals.

Not only the shape but also ***the properties of the scintillator surfaces affect the light output.*** This is evidenced by research on the effect of different roughness and materials to coat the scintillators to improve the light collection [18]. Using metalenses or photonic crystals has also been shown to improve light collection in scintillators [19]. Topology optimization for the design of optical surfaces could

be used to tune the refractive indices of photodetectors or to create specific reflective properties along the crystals [20]. We could decouple the effects of energy deposition and reflective surfaces with metalenses and obtain improved light collection. However, these structures require the use of FDTD or FEM modelling rather than ray tracing, such as in GEANT4, for their design and optimization to obtain gradient information.

While the Finite Element Method (FEM) is not strictly required for gradient-based optimization – any system of C^1 functions can be optimized using these methods– its use facilitates the modeling and testing of complex structures. In particular, it enables the application of ***gradient-based optimization of scintillators***, where a major challenge lies in the stochastic nature of particle-matter interactions, typically requiring Monte Carlo simulations. The use of FEM, as in Chapter 5, enables the use of deterministic models and sensitivities. This can accelerate the optimization procedure. The use of FEM also enables a fully optimizable model of scintillating crystals and metalenses in a single simulation rather than having to extract the scintillation properties from GEANT4 and iterate with a FEM model. Furthermore, the optimized geometries found could be reintroduced into particle-matter software for a second optimization stage, leading to more accurate and improved objective values and designs at a lower cost than a full optimization in GEANT4.

The amount of light reflected on each surface also depends on the material's refractive index. Direct application to cheaper and 3D-printable plastic scintillators implies lower gains due to their lower refractive index and lower light yield [21, 22]. These disadvantages could be mitigated through the coating and the surface or topology optimization of these scintillators. Furthermore, ***3D-printing of scintillators*** can lead to the realization of composite scintillators, thereby combining their different material properties. This could lead to a scintillator composite with high refractive index, high light yield, and/or fast scintillation through local material changes. This research direction hints at tailoring *metascintillator* properties [23]. The material changes could be directly implemented in the GEANT4 optimization procedure through the methodology provided in this dissertation.

6.2.3. Design techniques for particle detectors

In the previous section, I mentioned that the techniques developed can be applied to other detector parts. The first components of interest are the SiPMs themselves, which provide σ^{DCR}. Research has been conducted on improving their efficiency by tailoring their cell size [24]. SiPMs are microdevices with limited changes available to their manufacturing. Their performance depends on factors such as the series quenching resistor, electric current density, self-heating, doping levels, and trenches or metal-filled cutouts between detector cells, which prevent electro-optical coupling [25].

Within the MTD detector, SiPMs will be cooled down and annealed in successive cycles to reduce their radiation damage and associated dark current or noise. This behaviour can be predicted, and an optimum cycling condition could be found to reduce the overall noise at the end of life for maximum operational time or maximize the detector life [26].

This can be achieved through models of parts of the overall detector. However, these optimizations could benefit from their integration into a single model to understand the system's performance. This could lead to new challenges in computational complexity and the ability to model the entire detector accurately. For this purpose, it would be convenient to use available data from detector runs to create surrogate models of the detector that are not subject to the optimization procedure, such as the electronic response. Current efforts are to integrate AI and optimization procedures into the design of multiple high-energy physics particle detectors [27, 28]. All these references and future research recommendations establish the opportunities that numerical optimization and design space exploration have over conceptual design for future particle detectors. Furthermore, this is also applicable not only to timing or scintillation-based detectors, but to other particle detectors as well. Given the common use of scintillators and waveguides in calorimeters, the developed approaches in this thesis are directly applicable to them. Electromagnetic shields protect sensitive components from external electromagnetic interference (such as background suppression) can make use of optimization techniques to enhance detector signal integrity at reduced overall weight [29, 30]. The use of specific collimator shapes or designs and simplified models that allow for gradient-based optimizers is also noted in the literature [31]. Drift chambers require optimized layouts and structural elements to maximize particle tracking efficiency while maintaining mechanical stability [32, 33]. Sensor layout and size significantly impact detection area and resolution, requiring careful optimization for specific applications. Examples of this study in the literature include Shi *et al.* [34] and Dubé *et al.* [35], which provide research on the optimal location of sensors for non-intrusive radioactive particle tracking to monitor the behaviour of hydrodynamic systems. Resistive plate chambers depend on material and geometric configurations to improve performance [36]. Photomultiplier tubes, require optimization of the focusing electrodes, voltage applications, and bulbs to maximize photon collection and signal output [37, 38]. Finally, silicon strip sensors within tracking detectors provide precise spatial resolution by detecting charged particle trajectories and are dependent, as SiPMs, on the microdevice layers to reduce hot-spots [39–41]. These are only some elements I have identified, and I have no doubt that more will arise as technology progresses in additive manufacturing and numerical modelling.

The selection and usage of different optimization algorithms for detectors also require careful evaluation. This thesis applies heuristics to optimize scintillator shapes and gradient-based methods for thermoelectrical elements. Each method offers distinct advantages and trade-offs that affect computational cost and research effort. Gradient-based optimizers converge quickly to local minima using sensitivity information, but are sensitive to hyperparameters and non-convex functions. Although computationally expensive, heuristic optimizers handle discontinuous objective functions in ray-tracing software without requiring surrogate models or sensitivity analysis and can use standard particle-matter interaction tools in high-energy physics. Further research should guide optimizer selection for specific problems or hybrid approaches that combine both methods. Both methods face the curse of dimensionality, where the increase of design variables increases runtime

exponentially. Isogeometric analysis and geometric projection parameterizations for scintillators and semiconductors offer a promising mitigation strategy and require further exploration. These parameterizations also highlight the differences between the traditional sizing optimization in high-energy physics and the higher flexibility of the shape and topology optimization discussed in this thesis. Despite manufacturing constraints on topology optimization, advances like additive manufacturing and free-form optics present opportunities for further research.

References

[1] E. Roncali and S. R. Cherry. “Application of silicon photomultipliers to positron emission tomography”. en. In: *Ann Biomed Eng* 39.4 (Feb. 2011), pp. 1358–1377.

[2] J. Baran, W. Krzemien, S. Parzych, L. Raczyński, M. Bała, A. Coussat, N. Chug, E. Czerwiński, C. O. Curceanu, M. Dadgar, K. Dulski, K. Eliyan, J. Gajewski, A. Gajos, B. C. Hiesmayr, K. Kacprzak, Ł. Kapłon, K. Klimaszewski, G. Korcyl, T. Kozik, D. Kumar, S. Niedźwiecki, D. Panek, E. Perez del Rio, A. Ruciński, S. Sharma, Shivani, R. Y. Shopa, M. Skurzok, E. Stępień, F. Tayefiardebili, K. Tayefiardebili, W. Wiślicki, and P. Moskal. “Realistic total-body J-PET geometry optimization: Monte Carlo study”. In: *Medical Physics* 52.5 (2025), pp. 2961–2975. DOI: https://doi.org/10.1002/mp.17627. eprint: https://aapm.onlinelibrary.wiley.com/doi/pdf/10.1002/mp.17627. URL: https://aapm.onlinelibrary.wiley.com/doi/abs/10.1002/mp.17627.

[3] J. Kasper, A. Wrońska, A. Awal, R. Hetzel, M. Kołodziej, K. Rusiecka, A. Stahl, and M.-L. Wong. *Genetic algorithm as a tool for detection setup optimisation: SiFi-CC case study*. 2024. arXiv: 2411.18239 [physics.med-ph]. URL: https://arxiv.org/abs/2411.18239.

[4] A. R. Altamura, F. Acerbi, B. Di Ruzza, E. Verroi, S. Merzi, A. Mazzi, and A. Gola. “Radiation damage on SiPMs for space applications”. In: *Nuclear Instruments and Methods in Physics Research Section A: Accelerators, Spectrometers, Detectors and Associated Equipment* 1045 (2023), p. 167488. ISSN: 0168-9002. DOI: https://doi.org/10.1016/j.nima.2022.167488. URL: https://www.sciencedirect.com/science/article/pii/S016890022200780X.

[5] E. I. Novikova, M. S. Strickman, C. Gwon, B. F. Phlips, E. A. Wulf, C. Fitzgerald, L. S. Waters, and R. C. Johns. “Designing SWORD–SoftWare for Optimization of Radiation Detectors”. In: *2006 IEEE Nuclear Science Symposium Conference Record*. Vol. 1. 2006, pp. 607–612. DOI: 10.1109/NSSMIC.2006.356228.

[6] G. Chesi, L. Malinverno, A. Allevi, R. Santoro, M. Caccia, A. Martemiyanov, and M. Bondani. “Optimizing Silicon photomultipliers for Quantum Optics”. In: *Scientific Reports* 9.1 (May 2019), p. 7433.

[7] A. Bornheim, W. Lustermann, K. Stachon, G. Reales Gutiérrez, A. Benaglia, F. De Guio, A. Ghezzi, M. T. Lucchini, M. Malberti, S. Palluotto, T. Tabarelli De Fatis, M. Benettoni, R. Carlin, M. Tosi, R. Rossin, P. Meridiani, R. Paramatti, F. Santanastasio, J. C. Silva, J. Varela, A. Heering, A. Karneyeu, Y. Musienko, M. Wayne, T. Anderson, B. Cox, C. E. Perez Lara, A. Ledovskoy, S. White, and I. Schmidt. “Integration of thermo-electric coolers into the CMS MTD SiPM arrays for operation under high neutron fluence”. In: *Journal of Instrumentation*

18.8 (2023). ISSN: 17480221. DOI: 10.1088/1748-0221/18/08/P08020. arXiv: 2306.00818.

[8] C. Lundgaard and O. Sigmund. “A density-based topology optimization methodology for thermoelectric energy conversion problems”. In: *Structural and Multidisciplinary Optimization* 57.4 (2018), pp. 1427–1442. ISSN: 16151488. DOI: 10.1007/s00158-018-1919-1.

[9] K. M. Malan. “A Survey of Advances in Landscape Analysis for Optimisation”. In: *Algorithms* 14.2 (2021). ISSN: 1999-4893. DOI: 10.3390/a14020040. URL: https://www.mdpi.com/1999-4893/14/2/40.

[10] S. Shittu, G. Li, X. Zhao, and X. Ma. “Review of thermoelectric geometry and structure optimization for performance enhancement”. In: *Applied Energy* 268.December 2019 (2020), p. 115075. ISSN: 03062619. DOI: 10.1016/j.apenergy.2020.115075.

[11] S. Zhu, Z. Fan, B. Feng, R. Shi, Z. Jiang, Y. Peng, J. Gao, L. Miao, and K. Koumoto. “Review on Wearable Thermoelectric Generators: From Devices to Applications”. In: *Energies* 15.9 (2022). ISSN: 1996-1073. DOI: 10.3390/en15093375. URL: https://www.mdpi.com/1996-1073/15/9/3375.

[12] T. Pan, T. Gong, W. Yang, and Y. Wu. “Numerical Study on the Thermal Stress and its Formation Mechanism of a Thermoelectric Device”. In: *Journal of Thermal Science* 27.3 (June 2018), pp. 249–258. ISSN: 1993-033X. DOI: 10.1007/s11630-018-1006-3. URL: https://doi.org/10.1007/s11630-018-1006-3.

[13] J. Wu, O. Sigmund, and J. P. Groen. “Topology optimization of multi-scale structures: a review”. jpn ; eng. In: *Structural and Multidisciplinary Optimization* 63.3 (2021), pp. 1455–1480. ISSN: 1615-147X.

[14] U. Ijaz, M. Siyar, and C. Park. “The power of pores: review on porous thermoelectric materials”. In: *RSC Sustainability* 00 (2024), pp. 1–19. ISSN: 27538125. DOI: 10.1039/d3su00451a. URL: http://dx.doi.org/10.1039/D3SU00451A.

[15] K. Song, A. N. M. Tanvir, M. O. Bappy, and Y. Zhang. “New Directions for Thermoelectrics: A Roadmap from High-Throughput Materials Discovery to Advanced Device Manufacturing”. In: *Small Science* (Apr. 2024). DOI: 10.1002/smsc.202300359.

[16] J. Mao, Z. Liu, and Z. Ren. “Size effect in thermoelectric materials”. In: *npj Quantum Materials* 1.1 (Dec. 2016), p. 16028. ISSN: 2397-4648. DOI: 10.1038/npjquantmats.2016.28. URL: https://doi.org/10.1038/npjquantmats.2016.28.

[17] S. Liu, M. Chen, C. Fu, and T. Zhu. “The Interplay of Magnetism and Thermoelectricity: A Review”. In: *Advanced Physics Research* 2.9 (2023). ISSN: 2751-1200. DOI: 10.1002/apxr.202300015.

[18] E. Berg, E. Roncali, and S. R. Cherry. “Optimizing light transport in scintillation crystals for time-of-flight PET: an experimental and optical Monte Carlo simulation study”. In: *Biomedical Optics Express* 6.6 (2015), p. 2220. ISSN: 2156-7085. DOI: 10.1364/boe.6.002220. URL: https://doi.org/10.1364/boe.6.002220.

[19] A. Knapitsch and P. Lecoq. “Review on photonic crystal coatings for scintillators”. In: *International Journal of Modern Physics A* 29.30 (2014), p. 1430070. DOI: 10.1142/S0217751X14300701.

[20] R. E. Christiansen and O. Sigmund. “Inverse design in photonics by topology optimization: tutorial”. In: *Journal of the Optical Society of America B* 38.2 (Jan. 2021), p. 496. ISSN: 1520-8540. DOI: 10.1364/josab.406048. URL: http://dx.doi.org/10.1364/JOSAB.406048.

[21] Ł. Kapłon, D. Kulig, S. Beddar, T. Fiutowski, W. Górska, J. Hajduga, P. Jurgielewicz, D. Kabat, K. Kalecińska, M. Kopeć, S. Koperny, B. Mindur, J. Moroń, G. Moskal, S. Niedźwiecki, M. Silarski, F. Sobczuk, T. Szumlak, and A. Ruciński. “Investigation of the light output of 3D-printed plastic scintillators for dosimetry applications”. In: *Radiation Measurements* 158 (2022), p. 106864. ISSN: 1350-4487. DOI: https://doi.org/10.1016/j.radmeas.2022.106864. URL: https://www.sciencedirect.com/science/article/pii/S135044872200155X.

[22] T. Sibilieva, V. Alekseev, S. Barsuk, S. Berns, E. Boillat, I. Boiaryntseva, A. Boyarintsev, A. Carbone, A. De Roeck, S. Dolan, T. Driuk, A. Gendotti, I. Gerasymov, B. Grynyov, S. Hugon, U. Kose, O. Opolonin, A. Rubbia, D. Sgalaberna, M. Sibilyev, S. Tretyak, T. Weber, J. Wuthrich, and X. Y. Zhao. “3D printing of inorganic scintillator-based particle detectors”. In: *Journal of Instrumentation* 18.3 (2023). ISSN: 17480221. DOI: 10.1088/1748-0221/18/03/P03007.

[23] G. Konstantinou, P. Lecoq, J. M. Benlloch, and A. J. Gonzalez. “Metascintillators for Ultrafast Gamma Detectors: A Review of Current State and Future Perspectives”. In: *IEEE Transactions on Radiation and Plasma Medical Sciences* 6.1 (2022), pp. 5–15. DOI: 10.1109/TRPMS.2021.3069624.

[24] F. Addesa, T. Anderson, P. Barria, C. Basile, A. Benaglia, R. Bertoni, A. Bethani, R. Bianco, A. Bornheim, G. Boldrini, A. Boletti, A. Bulla, M. Campana, B. Cardwell, P. Carniti, F. Cetorelli, F. De Guio, K. De Leo, F. De Riggi, J. Dervan, E. Fernandez, A. Gaile, M. Gallinaro, A. Ghezzi, C. Gotti, R. Goldouzian, V. Guglielmi, A. Heering, Z. Hu, M. Jose, A. Karneyeu, A. Krishna, B. Kronheim, C. Kuo, A. La Torre, A. Li, F. Lombardi, M. Lucchini, M. Malberti, Y. Mao, B. Marzocchi, P. Meridiani, Y. Musienko, C. Neu, G. Organtini, T. Orimoto, C. Palmer, M. Paganoni, S. Palluotto, R. Paramatti, G. Pessina, R. Perelman, C. Quaranta, N. Redaelli, S. Redaelli, G. R. Gutiérrez, S. Ronchi, F. Santanastasio, I. Schmidt, J. Silva, G. Sorrentino, X. Sun, T. T. de Fatis, M. Tosi, B. Ujvari, J. Varela, J. Wang, M. Wayne, S. White, L. Zhang, and M. Zhang. “Optimization of LYSO crystals and SiPM parameters for the CMS MIP timing detector”. In:

JINST 19.12 (2024), P12020. DOI: 10.1088/1748-0221/19/12/P12020. arXiv: 2410.08738. URL: https://cds.cern.ch/record/2914564.

[25] F. Acerbi and S. Gundacker. "Understanding and simulating SiPMs". In: *Nuclear Instruments and Methods in Physics Research Section A: Accelerators, Spectrometers, Detectors and Associated Equipment* 926 (2019). Silicon Photomultipliers: Technology, Characterisation and Applications, pp. 16–35. ISSN: 0168-9002. DOI: https://doi.org/10.1016/j.nima.2018.11.118. URL: https://www.sciencedirect.com/science/article/pii/S0168900218317704.

[26] A. Bornheim, W. Lustermann, K. Stachon, G. Reales Gutiérrez, A. Benaglia, F. De Guio, A. Ghezzi, M. Lucchini, M. Malberti, S. Palluotto, T. Tabarelli de Fatis, M. Benettoni, R. Carlin, M. Tosi, R. Rossin, P. Meridiani, R. Paramatti, F. Santanastasio, J. Silva, J. Varela, A. Heering, A. Karneyeu, Y. Musienko, M. Wayne, T. Anderson, B. Cox, C. Perez Lara, A. Ledovskoy, S. White, and I. Schmidt. "Integration of thermo-electric coolers into the CMS MTD SiPM arrays for operation under high neutron fluence". In: *Journal of Instrumentation* 18.08 (Aug. 2023), P08020. DOI: 10.1088/1748-0221/18/08/P08020. URL: https://dx.doi.org/10.1088/1748-0221/18/08/P08020.

[27] M. Diefenthaler, C. Fanelli, L. Gerlach, W. Guan, T. Horn, A. Jentsch, M. Lin, K. Nagai, H. Nayak, C. Pecar, K. Suresh, A. Vossen, T. Wang, T. Wenaus, and on behalf of the AID(2)E collaboration. "AI-assisted detector design for the EIC (AID(2)E)". In: *Journal of Instrumentation* 19.07 (July 2024), p. C07001. DOI: 10.1088/1748-0221/19/07/C07001. URL: https://dx.doi.org/10.1088/1748-0221/19/07/C07001.

[28] T. Dorigo, A. Giammanco, P. Vischia, M. Aehle, M. Bawaj, A. Boldyrev, P. de Castro Manzano, D. Derkach, J. Donini, A. Edelen, F. Fanzago, N. R. Gauger, C. Glaser, A. G. Baydin, L. Heinrich, R. Keidel, J. Kieseler, C. Krause, M. Lagrange, M. Lamparth, L. Layer, G. Maier, F. Nardi, H. E. Pettersen, A. Ramos, F. Ratnikov, D. Röhrich, R. R. de Austri, P. M. R. del Árbol, O. Savchenko, N. Simpson, G. C. Strong, A. Taliercio, M. Tosi, A. Ustyuzhanin, and H. Zaraket. "Toward the end-to-end optimization of particle physics instruments with differentiable programming". In: *Reviews in Physics* 10 (2023), p. 100085. ISSN: 2405-4283. DOI: https://doi.org/10.1016/j.revip.2023.100085. URL: https://www.sciencedirect.com/science/article/pii/S2405428323000047.

[29] A. Grandchamp. "Conception and optimisation of the electromagnetic shield for the SHIP experiment". In: 2018. URL: https://api.semanticscholar.org/CorpusID:119091081.

[30] E. Kurbatov, F. Ratnikov, and E. Ursov. "Multi-parameter detector optimization: SHiP case". In: *EPJ Web Conf.* 295 (2024), p. 03023. DOI: 10.1051/epjconf/202429503023.

[31] L. Grzanka, M. Korcyl, P. Olko, and M. P. Waligórski. “A numerical method to optimise the spatial dose distribution in carbon ion radiotherapy planning”. In: *Radiation Protection Dosimetry* 166.1-4 (Sept. 2015). Epub 2015 May 5, pp. 351–355. DOI: 10.1093/rpd/ncv195.

[32] R. Rawat. “Structural Analysis of an Ultra-Light Drift Chamber in Composite Materials for High Energy Particle Physics experiments”. Thesis submitted to the Department of Structural, Geotechnical and Building Engineering (DISEG) in partial fulfillment of the Requirements for the Degree of Master of Science in Civil Engineering (Structures and Infrastructures). PhD thesis. Turin, Italy: POLITECNICO DI TORINO, July 2023.

[33] F. Fernandez, I. Ramos-Lerate, M. Kocsis, J. Martinez, D. Beltran, J. Bordas, and J. Toledo. “Study and optimization of multiwire proportional chambers for Synchrotron facilities”. In: *IEEE Transactions on Nuclear Science* 53.2 (2006), pp. 544–548. DOI: 10.1109/TNS.2006.871257.

[34] S. Shi, V. Mahzoon, G. Lindner, S. Vucetic, and S. Miskovic. *Optimizing Detector Placement, Number, and Size in Radioactive Particle Tracking Using Feature Selection*. Available at SSRN: https://ssrn.com/abstract=4981575 or http://dx.doi.org/10.2139/ssrn.4981575. 2023.

[35] O. Dubé, D. Dubé, J. Chaouki, and F. Bertrand. “Optimization of detector positioning in the radioactive particle tracking technique”. In: *Applied Radiation and Isotopes* 89 (2014), pp. 109–124. ISSN: 0969-8043. DOI: https://doi.org/10.1016/j.apradiso.2014.02.019. URL: https://www.sciencedirect.com/science/article/pii/S0969804314000712.

[36] A. L. Lopes, M. Couceiro, P. Crespo, and P. Fonte. “Optimization through Monte Carlo Simulations of a novel High-Resolution Brain-PET System based on Resistive Plate Chambers”. In: *2021 IEEE Nuclear Science Symposium and Medical Imaging Conference (NSS/MIC)*. 2021, pp. 1–5. DOI: 10.1109/NSS/MIC44867.2021.9875731.

[37] L. Chen, X. Wang, S. Qian, X. Zhang, Q. Wu, L. Ma, P. Zeng, and C. Sun. “Optimizing the design of ultrafast photomultiplier tubes”. In: *Opt. Express* 31.18 (Aug. 2023), pp. 29975–29985. DOI: 10.1364/OE.498230. URL: https://opg.optica.org/oe/abstract.cfm?URI=oe-31-18-29975.

[38] P. Chen, J. Tian, Y. Wei, H. Liu, X. Sai, J. He, L. Chen, X. Wang, and Y. Lu. “Optimization design of a 20-in. elliptical MCP-PMT”. In: *Nuclear Instruments and Methods in Physics Research Section A: Accelerators, Spectrometers, Detectors and Associated Equipment* 841 (2017), pp. 104–108. ISSN: 0168-9002. DOI: https://doi.org/10.1016/j.nima.2016.10.036. URL: https://www.sciencedirect.com/science/article/pii/S0168900216310749.

[39] Y. Unno *et al.* “TCAD simulations of silicon strip and pixel sensor optimization”. In: *PoS* VERTEX2011 (2011), p. 024. DOI: 10.22323/1.137.0024.

[40] X. Fernandez-Tejero. “Design and Optimization of Advanced Silicon Strip Detectors for High Energy Physics Experiments”. Presented 24 Jul 2020. Barcelona, Autonoma U., 2020. URL: https://cds.cern.ch/record/2722118.

[41] M. Valentan, T. Bergauer, M. Dragicevic, M. Friedl, C. Irmler, E. Huemer, and W. Treberspurg. “Optimization of Strip Isolation for Silicon Sensors”. In: *Physics Procedia* 37 (2012). Proceedings of the 2nd International Conference on Technology and Instrumentation in Particle Physics (TIPP 2011), pp. 891–898. ISSN: 1875-3892. DOI: https://doi.org/10.1016/j.phpro.2012.04.098. URL: https://www.sciencedirect.com/science/article/pii/S1875389212017853.

Appendices

This section presents all complementary information for previous chapters included in the corresponding journal papers for clarification purposes.

The structure for the appendices chronologically follows the presentation of each chapter. The contents of each appendix can be summarized as:

- Appendix A: presents the FEM element and integration used in Chapter 2.
- Appendix B: presents the analytical solution equations for the results in Chapter 2.
- Appendix C: presents the thermoelectric equations sensitivities required to run TO in Chapter 3
- Appendix D: presents the finite differences validation of the sensitivities used in Chapter 3.
- Appendix E: presents the thermoelectric non-linear material properties used in Chapter 3.
- Appendix F: presents material and model properties used for the optical materials used in Chapter 4.
- Appendix G: presents material and model properties used for the optical materials used for the COMSOL simulations in Chapter 5.
- Appendix H: presents provides the references of the codes required for the replication of the results in this document.

Appendix A Serendipity 20 node element formulation

Serendipity 20 node elements are used in this work to reduce the complexity of the calculations while using second-order approximation polynomials. These elements and their reduced points of integration following a 14-point scheme developed in [1] are represented in Figure 7.1.

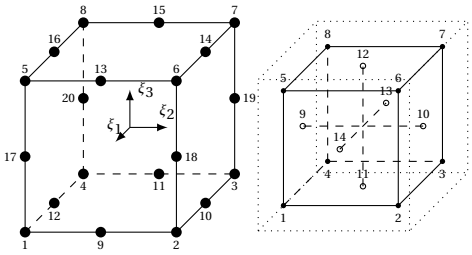

Figure 7.1.: Hexahedral 20 node element and 14 point reduced integration points with the superimposed element in dotted lines.

In Figure 7.1, we see the local coordinate system of the element in terms of ξ_i, the numbering system of each node. Table 7.1 represents the location of each of these nodes and their associated shape function.

Finally, we perform the element's integration in an internal hexahedron to the element. The integration points are then located in the internal hexahedron corners and face centres as defined in Table 7.2.

Node	ξ_1	ξ_2	ξ_3	**Shape Functions**
1	-1	-1	-1	$(1-\xi_2)(1-\xi_3)(1-\xi_1)(-\xi_2-\xi_3-\xi_1-2)/8$
2	1	-1	-1	$(1+\xi_2)(1-\xi_3)(1-\xi_1)(\xi_2-\xi_3-\xi_1-2)/8$
3	1	1	-1	$(1+\xi_2)(1+\xi_3)(1-\xi_1)(\xi_2+\xi_3-\xi_1-2)/8$
4	-1	1	-1	$(1-\xi_2)(1+\xi_3)(1-\xi_1)(-\xi_2+\xi_3-\xi_1-2)/8$
5	-1	-1	1	$(1-\xi_2)(1-\xi_3)(1+\xi_1)(-\xi_2-\xi_3+\xi_1-2)/8$
6	1	-1	1	$(1+\xi_2)(1-\xi_3)(1+\xi_1)(\xi_2-\xi_3+\xi_1-2)/8$
7	1	1	1	$(1+\xi_2)(1+\xi_3)(1+\xi_1)(\xi_2+\xi_3+\xi_1-2)/8$
8	-1	1	1	$(1-\xi_2)(1+\xi_3)(1+\xi_1)(-\xi_2+\xi_3+\xi_1-2)/8$
9	0	-1	-1	$(1-\xi_2^2)(1-\xi_3)(1-\xi_1)/4$
10	1	0	-1	$(1+\xi_2)(1-\xi_3^2)(1-\xi_1)/4$
11	0	1	-1	$(1-\xi_2^2)(1+\xi_3)(1-\xi_1)/4$
12	-1	0	-1	$(1-\xi_2)(1-\xi_3^2)(1-\xi_1)/4$
13	-1	-1	0	$(1-\xi_2^2)(1-\xi_3)(1+\xi_1)/4$
14	1	-1	0	$(1+\xi_2)(1-\xi_3^2)(1+\xi_1)/4$
15	1	1	0	$(1-\xi_2^2)(1+\xi_3)(1+\xi_1)/4$
16	-1	1	0	$(1-\xi_2)(1-\xi_3^2)(1+\xi_1)/4$
17	0	-1	1	$(1-\xi_2)(1-\xi_3)(1-\xi^2)/4$
18	1	0	1	$(1+\xi_2)(1-\xi_3)(1-\xi^2)/4$
19	0	1	1	$(1+\xi_2)(1+\xi_3)(1-\xi^2)/4$
20	-1	0	1	$(1-\xi_2)(1+\xi_3)(1-\xi^2)/4$

Table 7.1.: Node Locations and Shape Functions for Hexahedral 20-Node Serendipity Element

Type	Integration Point Location		Weight
Corner Points	$\xi_1 = \pm.7587869106$		0.3351800554
	$\xi_2 = \pm.7587869106$		
	$\xi_3 = \pm.7587869106$		
Center Points	$\xi_1 = \pm.7958224257$	ξ_2=ξ_3=0	0.8864265927
	$\xi_2 = \pm.7958224257$	ξ_1=ξ_3=0	
	$\xi_3 = \pm.7958224257$	ξ_1=ξ_2=0	

Table 7.2.: 14 point integration scheme for a 20 node hexahedral element

Appendix B Analytical Problem Solution

The system of equations formed by Equations (2.43) and (2.44) can be solved, imposing a value of $V_0 = 0$, obtaining a value of T_c equal to,

$$T_c = \frac{T_n}{T_d}, \tag{7.1}$$

$$\begin{aligned} T_n = k\,(& 2\alpha\sigma V_f x_2^{2p_\alpha+p_\sigma+p_k} x_1^{p_\alpha+p_\sigma} - 4k x_2^{2p_k} x_1^{2p_\alpha+p_\sigma} \\ & - 4\alpha^2\sigma T_h x_2^{2p_\alpha+p_\sigma+p_k} x_1^{2p_\alpha+p_\sigma} \\ & - 4\alpha^2\sigma T_h x_2^{p_k} x_1^{2(2p_\alpha+p_\sigma)} + 2\alpha\sigma V_f x_2^{p_k} x_1^{3p_\alpha+2p_\sigma} \\ & + 4k x_2^{2p_\alpha+p_\sigma+p_k} x_1^{p_k} \\ & \pm \alpha^2\sigma L x_2^{2(2p_\alpha+p_\sigma)}(Sq) x_1^{p_k} + 4k x_2^{2p_\alpha+p_\sigma} x_1^{2p_k} \\ & + 2\alpha\sigma V_f x_2^{2p_\alpha+p_\sigma} x_1^{p_\alpha+p_\sigma+p_k} \\ & - 4\alpha^2\sigma T_h x_2^{2p_\alpha+p_\sigma} x_1^{2p_\alpha+p_\sigma+p_k} \\ & - 4k x_2^{p_k} x_1^{2p_\alpha+p_\sigma+p_k} \\ & \pm 2\alpha^2\sigma L x_2^{2p_\alpha+p_\sigma}(Sq) x_1^{2p_\alpha+p_\sigma+p_k} \\ & + 2\alpha\sigma V_f x_1^{3p_\alpha+2p_\sigma+p_k} - 4\alpha^2\sigma T_h x_1^{4p_\alpha+2p_\sigma+p_k} \\ & \pm \alpha^2\sigma L(Sq) x_1^{4p_\alpha+2p_\sigma+p_k}\,), \end{aligned} \tag{7.2}$$

$$\begin{aligned} T_d = & 2\alpha^2\sigma(x_1^{2p_\alpha+p_\sigma} + x_2^{2p_\alpha+p_\sigma})(-\alpha\sigma V_f(x_1^{2p_\alpha+p_\sigma} + \\ & x_2^{2p_\alpha+p_\sigma}) x_1^{p_\alpha+p_\sigma} + 2\alpha^2\sigma T_h(x_1^{2p_\alpha+p_\sigma} + x_2^{2p_\alpha+p_\sigma}) \\ & x_1^{2p_\alpha+p_\sigma} + k(2x_1^{2p_\alpha+p_\sigma} x_2^{p_k} - 2x_1^{p_k} x_2^{2p_\alpha+p_\sigma})), \end{aligned} \tag{7.3}$$

with T_c providing two results to the system depending on the sign of the square root, S_q,

$$S_q = \sqrt{\frac{S_n}{S_d}}, \tag{7.4}$$

$$\begin{aligned} S_n = & x_1^{-2p_k}(\alpha\sigma V_f(x_1^{2p_\alpha+p_\sigma} + x_2^{2p_\alpha+p_\sigma}) x_1^{p_\alpha+p_\sigma} \\ & - 2\alpha^2\sigma T_h(x_1^{2p_\alpha+p_\sigma} + x_2^{2p_\alpha+p_\sigma}) x_1^{2p_\alpha+p_\sigma} \\ & + 2k(x_1^{p_k} x_2^{2p_\alpha+p_\sigma} - x_1^{2p_\alpha+p_\sigma} x_2^{p_k}))^2 \\ & (4A\sigma^2 T_h^2(x_1^{2p_\alpha+p_\sigma} + x_2^{2p_\alpha+p_\sigma})^2\alpha^4 \\ & - 4A\sigma^2 T_h V_f(x_2^{2p_\alpha+p_\sigma} x_1^{p_\alpha+p_\sigma} + x_2^{p_\alpha+p_\sigma} x_1^{2p_\alpha+p_\sigma} \\ & + x_1^{3p_\alpha+2p_\sigma} + x_2^{3p_\alpha+2p_\sigma})\alpha^3 \\ & + \sigma(x_1^{2p_\alpha+p_\sigma} + x_2^{2p_\alpha+p_\sigma})(A\sigma(x_1^{p_\sigma} + x_2^{p_\sigma}) V_f^2 \\ & + 4Lq + 8Ak T_h(x_1^{p_k} + x_2^{p_k}))\alpha^2 \\ & + 4Ak^2(x_1^{p_k} + x_2^{p_k})^2), \end{aligned} \tag{7.5}$$

$$S_d = A\alpha^4\sigma^2k^2L^2\left(x_1^{2p_\alpha+p_\sigma} + x_2^{2p_\alpha+p_\sigma}\right)^4. \tag{7.6}$$

The other result we need to extract from the analytical formulation is the device's power consumption. We can define this power consumption as

$$P = \sum \left| j_i A V_c \right|, \tag{7.7}$$

where the V_c value is evident, noting that both electrical contacts, made by legs influenced by both x_i, will always have the same material properties overall and are written as,

$$V_c = \frac{V_f}{2}. \tag{7.8}$$

The current densities j_i are then equal for each leg with the same density variable with opposite signs,

$$j_1 = -j_4, \tag{7.9}$$

$$j_2 = -j_3. \tag{7.10}$$

We can write the results for these current densities as,

$$j_i = \frac{j_{ni}}{j_d}, \tag{7.11}$$

with the equations,

$$\begin{aligned}
j_{n4} =& x_1^{p_\sigma}(-\alpha^2\sigma^2V_f^2x_2^{2(2p_\alpha+p_\sigma)}x_1^{p_\alpha+p_\sigma} + 4\alpha^3\sigma^2T_hV_fx_2^{2(2p_\alpha+p_\sigma)}x_1^{2p_\alpha+p_\sigma} \\
&+ 4\alpha\sigma kV_fx_2^{2p_\alpha+p_\sigma+p_k}x_1^{2p_\alpha+p_\sigma} + 8\alpha^3\sigma^2T_hV_fx_2^{2p_\alpha+p_\sigma}x_1^{2(2p_\alpha+p_\sigma)} \\
&+ 4\alpha\sigma kV_fx_2^{p_k}x_1^{2(2p_\alpha+p_\sigma)} + 4\alpha^3\sigma^2T_hV_fx_1^{3(2p_\alpha+p_\sigma)} \\
&- 4\alpha^4\sigma^2T_h^2x_2^{2(2p_\alpha+p_\sigma)}x_1^{3p_\alpha+p_\sigma} - 4k^2x_2^{2p_k}x_1^{3p_\alpha+p_\sigma} \\
&- 8\alpha^2\sigma kT_hx_2^{2p_\alpha+p_\sigma+p_k}x_1^{3p_\alpha+p_\sigma} \\
&- 2\alpha^2\sigma^2V_f^2x_2^{2p_\alpha+p_\sigma}x_1^{3p_\alpha+2p_\sigma} - 8\alpha^4\sigma^2T_h^2x_2^{2p_\alpha+p_\sigma}x_1^{5p_\alpha+2p_\sigma} \\
&- 8\alpha^2\sigma kT_hx_2^{p_k}x_1^{5p_\alpha+2p_\sigma} - \alpha^2\sigma^2V_f^2x_1^{5p_\alpha+3p_\sigma} \\
&- 4\alpha^4\sigma^2T_h^2x_1^{7p_\alpha+3p_\sigma} - 2\alpha\sigma kV_fx_2^{2(2p_\alpha+p_\sigma)}x_1^{p_k} \\
&+ 4\alpha^2\sigma kT_hx_2^{2(2p_\alpha+p_\sigma)}x_1^{p_\alpha+p_k} \\
&+ 4k^2x_2^{2p_\alpha+p_\sigma+p_k}x_1^{p_\alpha+p_k} \pm \alpha^2\sigma kLx_2^{2(2p_\alpha+p_\sigma)}(S_q)x_1^{p_\alpha+p_k} \\
&- 4k^2x_2^{p_k}x_1^{3p_\alpha+p_\sigma+p_k} \\
&\pm 2\alpha^2\sigma kLx_2^{2p_\alpha+p_\sigma}(S_q)x_1^{3p_\alpha+p_\sigma+p_k} \\
&+ 2\alpha\sigma kV_fx_1^{4p_\alpha+2p_\sigma+p_k} \\
&- 4\alpha^2\sigma kT_hx_1^{5p_\alpha+2p_\sigma p_k} \pm \alpha^2\sigma kL(S_q)x_1^{5p_\alpha+2p_\sigma+p_k} + 4k^2x_2^{2p_\alpha+p_\sigma}x_1^{p_\alpha+2p_k}),
\end{aligned} \tag{7.12}$$

and,

$$
\begin{aligned}
j_{n2} = & x_2^{p_\sigma}(4\alpha^4\sigma^2 T_h^2 x_1^{3(2p_\alpha+p_\sigma)} x_2^{p_\alpha} \\
& - 2\alpha^3\sigma^2 T_h V_f x_1^{5p_\alpha+3p_\sigma} x_2^{p_\alpha} \\
& - 2\alpha\sigma k V_f x_1^{3p_\alpha+2p_\sigma+p_k} x_2^{p_\alpha} \\
& + 4\alpha^2\sigma k T_h x_1^{4p_\alpha+2p_\sigma+p_k} x_2^{p_\alpha} \\
& \mp \alpha^2\sigma k L x_1^{4p_\alpha+2p_\sigma+p_k}(S_q) x_2^{p_\alpha} \\
& - 4\alpha^3\sigma^2 T_h V_f x_1^{2(2p_\alpha+p_\sigma)} x_2^{2p_\alpha+p_\sigma} \\
& + 2\alpha^2\sigma^2 V_f^2 x_1^{3p_\alpha+2p_\sigma} x_2^{2p_\alpha+p_\sigma} \\
& + 2\alpha\sigma k V_f x_1^{2p_\alpha+p_\sigma+p_k} x_2^{2p_\alpha+p_\sigma} \\
& + \alpha^2\sigma^2 V_f^2 x_1^{p_\alpha+p_\sigma} x_2^{2(2p_\alpha+p_\sigma)} \\
& - 2\alpha^3\sigma^2 T_h V_f x_1^{2p_\alpha+p_\sigma} x_2^{2(2p_\alpha+p_\sigma)} \\
& + 2\alpha\sigma k V_f x_1^{p_k} x_2^{2(2p_\alpha+p_\sigma)} \\
& + 8\alpha^4\sigma^2 T_h^2 x_1^{2(2p_\alpha+p_\sigma)} x_2^{3p_\alpha+p_\sigma} \\
& - 4\alpha^3\sigma^2 T_h V_f x_1^{3p_\alpha+2p_\sigma} x_2^{3p_\alpha+p_\sigma} \\
& - 4k^2 x_1^{2p_k} x_2^{3p_\alpha+p_\sigma} \\
& - 2\alpha\sigma k V_f x_1^{p_\alpha+p_\sigma+p_k} x_2^{3p_\alpha+p_\sigma} \\
& \mp 2\alpha^2\sigma k L x_1^{2p_\alpha+p_\sigma+p_k}(S_q) x_2^{3p_\alpha+p_\sigma} \\
& - 2\alpha^3\sigma^2 T_h V_f x_1^{p_\alpha+p_\sigma} x_2^{5p_\alpha+2p_\sigma} \\
& + 4\alpha^4\sigma^2 T_h^2 x_1^{2p_\alpha+p_\sigma} x_2^{5p_\alpha+2p_\sigma} \\
& - 4\alpha^2\sigma k T_h x_1^{p_k} x_2^{5p_\alpha+2p_\sigma} \mp \alpha^2\sigma k L x_1^{p_k}(S_q)) x_2^{5p_\alpha+2p_\sigma} \\
& - 2\alpha\sigma k V_f x_1^{2(2p_\alpha+p_\sigma)} x_2^{p_k} \\
& + 8\alpha^2\sigma k T_h x_1^{2(2p_\alpha+p_\sigma)} x_2^{p_\alpha+p_k} \\
& - 2\alpha\sigma k V_f x_1^{3p_\alpha+2p_\sigma} x_2^{p_\alpha+p_k} \\
& + 4k^2 x_1^{2p_\alpha+p_\sigma+p_k} x_2^{p_\alpha+p_k} \\
& - 2\alpha\sigma k V_f x_1^{2p_\alpha+p_\sigma} x_2^{2p_\alpha+p_\sigma+p_k} \\
& - 2\alpha\sigma k V_f x_1^{p_\alpha+p_\sigma} x_2^{3p_\alpha+p_\sigma+p_k} \\
& + 8\alpha^2\sigma k T_h x_1^{2p_\alpha+p_\sigma} x_2^{3p_\alpha+p_\sigma+p_k} \\
& - 4k^2 x_1^{p_k} x_2^{3p_\alpha+p_\sigma+p_k} \\
& + 4k^2 x_1^{2p_\alpha+p_\sigma} x_2^{p_\alpha+2p_k} \\
& - 2\alpha^3\sigma^2 T_h V_f x_1^{3(2p_\alpha+p_\sigma)} + \alpha^2\sigma^2 V_f^2 x_1^{5p_\alpha+3p_\sigma}),
\end{aligned}
\tag{7.13}
$$

characterizing all current density flow numerators and with a common denominator for

all current densities,

$$\begin{aligned} j_d =& 2\alpha L(x_1^{2p_\alpha+p_\sigma} + x_2^{2p_\alpha+p_\sigma})(-\alpha\sigma V_f(x_1^{2p_\alpha+p_\sigma} + x_2^{2p_\alpha+p_\sigma}) \\ & x_1^{p_\alpha+p_\sigma} + 2\alpha^2\sigma T_h(x_1^{2p_\alpha+p_\sigma} + x_2^{2p_\alpha+p_\sigma})x_1^{2p_\alpha+p_\sigma} \\ & + k(2x_1^{2p_\alpha+p_\sigma}x_2^{p_k} - 2x_1^{p_k}x_2^{2p_\alpha+p_\sigma})). \end{aligned} \tag{7.14}$$

Appendix C Residual derivatives

In this appendix we develop the required derivatives of the residual for the thermo-electro-mechanical FEM system for the calculation related to of the adjoint sensitivities and tangent matrix.

To derive the residual derivatives for the thermo-electro-mechanical finite element system, the element-level dimensions of the involved matrices and vectors must be established. These sizes vary with the element type and determine the structure of both the tangent matrix and the adjoint sensitivities. Table 7.3 presents the relevant quantities at the element level for quadratic 2D (Quad8) and 3D (Hex20) elements, including field variables, constitutive matrices, and shape function representations. This information defines the computational framework used in the derivation of the sensitivity equations.

Symbol	Description	2D (Q8)	3D (H20)
$\mathbf{j}$	Curr. density	2×1	3×1
$\mathbf{q}$	Heat flux	2×1	3×1
$\hat{\boldsymbol{\sigma}}$	Stress (Voigt)	3×1	6×1
$\mathbf{u}$	Displacement	16×1	60×1
$\mathbf{t}$	Temperature	8×1	20×1
$\mathbf{v}$	Elec. potential	8×1	20×1
$\mathbf{C_0}$	Elastic matrix	3×3	6×6
$\boldsymbol{\beta}_T$	Thermal stress	3×1	6×1
$\mathbf{e}_{\text{tr}}$	Trace operator vector	3×1	6×1
$\nabla\mathbf{N}$	Shape func. (scalar)	8×3	20×3
$\mathbf{N}$	Shape func. (scalar)	8×1	20×1
$\mathbf{N_U}$	Shape func. (disp)	16×1	60×1
$\mathbf{B}$	Strain-displ. mat.	3×16	6×60
$\mathbf{r}_u$	Mech. residual	16×1	60×1
$\mathbf{r}_t$	Thermal residual	8×1	20×1
$\mathbf{r}_v$	Elec. residual	8×1	20×1

Table 7.3.: Matrix and vector sizes in thermo-electro-mechanical FEM (Quad8/Hex20).

The first derivatives we need to define are the derivatives of the residual with respect to the element level state vector $\mathbf{s}$ composed of the element level displacement $\mathbf{u}$, temperature $\mathbf{t}$, and voltage $\mathbf{v}$ degrees of freedom. These derivatives are,

$$\frac{\partial \mathbf{r_u}}{\partial \mathbf{t}} = \mathbf{k}_\Theta + \int_\Omega \mathbf{B}^\intercal \frac{\partial \boldsymbol{\beta_T}}{\partial T}\theta \mathbf{N}^\intercal \,\mathrm{d}\Omega - \int_\Omega \mathbf{B}^\intercal \frac{\partial \mathbf{C}}{\partial T}\mathbf{B}\mathbf{u}\mathbf{N}^\intercal \,\mathrm{d}\Omega\,, \tag{7.15}$$

$$\frac{\partial \mathbf{r_u}}{\partial \mathbf{u}} = -\mathbf{k_U}\,, \tag{7.16}$$

$$\frac{\partial \mathbf{r_t}}{\partial \mathbf{t}} = -\int_\Omega \nabla\mathbf{N}\frac{\partial \mathbf{q}}{\partial \mathbf{t}}\,\mathrm{d}\Omega + \int_\Omega \mathbf{N}(\frac{\partial \mathbf{j}}{\partial \mathbf{t}}^\intercal \nabla\mathbf{N}^\intercal \mathbf{v})^\intercal \,\mathrm{d}\Omega\,, \tag{7.17}$$

$$\begin{aligned}\frac{\partial \mathbf{r_t}}{\partial \mathbf{v}} &= -\int_\Omega \nabla \mathbf{N} \frac{\partial \mathbf{q}}{\partial \mathbf{v}} \,\mathrm{d}\Omega \\ &+ \int_\Omega \mathbf{N}(\frac{\partial \mathbf{j}}{\partial \mathbf{v}}^\mathsf{T} \nabla \mathbf{N}^\mathsf{T} \mathbf{v})^\mathsf{T} \,\mathrm{d}\Omega \\ &+ \int_\Omega \mathbf{N}\mathbf{j}^\mathsf{T} \nabla \mathbf{N}^\mathsf{T} \,\mathrm{d}\Omega,\end{aligned} \tag{7.18}$$

$$\frac{\partial \mathbf{r_v}}{\partial \mathbf{t}} = -\int_\Omega \nabla \mathbf{N} \frac{\partial \mathbf{j}}{\partial \mathbf{t}} \,\mathrm{d}\Omega, \tag{7.19}$$

$$\frac{\partial \mathbf{r_v}}{\partial \mathbf{v}} = -\int_\Omega \nabla \mathbf{N} \frac{\partial \mathbf{j}}{\partial \mathbf{v}} \,\mathrm{d}\Omega. \tag{7.20}$$

The temperature derivative of $\mathbf{C}$ and β_T are

$$\begin{aligned}\frac{\partial \mathbf{C}}{\partial T} &= \mathbf{C}_0 \bar{x}_\rho^{p_E} \frac{\partial E}{\partial T}, \\ \frac{\partial \boldsymbol{\beta_T}}{\partial T} &= \frac{\bar{x}_\rho^{p_E}}{1-2\nu} \mathbf{e}_{\mathrm{tr}} \left(\alpha_T \frac{\partial E}{\partial T} + E \frac{\partial \alpha_T}{\partial T} \right).\end{aligned} \tag{7.21}$$

From these equations, we can recognize that the derivatives of the thermoelectrical degrees of freedom concerning the displacements are zero,

$$\frac{\partial \mathbf{r_t}}{\partial \mathbf{u}} = \mathbf{0}, \qquad \frac{\partial \mathbf{r_v}}{\partial \mathbf{u}} = \mathbf{0}, \qquad \frac{\partial \mathbf{r_u}}{\partial \mathbf{v}} = \mathbf{0}. \tag{7.22}$$

These equations still require the calculation of the derivative of the heat and current flows with respect to the nodal degrees of freedom,

$$\begin{aligned}\frac{\partial \mathbf{j}}{\partial \mathbf{v}} &= -\gamma \nabla \mathbf{N}^\mathsf{T}, \\ \frac{\partial \mathbf{j}}{\partial \mathbf{t}} &= -\alpha\gamma \nabla \mathbf{N}^\mathsf{T} - \frac{\partial \alpha}{\partial T} \gamma \nabla \mathbf{N}^\mathsf{T} \mathbf{t} \mathbf{N}^\mathsf{T} - \frac{\partial \gamma}{\partial T} \alpha \nabla \mathbf{N}^\mathsf{T} \mathbf{t} \mathbf{N}^\mathsf{T}, \\ \frac{\partial \mathbf{q}}{\partial \mathbf{v}} &= \alpha (\mathbf{N}^\mathsf{T} \mathbf{t}) \frac{\partial \mathbf{j}}{\partial \mathbf{v}}, \\ \frac{\partial \mathbf{q}}{\partial \mathbf{t}} &= \alpha (\mathbf{N}^\mathsf{T} \mathbf{t}) \frac{\partial \mathbf{j}}{\partial \mathbf{v}} + \frac{\partial \alpha}{\partial T} (\mathbf{N}^\mathsf{T} \mathbf{t}) \mathbf{j} + \alpha \mathbf{j} \mathbf{N}^\mathsf{T} + \frac{\partial \alpha}{\partial T} \mathbf{j} \mathbf{N}^\mathsf{T} \mathbf{t} \mathbf{N}^\mathsf{T} \\ &\quad - \kappa \nabla \mathbf{N}^\mathsf{T} - \frac{\partial \kappa}{\partial T} \nabla \mathbf{N}^\mathsf{T} \mathbf{t} \mathbf{N}^\mathsf{T}.\end{aligned} \tag{7.23}$$

The derivative and formulation of the thermoelectrical material properties with respect to the temperature is shown in Appendix F, completing these sensitivities.

We also require the sensitivities of the residual with respect to its physical density design variable for the MMA algorithm. The sensitivities of the thermoelectrical element level residuals with respect to the physical design are

$$\begin{aligned}\frac{\partial \mathbf{r_t}}{\partial \bar{x_\rho}} &= -\int_\Omega \nabla \mathbf{N} \frac{\partial \mathbf{q}}{\partial \bar{x_\rho}} \,\mathrm{d}\Omega + \int_\Omega \mathbf{N}(\frac{\partial \mathbf{j}}{\partial \bar{x_\rho}}^\mathsf{T} \nabla \mathbf{N}^\mathsf{T} \mathbf{v})^\mathsf{T} \,\mathrm{d}\Omega, \\ \frac{\partial \mathbf{r_v}}{\partial \bar{x_\rho}} &= -\int_\Omega \nabla \mathbf{N} \frac{\partial \mathbf{j}}{\partial \bar{x_\rho}} \,\mathrm{d}\Omega.\end{aligned} \tag{7.24}$$

Knowing that the heat and current flow derivatives, with material properties dependent only on each elemental density variable,

$$\begin{aligned}\frac{\partial \mathbf{j}}{\partial \bar{x_\rho}} &= -\frac{\partial \gamma}{\partial \bar{x_\rho}}\left(\nabla \mathbf{N}^\intercal \mathbf{v} + \alpha \nabla \mathbf{N}^\intercal \mathbf{t}\right) - \gamma \frac{\partial \alpha}{\partial \bar{x_\rho}} \nabla \mathbf{N}^\intercal \mathbf{t}, \\ \frac{\partial \mathbf{q}}{\partial \bar{x_\rho}} &= \frac{\partial \alpha}{\partial \bar{x_\rho}}\left(\mathbf{N}^\intercal \mathbf{t}\right)\mathbf{j} + \alpha\left(\mathbf{N}^\intercal \mathbf{t}\right)\frac{\partial \mathbf{j}}{\partial \bar{x_\rho}} - \frac{\partial \kappa}{\partial \bar{x_\rho}} \nabla \mathbf{N}^\intercal \mathbf{t}.\end{aligned} \tag{7.25}$$

Finally, the derivatives of the material properties with respect to their elemental, following Equation (3.24), value are

$$\begin{aligned}\frac{\partial \alpha}{\partial \bar{x_\rho}} &= p_\alpha \bar{x_\rho}^{p_\alpha - 1}(\alpha_0 - \alpha_{\min}), \\ \frac{\partial \kappa}{\partial \bar{x_\rho}} &= p_\kappa \bar{x_\rho}^{p_\kappa - 1}(\kappa_0 - \kappa_{\min}), \\ \frac{\partial \gamma}{\partial \bar{x_\rho}} &= p_\gamma \bar{x_\rho}^{p_\gamma - 1}(\gamma_0 - \gamma_{\min}). \\ \frac{\partial E}{\partial \bar{x_\rho}} &= p_E \bar{x_\rho}^{p_E - 1}(E_0 - E_{\min}).\end{aligned} \tag{7.26}$$

where the last two components have been calculated in Equation (7.24). Finally, the derivative of the displacement associated residual at element level is

$$\begin{aligned}\frac{\partial \mathbf{r_u}}{\partial \bar{x_\rho}} &= -\frac{\partial \mathbf{k}_U}{\partial \bar{x_\rho}}\mathbf{u} + \frac{\partial \mathbf{k}_\Theta}{\partial \bar{x_\rho}}\boldsymbol{\theta}, \\ \frac{\partial \mathbf{k_U}}{\partial \bar{x_\rho}} &= \int_\Omega \mathbf{B}^\intercal \frac{\partial \mathbf{C}}{\partial \bar{x_\rho}} \mathbf{B}\, \mathrm{d}\Omega, \\ \frac{\partial \mathbf{k}_\Theta}{\partial \bar{x_\rho}} &= \int_\Omega \mathbf{B}^\intercal \frac{\partial \boldsymbol{\beta_T}}{\partial \bar{x_\rho}} \mathbf{N}^\intercal \, \mathrm{d}\Omega.\end{aligned} \tag{7.27}$$

Depending on the derivative of the constitutive equation and thermoelastic material properties

$$\begin{aligned}\frac{\partial \mathbf{C}}{\partial \bar{x_\rho}} &= \mathbf{C}_0 p_E \bar{x}_\rho^{p_E - 1}(E_0 - E_{min}), \\ \frac{\partial \boldsymbol{\beta_T}}{\partial \bar{x_\rho}} &= \frac{\left(p_E \bar{x}_\rho^{p_E - 1}(E_0 - E_{min})\right)}{1 - 2\nu}\mathbf{e}_{\mathrm{tr}}\alpha_T,\end{aligned} \tag{7.28}$$

The derivatives of each material property with respect to the temperature field are provided in Appendix F as Equation (7.36) using the coefficients in Table 7.5.

Appendix D Finite Differences and Sensitivity Validation

To validate the sensitivities within our code, we use forward finite differences for a simplified problem to obtain and compare the sensitivity values.

Let the objective function or constraint be denoted by $f(x_i)$, where x_i is the design variable. The finite difference approximation of the sensitivity with respect to the design variable x_i is given by

$$\frac{\mathrm{d}f}{\mathrm{d}x_i} \approx \frac{f(x_i+\epsilon)-f(x_i)}{\epsilon}, \tag{7.29}$$

where and ϵ is a small perturbation. The error between the finite difference and the FEM formulation for the sensitivites in Section 3.3 can be quantified by the relative error between both

$$\delta_{\mathrm{rel}}(\epsilon) = \left| \frac{\frac{\mathrm{d}\psi}{\mathrm{d}x_i} - \frac{\mathrm{d}f}{\mathrm{d}x_i}}{\frac{\mathrm{d}\psi}{\mathrm{d}x_i}} \right|. \tag{7.30}$$

Using the Taylor approximation for $f(x_i+\epsilon)$ we can also observe that the relative error scales with

$$\delta_{\mathrm{rel}}(\epsilon) \approx \frac{\epsilon}{2} \left| \frac{\frac{\mathrm{d}^2 f}{\mathrm{d}x_i^2}}{\frac{\mathrm{d}f}{\mathrm{d}x_i}} \right| + \mathcal{O}(\epsilon^2). \tag{7.31}$$

In a log-log plot of $\delta_{\mathrm{rel}}(\epsilon)$ versus ϵ, we can make a prediction of the expected shape of the convergence of finite differences, expressing this relationship as

$$\log(\delta_{\mathrm{rel}}(\epsilon)) \approx \log\left(\left| \frac{\frac{\mathrm{d}^2 f}{\mathrm{d}x_i^2}}{2\frac{\mathrm{d}f}{\mathrm{d}x_i}} \right| \right) + \log(\epsilon), \tag{7.32}$$

where the first variable is a constant, the slope of this plot is ≈ 1, indicating first-order convergence.

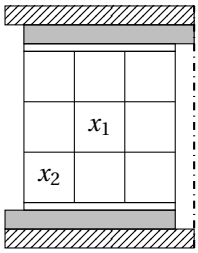

Figure 7.2.: Mesh simplification description for a coarse mesh from the model used in Section 3.4 and location of the studied design variables for the finite differences validation, x_1 and x_2, in one of the thermocouple legs.

We now apply finite differences to the same model as for the optimization in Figure 3.2f with a reduced mesh to 3x3 within each semiconductor. To validate the sensitivity results

obtained via topology optimization, the error is plotted as a function of ϵ. The perturbation ϵ is varied, and the error is computed for each value. This comparison provides insight into the accuracy of the finite difference method relative to the FEM solution. This figure shows a linear rate of convergence for all objectives and constraints until the rounding errors dominate the problem for $\epsilon < 10^{-6}$ and errors under 10^{-5} at these perturbation levels. The volume constraint is removed from this validation as it can be validated through the volume calculation of the elements themselves.

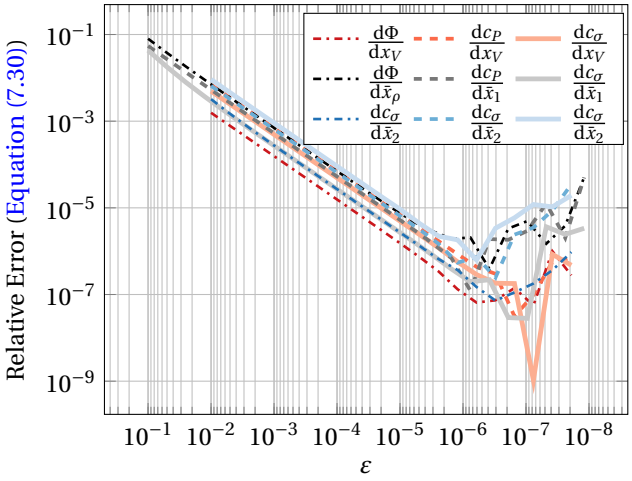

Figure 7.3.: Convergence of Error with ϵ for each constraint and objective function used.

Appendix E Thermoelectromechanical Material properties

There are multiple studies of the properties of thermoelectrical materials within the literature. We use the measured thermoelectric values for Bi_2Te_3 from Witting *et al.* [2] where the effect of doping agents in Bi_2Te_3 over its material properties is studied. The thermal expansion values with respect to temperature for Bi_2Te_3 are taken from Pavlova, Shtern, and Mironov [3]. The experimental data have been fitted to a sixth-order polynomial,

$$f_p(T) = a_6 T^6 + a_5 T^5 + a_4 T^4 + a_3 T^3 + a_2 T^2 + a_1 T + a_0 \tag{7.33}$$

which allows the capture of the quadratic behaviour of the materials. For each material property, we fit this polynomial to the temperature ranges provided and to a constant value for higher or lower values to avoid discontinuities in the definition,

$$f(T) = \begin{cases} f_p(T_0) & \text{if } T < T_0\,, \\ f_p(T) & \text{if } T_0 \le T \le T_1 \\ f_p(T_1) & \text{if } T > T_1 \end{cases} \tag{7.34}$$

To have a continuous material model up to $\mathscr{C}^1$, we enforce a zero derivative in the intersection point of the functions, $f_p'(T_0) = f_p'(T_1) = 0$. Notice that for an accurate result, we must ensure the optimization lies within the measured temperature range.

The derivatives of these functions with respect to the temperature required to calculate the residual can be written as,

$$f'(T) = \begin{cases} 0 & \text{if } T < T_0 \\ f_p'(T) & \text{if } T_0 \le T \le T_1 \\ 0 & \text{if } T > T_1 \end{cases} \tag{7.35}$$

where $f'(T)$ is,

$$f_p'(T) = 6a_6 T^5 + 5a_5 T^4 + 4a_4 T^3 + 3a_3 T^2 + 2a_2 T + a_1\,. \tag{7.36}$$

The temperature dependent material properties used are plotted in Figure 7.4 together with the experimental data as dots and each polynomial coefficients are provided in Table 7.4.

The other materials involved in a thermocouple are treated as temperature constants for simplicity purposes, and their properties are summarized in Table 7.5.

In all these materials, the Seebeck coefficient is considered to be zero, either due to the lack of electrical conductivity of the material or for a symmetrical material distribution in the models.

Note that E represents Young's modulus, ν represents Poisson's ratio, κ represents thermal conductivity, α represents the Seebeck coefficient, α_T represents the coefficient of thermal expansion, and σ is the electrical conductivity. The σ value of the ceramic AlN is not provided as there is no expected electrical current flow through the material. The mechanical properties of Bi_2Te_3 are also considered equal for the $p+$ and $n-$ semiconductors. In terms of the α, all materials are considered to have zero thermal stresses at 25.15 °C.

Fit	a_0	a_1	a_2	a_3	a_4	a_5	a_6	T_0(K)	T_1(K)	f_p(350 K)
κ	-76.4	1.23	-7.64e-3	2.45e-05	-4.4e-08	4.1e-11	-1.6e-14	235.48	605.34	2.717 W/(m K)
σ_p	-2.73e7	5.88e5	-4996	21.95	-0.053	6.70e-05	-3.46e-08	173.5	451.5	$1.84e05$ S/m
σ_n	-3.31e7	4.75e5	-2768	8.48	-0.0144	1.29e-05	-4.75e-09	289.17	618.62	$1.79E05$ S/m
α_p	0.00396	-8.22e-05	7.00e-07	-3.09e-09	7.47e-12	-9.40e-15	4.80e-18	177.2	478.2	$1.30e-04$ V/K
α_n	-0.0253	3.79e-4	-2.37e-06	7.81e-09	-1.44e-11	1.42e-14	-5.75e-18	292.8	529.42	$-1.36E-04$ V/K
α_T	2.84e-06	9.25e-08	-2.34e-10	3.67e-13	-9.49e-16	1.64e-18	-9.47e-22	35	650	$14.86e-61$/K

Table 7.4.: Coefficients for the 6^{th} order polynomial fit for each semiconductor material according to Equation (7.36). The temperature range for the fit is represented in the last 2 columns as T_0 and T_1. The evaluated value at $T = 350$ K is shown in the last column.

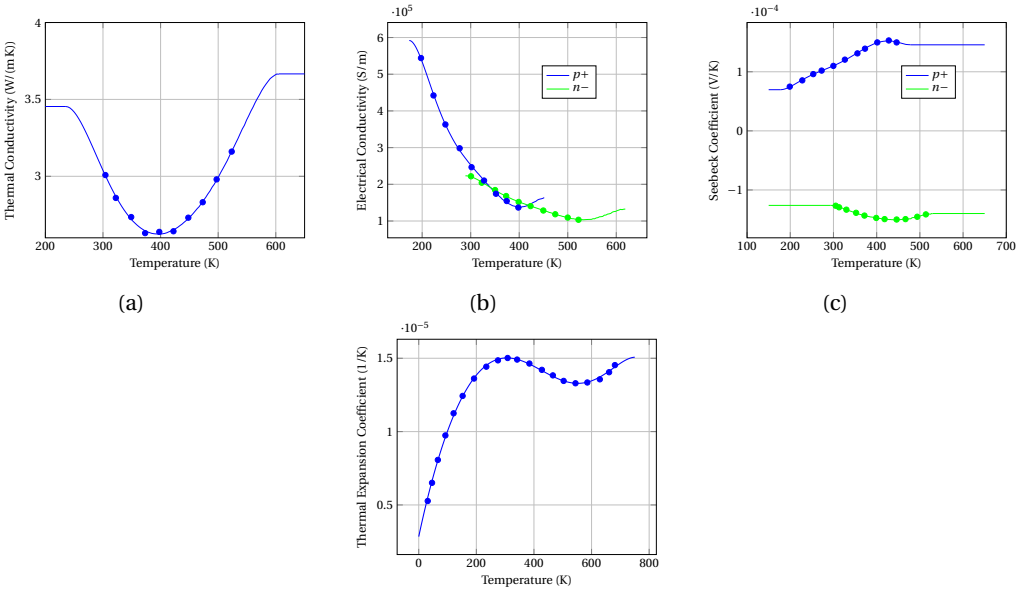

Figure 7.4.: Material properties of the semiconductor materials used in the optimization, including their Seebeck coefficients, and their thermal and electrical conductivities with respect to the temperature in °C. The results are plotted for the $p+$ and $n-$ semiconductors when the used data differs for each one of them.

	E (GPa)	ν	κ (WK/m)	$\sigma \times 10^7$ (S/m)	$\alpha_T \times 10^{-6}$ (1/K)
Cu	130	0.34	385	59.9	17
AlN	300	0.21	319	—	5
SAC	70	0.42	50	8.5	24
Bi_2Te_3	61.6	0.241	Figure 7.4	Figure 7.4	Figure 7.4
Air	—	—	0.033	—	—

Table 7.5.: Temperature Constant Material Properties for the models used in Section 3.4.

Appendix F Scintillation Detector Material

In this appendix, we provide the material data used in the model within GEANT4 to facilitate the reproduction of the results in this paper.

Appendix F.1 Material composition

The material composition and density are required for the energy deposition calculations. The properties of all the material involved are summarized in Table 7.6.

	Composition	Density (kg/m^3)
LYSO:Ce	$(Lu_{2(1-x)}Y_{2x}SiO_5)_yCe_{1-y}$	7125
Epoxy Resin	$H_{32}N_2C_{15}O_4$	1160
RTV3145	$H_5Si_3O_5C_5$	1270
Silicon	Si	2400
SiO_2	SiO_2	2201
FR_4	$(SiO_2)_{0.528}Epoxy_{(0.472)}$	1451

Table 7.6.: Material compositions used in the GEANT4 BTL module model.

The LYSO:Ce composition, follows a density value dependent upon the Y content that was fitted in Addesa *et al.* [4] to the linear equation:

$$\rho_L = 7390 - 3020x\,. \tag{7.37}$$

In Equation (7.37), x represents the Y percentage and its relation to the LYSO:Ce density, ρ_L, in kg/m^3. Fixing the density of the crystal to the most common measured value in Addesa *et al.* [4], 7125 kg/m^3, we obtain a percentage of the mass of Ce given by $x = 0.0877$ in the LYSO:Ce composition. The percentage of Ce is fixed by a given value of $y = 0.981$, equivalent to 0.19% of Ce.

Appendix F.2 Optical Properties

In the context of the light propagation within the detector assembly, the material properties to include in the model are the refractive index, absorption coefficient, and scattering coefficient of the different materials involved.

Refraction Index

An accurate refractive index is required for a correct material boundary simulation for each photon trace. Furthermore, the different wavelengths and the dependence of the refractive index on their energy can lead to different outcomes.

The refractive index of the LYSO, optical glue coupling and epoxy resin is summarized in Figure 7.5. These materials are the most influential in the path of the photons as they will need to go through their interfaces before reaching the photodetectors.

For the rest of the materials, we assume a constant refractive index with respect to the involved photon wavelengths. These properties are summarized in Table 7.7.

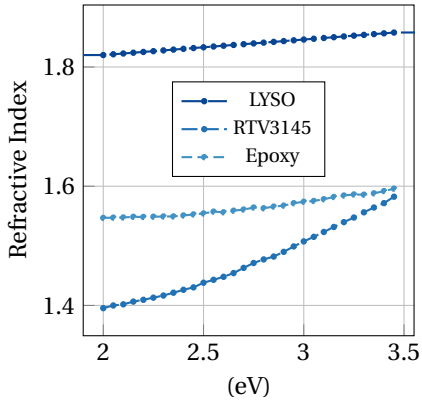

Figure 7.5.: LYSO [4], optical glue (RTV3145), and protective epoxy resin [5] refractive index depending on the photon wavelength or energy.

	Refractive Index	References
Air	1	Agostinelli *et al.* [6]
Si	4	*Refractive Index Database* [7]
SiO_2	1.4585	*Refractive Index Database* [7]
FR_4	1.4585	*Refractive Index Database* [7]

Table 7.7.: Material compositions used in the GEANT4 BTL module model.

Self-absorption Lengths

In the context of optical materials, wherein photons traverse the majority of their trajectory en route to the Silicon Photomultiplier (SiPM), the potential for re-absorption is a noteworthy consideration. To address this concern, we establish the self-absorption length of both the adhesive substance and the LYSO with respect to photon energy, as illustrated in Figure 7.6. These data serve as input for the GEANT4 simulation framework, enabling the determination of a threshold path length for the termination of generated photons.

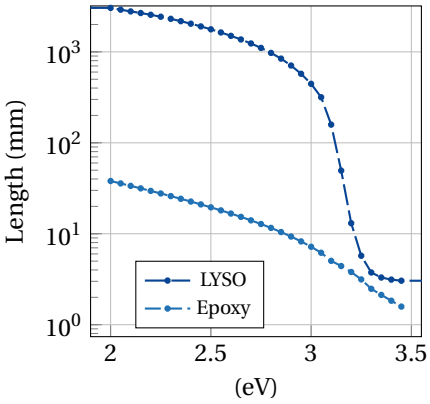

Figure 7.6.: Self-absorption and scattering lengths for LYSO [8], and protective epoxy resin depending on the photon wavelength or energy [5].

The rest of the components do not include self-absorption for simplification purposes.

Scattering Lengths

The scattering length, as illustrated in Figure 7.7, is delineated across the X-axis, representing the photon energies. Notably, while the scattering length for LYSO is meticulously characterized and highlighted in the figure, it is intentionally neglected for all other materials.

Enhanced-specular-reflector (ESR)

In order to prevent the loss of photons in the surrounding environment and to reduce the occurrence of false positives, it is common practice to coat or cover scintillators with a reflective layer. In our model, we employ an enhanced specular reflector (ESR) layer covering the LYSO, maximizing the air-LYSO contact area to capitalize on the substantial refractive index difference between these materials, which enhances the probability of photon reflection back into LYSO:Ce [9]. To achieve this, we use the *polishedbackpainted* model of GEANT4, which accounts for a thin layer of air without the need for an explicit geometric definition.

The ESR is assumed to be a perfect specular reflector [10], which does not include backscatter, Lambertian reflection, or specular spikes, as supported by the measure-

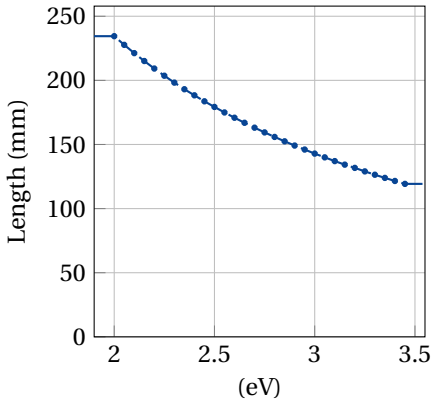

Figure 7.7.: Scattering length for LYSO [8].

ments presented in Padera and Lynch [11] and Janecek [12]. The reflectivity of the ESR, which represents the likelihood of an impacting photon to be reflected rather than absorbed – is illustrated in Figure 7.8.

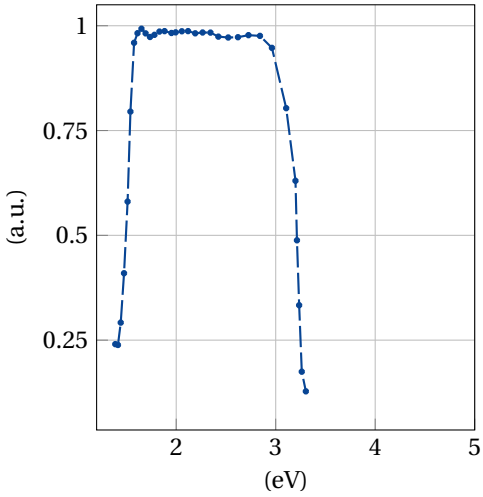

Figure 7.8.: ESR reflectivity as a function of the incident photon wavelength for multiple incident angles [11].

From the data available for multiple impact angles, we use the most limiting at 60 deg. This reflectivity still provides reflectivity values higher than 0.98 for the wavelengths measured by the LYSO scintillator.

Appendix F.3 LYSO:Ce scintillation

The LYSO:Ce crystals or scintillator for the particle detector need to be characterized in terms of light yield (L_Y) – the number of photons created within the scintillator per unit of energy deposited. To ensure accuracy in the model, we rely on the crystal properties measured in Addesa *et al.* [4] and M. Campana and R. Paramatti [13]. In contrast, other research works, such as Van Der Laan *et al.* [8] and Brown, Brunner, and Schaart [14], propose their own models, which further validate the material properties chosen.

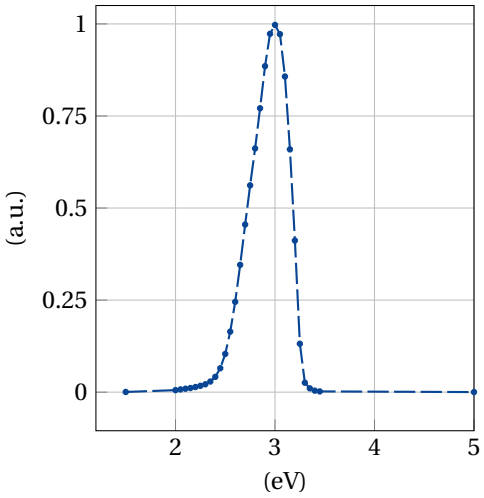

Figure 7.9.: LYSO emission spectra [4, 13].

Figure 7.9 provides the intensity of photon creation for each possible wavelength, with a nominal L_Y of 40000 γ/MeV.

Furthermore, to simplify the model, we select an r_s of zero with no statistical variance of L_Y. Finally, the time characteristics are given as a single rise and decay times of 60 ns and 39.1 µs respectively. These values are summarized in Table 7.8. These timing quantities for the LYSO scintillation measured in M. Campana and R. Paramatti [13] by the light detected from the crystals encompass the characteristic delay from the Ce_3^+ absorption and re-emission.

r_s	τ_r (ns)	τ_d (µs)	L_Y (γ/MeV)
0	60	39.1	40000

Table 7.8.: Characteristics of the LYSO scintillation process used in GEANT4 [13].

Appendix F.4 Silicon Photomultiplier (SiPM) detection

The SiPMs have a certain photon detection efficiency (PDE), which determines if a photon impact is detected. This PDE depends upon the photon energy and the overvoltage

applied. For this purpose, we use the PDE characteristics given by Hamamatsu of the S13360-1325CS SiPM adimensionalized with respect to its 420 nm value, Figure 7.10.

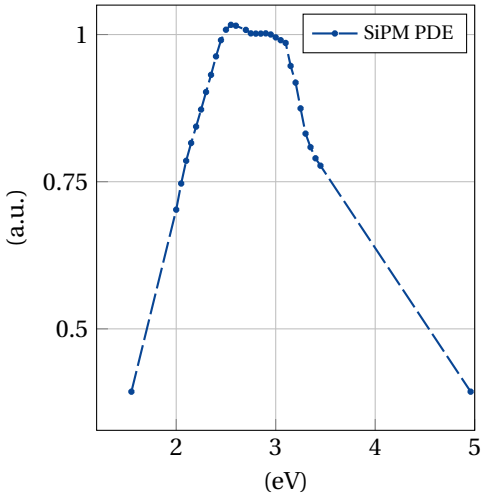

Figure 7.10.: 420 nm S13360-1325CS normalized PDE_λ.

The measured dependence of the rest of the spectrum is considered linear with respect to the 420 nm peak and is represented by the formula Equation (4.6).

Appendix G COMSOL material properties

This appendix summarizes all material properties required to run the scintillation simulations within COMSOL.

For all subsequent models, we use the defined optical material properties summarized in Table 7.9. This table includes the required optical properties for the LYSO, glue, resin and photodetector models, considered a Si block.

Material Name	LYSO	Glue	Resin	Silicon
Refractive Index (n)	1.8	1.5	1.55	5.099
Relative Permeability	1	1	1	1
Electrical Conductivity	0	0	0	0
Extinction Coefficient (k)	8.356e-05	2.571e-06	4.178e-07	0.2379
References	[4, 6–8]	[5, 7]	[5, 7]	[7]

Table 7.9.: Optical Material Properties.

We also define in Section 5.2.2 the parameters on which the scintillation photon generation process depends. The parameters required for the electrical amplitude wave introduced in the COMSOL model are defined in Table 7.10. These parameters influence the boundary condition of the introduced electrical amplitude wave according to Equation (5.14).

Properties	t_d (ns)	t_r (µs)	A	β	v (m/s)	T
	39	60	1e3	$\frac{t_r}{100}$	$c \times 0.99$	$5 \times t_d$

Table 7.10.: Scintillation parameters used within the COMSOL FEM transient model.

In this last table, a new parameter, A, is defined to introduce a modifier to the electric field amplitude, scaling it as a proportional coefficient. This parameter is an experimentally obtained value to avoid numerical precision issues, increasing the energy deposition values to values close to unity.

In GEANT4, these parameters depend on the wavelength of the emitted photons, including the absorption lengths converted to an extinction coefficient and refractive indexes. The values used within COMSOL are kept constant for simplicity, using a single pulse of the peak of 420 nm. The parameters required to calculate the number of photons created in GEANT4 for a particle impact include the definition of the yield Y of LYSO and the energy deposition by the ionizing particles per track length. These values are extracted from GEANT4 and summarized in Table 7.11.

Properties	Y ph/MeV	$\frac{dE}{dx}$ MeV/mm	Formula
	40000	2.9	$(Lu_{2(1-0.9123)}Y_{0.1754}SiO_5)_{0.981}Ce_{0.019}$

Table 7.11.: Scintillation parameters used within the GEANT4.

Appendix H Replication of results

In this section, we detail the data availability and repositories for the replication of results from each chapter in this dissertation.

- chapter 2 and chapter 3: All required code to replicate the results can be found in the TOTEM_M repository as the MATLAB version of TOTEM [15].
- chapter 4: The code used to obtain the results in this chapter can be found in the SO-CRYSTAL repository [16].
- chapter 5: The COMSOL files used for the models in this chapter can be found in the following repository together with the MATLAB codes required to run the scintillation optimization, [17]. The GEANT4 codes used for validation have been run using the SO-CRYSTAL repository.

All other data can be extracted from the plots and data provided in this dissertation or can be provided by the main author through the email provided at the beginning of this dissertation or *g.realesguti@gmail.com*.

References

[1] M. Hoit and K. Krishnamurthy. “A 14-Point reduced integration scheme for solid elements”. In: *Computers and Structures* 54.4 (1995), pp. 725–730. ISSN: 00457949. DOI: 10.1016/0045-7949(94)00360-F.

[2] I. T. Witting, T. C. Chasapis, F. Ricci, M. Peters, N. A. Heinz, G. Hautier, and G. J. Snyder. “The Thermoelectric Properties of Bismuth Telluride”. In: *Advanced Electronic Materials* 5.6 (2019), pp. 1–20. ISSN: 2199160X. DOI: 10.1002/aelm.201800904.

[3] L. M. Pavlova, Y. I. Shtern, and R. E. Mironov. “Thermal expansion of bismuth telluride”. In: *High Temperature* 49.3 (June 2011), pp. 369–379. ISSN: 1608-3156. DOI: 10.1134/S0018151X1103014X. URL: https://doi.org/10.1134/S0018151X1103014X.

[4] F. Addesa, P. Barria, R. Bianco, M. Campana, F. Cavallari, A. Cemmi, M. Cipriani, I. Dafinei, B. D’Orsi, D. del Re, M. Diemoz, G. D’Imperio, E. Di Marco, I. Di Sarcina, M. Enculescu, E. Longo, M. Lucchini, F. Marchegiani, P. Meridiani, S. Nisi, G. Organtini, F. Pandolfi, R. Paramatti, V. Pettinacci, C. Quaranta, S. Rahatlou, C. Rovelli, F. Santanastasio, L. Soffi, R. Tramontano, and C. Tully. “Comparative characterization study of LYSO:Ce crystals for timing applications”. In: *Journal of Instrumentation* 17.08 (Aug. 2022), P08028. DOI: 10.1088/1748-0221/17/08/P08028. URL: https://dx.doi.org/10.1088/1748-0221/17/08/P08028.

[5] M. Montecchi and Q. Ingram. “Study of some optical glues for the Compact Muon Solenoid at the Large Hadron Collider of CERN”. In: *Nuclear Instruments and Methods in Physics Research, Section A: Accelerators, Spectrometers, Detectors and Associated Equipment* 465.2-3 (2001), pp. 329–345. ISSN: 01689002. DOI: 10.1016/S0168-9002(01)00678-7. URL: https://doi.org/10.1016/S0168-9002(01)00678-7.

[6] S. Agostinelli *et al.* “GEANT4 - A simulation toolkit”. In: *Nuclear Instruments and Methods in Physics Research, Section A: Accelerators, Spectrometers, Detectors and Associated Equipment* 506.3 (2003), pp. 250–303. ISSN: 01689002. DOI: 10.1016/S0168-9002(03)01368-8.

[7] *Refractive Index Database*. https://refractiveindex.info/.

[8] D. J. Van Der Laan, D. R. Schaart, M. C. Maas, F. J. Beekman, P. Bruyndonckx, and C. W. Van Eijk. “Optical simulation of monolithic scintillator detectors using GATE/GEANT4”. In: *Physics in Medicine and Biology* 55.6 (2010), pp. 1659–1675. ISSN: 00319155. DOI: 10.1088/0031-9155/55/6/009. URL: http://dx.doi.org/10.1088/0031-9155/55/6/009.

[9] F. Loignon-Houle, C. M. Pepin, S. A. Charlebois, and R. Lecomte. “Reflectivity quenching of ESR multilayer polymer film reflector in optically bonded scintillator arrays”. In: *Nuclear Instruments and Methods in Physics Research, Section A: Accelerators, Spectrometers, Detectors and Associated Equipment* 851 (Apr. 2017), pp. 62–67. ISSN: 01689002. DOI: 10.1016/j.nima.2017.01.051. URL: http://dx.doi.org/10.1016/j.nima.2017.01.051.

[10] M. Janecek and W. W. Moses. “Optical Reflectance Measurements for Commonly Used Reflectors Publication Date”. In: (2009). URL: https://escholarship.org/uc/item/82r9k9rn.

[11] F. Padera and C. Lynch. “Measurement of Enhanced Specular Reflector (ESR) Films Using a LAMBDA 1050+ UV/Vis/NIR Spectrometer and URA Accessory”. In: (2015). URL: https://www.perkinelmer.com/.

[12] M. Janecek. “Reflectivity Spectra for Commonly Used Reflectors Permalink”. In: (2012). URL: https://escholarship.org/uc/item/75v883cf.

[13] M. Campana and R. Paramatti. *Study of light output and characterization of LYSO crystals for the new timing detector of the CMS experiment*. Tech. rep. 2018.

[14] J. M. C. Brown, S. E. Brunner, and D. R. Schaart. “A High Count-Rate and Depth-of-Interaction Resolving Single-Layered One-Side Readout Pixelated Scintillator Crystal Array for PET Applications”. In: *IEEE Transactions on Radiation and Plasma Medical Sciences* 4.3 (2020), pp. 361–370. DOI: 10.1109/TRPMS.2019.2948106.

[15] G. Reales Gutierrez. *TOTEM_M*. Version 0.3.0. May 2025. DOI: 10.5281/zenodo.15511240. URL: https://doi.org/10.5281/zenodo.15511240.

[16] G. Reales Gutierrez. *SO-CRYSTAL*. Version v1.0.0. May 2024. DOI: 10.5281/zenodo.11127532. URL: https://doi.org/10.5281/zenodo.11127532.

[17] G. Reales Gutierrez. *SCINTILLATION_COMSOL: Initial Release*. Version 0.1.0. June 2024. DOI: 10.5281/zenodo.12534294. URL: https://doi.org/10.5281/zenodo.12534294.

Acknowledgements

I would like to thank all institutes and projects involved in this dissertation, including the support from TU DELFT, CALTECH and the CERN Doctoral programme, and the CMS US collaboration, who have put their effort to make this PhD and the MTD detector a reality.

This thesis started as a simple idea to continue my Technical Programme at CERN as a researcher on the design of MTD. I am really thankful to all the support provided by Dr. Adolf Bornheim, who believed in this project from the start and provided me the opportunity to keep collaborating for the discovery of new physics through the Minimum Ionising Particle Timing Detector.

I am also thankful to all professors involved in TUD who have had to manage a PhD student 854 km away. I thank Prof. van Keulen for accepting this collaboration, introducing me to TopOpt and following up with the project as much as possible all these years. I thank Dr. Goosen for his input into the physics of the project and for standing with me all along. I finally want to thank Dr. Aragón for all the feedback provided, his patience, and for teaching me how to present and write from scratch once again.

I also want to thank all my friends and colleagues at CERN who helped me avoid focusing on my PhD as much as they could and to my friends back in Spain that never forgot about me.

I also want to thank my parents for their drafting and listening skills during this period and all previous to it.

Finally, I am forever grateful to my best girlfriend who has stood by my side, even with late dinners, phone calls during holidays, last-minute trips, and who allowed me to pass through my Go-NoGo.